Electrochemistry of Silver Nanoparticles

A thesis submitted for the degree of
Doctor of Philosophy
in Physical & Theoretical Chemistry

Her Shuang Toh
Keble College

July 2015

Abstract

This thesis presents findings realising two main objectives. The first aim is to investigate the electrochemical detection of nanomaterials with an emphasis on silver nanoparticles. The second goal is to employ silver nanoparticles in electroanalysis to aid in the detection of other analytes.

First, the detection of silver nanoparticles was demostrated through two different electrochemical methods, stripping voltammetry and 'nano-impacts'. For stripping voltammetry, the potential of metallic nanoparticles oxidation was quantified by various new analytical expressions for peak potential. For the novel method of 'nano-impacts', individual silver nanoparticles were successfully detected in an optically opaque suspension. Then, a comparison between the two techniques was achieved via the oxidation of silver nanoparticles with different capping agents. Strong capping agent effects was found for stripping voltammetry and one may markedly underestimate the amount of silver nanoparticle present on the electrode surface. The electrochemical sizing of nanoparticles via 'nano-impacts' remained unaffected by the capping agent effect. Amidst the study on the various types of capping agent, it was discovered that cetyltrimethylammonium bromide (CTAB) is electroactive due to the oxidation of its bromide content. This inspired the use of 'nano-impacts' to detect the presence of large CTAB micelles which self-assembled at concentrations above the critical micelle concentration.

Next, various types of silver nanoparticles were applied to different electroanalytical systems to aid in the measurement of other analytes. (a) Small silver nuclei, remaining after the oxidative stripping of an electrode modified by silver nanoparticle suspension drop casting, allowed subsequent signal enhancement (at least a factor of three) in anodic stripping voltammetry of silver ions. (b) The thermodynamic favourable formation of silver halide complexes allowed the silver nanoparticle modified electrode to analyse the halide content of a solution. Hence, a proof-of-concept for an electrochemical sensor based on silver nanoparticle modified electrode for chloride ions was established. This might be applied to the pre-screening of cystic fibrosis, a genetic disease detrimental to many infants' lives. (c) Another key halide in human body, iodide ions, was also measured using a related concept. The level of iodide ions in synthetic human urine was determined.

Last, the strong affinity of silver to thiol groups also warranted a study devoted to their interaction through electrochemical and spectroscopic measurements. It was found that there is no general mechanism for silver-thiol interaction and each thiol must be treated as a separate entity.

Acknowledgement

First, I would like to thank Prof. Richard Compton, for all his advice and support. Thank you for your open-door policy and all the effort you spend on students. I am really lucky to find a boss with your passion to teach, guide and nurture. Please do not ever lose this enthusiasm!

Thank you to Prof. Martin Pumera for introducing me to the world of electrochemistry and NRF-EWI (National Research Foundatin-Environment and Water Industry Programme Office). Without the scholarship from NRF-EWI, I would not have the opportunity to study here.

To Chris, a big thank you for all your help and accomadating support. I was never the easiest student to supervise due to my stubborn streak. Thank you for not giving up! I have grown a lot under your guidance. I am proud to have work under your wing.

Thank you, Kristina, for going through so much trouble to co-ordinate with Dresden. TEM, SEM and ICP-OES would not have been possible without your help. I absolutely adore the high resolution TEM image Christine took for us.

Enormous thanks goes to my partner-in-crime in the lab, Patty! We have learn and grown so much due to our conflicting ideas and style. I am (hopefully?) less stubborn and your creative flair has definitely thrived. I am so proud that you are using Blender instead of Paint! Be it bouncing and discussing ideas, paper and thesis proof-reading, a place to sleepover during fire alarms or advice on life, thank you for being there. Life in Oxford would have been dull without you.

To Denise, Emma, Dia, Jeffrey, Tom, Sam, Graziela, Crystal, Ivana, Xiao Jun, Joanna, Chris and many more, the Compton group members of past and present have always made me feel welcome and added fun to lab life. The crazy things we have done (12 star jumps at 12.12 pm on 12 Dec '12, tapping tables and opening cabinents to find the origin of potentiostat noise) are fond memories as I remincise the past. Enno, thank you for answering my silly questions on fundamentals!

To Kerstin, thank you very much for reaching out a helping hand to teach me NTA and DLS.

A big thank you goes out to the support staff (Levi, Paul, Bill, Phil and Charlie) for going the extra mile to help. Having ran across all three departments of chemistry for paraffin oil and dragging a nitrogen cyclinder across icy road always reminds me of the tough jobs the unsung heroes do daily.

Thank you to the many friends I have met here who help me maintain my work-life balance! You guys are the reason behind my reputation of 'travelling too much'.

Lastly, thank you to my family for all the love, care and willingness to learn 'Skype'!

Contents

Publications

The publications are listed in chronological order.

The Anodic Stripping Voltammetry of Nanoparticles: Electrochemical Evidence for the Surface Agglomeration of Silver Nanoparticles
H. S. Toh, C. Batchelor-McAuley, K. Tschulik, M. Uhlemann, A. Crossley, R. G. Compton, *Nanoscale* **2013**, *5*, 4884-4893.

Electrochemical Detection of Chloride Levels in Sweat using Silver Nanoparticles: A Basis for the Preliminary Screening for Cystic Fibrosis
H. S. Toh, C. Batchelor-McAuley, K. Tschulik, R. G. Compton, *Analyst* **2013**, *138*, 4292-4297.

UK Patent Application Number 1309055.0 (submitted by R. G. Compton, H. S. Toh, K. Tschulik and C. Batchelor-McAuley)

The Surface Energy of Single Nanoparticles Probed via Anodic Stripping Voltammetry
C. C. M. Neumann, C. Batchelor-McAuley, K. Tschulik, H. S. Toh, P. Shumbula, J. Pillay, R. Tshikhudo, R. G. Compton, *ChemElectroChem* **2014**, *1*, 87-89.

Electrochemical Studies of Silver Nanoparticles: A Guide for Experimentalists and a Perspective
K. Tschulik, C. Batchelor-McAuley, H. S. Toh, E. J. Stuart, R. G. Compton, *Phys. Chem. Chem. Phys.* **2014**, *16*, 616-623.

A Proof-of-concept – Using Pre-created Nucleation Centres to Improve the Limit of Detection in Anodic Stripping Voltammetry
H. S. Toh, C. Batchelor-McAuley, K. Tschulik, C. Damm, R. G. Compton, *Sens. Actuators, B* **2014**, *193*, 315-319.

Chemical Interactions between Silver Nanoparticles and Thiols: A Comparison of Mercaptohexanol against Cysteine
H. S. Toh, C. Batchelor-McAuley, K. Tschulik, R. G. Compton, *Sci. China: Chem.* **2014**, *57*, 1199-1210.

Electrochemical Quantification of Iodide Ions in Synthetic Urine using Silver Nanoparticles: A Proof-of-concept
H. S. Toh, K. Tschulik, C. Batchelor-McAuley, R. G. Compton, *Analyst* **2014**, *139*, 3986-3990.

Anodic Stripping Voltammetry of Silver Nanoparticles: Aggregation leads to Incomplete Stripping
S. J. Cloake, H. S. Toh, P. T. Lee, C. Salter, C. Johnston, R. G. Compton, *ChemistryOpen* **2015**, *4*, 22-26.

The Influence of the Capping Agent on the Oxidation of Silver Nanoparticles: Nano-impacts versus Stripping Voltammetry
H. S. Toh, K. Jurkschat, R. G. Compton, *Chem.-Eur. J.* **2015**, 21, 2998-3004.

'Nano-impacts': An Electrochemical Technique for Nanoparticle Sizing in Optically Opaque Solutions
H. S. Toh, R. G. Compton, *ChemistryOpen* **2015**, *4*, 261-263.

Nanoelectrocatalytic Oxidation of Lactic Acid Using Nickel Nanoparticles
G. C. Sedenho, P. T. Lee, H. S. Toh, C. Salter, C. Johnston, N. R. Stradiotto, R. G. Compton, *J. Phys. Chem. C* **2015**, *119*, 6896-6905.

The electro-oxidation of lactic acid at platinum particles and polycrystalline platinum electrode
G. C. Sedenho, P. T. Lee, H. S. Toh, C. Salter, C. Johnston, N. R. Stradiotto, R. G. Compton, submitted.

Voltammetric Study of the Influence of Various Phosphate Anions on Silver Nanoparticle Oxidation
D. V. Navolotskaya, H. S. Toh, C. Batchelor-McAuley, R. G. Compton, *ChemistryOpen* **2015**. DOI: 10.1002/open.201500100

Electrochemical Detection of Single Micelles through 'Nano-Impacts'
H. S. Toh, R. G. Compton, *Chem. Sci.* **2015**, *6,* 5053-5058.

H. S. Toh and R. G. Compton, *Electrochemical Strategies in Detection Science,* ed. D. W. M. Arrigan, RSC Publishing, Abingdon, 2015, Ch. 5. (Publishing in October 2015)

Roman Symbols

Symbol	Meaning	Units
A_{elec}	Area of Electrode	m^2
A_{NP}	Surface Area of a Nanoparticle	m^2
A_r	Molecular Weight	$g\ mol^{-1}$
$A_{r,Ag}$	Molecular Weight of Silver, 107.9 $g\ mol^{-1}$	
a	Constant for Surface Energy, $\frac{2\gamma A_r}{\rho F}$	$J\ m\ C^{-1}$
C	Concentration of a Species	$mol\ dm^{-3}$
C^*	Bulk Concentration of a Species	$mol\ dm^{-3}$
C_A	Concentration of Species A	$mol\ dm^{-3}$
C_A^0	Concentration of Species A at Electrode Surface	$mol\ dm^{-3}$
C_A^*	Bulk Concentration of Species A	$mol\ dm^{-3}$
C_B	Concentration of Species B	$mol\ dm^{-3}$
C_B^0	Concentration of Species B at Electrode Surface	$mol\ dm^{-3}$
C_1, C_2	Graph Intercept	$mol\ dm^{-3}$
C_{NP}^*	Bulk Concentration of Nanoparticles	$mol\ dm^{-3}$
D	Diffusion Coefficient	$cm^2\ s^{-1}$
D_A	Diffusion Coefficient of Species A	$cm^2\ s^{-1}$
D_{Ag^+}	Diffusion Coefficient of Silver(I) Ion in water, 1.65 x 10^{-9} $cm^2\ s^{-1}$	
D_{NP}	Diffusion Coefficient of Nanoparticle	$cm^2\ s^{-1}$
E	Electrode Potential	V
E_i	Initial Electrode Potential	V
E_f^θ	Formal Electrode Potential	V
$E_{f(Ag/Ag^+)}^\theta$	Formal Potential of Silver/Silver Ion Redox Couple	V
$E_{f(NP)}^\theta$	Formal Electrode Potential for Nanoparticles	V
E_p	Peak Potential	V

F	Faraday Constant, 96 485 C mol^{-1}	
I	Current	A
I_{lim}	Steady-State Current	A
I_p	Peak Current	A
$[I^-]$	Concentration of Iodide Ion	mol dm^{-3}
j	Flux	mol cm^{-2} s^{-1}
j_{NP}	Flux at a Single Nanoparticle	mol cm^{-2} s^{-1}
k^0	Standard Electrochemical Rate Constant	cm s^{-1}
k_B	Boltzmann Constant, 1.38 x 10^{-23} J K^{-1} $molecule^{-1}$	
k_{MT}	Mass Transport Coefficient	m s^{-1}
k_{ox}	Rate Constant for the Oxidation Reaction	cm s^{-1}
k_{red}	Rate Constant for the Reduction Reaction	cm s^{-1}
k_s	Surface Electron Transfer Rate	s^{-1}
$[M^{n+}]$	Concentration of Metallic Species on Nanoparticle Surface	mol dm^{-3}
m_1, m_2	Slope Gradient	A mol^{-1}
N	Number of Moles of Analyte	moles
N_A	Avogadro Constant, 6.022 x 10^{23} mol^{-1}	
N_{impact}	Number of Nanoparticle-Electrode Collision	Dimensionless
N_{surf}	Number of Moles of Surface Immobilised Analyte	moles
N_{NP}	Number of Atoms in a Nanoparticle	atoms
n	Number of Moles of Electrons Transferred per Mole of Reaction	Dimensionless
n'	Number of Electrons Passed before the Rate Determining Step	Dimensionless
n_{NP}	Number of Nanoparticles on Electrode Surface	Dimensionless
Q	Charge	C
q	Charge Passed per Nanoparticle	C
R	Gas Constant, 8.314 J K^{-1} mol^{-1}	
r	Radius	m

r_e	Radius of Electrode	m
r_{hyd}	Hydrodynamic Radius	m
r_{NP}	Radius of a Nanoparticle	m
$r_{NP,t}$	Radius of Nanoparticle at Time t	m
T	Temperature	K
t	Time	s
x	Number of Silver Atoms in a Single Silver Nanoparticle	Dimensionless

Greek Symbols

Symbol	Meaning	Units
α	Transfer Coefficient	Dimensionless
β	Transfer Coefficient	Dimensionless
δ	Diffusional Layer Thickness	m
ϕ_M	Electrostatic Potential at Electrode	V
ϕ_S	Electrostatic Potential at Solution Phase	V
Γ_A^0	Surface Coverage of Species A at Electrode Surface	mol m^{-2}
Γ_{Ag}	Silver Surface Coverage	mol m^{-2}
Γ_M	Metal Surface Coverage	mol m^{-2}
Γ_{NP}	Nanoparticle Surface Coverage	m^{-2}
γ	Surface Energy	J m^{-2}
γ_A	Activity Coefficient of Species A	Dimensionless
γ_{Ag}	Surface Energy of Silver Nanoparticle	J m^{-2}
γ_B	Activity Coefficient of Species B	Dimensionless
η	Overpotential, $E - E^{\theta}_f$	V
η_l	Viscosity of a Liquid	g cm^{-1} s^{-1}
θ	Dimensionless Potential, $\frac{F}{RT}(E_i + \upsilon t - E^{\theta}_f)$	

$\boldsymbol{\theta_i}$	Initial Dimensionless Potential, $\frac{F}{RT}(E_i - E^{\theta}_f)$	
$\boldsymbol{\rho}$	Density	g m^{-3}
$\boldsymbol{\rho_{Ag}}$	Density of Silver, 10.5 x 10^6 g m^{-3}	
$\boldsymbol{v}$	Scan Rate	V s^{-1}

Other Symbols

Symbol	Meaning	Units
$[\,]^{\boldsymbol{0}}$	Standard Concentration of 1 mol dm^{-3}	

Abbreviations

Symbol	Meaning
Ag_2S	Silver(I) Sulfide
AgSR	Silver(I) Thiolate Complex
$AgSR_c$	Silver(I) Thiolate Complex, R_c = -$C_3H_6NO_2$
$AgSR_m$	Silver(I) Thiolate Complex, R_m = -$(CH_2)_6OH$
BPEI	Branched Polyethylenimine
CdTe	Cadmium Telluride
CF	Cystic Fibrosis
CFTR	Cystic Fibrosis Transmembrane Conductance Regulator
CMC	Critical Micelle Concentration
CTAB	Cetyltrimethylammonium Bromide
DLS	Dynamic Light Scattering
DMSA	Di-Mercaptosuccinic Acid
EDX	Dispersive X-Ray Spectrometer
EU	European Union
FTIR	Fourier Transform Infrared

HOMO	Highest Occupied Molecular Orbital
ICP-MS	Inductively Coupled Plasma Mass Spectroscopy
IHP	Inner Helmholtz Plane
IUPAC	International Union of Pure and Applied Chemistry
KI	Potassium Iodide
LUMO	Lowest Unoccupied Molecular Orbital
MSE	Mercury/Mercurous Sulphate Electrode, $Hg/Hg_2SO_4/K_2SO_4$ (saturated)
NTA	Nanosight Tracking Analysis
NTP	1,4-Nitrothiophenol
OHP	Outer Helmholtz Plane
PEG	Polyethylene Glycol
PVA	Polyvinyl Alcohol
PVP	Polyvinylpyrrolidone
PZC	Potential of Zero Charge
REACH	Registration, Evaluation, Authorisation and Restriction of Chemicals
SCE	Saturated Calomel Electrode, $Hg/Hg_2Cl_2/KCl$(saturated)
SDS	Sodium Dodecyl Sulphate
SEM	Scanning Electron Microscopy
SHE	Standard Hydrogen Electrode, Pt/H_2(1 atm)/H^+(activity of unity)
TEM	Transmission Electron Microscopy
UV-vis	Ultra-violet Visible
XPS	X-ray Photon Spectroscopy
XRD	X-ray Diffraction

Chapter 1 Fundamentals of Electrochemistry

This chapter provides a brief introduction to some of the fundamental concepts in electrochemistry[1-4] which are relevant for the work presented in this thesis. The influence of mass transport and electron transfer kinetics in voltammetry is discussed. The understanding of the key differences between macro electrodes (dimensions of cm or mm) and micro (dimensions of μm) electrodes will aid in the understanding of the experimental results reported later in this thesis.

1.1 The Nernst Equation

Electrochemistry studies the interplay of electrical and chemical effects at an electrode/solution interface.[1] It deals with the electrical current and chemical reactions.[2] Consider the simple heterogeneous electron transfer:

$$A(aq) + e^- \rightleftharpoons B(aq) \qquad \text{Equation 1.1}$$

which may occur at an electrode/solution interface. A and B are a redox couple in the solution phase related by a single electron transfer. If a piece of metal is inserted into the solution consisting of A and B, it may facilitate the electron transfer within the redox couple. Figure 1.1 describes the situation when the electrode has a higher energy than the lowest unoccupied molecular orbital (LUMO) of A, an electron is transferred to A and hence reducing A to B. When the highest occupied molecular orbital (HOMO) of B is of a higher energy compared to the electrode energy level, B loses an electron and is hence oxidised. A dynamic equilibrium can be achieved if the electrode reaches an energy level between the LUMO of A and the HOMO of B and both oxidation and reduction occur at the same rate. At this point of equilibrium, no further net charge is observed and the charge separations at the interface between the electrode and the solution give rise to an electrode potential.[5] The electrode potential in an electrochemical system is measured against a reference electrode with a fixed potential to allow comparison.[5, 6] The concept of a reference electrode is further discussed in Section 1.3.

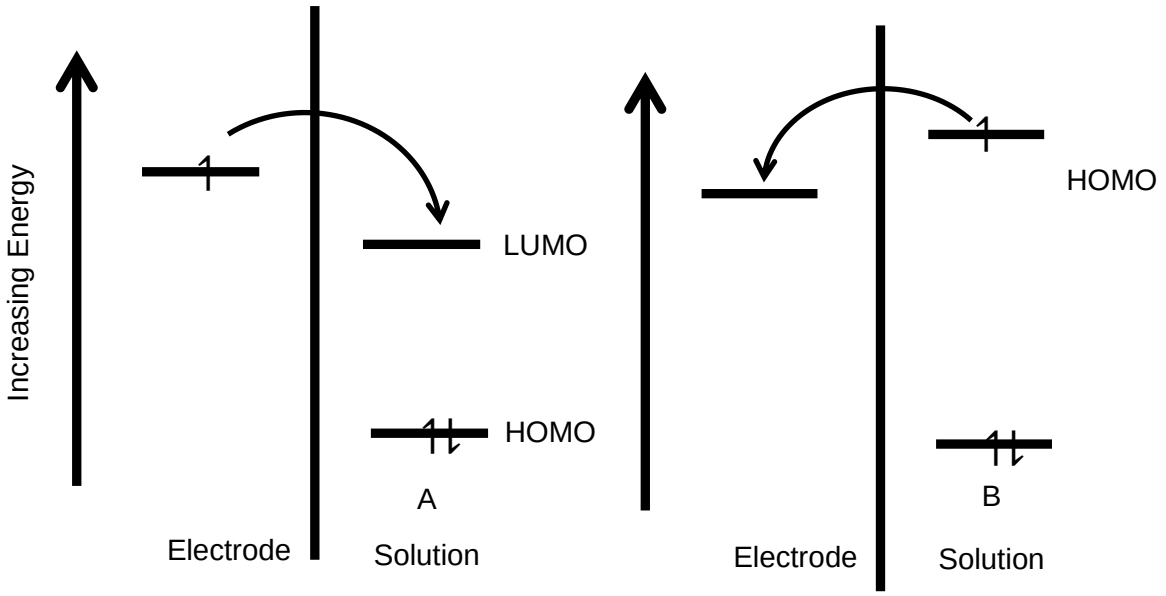

Figure 1.1 A schematic diagram of the energy levels (not to scale) during reduction of A (left) and oxidation of B (right).

The electrode potential is influenced by the concentration of A and B and this relationship is summarised by the Nernst equation,[1]

$$E = E_f^{\theta} + \frac{RT}{F}\ln\left(\frac{C_A^0}{C_B^0}\right) \qquad \text{Equation 1.2}$$

where E is the electrode potential, E_f^{θ} is the formal electrode potential at unit concentration, R is the gas constant of 8.314 J K^{-1} mol^{-1}, T is the temperature in Kelvin and F is the Faraday constant. C_A^0 and C_B^0 are the concentrations of species A and B at the electrode surface respectively. Note that the Nernst equation is only applicable to a system at a dynamic equilibrium. The activity coefficients of the species are embedded within the formal potential, E_f^{θ},

$$E_f^{\theta} = E^{\theta} + \frac{RT}{F}\ln\left(\frac{\gamma_A}{\gamma_B}\right) \qquad \text{Equation 1.3}$$

where E^{θ} is the standard electrode potential at unit activity (activity equals to one). γ_A and γ_B are the activity coefficients of species A and B respectively.

Although the Nernst equation provides a description of the electrode potential for an electrochemical reaction under equilibrium, almost all the electrochemical experiments in this thesis are performed under non-equilibrium situations. The latter are elaborated in Section 1.2.

1.2 Non-equilibrium Electrochemistry

At dynamic equilibrium (Section 1.1), no current flows through the system. In reality, most electrochemists depend on disturbing this equilibrium to obtain information on the redox couple of interest. Take an instance where a potential, E, more positive than the formal potential, E_f^θ, is applied. From Equation 1.2, the ratio of A to B has to increase to conform to the new potential (even though equilibrium is not necessary achieved). Thus, the new potential promotes the oxidation of B to A and an anodic current passes through the working electrode. This change in current with regards to potential or time gives data in the form of voltammograms (discussed in Section 1.4). They aid in the understanding the electrochemical process which occurs on the electrode. There are two main factors that influence the voltammogram and they are further discussed below in Section 1.2.1 (electrode kinetics) and 1.2.2 (mass transport).

1.2.1 Electrode Kinetics

This section deals with the rate of electron transfer. From Equation 1.1, as A is reduced to B, the rate of reaction is related to k_{red} and k_{ox}, which are the rate constants of the reduction and oxidation reaction respectively. They can be defined as:

$$k_{red} = k^0 exp\left[-\frac{\alpha F\eta}{RT}\right] \qquad \text{Equation 1.4}$$

$$k_{ox} = k^0 exp\left[\frac{\beta F\eta}{RT}\right] \qquad \text{Equation 1.5}$$

where R is the gas constant of 8.314 J K^{-1} mol^{-1}, T is the temperature in Kelvin, F is the Faraday constant and k^0 is the standard electrochemical rate constant. α and β are dimensionless transfer coefficients which normally lie in the range from 0 to 1 for an one electron process and usually $\alpha + \beta = 1$. The overpotential, η, is the potential applied relative to the formal potential and is defined as:

$$\eta = E - E_f^\theta \qquad \text{Equation 1.6}$$

The rate of reaction is strongly dependent on the overpotential and the rate constants (k_{red} and k_{ox}). The Butler-Volmer equation (Equation 1.7) explains the relationship between the net current

observed at the electrode/solution interphase, I, the amount of overpotential, η, the standard electrochemical rate constant, k^0, and the concentration of the species involved.[1, 5, 7-9]

$$I = -FA_{elec}k^0\left(exp\left[-\frac{\alpha F\eta}{RT}\right]\cdot C_A^0 - exp\left[\frac{\beta F\eta}{RT}\right]\cdot C_B^0\right) \quad \text{Equation 1.7}$$

where A_{elec} is the area of the electrode. C_A^0 and C_B^0 are the concentrations of species A and B at the electrode surface respectively. Combining Equations 1.4, 1.5 and 1.7, the Butler-Volmer equation can be rewritten in the form:

$$I = FA_{elec}\left(k_{red}\cdot C_A^0 - k_{ox}\cdot C_B^0\right) \quad \text{Equation 1.8}$$

As observed from Equations 1.4, 1.5 and 1.7, the rate of reaction increases when the deviation of the potential from the formal potential increases. From the Butler-Volmer equation, it is seen that the current correlates directly with the rate constants. When the value of the standard rate constant, k^0, is large, the electron transfer rate is faster, more species can be converted and hence a larger current is passed.

1.2.2 Mass Transport

The mass transport of a species involves the movement of the reactants towards the electrode surface and of products away from the electrode surface. If the electron transfer rate is fast, mass transport limits the amount of current passed via the amount of reactant/product moved towards/away from the electrode. The three main modes of mass transport (diffusion, convection and migration) are introduced within this section.

First, diffusion is a phenomenon where a species spontaneously moves down its concentration gradient to maximise entropy. This is quantified by the flux (mol cm^{-2} s^{-1}), j, through Fick's first law where the number of moles of the species passing through a point, x, is given by,

$$j = -D\frac{\partial C}{\partial x} \quad \text{Equation 1.9}$$

where D is the diffusion coefficient of the species involved and $\frac{\partial C}{\partial x}$ is the concentration gradient. The diffusion coefficient ($cm^2\ s^{-1}$) determines how fast a species move across the solution and the negative sign involved in Fick's first law accounts for the species moving from an area of higher concentration to lower concentration.

Fick's second law gives the rate of change in concentration at point x,

$$\frac{\partial C}{\partial t} = D\frac{\partial^2 C}{\partial x^2} \qquad \text{Equation 1.10}$$

One of the solutions of Fick's second law is the Cottrell equation. This equation is applicable to the current response of a single potential step on a large electrode and it is further discussed in Section 1.4.2.

The second form of mass transport is convection. It is the movement of species due to external forces. There are two forms of convection: natural convection and forced convection. Natural convection arises in the presence of a thermal or density gradient within the solution. To minimise natural convection, the electrochemical cell can be kept under strict thermostat control to avoid differences in temperature and to distribute any heat formed at the electrodes as a result of electrolysis. The experimental time can be kept short to avoid the build-up of density gradients. Forced convection comes from actions such as stirring, sonication, solution agitation and forcing a gas to bubble through the solution. Forced convection keeps the diffusion layer to a minimum. The diffusion layer is the distance adjacent to the electrode where the reactant is depleted. Hence, fresh reactant has to move through the diffusion layer before reaching the electrode surface. Since forced convection improves the mass transport rate and ensures that sufficient species is delivered to and removed from the electrode surface, the diffusion layer is compressed, ideally allowing the focus of the study to shift to the influence of electrode kinetics.[10]

The third and final form of mass transport is migration. It is the movement of a charged species in an electric field. The potential drop across the electrode/solution interface generates an electrical field which leads to migration of charged species.[1] This is complicated to model. Hence, in most

electrochemical experiments, a high concentration (> 100 times of the analyte) of inert electrolyte is added to the solution to supress migration. Figure 1.2 depicts a schematic diagram in the presence of a high ion concentration. The arrangement of the ions at the electrode/solution interface forms an electrical double layer so that most of the potential drop, $\phi_M - \phi_S$, occurs within a short distance from the electrode (usually 10 – 20 Å) for electrolyte concentrations of *ca.* 0.1 M or above.[1] If the potential applied at the electrode is more positive than the solution, anions and solvent molecules will adsorb onto the electrode surface, forming the Inner Helmholtz Plane (IHP). The Outer Helmholtz Plane (OHP) consists of solvated anions (which are attracted electrostatically) non-specifically adsorbed to the electrode. The two layers help to maintain electrical charge

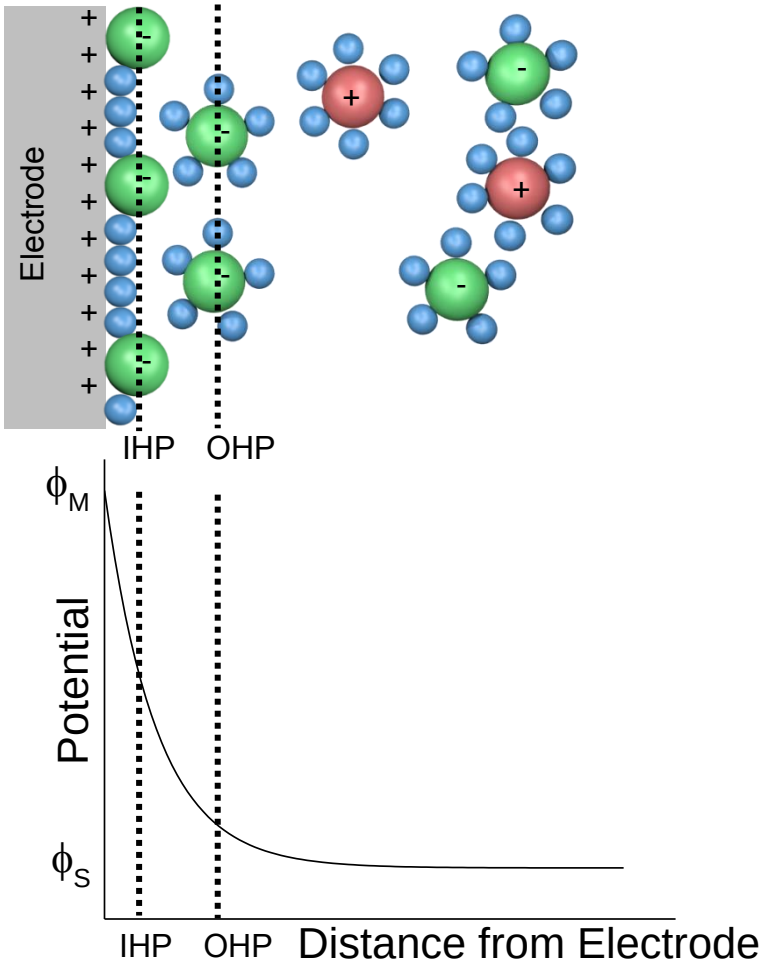

Figure 1.2 Top: Schematic diagram showing the double layer at the electrode-solution interface. Green sphere: anion; red sphere: cation; blue sphere: water molecule. Bottom: Schematic diagram showing the drop in potential across the double layer.

neutrality at the electrode/solution interface. Both solvated cations and anions form the diffuse layer which extends from the OHP to the bulk solution. Due to the compact double layer (OHP and IHP), the large potential gradient (caused by the difference between ϕ_M and ϕ_S) is kept within a short distance of the electrode. This potential drop within the double layer is the driving force for electrochemical reaction to occur when the reactant is within the electron tunnelling distance from the electrode (also around 10 – 20 Å).[1] Thus, with the addition of large amount of electrolyte (> 0.1 M), the potential gradient within the bulk solution is approximately zero where the electrical field is minimised and migration of charged species is reduced.

The addition of the inert electrolyte also has several other advantages apart from minimising migration. It improves the conductivity of aqueous solution which is otherwise highly resistive. This mitigates potential problems such as a loss of current or a requirement of high overpotential associated with high solution resistance. In addition, the presence of electrolyte also keeps the ionic strength relatively constant, allowing the activity of the redox couple to be kept consistent, facilitating the use of formal potentials (as discussed above).

Assuming fast electrode kinetics, the voltammogram is usually controlled by mass transport. However, with the three different modes of mass transport, it is hard to determine the influence of each individual component. Thus, in this thesis, migration and convection are minimised to determine the diffusional controlled response. However, there is an exception in Chapter 6, Section 6.1 where forced convection was induced through solution stirring to maximise the amount of silver ions arriving at the electrode surface prior to electrodeposition. This is discussed in further detail in the corresponding chapter.

1.3 The Electrochemical Cell

In order to observe the changes in an electrochemical reaction under the influence of mass transport and/or electrode kinetics, the classic three electrode system in Figure 1.3 is used to perform electrochemical experiments.[1, 11] The reaction of interest occurs at the interface of the working electrode and solution. Most working electrodes are made of inert materials such as gold,

glassy carbon or platinum to avoid interference with the reaction of interest.[12] At other times, the working electrode may act as a catalyst to promote the redox reaction (e.g. proton reduction on platinum electrode).[13, 14]

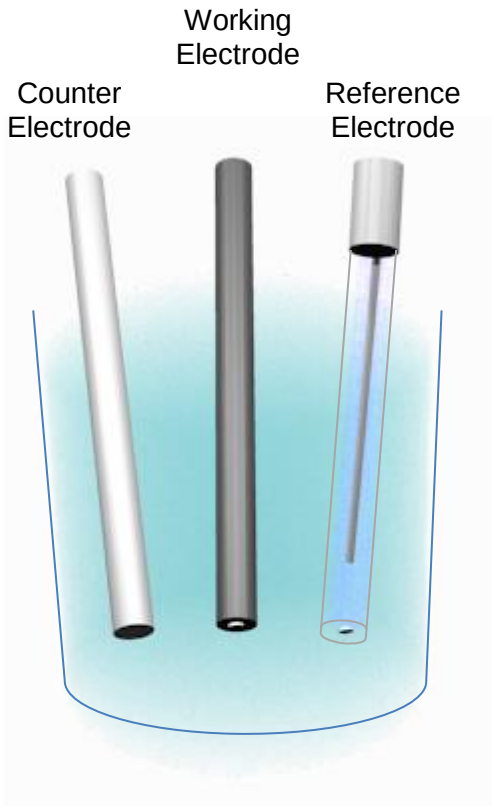

Figure 1.3 A schematic diagram showing the working electrode in the three electrode system.

As mentioned in Section 1.1, the potential of the electrode in an electrochemical system is reported relative to a reference electrode. Conventionally, the potentials are reported against the standard hydrogen electrode (SHE) at 25 °C.[1] A SHE consists of a platinum electrode immersed in a solution containing protons at unity activity and hydrogen gas of pressure 1 atm. However, the difficulty of handling hydrogen gas has driven scientists to adopt more convenient reference electrodes such as the saturated calomel electrode (SCE) and the mercury/mercurous sulphate electrode (MSE).[15, 16] In a SCE, mercury and insoluble mercury(I) chloride are immersed in a saturated solution of potassium chloride to give a potential of +0.24 V *vs.* SHE.[17] Within a MSE, mercury and insoluble mercurous sulphate are immersed in a saturated potassium sulphate solution to maintain a stable potential of +0.62 V *vs.* SHE.[17] A MSE is useful for systems which are sensitive to chloride ions.

In all of the experiments performed within the thesis, a potential is applied at the working electrode to observe the change in voltammograms. The potential applied is with respect to the reference electrode.[6] Considering Section 1.2.2 where the electrostatic potential at the electrode, ϕ_M, and the electrostatic potential in the solution, ϕ_S, are defined, the potential applied at the working electrode follows the expression below:

$$Potential\ Difference = (\phi_M - \phi_S)_{WE} - (\phi_M - \phi_S)_{RE} \qquad \text{Equation 1.11}$$

where the $(\phi_M - \phi_S)_{WE}$ is the potential at the working electrode interface and $(\phi_M - \phi_S)_{RE}$ is the known potential which occurs at the reference electrode interface. This potentiostat system works in a feedback mode and changes the potential difference between the working and reference electrodes till the desired value is obtained.

Considering Equation 1.1, when a suitable potential is applied between the working and reference electrode, the electrochemical reaction is driven to favour either the formation of A or B. Hence, the concentration change of A and B results. Thus, a redox reaction occurs on the working electrode, charges are passed and information on the redox couple is obtained. With a redox reaction occurring on the working electrode, hence, a counter reaction is required to balance the amount of electron flow. However, if the counter reaction was to occur on the reference electrode, its equilibrium and hence the reference electrode potential would be disturbed, resulting in an inaccurate reference potential. Thus, a third electrode known as the auxiliary or counter electrode is introduced to allow the counter reaction to occur on its surface. Commonly, it is made of relatively inert materials such as platinum or carbon in order to minimise its influence on the reaction occurring on the working electrode. With a counter electrode in the circuit, no current needs to flow through the reference electrode and a stable reference potential can be maintained. In a three electrode system, the potential difference is applied and measured between the working and reference electrode while the current flows between the working and counter electrode. This completes the three electrode system which is a cornerstone for performing electrochemical experiments.

1.4 Electrochemical Methods

When a suitable potential is applied to the electrochemical cell, the plot of measured current against potential or time will give information on the redox couple via a voltammogram or chronoamperogram. The two main techniques of cyclic voltammetry and chronoamperometry used in this thesis are discussed in Section 1.4.1 and 1.4.2 respectively.

1.4.1 Cyclic Voltammetry

Cyclic voltammetry changes the potential of the working electrode linearly in a forward and then a backward direction, recording the current as the potential changes.[1, 12, 18, 19] In practice, digitally generated small potential steps ('a staircase') are made and the current is measured as the potential is applied (Figure 1.4). The current, I, is measured at one point along each step.[20] The current measurements are plotted against the potential to give a cyclic voltammogram. The scan rate is determined by the how fast the potential changes with time.

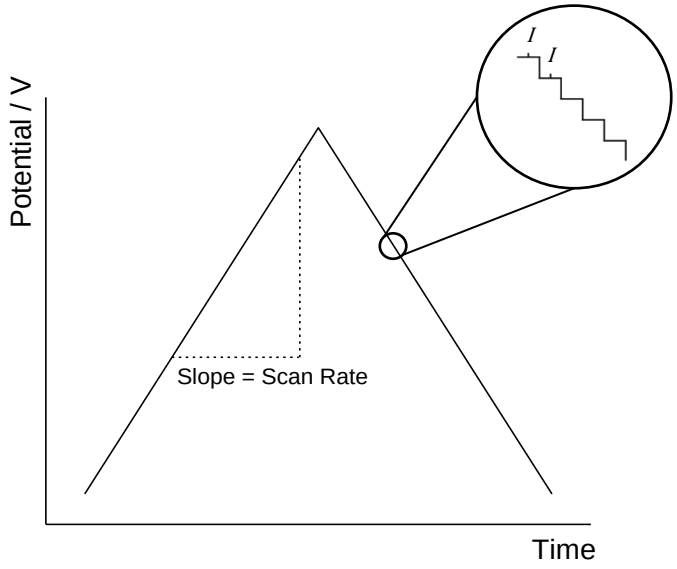

Figure 1.4 A schematic diagram showing the waveform of a cyclic voltammogram. The current, I, is measured at each potential step. The scan rate can be determined by the slope.

The size of the working electrode also determines the wave form of the cyclic voltammogram. This is because the mass transport on a macro electrode (usually with dimensions of cm or mm) is

mainly attributed to linear diffusion while convergent diffusion ('edge effects') is responsible for the main mode of mass transport towards a micro electrode (usually with dimensions of μm) (Figure 1.5). Hence, the micro electrode has a more efficient diffusional transport towards the electrode surface compared to a macro electrode.

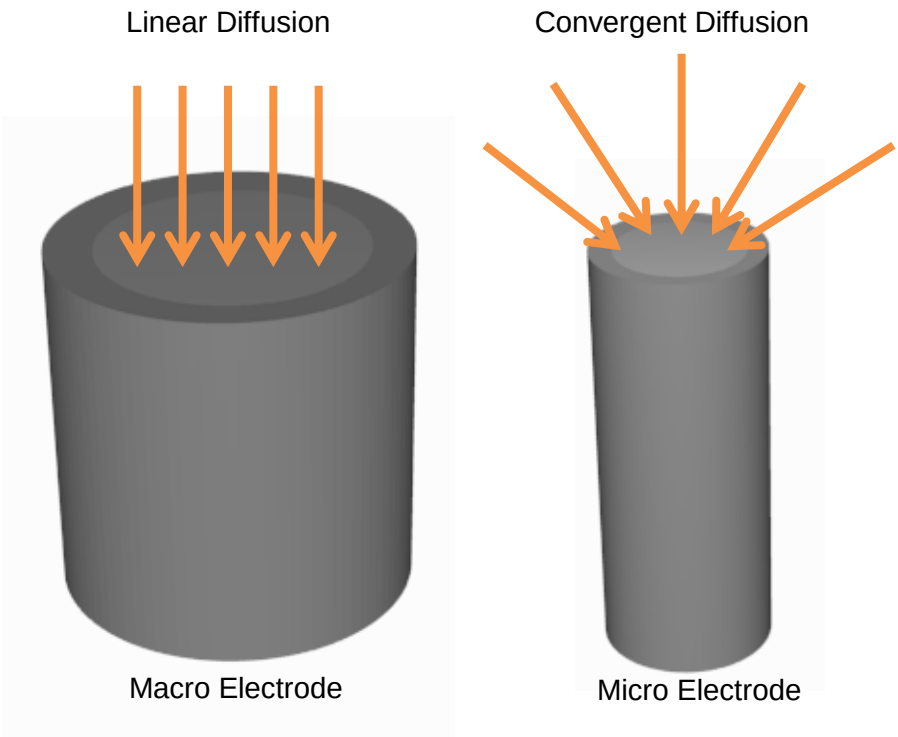

Figure 1.5 The different mode of mass transport at a macro electrode and a micro electrode.

Typical voltammograms obtained on a macro electrode are summarised in Figure 1.6. For an electrochemically reversible reaction, where the rate of electron transfer is much faster than the rate of mass transport. The solid black line in Figure 1.6 reflects Equation 1.1 where A is reduced to B. As the potential applied, E, is more positive than the formal potential, E_f^{θ}, no current is passed as the potential is not sufficiently negative to convert A. As the potential grows increasingly negative, the potential is now suitable to reduce A to B and a large increase current is observed. While all the species A next to the electrode surface is consumed; now the reactant has to diffuse from the bulk solution to reach the electrode surface, thus the diffusion layer becomes thicker. Thus, the current starts to decay away, giving a peak in the voltammogram. The reverse reaction of oxidising B to A is recorded by an oxidation signal on the backward scan. As the rate of electron transfer slows down,

the voltammetry is increasingly irreversible and from Figure 1.6, it is observed that peak current decreases slightly and the peak to peak separation increases substantially.

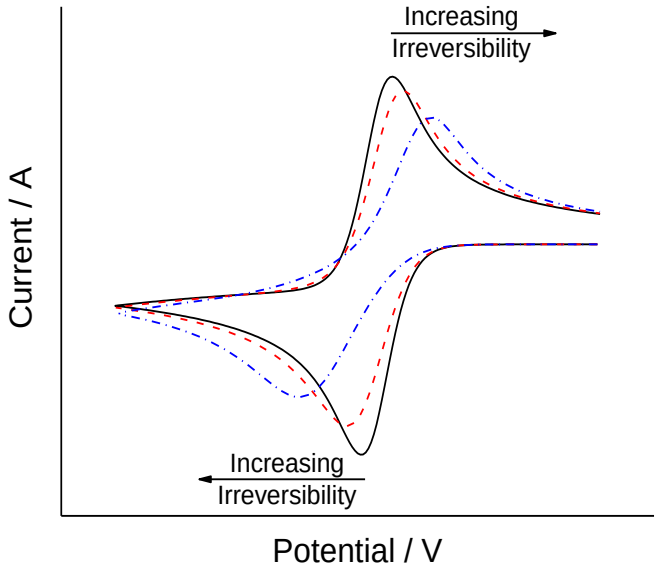

Figure 1.6 The ideal cyclic voltammogram of a solution phase electrochemical reaction occuring on a macro electrode with varying degree of electrochemical reversibility.

Equation 1.12 and 1.13 represents the Randles-Ševčík equations at 298 K for reversible and irreversible reactions respectively.

$$I_p = (2.69 \times 10^5) A_{elec} D_A^{0.5} C_A^* \upsilon^{0.5} \qquad \text{Equation 1.12}$$

$$I_p = (2.99 \times 10^5) \alpha^{0.5} A_{elec} D_A^{0.5} C_A^* \upsilon^{0.5} \qquad \text{Equation 1.13}$$

The Randles-Ševčík equation relates how the peak current, I_p, changes with the bulk concentration of species A, C_A^*, the scan rate, υ, the diffusion coefficient of species A, D_A and the area of electrode, A_{elec}. α is the transfer coefficient.

At a macro electrode, assuming $\alpha \sim 0.5$, Matsuda and Ayabe categorised reactions into reversible, quasi-reversible and irreversible based on the magnitude of the standard electrochemical rate constant, k^0.[21] Table 1.1 shows the relation between scan rate, υ, and k^0 which determines the electrochemical reversibility of a system.

	Classification Boundary
Reversible	$k^0 \geq 0.3\, v^{1/2}$ cm s^{-1}
Quasi-Reversible	$0.3\, v^{1/2} > k^0 > 2 \times 10^{-5}\, v^{1/2}$ cm s^{-1}
Irreversible	$k^0 \leq 2 \times 10^{-5}\, v^{1/2}$ cm s^{-1}

Table 1.1 Criteria for the classification of electrochemical reversibility of macroelectrode voltammetry

At a micro electrode, where convergent diffusion takes place, the diffusion layer thickness is small due to edge diffusion enhancing the reactant flux. Hence, in Figure 1.7, instead of having voltammetric peaks, the current reaches a steady state as only a thin diffusional layer builds up.

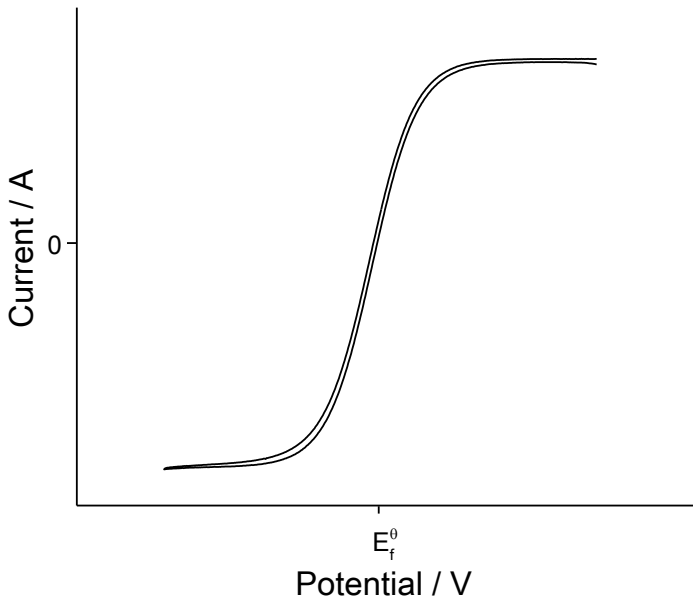

Figure 1.7 A typical "steady-state" cyclic voltammogram on a micro electrode.

At a microdisc electrode, the steady-state current is limited by the flux of the reactant and it can be expressed as:

$$I_{lim} = 4FDC^*r_e \qquad \text{Equation 1.14}$$

I_{lim} is the steady state current, F is the Faraday constant, D is the diffusion coefficient, C^* is the bulk concentration of the reactant and r_e is the radius of the electrode. Efficient mass transport at the

electrode meant that a steady state current is observed as a thin diffusion layer builds up. However, if the scan rate is increased sufficiently, the voltammogram looks similar to the ones in Figure 1.6.

In the above sections, a single electron transferred to A to form B (Equation 1.1) at the electrode/solution interface has been considered. This heterogeneous electron transfer has assumed both A and B as chemically stable in solution within the experimental time scale. However, if either A or B are not stable, this can lead to different, more complex, mechanisms such as $\mathbf{EC}$ and $\mathbf{ECE}$. $\mathbf{E}$ is used to define a heterogeneous electron transfer while $\mathbf{C}$ is used to indicate a non-electrochemical reaction.

If B is not chemically stable, the reaction may follow an $\mathbf{EC}$ mechanism. The reaction mechanism can be written as:

$$A + e^- \rightleftharpoons B \qquad \text{Equation 1.15}$$

$$B \rightarrow C \qquad \text{Equation 1.16}$$

where A and B are involved in the electrochemical step. B is formed as an instable product which is chemical converted to C, an electrochemically inert and stable product. A good example of the $\mathbf{EC}$ reaction would be the oxidation of 1,4-aminophenol in an aqueous acidic environment, as shown in Figure 1.8.[1, 22]

However, if C in Equation 1.16 was electroactive, it would lead to the mechanism of $\mathbf{ECE}$. A second $\mathbf{E}$ step involving C may takes place, resulting in:

$$A + e^- \rightleftharpoons B \qquad \text{Equation 1.17}$$

$$B \rightarrow C \qquad \text{Equation 1.18}$$

$$C + e^- \rightleftharpoons D \qquad \text{Equation 1.19}$$

Two electrons are transferred per species A due to the two heterogeneous electron transfer steps. One of the possible pathway for the reduction of 1,2-bromonitrobenzene in the absence of protons is the ECE mechanism, as shown in Figure 1.9. [1, 23]

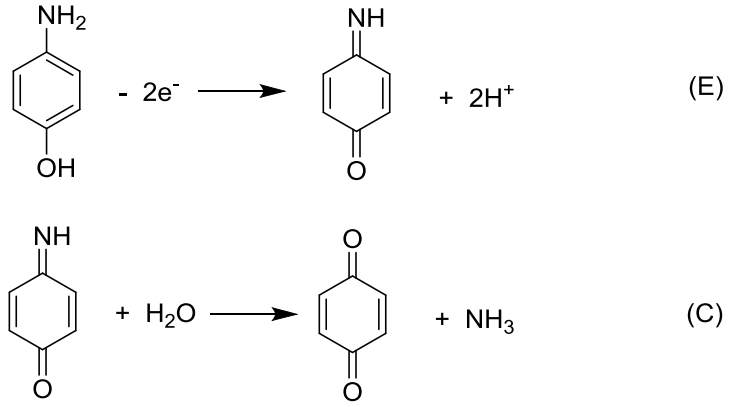

Figure 1.8 The oxidation of 1,4-aminophenol, following an EC mechanism

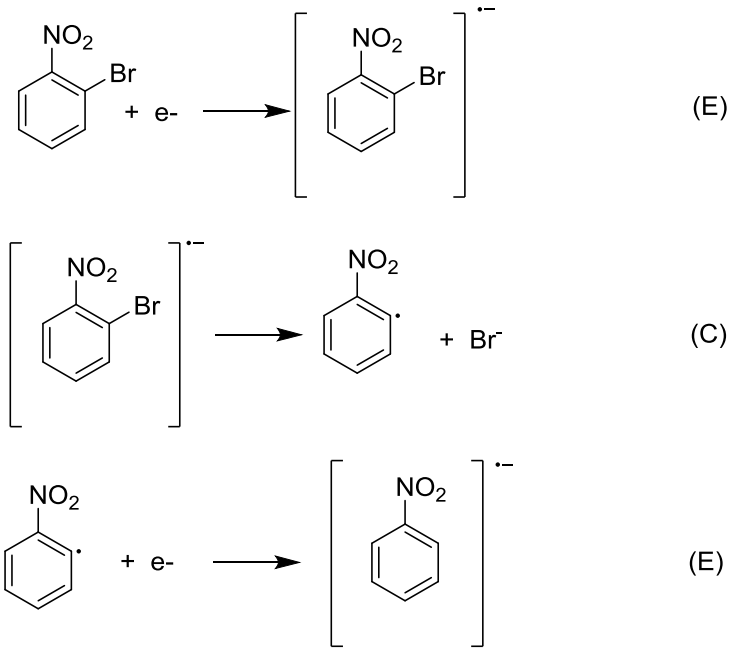

Figure 1.9 The reduction of 1,2-bromonitrobenzene in an aprotic solvent, following an ECE mechanism

Apart from the various mechanisms that can occur with heterogeneous electron transfer, another factor that has to be brought into consideration is adsorption. Hitherto, all the reactions discussed assume the reactants and products are in solution and move to the electrode via diffusion. However, if both the reactant and product adsorb onto the electrode surface, it greatly alters the waveshape of the voltammogram. Given an electrochemical reversible reaction of reducing A to B (where both A and B adsorb onto the electrode surface), the voltammogram on a macro electrode is expected to have the forward and backward peaks as symmetrical signals and peak potentials at the formal potential of the A/B redox couple (Figure 1.10). As the reaction become increasingly irreversible, the two signals occur at either side of the formal potential and the peaks become significantly asymmetric. The net peak current of the signal from $\mathrm{A(ads)+e^{-}\rightleftharpoons B(ads)}$, is governed by the following equations:

For a reversible surface bound reaction,Compton, 2011 #350}

$$I_p = \frac{F^2}{4RT}\upsilon A_{elec}\Gamma_A^0 \qquad \text{Equation 1.20}$$

For a irreversible surface bound reaction,[1]

$$I_p = \frac{\alpha F^2 A_{elec}\upsilon\Gamma_A^0}{2.718RT} \qquad \text{Equation 1.21}$$

where I_p is the peak current, F is the Faraday constant, R is the gas constant, T is temperature, υ is the scan rate, A_{elec} is the electrode surface area, Γ_A^0 is the surface coverage of reactant at the electrode surface and α is the transfer coefficient.

The technique of cyclic voltammetry and the influence of reversibility, diffusion, reaction mechanism and adsorption on the voltammogram have been discussed in the present section. In next section, we explore the method of chronoamperometry.

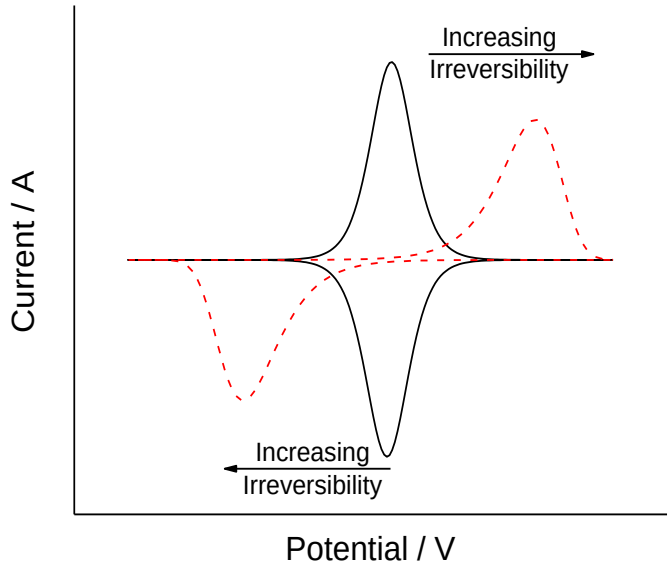

Figure 1.10 Ideal cyclic voltammetric response of surface bound species. Black line: reversible reaction; red dashed line: irreversible reaction.

1.4.2 Chronoamperometry

Chronoamperometry is an electrochemical technique which studies the change in current with time as a potential step is applied at the working electrode. If the potential is held at a suitable potential, all of the reactant near the electrode surface is consumed. Thus, in Figure 1.11, it is observed that a huge current flows at the start of the chronoamperogram while the diffusion layer builds up. This is attributed to Faradaic and capacitative current. As time passes, the current decreases and this is mainly associated with Faradaic current. Assuming that the reactant is solely arriving at the electrode surface via linear diffusion, the Cottrell equation is a solution for Fick's second law for a measurement at a macro electrode at a potential step from zero current to a diffusion controlled current (chronoamperometry). It allows the net flow of reactants towards the electrode surface to be converted into the form of a current response. At a suitable potential where all substrate reaching the electrode surface is consumed, the Cottrell equation is written as:

$$I = \frac{FA_{elec}\sqrt{D}C^*}{\sqrt{\pi t}} \qquad \text{Equation 1.22}$$

where I is the net current, F is the Faraday constant, A_{elec} is the electrode surface area, D is the diffusion coefficient, C^* is the bulk concentration and t is time. As time approaches infinity, the current decays to zero as all the reactant is converted into product.

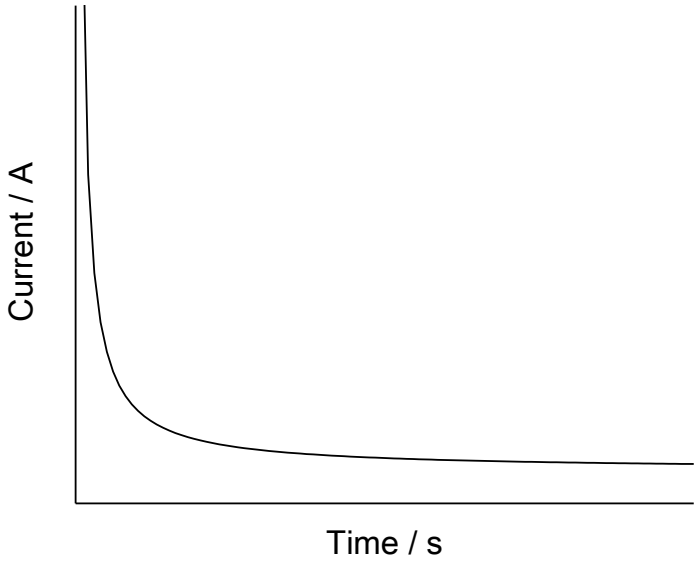

Figure 1.11 A typical chronoamperogram which plots current against time.

On the other hand, when a microdisc electrode is used, as mentioned in Section 1.4.1, edge diffusion comes into play. Hence, another equation is required to determine the current decay at a fixed potential.[24]

$$I = 4FC^*Dr_e f(\tau) \qquad \text{Equation 1.23}$$

where r_e is the electrode radius and $\tau = 4Dt/r_e^2$.

Shoup and Szabo have estimated $f(\tau)$ at all times to be:[25]

$$f(\tau) = 0.7854 + 0.8862\tau^{-1/2} + 0.2146\, exp^{-0.7823\tau^{-1/2}} \qquad \text{Equation 1.24}$$

For both macro and micro electrodes, the current is solely determined by the mass transport process, making chronoamperometry an attractive option for mass transport study.

In this thesis, a current-time transient is employed for the novel techniques of 'nano-impact'. This method holds the electrode at a suitable potential; as a single nanoparticle comes into contact with the electrode, the former is oxidised or reduced, resulting in a current 'spike' seen on the current-time transient. Hence, the study of single nanoparticles diffusing towards the electrode surface is possible. Characterisation of the nanoparticle size and identity is achievable through the charge passed and onset potential. It is possible to convert Equation 1.24 to estimate the number of nanoparticle-electrode impacts via the equation below:[26]

$$N_{impact} = N_A C_{NP}^{*} {r_{NP}}^3 \left(\tau + 1.437\tau^{1/2} + 6.57 \times 10^{-2} \ln \tau - 3.35 \times 10^{-3}\tau^{-1} + 3.43 \times 10^{-3}\, \tau^{-1/2} + 3.49 \times 10^{-4}\tau^{-3/2}\right) \quad \text{Equation 1.25}$$

where N_{impact} is the number of nanoparticle-electrode impacts, N_A is the Avogadro constant of 6.022 x 10^{23} atoms per mole, C_{NP}^{*} is the bulk concentration of the nanoparticles, r_{NP} is the radius of the nanoparticle. The diffusion coefficient embedded in τ (as seen above in page 18) can be estimated via the Stokes-Einstein equation:

$$D_{NP} = \frac{k_B T}{6\pi\eta_l r_{hyd}} \quad \text{Equation 1.26}$$

The equation assumes that the nanoparticles are perfectly spherical where D_{NP} is the diffusion coefficient of a nanoparticle, k_B is the Boltzmann constant, η_l is the liquid viscosity and r_{hyd} is the hydrodynamic nanoparticle radius. The technique of 'nano-impacts' is further discussed in Section 2.4 with examples.

Chapter 2 Nanoparticles and Their Detection

Nanoparticles are a part of our daily lives due to their wide application in consumer products.[27] Their novel properties have allowed technological advances (e.g. nanoelectronics[28, 29]) which would be otherwise be impossible.[27] Although there are many conveniences and benefits brought along by these small particles, the extent of the detrimental effects they may bring to the environment and organisms is still unknown.[30-33] Given their small size, new techniques are required to detect nanoparticles through various means. Electrochemical methods such as stripping voltammetry[34-38] and 'nano-impacts'[39-43] have been widely introduced for nanoparticle detection and are overviewed in this chapter. A brief description on the available non-electrochemical techniques for nanoparticle detection is also given this chapter.[44-48] This chapter is partly based on an introductory survey co-authored with Professor Richard G. Compton in 'Electrochemical Strategies in Detection Science' edited by Professor Damien Arrigan. The book is due to be published by the Royal of Society Chemistry in October 2015.

2.1 Nanoparticles and Their Properties

Nanoparticles are a special class of material of any shape with at least one dimension between 1 to 100 nm based on the guidelines of IUPAC (International Union of Pure and Applied Chemistry).[49] They are important because their properties may deviate significantly from that of the bulk material. One of the most studied aspects is their optical characteristics.[50] Taking the nanoplasmonic properties of silver nanoparticles as example, spherical silver nanoparticles are known to have a yellow colour and a surface plasmon absorption around 400 nm.[51] As the size of the silver decreases to subnano (usually clusters smaller than 2 nm in diameter), fluorescent properties start to develop.[52] Bulk silver shows different optical properties[53] and it does not fluoresce. For such metallic nanoparticles, fluorescence develops at a size smaller than ~ 2 nm because the continuum of energy levels found in bulk metal that allows the free flow of electrons across the material breaks down and the energy levels become more distinct at this size.[54] For other

types of nanoparticles such as quantum dots, fluorescence may arise at sizes greater than 2 nm due to the electronic structure present in the semiconductor materials.[55]

Apart from the prominent field of nanoplasmonics, the physical properties of the particles may also change at the nanoscale. First, the percentage of the surface atoms increases.[56] A 1 nm diameter palladium nanoparticle has about 80% of the atoms on the surface.[56] This increases the surface area to volume ratio leading to their possible application as effective catalysts.[57-59] Second, the decrease in nanoparticle size increases the degree of surface curvature, resulting in a higher energy.[60] This leads to phenomena such as lowering of the melting temperature[61] and alteration of the potential of metal oxidation.[62, 63] A difference of around 500 °C in the melting temperature is found for cadmium sulphide nanoparticles of radii 25 Å and 50 Å.[61] The change in potential due to nanoparticle size under different diffusion regimes is studied in Chapter 4, Section 4.1.

The properties of nanoparticles are also heavily influenced by the presence of capping agents. They reduce agglomeration of the nanoparticles by using different mechanisms (i.e. electrostatic forces, steric repulsions).[64-66] However, the capping agents are used for much more than stabilisation. The shape of silver nanoparticles synthesised can be controlled through the use of organic capping agents such as poly(vinyl pyrrolidone) and sodium citrate.[67] In turn, the surface plasmon peak occurs at different wavelengths depending on the particle shape.[68] With the variation of triethanolamine, oleic acid or thioglycerol as capping agents, the luminescence properties of zinc oxide nanoparticles differ.[69] Likewise, the extinction coefficient of the gold nanoparticles changes as the citrate capping agent is replaced by 1-decanethiol or oleylamine.[70] This inspired a study in Chapter 4, Section 4.3 which addresses the influence of capping agents on the two main electrochemical techniques of cyclic voltammetry and chronoamperometry.

The novel properties of nanoparticles, such as a large surface area, can bring advantages that greatly benefit the society through the form of improved or new industrial and consumer products.[27] For example, elemental silver is known to react with thiol groups and inhibit enzymes with thiol groups, hence granting silver anti-bacterial activity.[71] Silver nanoparticles are known to

generate reactive oxygen species,[72, 73] which put stress on cells.[74, 75] Thus, they are now incorporated into products such as carpets[76], socks[77] and fabric softener[27] as an anti-bacterial agent.[72, 78-81] A study on silver-thiol interactions was attempted in Chapter 7 to observe the influence of thiol groups. On the other hand, the capability of zinc oxide nanoparticles to remain invisible while blocking a wide spectrum of harmful ultraviolet rays makes them popular in sunscreens.[82] The tiny size of the nanoparticles allows them to be transparent compared to their bulk counter parts that appear white.[83] Janus particles, which have at least two surfaces of different chemistry and/or polarity[84], can be used in water repellent fabrics.[85] The hydrophilic side attaches to the fabric, leaving the exposed hydrophobic portion to repel water.[85] These products are just a few examples of the thousands of items which employ 'nanotechnology'. This industry is estimated to be worth USD 20.7 billion in 2012 and predicted to expand to USD 48.9 billion in 2017 according to BCC Research.[86] By October 2013, 1628 nanotechnology-enabled consumer products have been registered with the 'Consumer Products Inventory' on 'The Project on Emerging Nanotechnologies'.[27] The number of consumer products has increased rapidly over recent years. The most popular nanomaterials, according to their major elements, are silver, followed by titanium (including titanium dioxide and other forms), carbon (including fullerene, carbon nanotubes, graphene, graphite and other forms), silica (found as silica oxide and other forms), zinc (including zinc oxide and other forms) and gold.[27]

Given the flourishing growth of nanotechnology based consumer products, there are also *possible* negative implications. It is suggested that for pregnant mice injected with 100 μg of titanium dioxide nanoparticles, the nanoparticles are passed to their offspring.[30] Oral ingestion is also a possible route for nanoparticles to pass from parent mice to child.[31] A study in 2012 reported that the exposure of an average American to titanium dioxide nanoparticles is less than 2 mg per kg of body mass per day.[32] A study on carbon-based nanomaterials showed that they might activate inflammatory genes in pulmonary tissues in mice if their lung tissues are directly exposed to 125 μg of nanoparticles.[33] Given the possible health implications, nanomaterial usage likely needs regulation and laws to construct a safety net.

Current regulations are at an early stage but many countries and associations, including the European Union (EU), China, India, Taiwan and Thailand, are making significant efforts in nanoparticle research so as to make better legislation.[87] For the EU, there are no current regulations *specific* to nanotechnology.[88] Instead, they actively promote research and discussions. The programme of REACH (Registration, Evaluation, Authorisation and Restriction of Chemicals) has stringent and broad regulations on chemicals and drugs to cover the risk of nanotechnology in the EU.[89] In 2012, France passed a decree for mandatory reporting of products containing nanomaterials.[90] China contributes significantly to the global joint effort to understand nanoparticles so as to make better guidelines.[91] Internationally, many properties (like concentrations, size distributions, impurities present, in vivo and in vitro toxicology effect) have been recommended as should be reported and diverse techniques like microscopy, elemental analysis, centrifuging and spectroscopy are recommended for nanoparticle analysis.[92]

2.2 Non-electrochemical Techniques

To characterise nanoparticles, the International Life Science Institute Research Foundation/Risk Science Institute suggests a wide variety of laboratory methods for analysis.[92] These include microscopy techniques such as transmission electron microscopy (TEM) and scanning electron microscopy (SEM). Laser techniques, such as nanoparticle tracking analysis (NTA) and dynamic light scattering (DLS) are also recommended. Elemental analysis can be performed through inductively coupled plasma mass spectroscopy (ICP-MS). A wide range of surface analysis techniques such as X-ray diffraction (XRD) and X-ray photon spectroscopy (XPS) also play main roles in nanoparticle characterisation. Ultra-violet visible (UV-vis) spectroscopy, capable of measuring surface plasmon resonance, is also among the suggested techniques. As reported in Table 2.1, different characteristics of the nanoparticles such as size, concentration, elemental composition, surface properties and shape can be measured by various methods.[92] In general, however, a combination of techniques is required to fully characterise the nanoparticles. In the paragraphs below, the various characterisation methods mentioned earlier are surveyed for their relative merits.

		Analytical technique														
		Transmission Electron Microscopy (TEM)	Scanning Electron Microscopy (SEM)	X-Ray Diffraction (XRD)	X-ray Photon Spectroscopy (XPS)	Auger Spectroscopy (AES)	Secondary Ion Mass Spectrometry (SIMS)	Scanning Probe Microscopy	Dynamic Light Scattering (DLS)	Zeta potential	Size Exclusion Chromatography	Analytical Ultracentrifugation	Differential Mobility Analysis (DMA)	Isothermal Adsorption (e.g. BET)	Spectroscopic techniques (UV vis, IR, Raman, NMR)	Elemental analysis (eg ICP-MS/AA etc)
Physicochemical Characteristic	Size distribution (primary particles)	▲	●	●				●	●		●	●	●			
	Shape	▲	●					●	✓				✓			
	Surface area	●	◊					◊	◊			◊	✓	●		
	Composition	●	●	●			▲								●	▲
	Surface chemistry	●	✓		●	●	✓	✓		◊					✓	
	Surface contamination	✓			●	●		✓							✓	
	Surface charge – suspension/ solution									▲						
	Surface charge – powder (use bio fluid surrogate)									▲						
	Crystal structure	●	◊	▲												
	Particle physicochemical structure	▲	●				✓									
	Agglomeration state	▲	●	✓				●	✓		✓	✓	●			
	Porosity	◊											●	●		
	Heterogeneity	▲	●					◊							✓	

Other applicable techniques are available that have not been listed.
▲Highly applicable
● Capable of providing information in some cases
✓ Capable of providing information in some cases, with validation from more accurate/applicable techniques
◊ Capable of providing qualitative or semi-quantitative information

Table 2.1 Range of analytical techniques used for nanoparticle characterisation. Reproduced from ref 92 under the terms of Creative Commons Attribution 4.0 International. This permits use, distribution and reproduction in any medium, provided the original work is properly cited and is not used for commercial purposes.

Microscopy techniques such as SEM and TEM provide powerful magnification. SEM uses an electron beam to scan and generate images and it is capable of resolving detail down to 3 nm.[93] The ability of SEM to 'see' the nanoparticles provides information on their size, shape and surface area. However, SEM is incapable of differentiating between any capping agent and nanoparticle surface features.[54] Moreover, in order to be examined by SEM, the samples have to be conductive. Thus, a thin layer of sputtered metal coating is often used for non-conducting samples.[94] In addition, the SEM sample studied has to be non-volatile and capable of tolerating vacuum conditions.[95] SEM also has a possible destructive nature as the electron beams may damage the sample.[96]

The other powerful magnification technique, TEM, uses an electron beam to transmit through the sample for imaging.[97] TEM is able to detect particles as small as 0.1 nm.[93, 97] With aberration correction, TEM is capable of reaching a higher resolution where single atoms can be seen.[98] Figure 2.1 shows a high resolution TEM image of a gold nanoparticle.[99]

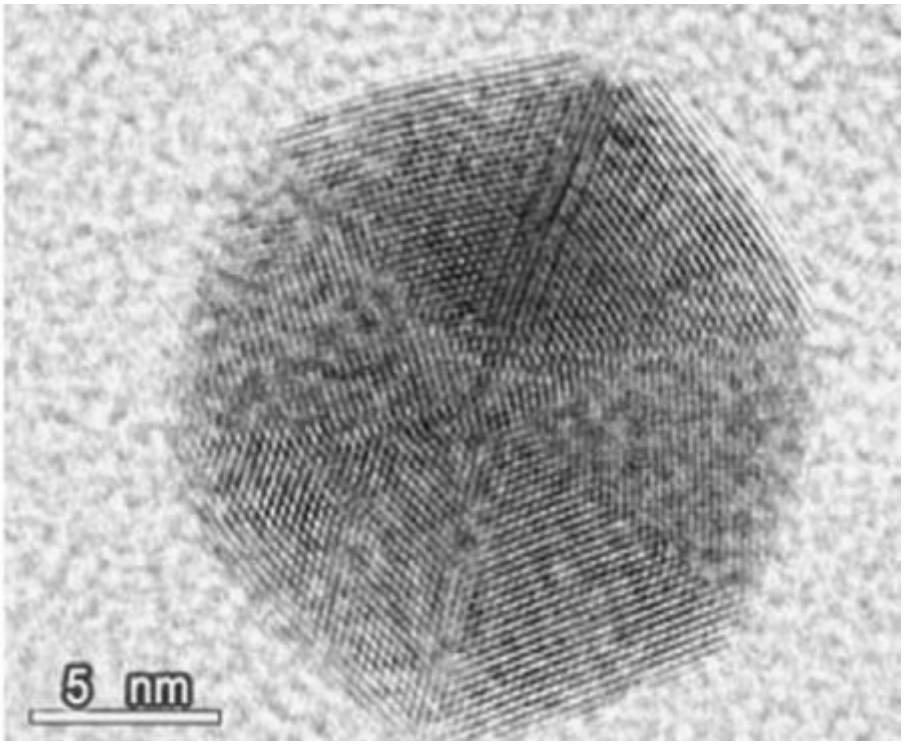

Figure 2.1 High resolution TEM image of a gold nanoparticle. Scale bar of 5 nm. Adapted from ref 99 with permission from Elsevier.

The lattice structure is atomically resolved. Each individual bright spot represents a single atomic column. Similar to SEM, TEM is able to visualise and characterise nanoparticles. Viable samples for TEM are subjected to strict criteria; they must be electron transparent and able to withstand the vacuum environment.[95, 97, 100] In TEM, the energy from electron beam may damage the samples to different extents (especially organic samples).[96] Various sample preparations have been improvised to reduce the sample damage (e.g. TEM sample freezing with liquid nitrogen[101], electrochemical pre-treatment of metal nanoparticles etc.).[102]

The usage of lasers gives rise to the two different techniques of NTA and DLS. NTA uses a laser to illuminate particles and a microscope to track the individual particles.[103] By tracking the Brownian motion of the particles, the diffusion coefficient (D) is obtained. The hydrodynamic radius of the particle (r_{hyd}) is then calculated with the use of the Stokes-Einstein equation:[104]

$$D = \frac{k_B T}{6\pi\eta_l r_{hyd}} \qquad \text{Equation 2.1}$$

where k_B is the Boltzmann constant of 1.38 x 10^{-23} J K^{-1} $molecule^{-1}$, T is the temperature in Kelvin and η_l is the viscosity of the liquid sample. The use of the Stokes-Einstein equation assumes that the measured particle is a perfect sphere. In reality, spherical nanoparticle samples often contain particles close to a spherical shape rather than being perfect spheres. Figure 2.2 shows a typical sample of spherical silver nanoparticles (used in Chapter 6, Section 6.1) imaged by TEM and most of them are not perfect spheres. However, NTA is not without advantages. This technique is easy to use and only a small volume of sample is required (around 0.3 mL) each time.[105] The sample does not have to undergo any special pre-treatment apart from dilution to the appropriate concentration. Nonetheless, NTA has a narrow optimal concentration range of 10^7 – 10^9 particles/mL in order to track sufficient particles to measure a proper size distribution.[105] Therefore, an estimation of the sample concentration is usually required before NTA is performed.

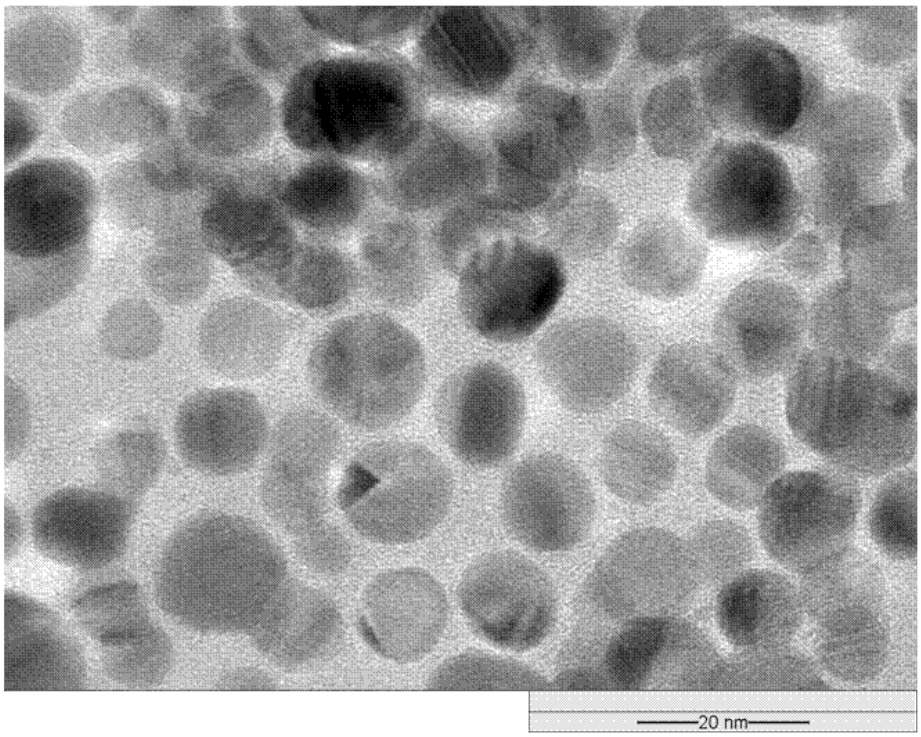

Figure 2.2 TEM brightfield image of a silver nanoparticle sample used in Chapter 6, Section 6.1. Scale bar of 20 nm.

DLS measures the hydrodynamic radius through the light scattered by the particles.[106] A shorter wavelength is favourable for analysis as it is scatters more efficiently, thus lowering the limit of particle size measurable.[107] According to the DLS manufacturer Malvern, the technique is capable of detecting a large range of sizes from 0.3 nm to 10 μm.[108] Pre-knowledge of the reflective index and absorbed wavelength of the sample are required for the size analysis.[109] Similar to NTA, DLS is easy to use and sample preparation includes simple filtration and dilution. As both NTA and DLS measure the particle hydrodynamic radii, a careful choice of capping agent of the nanoparticles is required as certain capping agents, such as polyethylene glycol (PEG), can cause a significant difference between the hydrodynamic radius and the actual radius.[45] In addition, they are unable to measure any optically opaque samples due to excessively light scattering. Chapter 4, Section 4.2 pioneers a novel electrochemical technique ('nano-impact') which is able to size nanoparticles in an optically opaque medium.

The elemental analysis of nanoparticles is often performed through ICP-MS. An argon plasma is utilised to dissociate the analytes into fragments.[110] The fragmented sample is separated according to the mass-to-charge ratio and then detected through an electron pulse with an electron multiplier. ICP-MS is capable of detecting certain metallic elements down to 1 part per trillion (10^{12}).[110] Moreover, isotopic analysis and screening for multiple elements in one single measurement is possible.[110] Due to its high sensitivity, contamination is a possible major concern. Argon, which is abundant in the plasma, generates fragments such as $^{40}Ar^{+}$, $^{56}ArO^{+}$ and $^{80}Ar_2^{+}$ which can interfere with ^{40}Ca, ^{56}Fe and ^{80}Se detection respectively; ^{56}Fe and ^{80}Se are found commonly as nanoparticles in the forms of iron oxide[67] and cadmium selenide[111] respectively.

Surface analysis is commonly performed with XRD and XPS. XRD is based on the principle of Bragg's law; using a source of X-ray, crystalline samples are scanned at various angles and the surface properties are derived from the way the electromagnetic waves are diffracted.[112, 113] It determines the structural composition of the sample and is also phase sensitive towards the different morphology of lattice planes.[112, 113] However, XRD is limited to crystalline samples.[54] Another method which use X-ray for the surface analysis is XPS.[114] It reveals information on the elemental composition on the sample surface. It is very sensitive towards changes on the surface which, for example, allows the study of metal nanoparticle oxidation in air.[114] XPS is also capable of identifying the capping agent on nanoparticles.[46] Samples are processed after the XPS chamber is carefully brought to ultra-high vacuum.[114] XPS can operate as a non-destructive or destructive technique (through mechanical sectioning).[114] The sample holder usually has to be cleaned through heating and ion bombardment.[114] Although both XRD and XPS uses X-rays for surface analysis, the key difference is that XRD deals primarily with physical properties (e.g. phase and orientation of lattice planes) while XPS essentially determines chemical properties (e.g. the chemical state of the elements).

Last, UV-vis spectroscopy measures the surface plasmon signals caused by the oscillating electron field of the nanoparticles.[115] Certain small changes on the nanoparticle surface can be detected

through UV-vis spectroscopy. For example, a layer of oxide on silver and gold nanoparticles causes a red shift in the surface plasmon signal.[44] Changes in shape of the nanoparticles[17] or presence of different capping agents[19] on the nanoparticles can modify the wavelength of the surface plasmon signal. Despite the capabilities of UV-vis spectroscopy, it is only able to give a rough gauge on the nanoparticle size.[51] In addition, the extinction coefficient changes with size, making it difficult to determine the concentration of nanoparticles since a typical sample contains a distribution of sizes.[51] Often, it is used to confirm the presence of nanoparticles instead of quantifying them.[47]

Although there are many approaches to detect and study nanoparticles, there is still *no* single ideal technique to fully characterise the nature of the dynamic nanoparticles.[48] Usually, a combination of methods is required to obtain the full picture. Nonetheless, various methods may measure a different size average.[48] SEM and TEM, which visualise nanoparticles, determine the number average while NTA obtains the number average based on the diffusion coefficient. A sample bias towards a larger particle mean size is probable because larger nanoparticles are easier to detect.[48] The three techniques of SEM, TEM and NTA record the responses from individual particles. On the other hand, DLS measures the ensemble feedback from the nanoparticles. Hence, the average size measured by DLS is a weighted average based on the translational diffusional coefficient. Signals generated by smaller nanoparticles can be difficult to detect due to the masking by the larger ones.[48] Therefore, the different techniques of nanoparticle sizing may result in various measured average sizes due to the different calculation of the average, the polydispersity of the sample[48] and the capping agents present on the particles.[45] Moreover, with techniques like TEM and SEM that operate under vacuum, the removal of solvent from the nanoparticles can cause the sample to change; for example, agglomeration occurs during drying after silver nanoparticles are drop cast on the sample holder (Chapter 4, Section 4.1). However, it may be overcome through freeze drying the sample or solvent sublimation.[48] Aggregation and dissolution are the two main processes which may cause a difference between the measured size and the actual size.

One major field that has not been fully utilised for nanoparticle characterisation is electrochemistry. Given its fast, robust methodology and the recent development of nanoparticle-electrode impact experiments, electrochemical methods have considerable scope and promise for nanoparticle characterisation. These are overviewed in the following Sections 2.3 and 2.4.

2.3 Stripping Voltammetry

Electrochemical methods have the advantages of being fast, sensitive and robust. With the invention of disposable screen printed electrodes[116-119] and the use of small portable potentiostats[120], it is possible to perform electrochemical experiments at almost any location. Blood glucose sensors[121, 122], gas sensors[123-125], metal ions sensors[126, 127] and chilli heat (capsaicin) sensors[128] are both successful point-of-use examples where electrochemistry is utilised. Given the advantageous properties of electrochemical methods, it is potentially beneficial to use them as nanoparticle detection techniques. Nanoparticles are often found in environmental settings such as river water or seawater but especially in the discharge of effluents.[129] Portable electrochemical systems would be suitable for quick onsite sampling of nanoparticles. Currently, most studies are at the fundamental levels where the nanoparticles are characterised and detected in laboratory settings. If the nanoparticles are redox active species, the simplest and most direct method of nanoparticle detection can be performed through stripping voltammetry.

Stripping voltammetry involves oxidising or reducing the nanoparticles immobilised on the electrode surface through electrochemical techniques such as linear sweep voltammetry, cyclic voltammetry and pulse voltammetry analysis (differential pulse voltammetry and square wave voltammetry) to generate an electrochemical signal.

Cyclic voltammetry, as described in Chapter 1, Section 1.4.1, gives a voltammogram which looks like Figure 2.3 when nanoparticles are immobilised on the working electrode surface. Figure 2.3 depicts an ideal cyclic voltammogram of an electrochemically irreversible oxidative stripping. The amount of analyte present can be quantified through Faraday's law.

$$N_{surf} = \frac{Q}{nF}$$ Equation 2.2

The charge passed under the voltammetric signal, Q, will correspond directly to the moles of surface immobilised analyte, N_{surf}, through the Faraday's law where n is the number of moles of electrons involved in one mole of reaction and F is the Faraday constant of 96 485 C mol^{-1}. Linear sweep voltammetry works in the same way as cyclic voltammetry but the potential only swept in one direction (half the cycle shown in Figure 2.3).

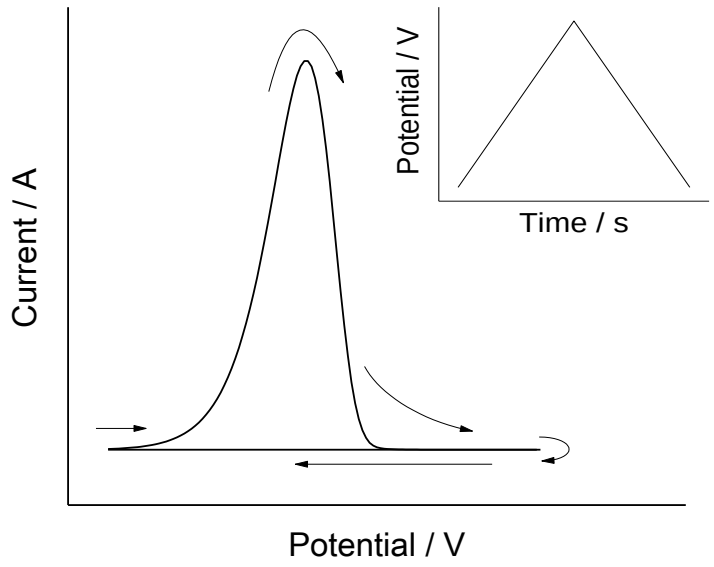

Figure 2.3 The ideal irreversible oxidation of an analyte on a cyclic voltammogram. The insert shows how the potential changes with time.

Pulse voltammetric methods such as differential pulse voltammetry and square wave voltammetry are receiving increasing attention as they are more sensitive.[130] The additional sensitivity is achieved by using a pulsed wave form in addition to a scanning potential.[131] The current differences between the pulsed steps are plotted against potential to give a voltammogram. Commonly, this subtraction allows the background current to be better offset, resulting in a greater resolution of the voltammetric peaks. As a result, the sensitivity towards the redox species is improved. Moreover, as the potential changes back and forth, the redox species is oxidised and reduced repeatedly if the redox reaction is reversible.[131] This gives a larger amount of charge measured under the

voltammetric signal. However, Equation 2.2 cannot determine the amount of nanoparticles immobilised on the electrode surface. Instead, a calibration curve is often used for pulse voltammetric methods.

Electrochemical methods are sensitive but nanoparticles often need to be analysed at very low concentrations. In many experiments, the total Faradaic charge passed[132] or the voltammetric signal peak height[34-36, 133-137] are used to determine the amount of nanoparticles present. The charge transfer at the electrode/solution interface is responsible for the Faradaic current. However, in order to achieve a quantifiable signal, the nanoparticle concentration required is much higher than those naturally found. Therefore, a pre-concentration step is part of the stripping voltammetry analysis. A wide assortment of tactics like drop casting and adsorption can be used.[138] Figure 2.4 shows the three main types of pre-concentration strategies (adsorption, drop casting and affinity enhancement) before stripping voltammetry is performed.

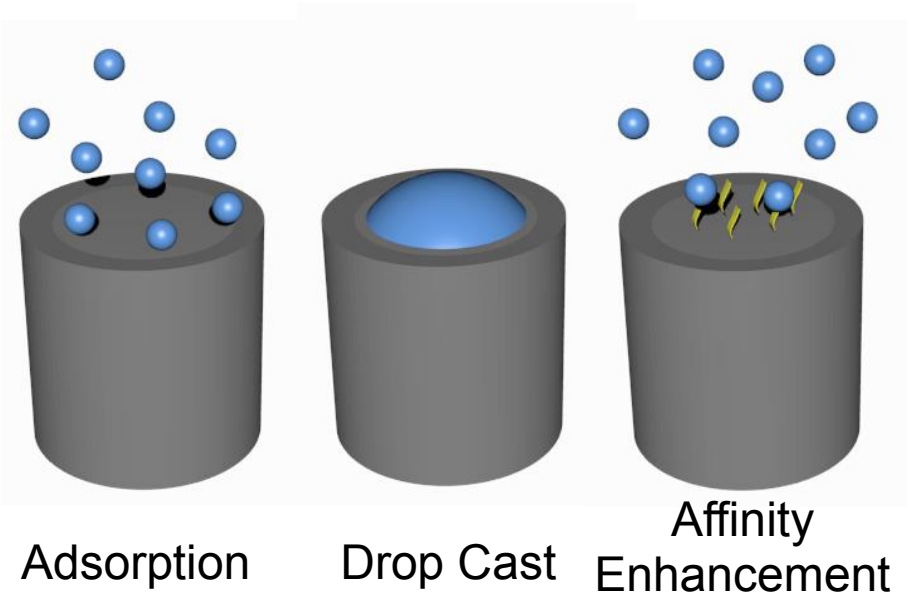

Figure 2.4 Main strategies for pre-concentration of nanoparticles. Drawings are not to scale.

First, the pre-concentration method of adsorption involves immersing the electrode into a nanoparticle suspension and waiting for adsorption to occur. Commonly, a potential is held at the electrode during adsorption to minimise the amount of nanoparticles desorbing.[139] Adsorption can also be performed at open circuit potential.[133, 138] One main advantage is that the adsorption period

can be extended when a sample of very low nanoparticle concentration is analysed. After the adsorption step, stripping voltammetry analysis is performed to determine the amount of particles present through Faraday's law (Equation 2.2). One good demonstration of using adsorption as a strategy for pre-concentration is a work by Neumann *et al.*[139] In their work, a carbon microelectrode is held at - 0.25 V *vs.* saturated calomel electrode (SCE) for a period of time to pre-concentrate the silver nanoparticles onto the electrode surface before stripping voltammetry is performed. As the adsorption time lengthens, the amount of silver nanoparticles adsorbed increases and the voltammetric signal grows larger.

The correct choice of medium is essential to obtain quantitative data from stripping experiments. For example, Pumera *et al.* have electro-oxidised adsorbed gold nanoparticles to the gold chloride complex $AuCl_4^-$ in strong hydrochloric acid.[133] Comparing the oxidation of gold nanoparticles to $AuCl_4^-$ and the reduction of $AuCl_4^-$ to metallic gold, the latter process allowed the concentration of the gold nanoparticles to be determined at a higher sensitivity through a better, well-defined signal. A similar concept has also been applied to the gold nanoparticles and bromide ions.[37] Judging from the success of changing nanoparticles into other forms, cathodic stripping voltammetry (CSV) may be applicable to detection of metal oxides nanoparticles.[134-137] Typical systems used include the oxides of manganese[134, 136] and lead.[135, 137]

Another way to promote adsorption is to use migratory forces.[140] In one method, gold nanoparticles are synthesized in situ in the presence of very little electrolyte.[140] A positive potential is held on the working electrode, attracting the negatively charged citrate capped gold nanoparticles. With the extra migratory forces, the efficiency of adsorption is improved.

The second pre-concentration strategy is drop casting. When the nanoparticles are isolated, they can be drop casted and immobilised onto the working electrode. This concept is illustrated in a report on poly(*N*-vinylcarbazole) (PVK) nanoparticles.[132] PVK undergoes a two electron oxidation and the amount of the redox active PVK can be determined through Equation 2.2.[141] The synthesized PVK nanoparticles are drop cast and dried on a glassy carbon electrode. Oxidation

signals are observed in a cyclic voltammogram and the charge passed under the voltammetric peak scales directly with the concentration of monomers present. It is reported that the moles of electrons transferred per mole of reactant is close to 2.[132] With this, a linear calibration is obtained between the peak charge and the number of monomers present, allowing the determination of unknown monomer concentrations on the electrode surface.

Instead of using the charge under peak area, the voltammetic peak height can also be used to determine the amount of nanoparticles present on the electrode surface. In the work by Teo *et al.*, copper oxide nanoparticles were drop casted onto the working electrode and a cyclic voltammogram was performed with the nanoparticle modified electrode.[34] The voltammetric peak height was linearly correlated to the amount of nanoparticles drop cast on the electrode. This method has been applied to nickel[36], nickel oxide[36], molybdenum[35] and silver[63] nanoparticle detection.

Apart from determining the concentration of nanoparticles, it is possible to size the nanoparticles through the measurement of the stripping peak potential with the strict control of surface coverage. This is further developed in Chapter 4, Section 4.1.

The third pre-concentration approach is electrode modification to enhance the affinity of the electrode surface for the nanoparticles. Making use of the strong interaction between silver and thiol, cysteine modified electrodes have been used to improve the adsorption of silver nanoparticles.[142] A similar concept has also been applied to gold electrodes with the modification agent of *meso*-2,3-di-mercaptosuccinic acid (DMSA). The thiol group at both ends of DMSA helps to anchor the silver nanoparticle onto the gold electrode.[38] The efficiency of silver nanoparticles adsorbing onto the DMSA modified electrode improved compared to an unmodified gold electrode. This shortened the time required for nanoparticles pre-concentrating onto the electrode surface. Currently, silver nanoparticles have been successfully captured on glassy carbon electrodes[142], carbon screen printed electrodes[143], gold electrodes[38] and home-made gold CD electrodes[144] in laboratory conditions[38, 142] and in seawater.[143, 144] Future developments include leaving disposable

electrodes in the environment for extended periods of time to capture nanoparticles before they are collected for analysis.[144]

Apart from pure electrochemical methods, other techniques like microscopy and electrophoresis have been combined with electrochemistry for nanoparticle detection. In the work by Batchelor-McAuley *et al.*, silver nanoparticles were tracked with a microscope through the scattered light from a green laser.[145] Through the light scattered, holograms were constructed to determine the size and the pathway taken by the nanoparticles as they adsorbed on an electrode. Stripping voltammetry confirmed the amount of silver the particles contained (Equation 2.2). A similar concept has been attempted by Munteanu *et al.* to track radical nanoparticles.[146] In a different work by Chua *et al.*, a lab on chip platform is used to separate nanoparticles of different sizes and sized using electrophoresis and the measurement of retention time.[147]

Stripping voltammetry detects numerous nanoparticles simultaneously. In the next section, experiments to detect single nanoparticles through impacts on the working electrode surface are surveyed.

2.4 'Nano-impacts'

The technique of studying the signal generated by a single nanoparticle impacting an electrode has gained much attention recently and it is one of the most promising methods for single nanoparticle detection.[148-151]

Before the 2000s, the detection of macroparticles[152] or large organic matters[153, 154] has been attempted. In the early 2000s, collisions between micron sized particles and electrodes were observed as 'spikes' on voltammograms.[155, 156] Scholz *et al.* recorded single micron size montmorillonite particles hitting the mercury drop electrode, disturbing the double layer around the electrode, generating non-Faradaic signals in the form of 'spikes'.[155] The non-Faradaic signals are caused by the change in structure of electrode/solution interface instead of electron transfer across the interface. The difference in the current between the 'spikes' and the background current

can be related to the size of the particles.[157-160] In an experiment by Banks *et al.*, heptane droplets were mixed into an aqueous solution of perchloric acid and studied with a gold working electrode.[158] As the heptane droplets hit the electrode surface, they momentarily block the electrode surface and disrupt the interface. After the impact, the double layer reforms. This results in non-Faradaic 'spikes' observed at different electrode potentials as heptane droplets impact a gold electrode in 0.1 M perchloric acid.[158] Depending on the potential held, it generates oxidative 'spikes' (potential held positive of the potential of zero charge (PZC)) or reductive 'spikes' (potential held negative of PZC) which are exclusively of a non-Faradaic nature. For this system, the PZC is measured to be at +0.01 V ± 0.01 V *vs.* Pd/H_2. Therefore, the transition of the spikes from oxidative to reductive occurs at PZC and this provides a means of measuring PZC.

More recently, *Faradaic* charges resulting from impacts of the nano sized particles have been studied and measured. Typically, this involves a chronoamperometric scan which holds the working electrode at a constant potential for a period of time to generate a stable background current. The nanoparticles are detected when they impact the electrode, giving a current transient. The change in current appears as a 'spike' or a 'step' in the current-time transient (chronoamperometry). It is usually performed on an electrode which is of a micro meter size to ensure a low background noise.

For impact experiments, the signal may arise directly from the redox reaction of the nanoparticles or the signal can result from an indirect redox reaction which happens on the nanoparticle surface. For indirect redox reactions, Wang *et al.* have sub-classified them into two categories of 'hit and run' and 'hit and stand'.[149] All of the three scenarios are illustrated in a schematic diagram in Figure 2.5. The first scenario (Figure 2.5A) involves a direct redox reaction. As the nanoparticle (light blue sphere) impacts the electrode, the potential held on the electrode allows a redox reaction to occur, generating a sharp voltammetry signal ('spike'). This is also applicable to nanoparticles which are reducible to generate reductive 'spikes'. After the direct redox reaction, the products (small dark blue spheres) diffuse away.

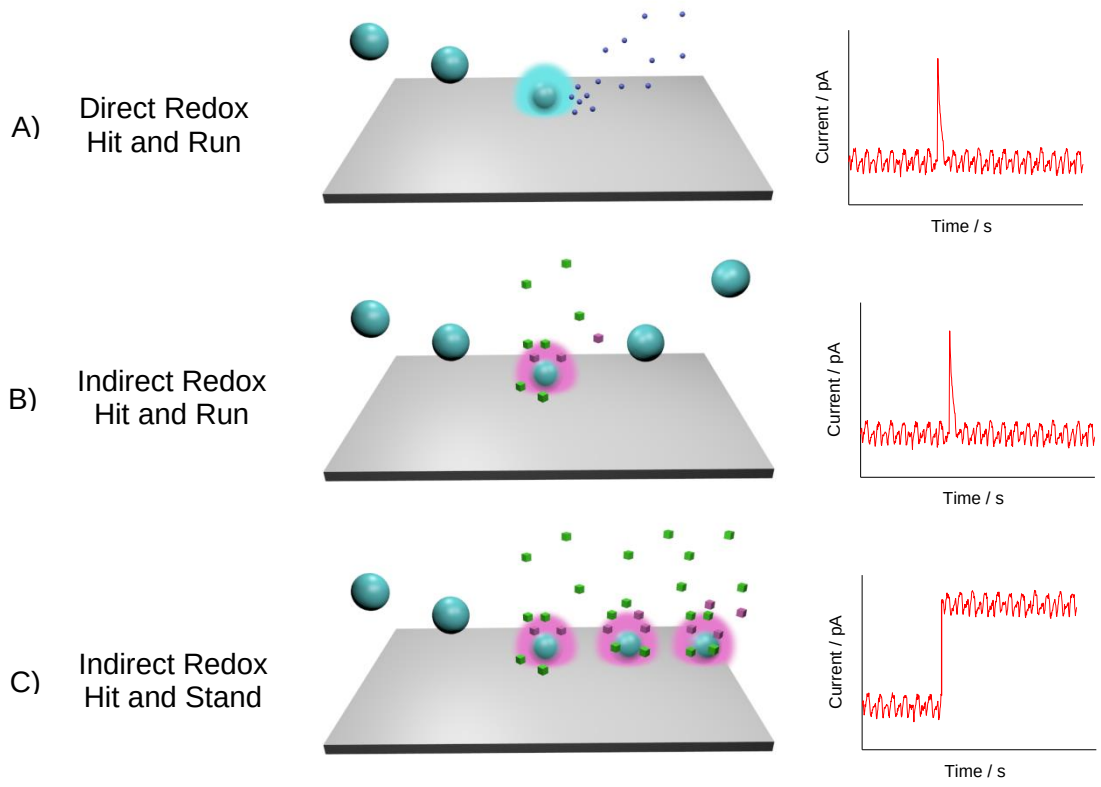

Figure 2.5 The three main scenarios of impact experiments. The voltammogram generated by each mechanism is next to the schematic diagram. A) Direct redox, hit and run B) Indirect redox, hit and run C) Indirect redox, hit and stand.

The second scenario (Figure 2.5B) involves a 'hit and run' and an indirect redox reaction. In this case, the nanoparticle itself does not undergo any redox reaction. Instead, it catalyses a redox reaction (green cubes to pink cubes). As the nanoparticle impacts on the electrode ('hit'), the electrons involved in the transformation generate a current. As the nanoparticle moves away from the electrode ('run'), the conversion stops and no further change in faradaic current is recorded. This results in a 'spike' recorded in the voltammogram. In this scenario, the nanoparticles are not consumed, making this a non-destructive detection technique. An advantage of this technique is the amplification of the signal. Comparing the catalysis of substrate (assuming a high concentration of reactants) to the direct oxidation or reduction of the nanoparticles, more electrons are passed in the former case. Thus, the signal generated is often larger in magnitude.

The third working scenario of impact experiments (Figure 2.5C) involves a 'hit and stand' and an indirect redox reaction. Similar to the second scenario, this is also a non-destructive technique. The nanoparticle once again catalyses a redox reaction (as illustrated by the conversion of green cubes to pink cubes). However, in the third scenario, once the nanoparticle hit the electrode surface ('hit'), it remains on the electrode surface for a considerable time ('stand') and continue to convert the reactants into products. Thus, a change in current ('step') is observed instead of a 'spike'.

Identification of the nanoparticles is possible with the impact experiments. In a paper by Stuart *et al.*, a mixture of nickel and silver nanoparticles are identified through the different potential where the 'spikes' occur at.[26] The onset of silver oxidation 'spikes' began at +0.45 V *vs.* a silver-silver chloride reference electrode whereas nickel oxidation 'spikes' only appeared beyond +1.55 V.[26] These onset potentials matched the potentials of the nanoparticles oxidation in the stripping voltammogram and hence the identity of the nanoparticles is confirmed.

Nanoparticles can be sized through two ways. First, in the case of direct redox reaction (first scenario), by relating the charge of a 'spike' through Faraday's law, to the number of atoms present in a nanoparticle and the size of the nanoparticle can thus be studied. Second, for the indirect redox methods (second and third scenarios), the radius of the nanoparticle (assumed spherical), at least in principle, can be determined through the current for the catalysed reaction.

In the first scenario of direct redox reaction, many redox active species have been identified.[26, 40, 42, 161-173] For example, various papers on single silver nanoparticle detection have been published.[26, 40, 42, 161-168] Silver nanoparticles are added into the electrolyte and the impact of silver nanoparticles on a micro carbon electrode is recorded.[26, 40, 42, 161-168] The signal results from the direct oxidation of the silver nanoparticles:

$$Ag_{(NP)} \rightarrow xAg^{+}(aq) + xe^{-}(m) \qquad \text{Equation 2.3}$$

where x is the number of silver atoms in a silver nanoparticle. Figure 2.6 depicts a typical 'spike' obtained by the impact experiments. Each 'spike' relates to a single nanoparticle impacting and

oxidising on the electrode and the size of the nanoparticles can be calculated through the equation below, assuming the nanoparticles are spherical in shape.[26]

$$Q = \frac{4n\pi F\rho {r_{NP}}^3}{3A_r} \qquad \text{Equation 2.4}$$

where Q is the charge passed under the 'spike', n is number of moles of electrons involved per mole of reaction, F is the Faraday constant, ρ is the density, r_{NP} is the radius of the nanoparticle and A_r is the relative atomic mass. It has been shown that the size of the silver nanoparticles derived from the 'spikes' matches with the sizing measured from SEM images.[162, 174] In addition to determining the size of the silver nanoparticles, if the size of the nanoparticles is plotted against time, the aggregation kinetics of silver nanoparticles in electrolyte can be monitored.[162] In a work by Ellison *et al.*, the proportion of monomer, dimer, trimer, tetramer, pentamer and hexamer of silver nanoparticles can be determined with the impact experiments.[163] Lees *et al.* showed that aggregation is slowed down in presence of high amount of citrate, the capping agent of silver nanoparticles.[164] As an ultimate aim to detect nanoparticles in the environment matrix, Stuart *et al.* showed through impact experiments, the detection of laboratory synthesized silver nanoparticles in seawater is possible.[40] They have further shown that the commercially available silver nanoparticles can also be characterised in the environmental medium of seawater.[165] The direct 'hit and run' method has also been applied to other nanoparticles including iron oxide (Fe_3O_4)[169], nickel[161, 170, 171], gold[171-173], cadmium[175] ,organic nanoparticles such as fullerene[41], indigo dye nanoparticles[174] and oil blue dye nanoparticles[176] and liposomes containing vitamin C[177] and catecholamine.[178]

As only a single nanoparticle undergoes the redox reaction each time upon impacting the microelectrode, the amount of Faradaic charge generated is relatively small. For example, the oxidation of a 20 nm radius silver nanoparticle will generate about 0.3 pC. Charges down to 1.22 fC has been detected for a nanoparticle with radius 3.1 nm.[179] The 'spikes' typically last from 5 milliseconds to 20 milliseconds.

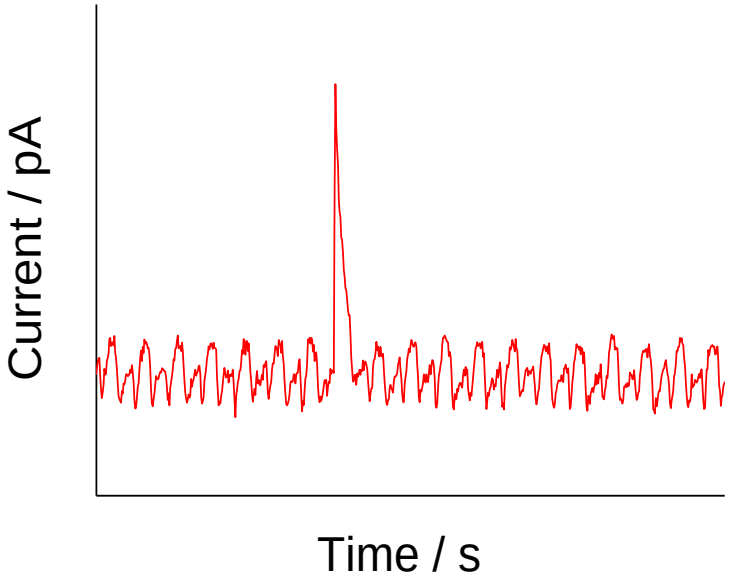

Figure 2.6 A typical 'spike' observed in the chronoamperogram.

In a variant, a type of impact experiments known as 'tagged redox coulometry' has been developed. It follows the first scenario where there is a direct redox reaction. However, in 'tagged redox coulometry', the nanoparticles themselves are not oxidised. Instead, redox molecules 'tagged' on the nanoparticles undergo the reaction.[166, 167, 180] The principle was demonstrated by Zhou *et al.*, where they attached 1,4-nitrothiophenol (NTP), which can undergo a 4 electron reduction, onto silver nanoparticles.[166, 167] As the nanoparticles hit the electrode surface, the NTP on the nanoparticle surface are reduced, generating a 'spike'. Thus, the 'tagged redox coulometry' method allows the detection of nanoparticles, which are not necessarily redox active, without destroying them.

The second scenario of indirect 'hit and run' involves three components: a redox reaction of reactant to product where the reactant is abundant in the electrolyte, an electrode inert to the redox reaction and a nanoparticle which catalyses the redox process. In this case, the electrochemical signal is detected as the electrocatalytic process (green cubes to pink cubes in Figure 2.5B) occurs when the catalytic nanoparticle hit the electrode surface.[43, 170, 181-183] The latter is inert to the redox reaction at the potential applied. The amount of reactant used in the

electrocatalytic process in the electrolyte brings about a signal amplification comparable to 'tagged redox coulometry'. One good example which demonstrates the second scenario is the catalysed reduction of hydrogen peroxide by silver nanoparticles on an inert carbon microdisc electrode.[181] As the silver nanoparticles hit the electrode surface, hydrogen peroxide is reduced on the nanoparticle surface, giving a 'spike' on the scan. The magnitude of the charge of the 'spikes' scales linearly with the hydrogen peroxide concentrations, showing that signal amplification is possible by increasing the reactant concentration. As the silver nanoparticle concentration increases, the frequency of impacts correlated linearly with it. This method has also been applied to numerous other redox systems such as water oxidation catalysed by iridium oxide nanoparticles,[43] proton reduction catalysed by nickel/nickel oxide nanoparticles,[170] hydrogen peroxide reduction by cerium(IV) oxide nanoparticle[184] and proton reduction promoted by platinum nanoparticles.[182] Proton reduction, possibly catalysed by silver or gold nanoparticles of different sizes, was studied by Kahk *et al.* who showed authentic nano-catalysis (kinetic acceleration due to small particle size) is observed for the studied silver nanoparticles.[183] Nano-catalysis was not observed on the gold nanoparticles.

The third scenario of indirect 'hit and stand' also depends on the nanoparticles to catalyse a redox reaction. Platinum nanoparticles are widely studied under this scenario on electrodes of various materials (carbon[185] and gold[185-187]). In work by Xiao *et al.*, proton reduction is chosen as the redox reaction to be catalysed by platinum nanoparticles on a carbon electrode.[185] The platinum nanoparticles remain on the carbon electrode for a substantial amount of time after hitting the carbon electrode ('hit and stand'). Proton reduction occurs at a lower potential on platinum compared to carbon. Thus, as more and more platinum nanoparticles are adsorbed on the carbon surface, an increased amount of proton reduction occurs on the electrode surface, resulting in a staircase-like voltammogram. Figure 2.7 shows a typical step observed in a chronoamperometry scan. The circled portion shows the current response when a single platinum nanoparticle hits the electrode surface. An increase in current is observed as the nanoparticle adds to the amount of electroactive surface where proton reduction can occur. This diffusional controlled process of converting reactant to product, assuming a perfect spherical particle on a perfectly flat electrode,

relates the radius of the nanoparticle, r_{NP}, to the amplitude of the current 'step', I, through Equation 2.5.[185, 188-190]

$$I = 4\pi(\ln 2)nFDC^{*}r_{NP} \qquad \text{Equation 2.5}$$

where n is the number of moles of electrons transferred per mole of reaction, F is the Faraday constant, D is the diffusion coefficient of the reactant, C^{*} is the bulk reactant concentration and r_{NP} is the radius of the nanoparticle.

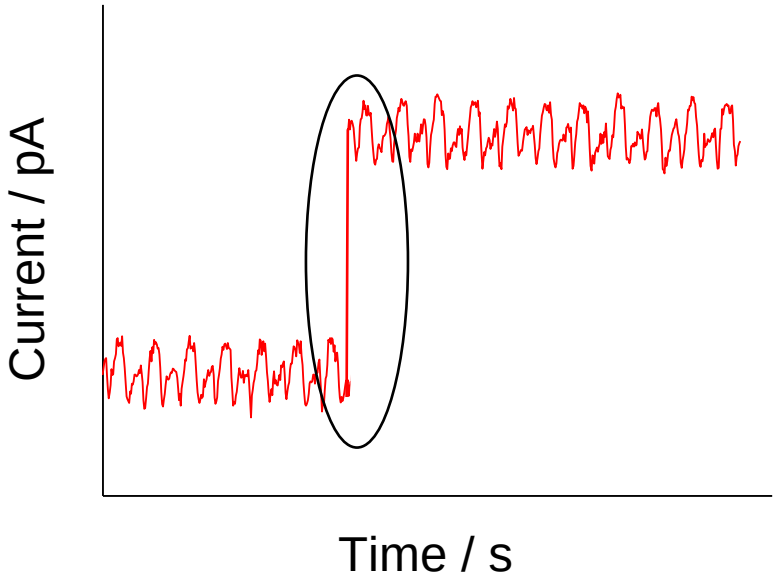

Figure 2.7 A typical 'step' observed in a chronoamperogram for an indirect redox, hit and stand mechanism.

Another well studied system to characterise platinum nanoparticles is through the catalysis of hydrazine oxidation to nitrogen and protons.[185, 187] It is suggested that for hydrazine oxidation, at low electrolyte concentrations (i.e. 5 mM), the impact frequency increases due to migration effects of the negatively charged citrate capped platinum nanoparticles.[187] If a mercury drop electrode is used instead of a gold or carbon electrode for hydrazine oxidation, as the platinum nanoparticles hit the electrode, the mercury poisons the catalytic property of platinum, resulting in current 'spikes' observed instead of 'steps'.[191] However, the presence of hydrazine in the platinum nanoparticle suspension may promote aggregation, leading to measurement of bigger clusters.[192] Titanium

dioxide nanoparticles have also been sized through similar experiments.[193] They photocatalyse the oxidation of methanol and in the presence of light, 'steps' were observed in the chronoamperometric scan.

How do the three scenarios compare to one another? All of them allow single nanoparticle detection and they are able to identify and size the nanoparticles.[26, 40, 42, 161-165, 167, 169, 172-174, 176, 181, 183, 185, 191, 192] All three experiments are also capable of studying nanoparticle aggregation.[163, 164] The seeming advantages of indirect redox reactions (Figure 2.5B and C) over direct redox reaction (Figure 2.5C) are that they are non-destructive and signal amplification can be attained. Thus, it is easier to detect smaller nanoparticles which generate small signals using indirect redox methods. However, direct redox reactions are less prone to false positive and system fouling. Further, across the impact experiments, there is also often an assumption, for example in Equations 2.4 and 2.5, that all the nanoparticles are perfect spheres.

The 'nano-impact' experiments give rise to other thoughts. First, for direct processes, the possibility of under sizing the nanoparticles due to partial reaction is established as statistically unlikely in a paper by Dickinson *et al.*[194] By studying the interplay of the Brownian motion and the timescale on which impacts occur, it is concluded that under direct oxidation or reduction, the nanoparticles are either 0% or 100% oxidised. Thus, partial reaction is statistically unlikely and hence the particles measured are not undersized. Second, for indirect processes, the presence of large capping agents on the working electrode surface such as 12-mercaptodocecanic acid and 16-mercaptohexadecanoic acid can stop the platinum nanoparticles from promoting hydrazine oxidation.[195] Thus, the size of the capping agent used is important in controlling charge transfer from the nanoparticle to the electrode. The capping agent used should not be too bulky. Third, the factor limiting the minimum measurable size is the signal to noise ratio. A lower limit of detection is achievable if the ratio is improved. One of the approaches to the issue is to reduce the size of the electrode. In most of the literature work, microelectrodes are used to minimize noise.[26, 39-42, 138, 150, 151, 162-168, 171, 172, 174-177, 181, 185, 186, 196-198] Kleijn *et al.* have developed a new prototype of

nanoelectrode where they limit the size of the electroactive surface through controlling the amount of electrolyte in contact with the electrode.[199] This limits the electrode size and hence reduce the noise of the system. Last, the microelectrodes used in most experiments may experience shielding effects from the sheath surrounding the electrode.[200] The nanoparticles approaching the electrode may adsorb onto the glass before they reach the electrode surface. A micro cylinder electrode, which consists of a wire protruding out from the surface, reduces the shielding effect of the glass sheath, resulting in an increased impact frequency and allows detection of a lower nanoparticle concentration.[201]

Impact experiments have also been combined with other electrochemical techniques which allow a 'twin prong' strategy for nanoparticle detection. When combined with the technique of stripping voltammetry in Section 2.3, the sticking coefficient of nanoparticles can be calculated.[171, 197] The electrode is suspended in a nanoparticle suspension for a period to allow adsorption. Then, stripping voltammetry is performed to obtain the number of nanoparticles adsorbed on the surface. After that, impact experiments are used to determine the number of nanoparticles hitting the electrode surface. The ratio of the number of nanoparticles sticking to the number of nanoparticles impacting the electrode surface is taken to be the sticking coefficient. This has been performed on silver[197], nickel[171] and gold[171] nanoparticles, showing that about 10% - 20% of the nanoparticles stick to the carbon electrode surface.[171, 197]

In conclusion, the novel method of 'nano-impact' has started to revolutionise single nanoparticle detection and characterisation. Though the work is still at the beginning stage, it has already provided significant insights and this area of nanoparticle detection is predicted to grow rapidly. The well-studied method of anodic stripping voltammetry complements it by providing both fundamental and analytical information. However, recent work[202] has shown that incomplete stripping of nanoparticles in anodic stripping voltammetry can lead to issues of quantification when aggregation of the nanoparticles takes place on the electrode surface (Chapter 4, Section 4.1 and

4.3). For this reason, single nanoparticle experiments may be preferred. In the next chapter, the experimental details and chemical information are summarised.

Chapter 3 Experimental

This chapter summarises the experimental reagents used in this thesis. The type of working electrodes and reference electrodes are also described in this chapter. As many different samples of silver nanoparticles are used within the thesis, their syntheses, characterisations and suppliers are detailed in the sections in which they are employed.

3.1 Chemicals

This section details all of the chemical reagents used within this thesis (with the exception of silver nanoparticles samples). All solutions were made up of ultrapure water with resistivity not less than 18.2 MΩ cm at 298 K (Millipore, UK).

Chemical Name	Chemical Formula	Purity	Supplier
6-mercapto-1-hexanol	$HO(CH_2)_6SH$	≥ 97%	Fluka Chemicals, Gillingham, UK
Alumina Powder, 0.05 μm	Al_2O_3		Buehler, Coventry, UK
Cetyltrimethylammonium Bromide (CTAB)	$(C_{16}H_{33})N(CH_3)_3Br$	95%	Sigma Aldrich, Gillingham, UK
Ethanol	C_2H_5OH	≥99.8%	Sigma Aldrich, Gillingham, UK
Hexaaminеruthenium(III) Chloride	$Ru(NH_3)_6Cl_3$	98%	Sigma Aldrich, Gillingham, UK
Hydrochloric Acid, Concentrated	HCl	~37%	Fisher Scientific, Loughborough, UK
Hydrogen Peroxide Solution	H_2O_2	>30% w/v	Fisher Scientific, Loughborough, UK
L-Cysteine	$C_3H_7NO_2S$	97%	Sigma Aldrich, Gillingham, UK
Lactic Acid (Solution in Water)	$C_3H_6O_3$	>85%	Sigma Aldrich, Gillingham, UK
Nitric Acid, Concentrated	HNO_3	>70%	Fisher Scientific, Loughborough, UK
Potassium Chloride	KCl	>99.5%	Sigma Aldrich, Gillingham, UK
Potassium Iodide	KI	≥99.5%	Sigma Aldrich, Gillingham, UK
Silver Nitrate	$AgNO_3$	>99%	Sigma Aldrich, Gillingham, UK

Sodium Borohydride	$NaBH_4$	99%	Sigma Aldrich, Gillingham, UK
Sodium Chloride	NaCl	>99%	Sigma Aldrich, Gillingham, UK
Sodium Nitrate	$NaNO_3$	>99.5%	Fisons Scientific, Loughborough, UK
Sodium Sulphide Nonahydrate	$Na_2S.9H_2O$	98+%	Acros Organics, Geel, Belgium
Sulphuric Acid, Concentrated	H_2SO_4	>95%	Fisher Scientific, Loughborough, UK
Synthetic Sweat			Synthetic Urine e.k., Eberdingen, Germany
Synthetic Urine			Synthetic Urine e.k., Eberdingen, Germany
Trisodium Citrate	$Na_3C_6H_5O_7$	>99%	BDH Laboratory Supplies, Poole, UK
Urea	CH_4N_2O	>99%	Sigma Aldrich, Gillingham, UK

Table 3.1 List of chemicals used

3.2 Electrochemistry

This section describes the different type of electrodes used within this thesis. All electrochemical experiments were performed in a thermostated Faraday cage at 25 ± 1 °C with a three electrode set up. For all the work in the thesis, a platinum mesh (99.99%) from Goodfellow Cambridge Ltd, Huntingdon, UK acted as a counter electrode. The electrochemical experiments were controlled by a μAutolab II or PGSTAT302N from Metrohm-Autolab BV (Utrecht, The Netherlands) using the software of GPES or NOVA 1.10. For a glassy carbon electrode, it was polished to a mirror finish on diamond sprays from Kemet (Kent, UK) in the sequence of size 3.0 μm, 1.0 μm and 0.1 μm for experiments. The micro carbon fibre electrode was polished on alumina powder from Buehler, Coventry, UK in the size sequence of 1.0 μm, 0.3 μm and 0.05 μm before experiments.

Working Electrode	Supplier	Size
Macro Glassy Carbon	CH instruments, Austin, USA	1.5 mm radius
Micro Carbon Fibre	BASi, West Lafayette, USA	11 μm diameter
Carbon Screen Printed Electrode	Dropsens, S. L., Llanera, Spain	2.0 mm radius

Table 3.2 Types of working electrode used

Reference Electrode		Supplier	Potential *vs.* SHE
Silver/Silver Ion Reference Electrode	$Ag/AgNO_3$ (10 mM)/ $NaNO_3$ (90 mM)	Homemade	+0.69 V *vs.* SHE[†]
Leak-less Silver/ Silver Chloride Electrode	Ag/AgCl/KCl (1 M)	Cypress Systems, Lawrence, USA	+0.23 V *vs.* SHE[‡]
MSE (Mercury/Mercurous Sulphate Electrode)	$Hg/Hg_2SO_4/K_2SO_4$ (saturated)	BASi, West Lafayette, USA	+0.62 V *vs.* SHE[17]
SCE (Standard Calomel Electrode)	Hg/Hg_2Cl_2/KCl (saturated)	Hach Lange, Salford, UK	+0.24 V *vs.* SHE[17]

Table 3.3 Types of reference electrodes used [†]Experimentally measured as +0.45 V *vs.* SCE

[‡]Experimentally measured as −0.012 V *vs.* SCE

For the 'nano-impact' experiments, chronoamperometric scans of fifty seconds duration with a sampling time of 0.0005 s were recorded. The number and magnitude of the 'spikes' were determined by the software of SignalCounter. The software SignalCounter was developed by Dr. Dario Omanović from Division for Marine and Environmental Research, Ruđer Bošković Institutue, Zagreb, Croatia for in-house use as a part of a collaboration. This software is programmed to pick up 'spikes' of a minimum intensity of 5 pA height. A linear baseline was taken and the charge underneath the peak calculated. The baseline was taken at the midpoint of the average noise to minimize the amount of background taken as signal. All signals were further checked manually to differentiate actual 'spikes' from noise through the signal shape.

3.3 Non-Electrochemical Instrumentation

All the ultra-violet visible (UV-vis) spectra were recorded on a UV-vis spectrometer (U-2001, Hitachi, Tokyo, Japan) with a tungsten iodide and a deuterium light source. The scan rate and the wavelength window are described in the respective sections. All of the nanosight tracking analysis (NTA) experiments are performed on LM10 (NanoSight Ltd, Wiltshire, UK) at 25 °C. Dynamic light scattering (DLS) (Zetasizer NanoZS, Malvern Instruments Ltd, Malvern, UK) was performed at 25 °C with a red laser of 633 nm. As different microscopes are used each time for SEM, the individual machines are detailed in the respective sections.

Chapter 4 Comparing Stripping Voltammetry and 'Nano-impacts' for Nanoparticle Detection

The strong demand for nanoparticle detection and characterisation propelled by the boom of the nanotechnology industry has driven electrochemists to deploy stripping voltammetry and 'nano-impacts' (Chapter 2, Section 2.3 and 2.4). In this chapter, we look at the detection of metallic nanoparticles via the two methods. First, stripping voltammetry, as discussed in Section 4.1, is used to investigate the oxidation of metal nanoparticles at various surface coverages. Then, analytical expressions for the potential of metal oxidation were developed. The second method, 'nano-impact', is studied in Section 4.2 where the detection of single silver nanoparticles in an optically opaque solution was performed successfully. This would otherwise be impossible for dynamic light scattering (DLS) and nanosight tracking analysis (NTA). Section 4.3 brings together the two electrochemical techniques for comparison and contrast through the oxidation of silver nanoparticles with different capping agents. These three works are published in Nanoscale,[203] ChemistryOpen[204] and Chemistry - A European Journal[205] respectively. They are performed in collaboration with Dr. Christopher Batchelor-McAuley, Dr. Kristina Tschulik, Dr. Kerstin Jurkschat, Prof. Margitta Uhlemann and Dr. Alison Crossley. Dr. Christopher Batchelor-McAuley is responsible for the theoretical equations used in Section 4.1. Dr. Kristina Tschulik synthesised the silver nanoparticles synthesis in Section 4.1. Both of them helped with NTA, ultra-violet visible (UV-vis) measurements and the experimental interpretation in Section 4.1. Prof. Margitta Uhlemann and Dr. Alison Crossley recorded the scanning electron microscope (SEM) images on the silver nanoparticles in Section 4.1. The transmission electron microscope (TEM) images of silver nanoparticles in Section 4.2 and 4.3 were kindly provided by Dr. Kerstin Jurkschat.

4.1 Anodic Stripping Voltammetry: Electrochemical Evidence for the Surface Agglomeration

4.1.1 Introduction

Nanoparticles and nanoparticle-modified electrodes find a number of uses within the field of electrochemistry and have specific importance for electroanalysis.[206-208] In the literature, nanoparticles have been employed in the detection of a wide range of analytes including, among many others, DNA,[209-211] proteins,[212] heavy metal ions[213] and glucose.[121] Although commonly used, the thermodynamics and chemical properties of these nanoparticles, which may be significantly altered from that of the bulk material, are still relatively poorly understood. This is especially true for an electrochemical system where the nanoparticles will interact with the surrounding electrolyte, any surface stabilising capping agent and the 'inert' supporting substrate.[214] For small nanoparticles (<2 nm in diameter), the electronic structure of the material will be altered from that of the bulk.[54] However, even at larger sizes, the properties of the metallic species may still be changed. Plieth proposed that for an isolated nanoparticle the formal potential for the oxidation of the metallic species should vary with the particle radius in accordance with the following equation:[60]

$$E^{\theta}_{f(NP)} = E^{\theta}_{f} - \frac{a}{r_{NP}} \qquad \text{Equation 4.1}$$

where $E^{\theta}_{f(NP)}$ is the formal potential for the oxidation of the nanoparticle, E^{θ}_{f} is the formal potential for the bulk process, a is a constant which is dependent upon the surface energy, γ, of the metal and r_{NP} is the radius of the nanoparticle. As the particle size decreases, the increased surface curvature will lead to an increase in the surface energy and hence this will lead to an associated decrease in the formal potential for the oxidation.[60] However, the magnitude of a nanoparticle surface energy is of debate; taking silver as an example, reports of the nanoparticulate surface energy range between 0.97 J m^{-2} to 7.2 J m^{-2}.[215, 216] The value for bulk silver is commonly estimated as being between 1.07 and 1.54 J m^{-2}.[216] This wide range of values for nanoparticles likely reflects, at least in part, the sensitivity of the surface energy to the supporting matrix.

Consequently, in terms of an electrochemical experiment it is unclear how influential the surface energy will be upon the thermodynamics of the nanoparticulate metal.

The use of electrochemical techniques to determine apparent 'size effects' of the nanoparticles through electro-oxidation has been previously investigated within the literature.[63, 217-220] Voltammetry provides a relatively facile experimental method by which to probe both the thermodynamics and kinetics of an electron transfer process. However, due to the necessary convolution of the time and energy domains, it is often found that the obtained voltammetric results are complex in nature and require simulation in order to extract physically significant information. To further complicate the issue, in the case of a reversible oxidation of an array of nanoparticles, the diffusion of the ions from the electrode resulting from the oxidation must be considered. For a particle on a surface, four diffusional cases for the mass-transport of the ions from the particle may be considered, as outlined in Figure 4.1.[221, 222] First, at short times, a linear diffusion regime will operate (case 1), provided the nanoparticles are sufficiently separated to be diffusionally independent of each other. Due to the small size of the particles, this case will only be operative at very short times ($\sim r^2/D$ i.e. for many systems less than 1 μs). Therefore, this limit is unlikely to be influential during normal voltammetric experiments on nanoparticle arrays; hence, this regime is not considered further within this thesis. At relatively short times (but longer than $\sim r^2/D$) or for lower surface coverages, the nanoparticles may still be considered to be diffusionally independent but the mass-transport of the material from the particles becomes radial (case 2). At further times and/or for larger surface coverages the diffusion layers of each nanoparticle will overlap weakly, such that the particles will no longer be diffusionally independent (case 3). At higher surface coverages or longer times still, the diffusion layers will overlap strongly, such that, the diffusion of the produced material away from the surface may be considered to be linear across the whole of the geometric area of the electrode (case 4).

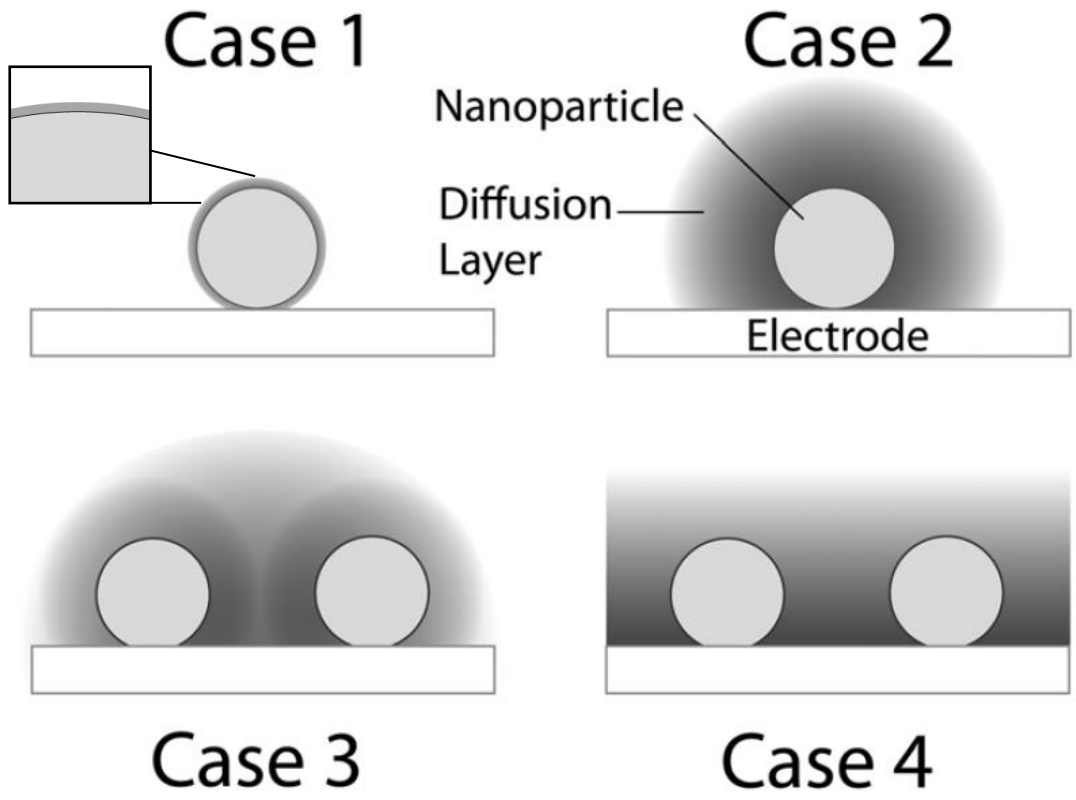

Figure 4.1 Schematic diagram showing the four limiting cases for diffusion at a nanoparticle and nanoparticle ensembles.

This section develops new analytically useful expressions for the oxidation of nanoparticles under the diffusional case 4 and case 2 limits. The voltammetric response due to irreversible electron transfer kinetics is also considered. In all cases, we have assumed the electrode to be a conductive support that is otherwise passive in the oxidation process. The transitional 'case 3' diffusion regime must be solved numerically and has been dealt with previously by Ward-Jones *et al.*[62] This section develops these expressions further so as to account for a possible variation in the formal potential of the oxidation, in accordance with the Plieth equation.[60] In total, these theoretical results demonstrate, first, that the peak potential for the nanoparticle oxidation is predicted to occur at values more negative than the associated formal potential. This shift in the peak potential can be large (hundreds of millivolts) and will occur even when the thermodynamics of the oxidation are unaltered from that of the bulk material. Second, for the oxidation of an array of nanoparticles the position of the peak potential is sensitive to the surface coverage of the metallic species. Changes

to the formal potential for the oxidation will only likely cause a relatively minor shift in the peak potential for many experimental cases.

Finally, experimental results for the oxidation of silver nanoparticles are presented showing good quantitative agreement with the presented theory. At higher surface coverages of silver ($\Gamma_{Ag} \geq 3 \times 10^{-6}$ mol m^{-2}), the peak potential is shown to be consistent with the theoretically presented expression for a case 4 diffusion regime. However, at lower surface coverages ($\Gamma_{Ag} \leq 1.5 \times 10^{-6}$ mol m^{-2}), the peak potential is found to become relatively insensitive to the surface coverage of silver. This insensitivity is analysed in terms of the surface clustering and agglomeration of the silver nanoparticles leading to a case 3 diffusion regime to become operative. The current work demonstrates how the surface agglomeration can have a significant impact upon the peak potential for the oxidation at low surface coverages. The measurement of the peak potential thus gives an analytically useful route to determining the extent of the surface agglomeration.

4.1.2 Theory

The theory presented herein first gives new analytically useful limiting cases for the situation originally studied exclusively via numerically simulation by Ward-Jones *et al.*[62] Second, these expressions are developed further to account for the predicted variation in the formal potential as a function of the particle radius. This alteration of the formal potential follows that proposed by Plieth.[60] All the theoretical equations in this section (Equation 4.3 – 4.29) were derived by Dr. Christopher Batchelor-McAuley. The key equations are listed in this section and all the detailed derivations are found in Appendix A.

In general, the oxidation of a metallic species, M, may be described by the following reaction,

$$M(s) \rightarrow M^{n+}(aq) + ne^{-}(m) \qquad \text{Equation 4.2}$$

where n is the number of moles of electrons passed per mole of reaction. For an array of randomly distributed nanoparticles upon an electrode surface, two limiting diffusional regimes will be considered. First, is the case in which the nanoparticle diffusion layers strongly overlap (case 4). The

mass-transport of the M^{n+} ions away from the electrode surface can be described as following a linear diffusion regime across the whole of the electrode. Second, is the case in which the nanoparticles are well separated and the diffusion layer at each nanoparticle does not overlap with those of the neighbouring nanoparticles (case 2). For such cases, the oxidation of each nanoparticle may be considered to occur independently. Under this regime, due to the small size of the particles, the mass-transport of the formed M^{n+} away from the metallic surface will be radial, such that, the mass-transport may be described as being at a steady-state at all times after an initial short period ($\sim r^2/D$).

The following sections serve to provide analytical expressions for the decrease (due to oxidation) in the radius of the nanoparticles as a function of the electrode potential. From consideration of the number of moles contained in a sphere of radius r_{NP}, the change in particle size can be related to the total charge passed,

$$q = 4\pi nF \frac{\rho}{3A_r}\left({r_{NP}}^3 - {r_{NP,t}}^3\right) \qquad \text{Equation 4.3}$$

$$Q = n_{NP} \cdot q \qquad \text{Equation 4.4}$$

where, Q is the total charge passed, q is the charge passed per nanoparticle, n is the number of electrons transferred per mole of reaction, F is the Faraday constant (96485 C mol^{-1}), ρ is the density of the metal, A_r is the atomic weight of the metal, r_{NP} is the particle radius at time equal zero, $r_{NP,t}$ is the particle radius [which varies as a function of time, t], Q is the total charge passed and n_{NP} is the total number of nanoparticles on the electrode surface. Moreover, current can be expressed as dQ/dt, where t is time. Therefore, differentiation of Equation 4.4 gives a route by which the size of the particles, r_{NP}, as a function of potential, E, may be related to the predicted current, I. Note, in the case of a linear-sweep voltammogram,

$$I = \upsilon \frac{dQ}{dE} \qquad \text{Equation 4.5}$$

where υ is the experimental scan rate.

4.1.2.1 The Influence of Mass Transport on Stripping Voltammetry

Initially, the models assume that the formal potential for the oxidation of the nanoparticulate metal is unaltered from that of the bulk material. This section serves to highlight both the significant effect that the mass-transport regime has upon the stripping voltammetry and also demonstrates the influence of the reversibility of the electron transfer.

4.1.2.1.1 Reversible Electron Transfer, Case 4

In the reversible limit, the surface concentration of M^{n+} is described by the Nernst equation:

$$E = E_f^{\theta} + \frac{RT}{nF} ln \frac{[M^{n+}]}{[\,]^0} \qquad \text{Equation 4.6}$$

where, E is the electrode potential, E_f^{θ} is the formal potential, R is the ideal gas constant (8.314 J K^{-1} mol^{-1}), T is the temperature, $[M^{n+}]$ is the concentration of M^{n+} at the nanoparticle surface, $[\,]^0$ is the standard concentration (1 mol dm^{-3}) and all other symbols are as earlier. In a linear-sweep voltammetric experiment, the potential held upon the electrode is varied linearly as a function of time, such that,

$$E = E_i + \upsilon t \qquad \text{Equation 4.7}$$

where E_i is the initial electrode potential, υ is the scan rate and t is the time. Therefore,

$$\frac{[M^{n+}]}{[\,]^0} = \exp(n\theta) = exp\left(\frac{nF}{RT}(E_i + \upsilon t - E_f^{\theta}\right) \qquad \text{Equation 4.8}$$

where θ is the dimensionless potential. The diffusion of the M^{n+} away from the metallic surface is taken to be linear across the whole of the electrode surface. This linear diffusion regime occurs due to strong overlapping of the diffusional layers between adjacent nanoparticles. Using Fick's first law, the change in the number of moles of metal (N) as a function of time, across the whole of the electrode may be described by the following equation;

$$\frac{dN}{dt} = -A_{elec} \frac{D}{\delta} [M^{n+}] \qquad \text{Equation 4.9}$$

where A_{elec} is the geometric area of the electrode, D is the diffusion coefficient ($m^2\ s^{-1}$), δ is the linear diffusion layer thickness and all other symbols are as before. Note, the diffusion layer thickness may be described by the value of $\sqrt{\pi Dt}$ at short times; for larger times a steady-state Nernst layer will be formed by the operation of natural convection.[223, 224] To find an expression for the diffusional flux (j) of the oxidised material away from the interface, Equation 4.9 is divided through by the number of nanoparticles on the surface (n_{NP}) and the surface area of a nanoparticle;

$$j = -\frac{1}{\Gamma_{NP} 4\pi {r_{NP}}^2} \cdot \frac{D}{\delta} \cdot [M^{n+}] \qquad \text{Equation 4.10}$$

where Γ_{NP} is the surface coverage of the nanoparticles (= n_{NP}/A_{elec}). The flux, j, may also be defined in terms of the change in the radius of the nanoparticle,

$$j = \frac{\rho}{A_r} \cdot \frac{dr_{NP}}{dt} \qquad \text{Equation 4.11}$$

By combining Equation 4.10 and 4.11, we get,

$$j = -\frac{1}{\Gamma_{NP} 4\pi {r_{NP}}^2} \cdot \frac{D}{\delta} \cdot [M^{n+}] = \frac{\rho}{A_r} \cdot \frac{dr_{NP}}{dt} \qquad \text{Equation 4.12}$$

Using Equation 4.8 and rearranging we obtain;

$$(r_{NP})^2 \ \frac{dr_{NP}}{dt} = -\frac{[\,]^0}{\Gamma_{NP} 4\pi} \frac{D}{\delta} \frac{A_r}{\rho} exp(n\theta_i)\ exp\left(\frac{nF\upsilon t}{RT}\right) \qquad \text{Equation 4.13}$$

where θ_i is the dimensionless initial potential $[(E_i - E_f^{\theta})F/RT]$. By assuming δ is a constant, selecting a suitable starting potential (where exp $\theta_i \approx 0$, i.e. $\theta_i \approx -\infty$) and solving the differential equation then we obtain an expression for the change in the particles radius as a function of potential:

$$(r_{NP,t})^3 = (r_{NP})^3 - \frac{3[\,]^0}{4\pi\Gamma_{NP}} \frac{D}{\delta} \frac{A_r}{\rho} \frac{RT}{n\upsilon F} \cdot exp(n\theta) \qquad \text{Equation 4.14}$$

Figure 4.2 depicts for a given set of parameters (see figure caption), the predicted voltammetric wave shape and how the peak potential (E_p) varies with both the nanoparticle surface coverage and the initial particle radius. From consideration of Equation 4.14, where it is assumed that the

diffusion layer thickness is rapidly established and constant,[224, 225] then the peak potential is also predicted to shift with RT/nF *vs.* the natural log of the scan rate.

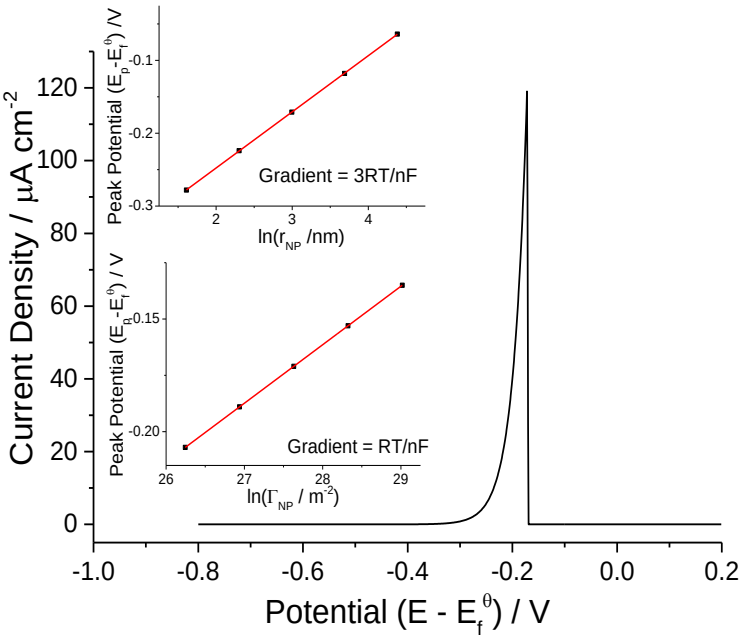

Figure 4.2 Theoretically predicted anodic stripping voltammetric wave shape for the case 4 diffusion regime. r_{NP} = 20 nm, n = 1, D = 1 × 10^{-9} m^2 s^{-1}, A_r = 100 g mol^{-1}, Γ_{NP} = 1 × 10^{12} particles per m^2, δ = 100 µm, ρ = 10 × 10^6 g m^{-3} and υ = 0.1 V s^{-1}. Inlays depict the variation in the peak potential (E_p) with the initial particle (top) (r_{NP} = 5 – 80 nm) radius and nanoparticle surface coverage (bottom) (Γ_{NP} = 0.25 – 4 × 10^{12} m^{-2}). For the inlays all other variables are kept the same as those used in the main figure.

In all of the cases presented in Figure 4.2 (under conditions of diffusion only mass-transport and in the absence of the thermodynamics being altered on the nanoscale), the oxidation occurs significantly below the formal potential. This lowering of the potential occurs due to the mass-transport of the oxidised material (M^{n+}) away from the electrode and the finite surface coverage of the metal. Experimentally, the variation of the peak potential as a function of surface coverage gives a practical method for determining the likely diffusion regime operative upon an electrode surface. A plot of the peak potential against natural log of the nanoparticle surface coverage should yield a straight line with gradient RT/nF. The peak potential is also strongly dependent upon the surface coverage of nanoparticles (Γ_{NP}) and initial nanoparticle radius. As the size decreases, the peak potential shifts to more negative values, where a plot of the peak potential *vs.* the natural log of the nanoparticles radius should yield a straight line of gradient $3RT/nF$. However, it should be

noted that this variation in the stripping peak with particle radius – for a given nanoparticle surface coverage (Γ_{NP}) – in fact only reflects the change in the total surface coverage of the metal (Γ_M) upon the electrode. This arises due to the fact that the surface coverage of nanoparticles is inversely proportional to the cube of the particle radius, consequently, for a given metal surface coverage (Γ_M) the oxidation is insensitive to the size of the nanoparticles.[a] These results demonstrate how for experiments involving the seed growth of nanoparticles on a surface (i.e. Γ_{NP} is constant and only r_{NP} is varied), the stripping voltammetry of nanoparticle arrays under a case 4 diffusion regime will exhibit a clear size dependency due to the alteration of the quantity of metal on the surface. This size dependency will be apparent even if the associated thermodynamics of the metallic nanoparticles are equivalent to that of the bulk material.

4.1.2.1.2 Reversible Electron Transfer, Case 2

Equation 4.14, presented above, describes the variation in the nanoparticle radius as a function of the potential for the case 4 limit. This equation predicts that the peak potential for the anodic stripping will decrease ad infinitum with decreasing surface coverage. This situation is not physically realistic. A lower limit for the peak potential may be obtained through consideration of the case 2 regime in which the nanoparticles are all considered to be diffusionally independent. The diffusion only mass-transport limiting current (I_{lim}) for a spherical particle on a flat electrode is given by,[188]

$$I_{lim} = 4\pi nFCDr_{NP}ln2 \qquad \text{Equation 4.15}$$

where C is the concentration of the reactant. Given that,

$$I = -nFA_{NP}j_{NP} \qquad \text{Equation 4.16}$$

where A_{NP} is the surface area of a single nanoparticle for the current model. The mass-transport limited oxidative flux at a nanoparticle, j_{NP}, can be given as,

[a] This point is more clearly exemplified by considering that $\Gamma_{NP} = (3A_r\Gamma_{Ag})/(4\rho\pi r_{NP}^3)$, using the *approximation* that the peak potential occurs when $r = 0$, then an expression for the peak potential in the case 4 regime may be given as $E_p - E^{\theta}_f = \ln[(\Gamma_{Ag}\delta nFv)/([\,]^0DRT)]$.

$$j_{NP} = -k_{MT}[M^{n+}] \qquad \text{Equation 4.17}$$

where k_{MT} is the mass-transport coefficient ($k_{MT} = (D \ln 2)/r$). The flux, j_{NP}, may again also be defined in terms of the change in the radius of the nanoparticle,

$$j_{NP} = \frac{\rho}{A_r} \cdot \frac{dr_{NP}}{dt} \qquad \text{Equation 4.18}$$

By combining Equations 4.17 and 4.18 we get,

$$r_{NP}\ \frac{dr_{NP}}{dt} = -[\,]^0 \frac{A_r}{\rho} Dln2\ exp(n\theta_i)\ exp\left(\frac{nF\upsilon t}{RT}\right) \qquad \text{Equation 4.19}$$

solving this differential equation and recognising that if we select a suitable starting potential (where exp $\theta_i \approx 0$, i.e. $\theta_i \approx -\infty$), we obtain an expression for the change in the particle radius as a function of potential:

$$(r_{NP,t})^2 = (r_{NP})^2 - 2[\,]^0 \frac{A_r}{\rho} Dln2 \frac{RT}{nF\upsilon} \cdot exp(n\theta) \qquad \text{Equation 4.20}$$

Figure 4.3 depicts for a given set of parameters – as indicated in the figure caption – the predicted voltammetric wave shape and how the peak potential varies as a function of both the particle initial radius and the experimental scan rate. This voltammetric response represents the lower limit at which the oxidation may occur (for a given initial particle radius, under conditions of diffusion only mass-transport and in the absence of the thermodynamics being altered on the nano-scale). Due to the particles being diffusionally independent, within this limit, the peak potential is insensitive to the surface coverage. However, the peak potential now directly depends upon the initial particle radius (Figure 4.3 inlay). Again, this demonstrates how even in the absence of the thermodynamics of the oxidation being altered, the voltammetry will exhibit a significant size effect. Finally, the variation of the peak potential as a function of the scan rate is significantly simplified in this limit due to the diffusional flux being at steady-state, hence the plot of peak potential *vs.* the natural log of scan rate is predicted to vary with RT/nF.

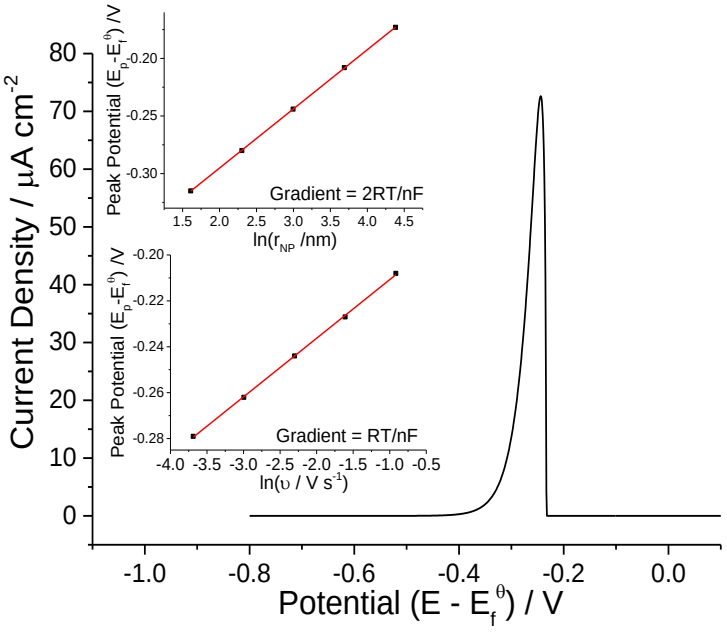

Figure 4.3 Theoretically predicted anodic stripping voltammetric wave shape for the case 2 diffusion regime. r_{NP} = 20 nm, n = 1, D = 1 × 10^{-9} m^2 s^{-1}, A_r = 100 g mol^{-1}, Γ_{NP} = 1 × 10^{12} particles per m^2, ρ = 10 × 10^6 g m^{-3} and υ = 0.1 V s^{-1}. Inlays depict the variation in the peak potential with the initial particle radius (top) (r_{NP} = 5 – 80 nm) and the experimental scan rate (bottom) (υ = 0.025 – 0.4 V s^{-1}). For the inlays all other variables are kept the same as those used in the main figure.

4.1.2.1.3 Irreversible Electron Transfer

In the irreversible limit, the oxidation process is insensitive to the mass-transport of the formed M^{n+} away from the metallic surface, hence the voltammetric responses for all diffusional cases are identical in this limit. Here the oxidative flux is described in terms of the Butler–Volmer equation and the change in the particle radius:

$$j_{NP} = \frac{\rho}{A_r}\frac{dr_{NP}}{dt} = -k^0[\,]^0\exp((n' + \beta)\theta) \qquad \text{Equation 4.21}$$

where, k^0 is the rate of electron transfer, n' is the number of electrons passed before the rate determining electrochemical step and β is the transfer coefficient of the rate determining step. It should be noted that for the current example $k^0[\,]^0$ is equal to $k_s\Gamma_M$, where k_s is the surface electron transfer rate and Γ_M is the surface coverage of metal atoms on the metallic surface.[62] The value of Γ_M will be of the order of 1 × 10^{-5} mol m^{-2} for macro surfaces, however, given that the current work is focused on nanoparticulate systems, accurate determination of the surface coverage of the

metal atoms is often not readily feasible. Consequently, it is more appropriate to use the value of k^0 as a measure of the electron transfer rate constant. Solving Equation 4.21, we obtain the following expression for the variation in the radius as a function of electrode potential:

$$r_{NP,t} = r_{NP} - k^0 \cdot [\,]^0 \cdot \frac{A_r}{\rho} \cdot \frac{RT}{(n'+\beta)\upsilon F} exp[(n'+\beta)\theta] \qquad \text{Equation 4.22}$$

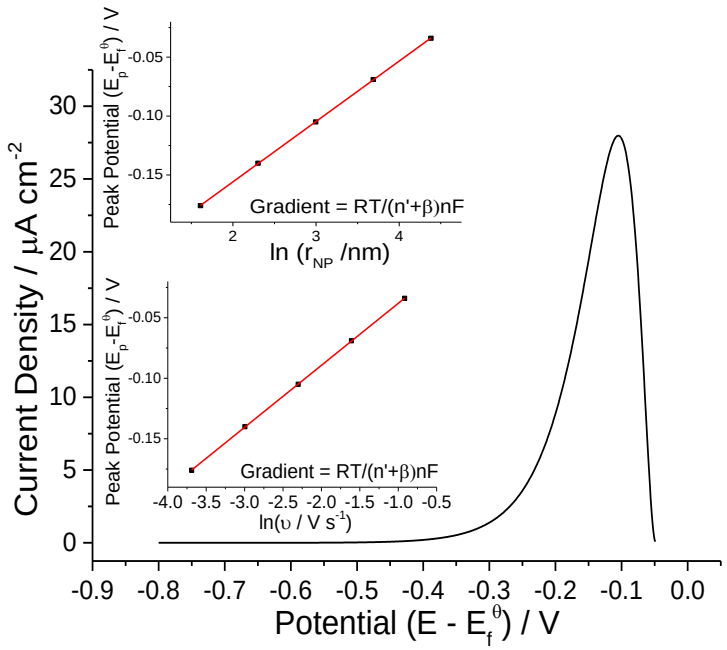

Figure 4.4 Theoretically predicted anodic stripping voltammetric wave shape for the case of irreversible electron transfer kinetics. r_{NP} = 20 nm, n' = 0, β = 0.5, D = 1 × 10^{-9} m^2 s^{-1}, k^0 = 1 × 10^{-5} m s^{-1}, A_r = 100 g mol^{-1}, Γ_{NP} = 1 × 10^{12} particles per m^2, ρ = 10 × 10^6 g m^{-3} and υ = 0.1 V s^{-1}. Inlays depict the variation in the peak potential with the initial particle radius (top) (r_{NP} = 5 – 80 nm) and the experimental scan rate (bottom) (υ = 0.025 – 0.4 V s^{-1}). For the inlays all other variables are kept the same as those used in the main figure.

Figure 4.4 depicts the predicted voltammetric response for this model for the set of parameters given within the figure caption. Again, the peak current is found to be insensitive to the surface coverage. This insensitivity arises due to the electron-transfer, and not the mass-transport of M^{n+}, being the rate limiting process. Also depicted is the variation in the peak potential as a function of the initial particle radius and the scan rate. The variation of the peak potential as a function of scan rate gives a readily analysable method for determining the value of (n'+ β). A final important point on this model is that from Equation 4.22 the peak potential is also predicted to vary with the

natural log of the rate of electron transfer. A plot of E_p against ln(k^0) should give a straight line of gradient $-RT/(n' + \beta)F$.

4.1.2.1.4 Theory Overview

In summary, the newly presented theory has demonstrated how in all three of the limits studied, not only is it possible for the peak potential for the oxidative stripping to occur significantly below the formal potential for the redox couple but the position of the peak will demonstrate a clear particle size dependency. This size dependency occurs even in the absence of the thermodynamics being altered from that of the bulk material and is related in part to the finite volume of metal present upon the electrode surface.

4.1.3 Plieth Correction to the Formal Potential

Next, we consider the situation in which the formal potential for the oxidation of the nanoparticulate metal is altered in accordance with the Plieth equation.[60] The Plieth equation predicts that due to the increase in surface curvature of the nanoparticle with decreasing size, the surface energy will correspondingly increase. This increase in the surface energy acts to decrease the formal potential required for oxidation as described by the following equation:

$$E^{\theta}_{f(NP)} = E^{\theta}_{f} - \frac{a}{r_{NP}} \qquad \text{Equation 4.23}$$

where

$$a = \frac{2\gamma A_r}{\rho F} \qquad \text{Equation 4.24}$$

where γ is the surface energy and ρ is the density of metal. Due to this variation in the formal potential as a function of the radius, the Nernst and Butler–Volmer equations require the addition of an extra term. For a reversible oxidation;

$$[M^{n+}] = [\,]^0 \, exp(n\theta) \, exp\left(\frac{anF}{r_{NP}RT}\right) \qquad \text{Equation 4.25}$$

And for irreversible cases;

$$j_{NP} = -k^0[\,]^0 \exp\big((n'+\beta)\theta\big)\, exp\left(\frac{(n'+\beta)aF}{r_{NP}RT}\right) \qquad \text{Equation 4.26}$$

Developing the previous sections we can show that for case 4:

$$\int_{r_{NP}}^{r_{NP,t}} {r_{NP}}^2 exp\left(\frac{-aF}{RTr_{NP}}\right)\, dr = -\frac{A_r}{\rho}\frac{D}{\delta}\frac{[\,]^0}{\Gamma_{NP}4\pi}\frac{RT}{nFv}exp(n\theta) \qquad \text{Equation 4.27}$$

For case 2:

$$\int_{r_{NP}}^{r_{NP,t}} r_{NP} exp\left(\frac{-aF}{RTr_{NP}}\right)\, dr = -\frac{A_r}{\rho}Dln2\cdot[\,]^0\frac{RT}{nFv}exp(n\theta) \qquad \text{Equation 4.28}$$

For an irreversible oxidation:

$$\int_{r_{NP}}^{r_{NP,t}} exp\left(\frac{-aF}{RTr_{NP}}\right)\, dr = -k^0[\,]^0\frac{A_r}{\rho}\frac{RT}{(n'+\beta)Fv}exp((n'+\beta)\theta) \qquad \text{Equation 4.29}$$

The integrals in the above three equations are best solved numerically. This may be readily achieved by calculating how the potential varies as a function of the radius. Once this has been undertaken, the charge and hence current as a function of potential may be calculated. It should also be recognised that the scan rate dependencies of the peak potentials predicted from Equation 4.27, 4.28 and 4.29, are equivalent to the non-altered formal potential equivalents (Equation 4.14, 4.20 and 4.22).

As previously discussed, the surface energy, γ, is a variable which is difficult to measure accurately. However, regardless of its exact value – which also likely varies as a function of size[215] – the important feature is that as the nanoparticles decrease in size upon the electrode, their oxidation will become progressively easier. Figure 4.5 depicts how the stripping voltammetry is predicted to vary as a function of the surface energy for the case 2 model, with values for the surface energy, γ, ranging from 0 – 4 J m^{-2}. Note that where the surface energy is set as zero, the voltammetric response is identical to the previous case 2 model in which the formal potential is assumed to be equivalent to that of the bulk material. The very sharp oxidation current reflects the fact that below a certain radius the nanoparticle is oxidised extremely rapidly due to the decrease in the formal potential as predicted by the Plieth equation. It should be noted that the peak current for all of the

predicted voltammograms in Figure 4.5 with a non-zero value of γ are off the scale of the current plot, and the scaling used has been selected so as to facilitate easy comparison between the models. One important feature is that as the value of the surface energy increases, the peak potential for the oxidation is shifted to more negative values. A second important feature is that with this current model, the peak position does not scale linearly with the natural log of the initial particle radius, as can be seen in the bottom inlay of Figure 4.5. This deviation away from linearity reflects the alteration in the formal potential as a function of the particle size as described by the Plieth equation. The influence of the 'Plieth correction' to the formal potential will only be significant for nanoparticles of diameters below approximately 30 nm (assuming that $\gamma \approx 1$ J m^{-2}).

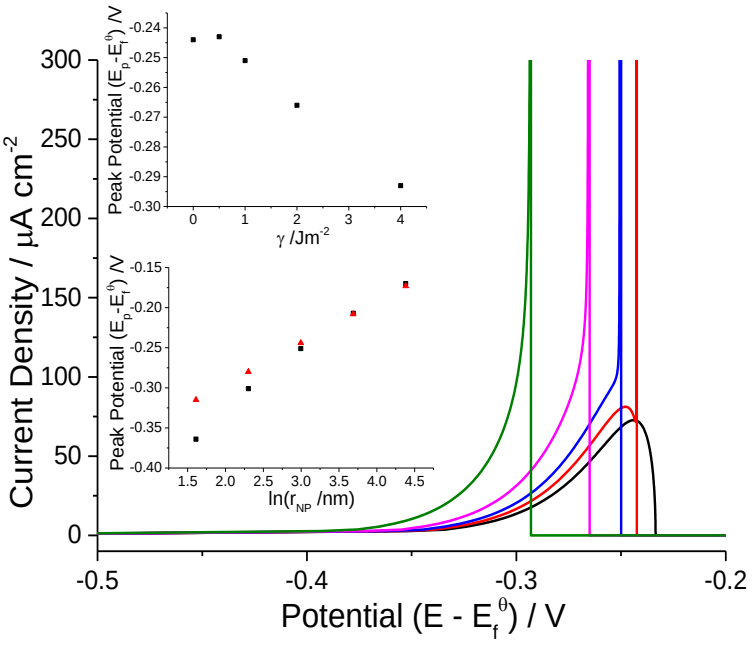

Figure 4.5 Theoretically predicted anodic stripping voltammetric wave shape for a case 2 diffusion regime where the Plieth correction to the formal potential has been considered. γ = 0 – 4 J m^{-2}, r_{NP} = 20 nm, n = 1, D = 1 × 10^{-9} m^2 s^{-1}, k^0 = 1 × 10^{-5} m s^{-1}, A_r = 100 g mol^{-1}, Γ_{NP} = 1 × 10^{12} particles per m^2, ρ = 10 × 10^6 g m^{-3} and υ = 0.1 V s^{-1}. The top inlay depicts the variation in the peak potential with the surface energy (γ = 0 J m^{-2} [black], 0.5 J m^{-2} [red] 1 J m^{-2} [blue], 2 J m^{-2} [purple] and 4 J m^{-2} [green]). The bottom inlay depicts the variation in the peak potential as a function of the initial particle radius, black squares the surface energy, γ, is 1.0 J m^{-2} and for the red triangles the surface energy is 0.0 J m^{-2}. For the inlays all other variables are kept the same as those used in the main figure.

Even for particles with diameters of ~10 nm, the surface energy of the nanoparticle is predicted to alter the stripping peak potential by approximately only 50 mV. In comparison for a particle of 10 nm in diameter, the change in the mass-transport regime and influence of the finite surface

coverage of metal upon the electrode will result in a shift of approximately 300 mV of the peak potential from formal potential of the bulk oxidation process (for a one electron process, in a case 2 diffusional regime). Consequently, it may be concluded that for many experimental cases, the dominant 'size effect' upon the stripping voltammetry will arise due to the variation in the surface coverage of the metal and not due to the possibly altered nano-scale thermodynamics of the metallic particles.

4.1.4 Experimental

4.1.4.1 Silver Nanoparticle Synthesis and Characterisation

Citrate-capped silver nanoparticles were synthesised via a method based on the work of Lee and Miesel.[226] The silver nanoparticles were synthesised by Dr. Kristina Tschulik. 25 mL of 0.01 M silver nitrate ($AgNO_3$) solution was added to 225 mL distilled water in a clean 250 mL flask. The flask was then heated in an oil bath at 100 °C with vigorous magnetic stirring. A solution of trisodium citrate was prepared by dissolving 1 g of the salt in 100 mL ultrapure water. When the silver nitrate solution reached boiling point, 5 mL of the citrate solution was added to the flask. Boiling continued for 1 h and the reaction mixture was then allowed to cool in a cold water bath.[227] The resulting unwashed silver particles were diluted with ultrapure water to the required concentration when needed. The synthesised nanoparticles were characterised in the solution-phase via nanosight track analysis (NTA) and UV-vis spectroscopy. The NTA data and UV-vis spectrum were obtained with the help of Dr. Christopher Batchelor-McAuley and Dr. Kristina Tschulik. For both the NTA and UV-vis analysis the synthesised nanoparticle solution was diluted by a factor of 10 prior to experimentation. For UV-vis spectroscopy, the sample is scanned from 700 to 250 nm at a scan rate of 100 nm min^{-1}. For NTA, the minimum required track-length was set automatically and the particle distributions analysed from the raw data. Figure 4.6 shows both the NTA data and UV-vis spectroscopy (inlay) of the synthesised nanoparticles. The NTA measurements showed that the mean diameter for the synthesised nanoparticles was 26.6 ± 12.4 nm. The UV-vis also shows the characteristic surface plasmon peak situated at 427 nm indicating the presence of silver

nanoparticles. The position of this peak is dependent upon the shape, size and environment (i.e. capping agent) of the nanoparticles,[51, 228, 229] however, a peak at 427 nm is broadly consistent with the presence of spherical particles in solution with a diameter of ~40 nm.

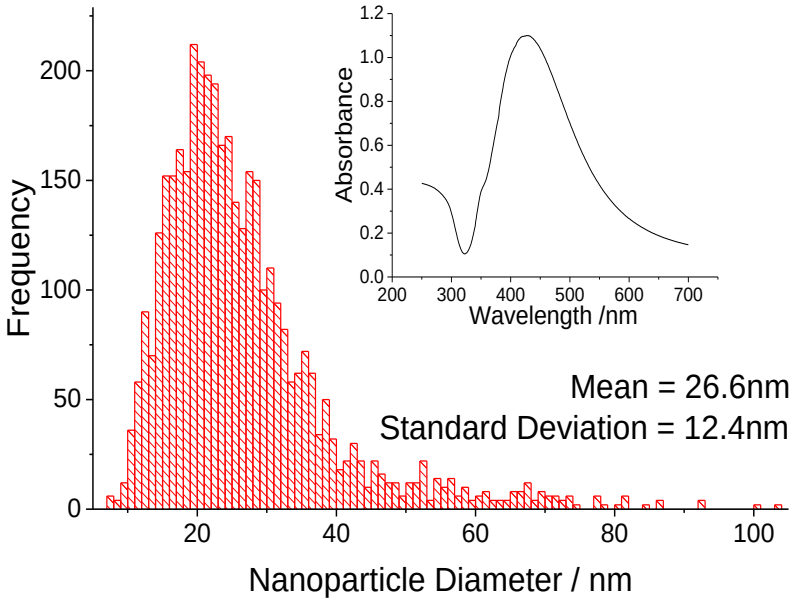

Figure 4.6 Characterisation data for the synthesised nanoparticles, showing their mean diameter in the solution phase to be 26.6 ± 12.4 nm from the NTA data. Inlay shows the UV-vis spectroscopy of the produced material, showing clearly the distinct surface plasmon peak at 427 nm.

For the SEM images, the nanoparticle suspension was sonicated for five minutes and then drop cast on a TEM grid modified SEM sample holder. The SEM used was a LEO Gemini 1530 (Zeiss, Oberkochen, Germany). Prof. Margitta Uhlemann and Dr. Alison Crossley were responsible for the SEM images.

4.1.4.2 Electrochemistry

A glassy carbon electrode was prepared as described in Chapter 3, Section 3.2. A leak-less silver/silver chloride (1 M KCl) functioned as a reference electrode. All experiments were conducted under a nitrogen atmosphere with the solution purged thoroughly with nitrogen.

Nanoparticle modification of the glassy carbon electrode was achieved through drop casting 3 µL of the diluted nanoparticle sample on to the electrode surface. The electrode was subsequently allowed to dry under nitrogen flow prior to experimentation.

4.1.5 Results and Discussion

The oxidative stripping of silver nanoparticles from a glassy carbon electrode was studied in 0.1 M sodium nitrate at a scan rate of 0.05 V s^{-1}. Variable surface coverages of silver nanoparticles were achieved through dilution of the synthesised nanoparticles in pure water. Subsequently, 3 µL of this diluted material was pipetted onto the electrode surface and allowed to dry under a nitrogen air flow prior to experimentation. It was ensured that the deposited droplet solely covered the electrode and did not encroach upon the insulating support. Figure 4.7 depicts the recorded cyclic voltammetric response; at least three repeats have been performed for each surface coverage. During the cyclic voltammogram, the potential has been scanned linearly between 0.0 V and +1.0 V (*vs.* Ag/AgCl/Cl^- [1 M]). A clear oxidative silver stripping peak is found at ~+0.4 V (*vs.* Ag/AgCl/Cl^- [1 M]). This peak is ascribed as corresponding to the one electron oxidation of the metallic silver to Ag^+.[62] Hence, measurement of the charge passed during the voltammetric scan gives a facile method by which the surface coverage of silver (Γ_{Ag}) may be analysed (assuming complete oxidation of the silver upon the electrode). Due to the produced nanoparticles exhibiting a distribution of sizes (as evidenced from the particle characterisation in the solution phase [Figure 4.6]) it is more appropriate to define the experimental surface coverages in terms of the quantity of silver upon the surface (Γ_{Ag}). For high surface coverages, on the reverse scan a small reductive peak – likely relating to the reduction of the formed Ag^+ – is observed at ~+0.15 V (*vs.* Ag/AgCl/Cl^- [1 M]). At potentials higher than the stripping of the silver there is an increase in the voltammetric current relating to the onset of the break-down of solvent.

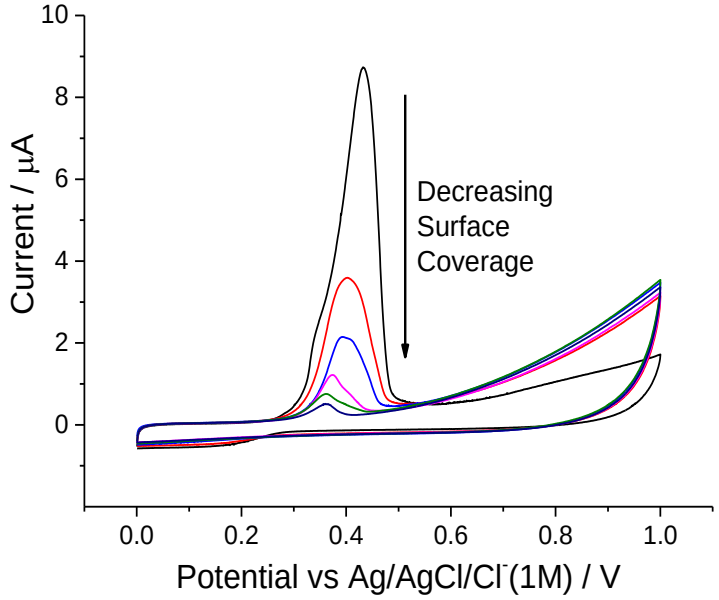

Figure 4.7 The oxidative stripping of silver nanoparticles from a glassy carbon electrode in 0.1 M sodium nitrate at a scan rate is 0.05 V s^{-1}. Variable surface coverages of silver; black: 2.5 × 10^{-5} mol m^{-2}; red: 8.3 × 10^{-6} mol m^{-2}; blue: 4.6 × 10^{-6} mol m^{-2}; purple: 2.3 × 10^{-6} mol m^{-2}; green: 1.0 × 10^{-6} mol m^{-2}, dark blue: 4.9 × 10^{-7} mol m^{-2} and black: 3.5 × 10^{-7} mol m^{-2}.

For the current experimental case of silver nanoparticle oxidation, it is of importance that the nitrate ion used for the supporting electrolyte will not ion-pair with the formed Ag^+, hence the formal potential for this oxidation is $E^{\theta}_{f(Ag/Ag+)}$ = +0.567 V (*vs.* Ag/AgCl/Cl^- [1 M]) and the diffusion coefficient of Ag^+ may be taken as D_{Ag^+} = 1.65 × 10^{-9} m^2 s^{-1}.[17] All of the physical constants used for the theoretical modelling of the silver stripping are summarised in Table 4.1. It should also be commented that as the oxidation of the nanoparticles proceeds, the organic capping agent initially present upon the metallic surface will be removed, consequently the stripping voltammetry should be relatively insensitive to the capping agent used within the synthesis. Figure 4.8 depicts the variation of the peak potential as a function of the surface coverage of silver. At high surface coverages, ≥ 3 × 10^{-6} mol m^{-2}, the peak potential is found to vary nearly linearly with the surface coverage of silver. This dependency suggests that the oxidation of the nanoparticles is not diffusionally independent. For the case 4 limit, as previously discussed, the position of the peak potential depends upon the surface coverage of the silver and is consequently only indirectly influenced by the size of the nanoparticles. The fitting of the high surface coverage data may be

achieved without pre-supposing the size of the nanoparticles. Overlaid on Figure 4.8 is the theoretically predicted peak potentials for diffusion layer thicknesses of 200 μm, 100 μm and 50 μm, where good agreement is found with the experimental data for surface coverages above 3×10^{-6} mol m^{-2}.

Physical Constant	Value
Diffusion Coefficient, D_{Ag^+} [17]	1.65 x 10^{-9} m^2 s^{-1}
Formal Potential, $E^{\theta}_{f(Ag/Ag^+)}$ [17]	0.567 V (*vs.* Ag/AgCl/Cl^- [1 M])
Molecular Weight, $A_{r,Ag}$ [17]	107.9 g mol^{-1}
Density of Silver, ρ_{Ag} [17]	10.5 x 10^6 g m^{-3}
Nanoparticle Radius, r_{NP}	13.3 x 10^{-9} m
Surface Energy, γ_{Ag} [b]	1.3 J m^{-2}
Geometric Electrode Area, A_{elec}	7.07 x 10^{-6} m^2

Table 4.1 Physical constants used within this section.

Although a good fit for the case 4 model is achieved at higher surface coverages of silver (≥ 3×10^{-6} mol m^{-2}), at low surface coverages (≤ 1.5×10^{-6} mol m^{-2}) the experimental peak potential occurs at significantly higher potentials than that predicted by the case 4 model. Furthermore, the peak potential becomes effectively insensitive to the silver surface coverage. Within the theoretical framework presented within the this section, the insensitivity of the peak potential with surface coverage may either be due to the particles being highly separated upon the electrode surface such that they may be treated as being diffusionally independent or alternatively this insensitivity with surface coverage may indicate that at these lower surface coverages the rate determining step has become the electron transfer and not the mass-transport of the formed Ag^+ away from the metallic surface.

[b] The reported values for the bulk surface energy of silver vary in the range of 1.07 – 1.54 J m^{-2}.[216] K. K. Nanda, A. Maisels, F. E. Kruis, H. Fissan and S. Stappert, *Phys. Rev. Lett.*, 2003, **91**, 106102.

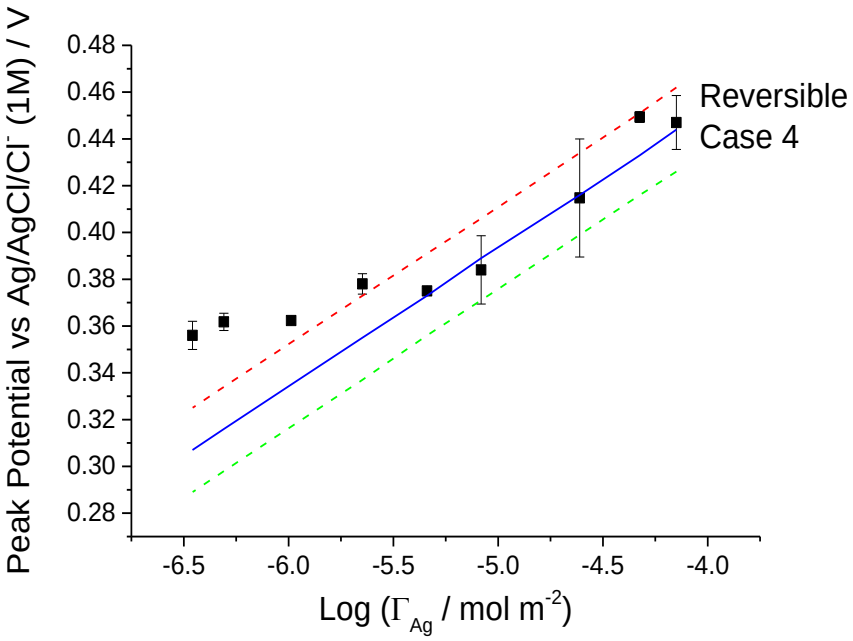

Figure 4.8 Variation in the peak potential (black squares) for the anodic stripping of silver nanoparticles in 0.1 M sodium nitrate as a function of the surface coverage of atomic silver at a scan rate of 0.05 V s^{-1}. Theoretical variation in the stripping peak potential for the case 4 regime: red dotted line, diffusion layer thickness is 200 μm; blue solid line, diffusion layer thickness is 100 μm and green dotted line, diffusion layer thickness is 50 μm, all other values are as given in Table 4.1.

Due to the known high sensitivity of silver oxidation towards chloride, as evidenced in Chapter 6, Section 6.2, it was necessary to fully ensure that the observed invariant peak potential at low surface coverages was not related to a chloride impurity present within the system. The sodium nitrate salt is one likely source, as such experiments were performed in which the concentration of the supporting electrolyte was increased to 1.0 M, however, this was found to have no influence upon the potential. Secondly, the leak-less reference electrode was separated from the working electrode by a glass frit, so as to further minimise any possible chloride leakage from the reference, again the electrochemical response was found to be unaltered. Hence, it was concluded that the invariance of the stripping peak potential at low surface coverages was not related to the presence of chloride impurities within the system.

In order to elucidate the operative mechanism for the nanoparticle oxidation at low surface coverages, the peak potential was investigated as a function of scan rate between 0.05 and

0.4 V s^{-1}, as shown in Figure 4.9. The peak potential is found to shift positively at higher scan rates, where the plot of peak potential *vs.* the natural log of scan rate yields a gradient of 24.1 mV/ln υ.

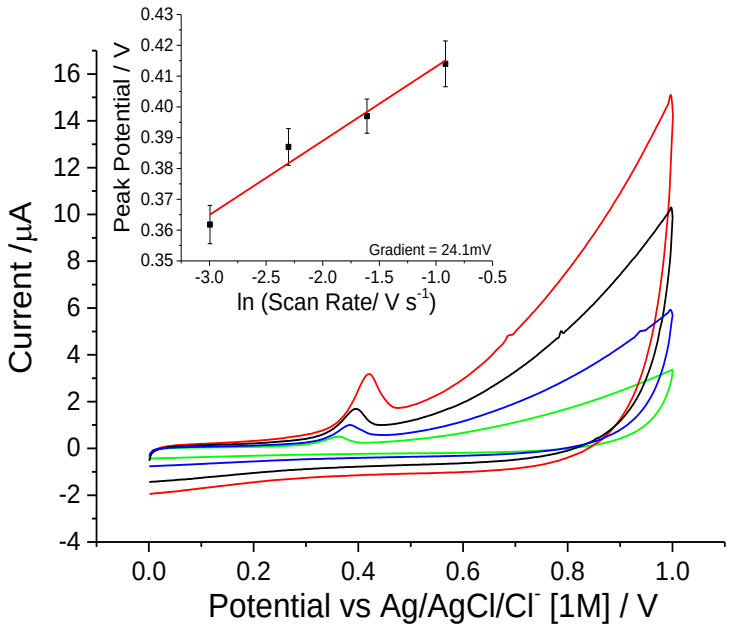

Figure 4.9 The voltammetric response of the oxidation of silver nanoparticles in 0.1 M sodium nitrate at variable scan rates (0.05 – 0.4 V s^{-1}) with a silver surface coverage of 4.9 × 10^{-7} mol m^{-2}. Inlay depicts the variation of the peak potential as a function of the natural log of scan rate, where the gradient was found to be 24.1 mV.

This value demonstrates that the electron transfer – although relatively insensitive to the surface coverage of silver – is reversible. For the reversible case 2 limit – taking the silver nanoparticle particle radius as being 13.3 nm as measured in the solution phase – the peak potential for this diffusion limited reaction is predicted to occur at +0.270 V (*vs.* Ag/AgCl/Cl^- [1 M]) assuming the thermodynamics are unaltered from that of the bulk or +0.248 V (*vs.* Ag/AgCl/Cl^- [1 M]) with a Plieth corrected formal potential using a surface energy of 1.3 J m^{-2}. Both of these values are considerably below the measured peak potential at low surface coverages. Consequently, it was inferred that significant agglomeration of the nanoparticles upon the electrode surface during the

drop casting results in the formation of relatively large silver agglomerates[c] upon the electrode. Previous work by Brainina *et al.* has discussed the influence of the dispersity of silver upon the shape of the voltammetric wave shape.[231] In order to validate this hypothesis of surface agglomeration SEM images of the silver nanoparticles were recorded.

Figure 4.10 shows two representative images of the particles after being drop cast from an undiluted sample of the synthesised material. The lower magnification image shows the non-random deposition of the individual nanoparticles, with clusters ranging in size from tens to hundreds of nanometers. The higher magnification image demonstrates that the clusters are formed from loosely agglomerated particles where the constituent particles are of comparable diameters to that found from the solution phase characterisation.

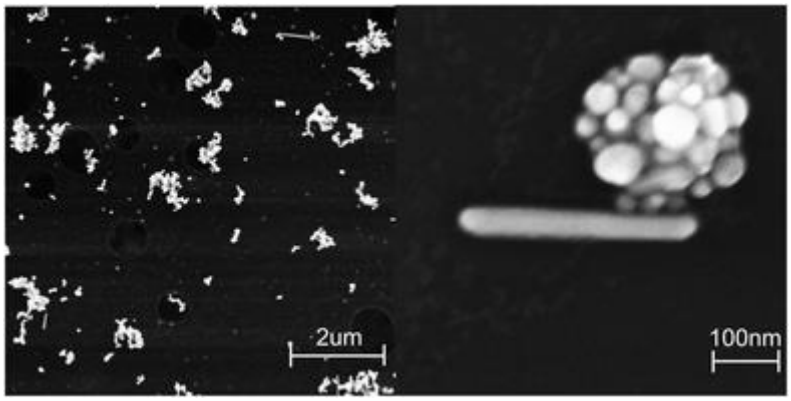

Figure 4.10 SEM images for the drop cast silver nanoparticles deposited from an undiluted sample of the synthesised material. The images indicate the high levels of clustering present after evaporation of the solvent.

Having validated the likely clustering and agglomeration of silver nanoparticles upon the electrode surface, the relative invariance of the electrochemical peak potential at low surface coverages may be reassessed. Assuming that the case 2 model is operative at the low surface coverages, the silver

[c] According to the IUPAC definition agglomeration and aggregation refer to a reversible and irreversible sticking of particles, respectively.[230] , DOI: 10.1351/goldbook.AT07608, IUPAC. Compendium of Chemical Terminology, 2nd ed. (the "Gold Book"). Compiled by A. D. McNaught and A. Wilkinson. Blackwell Scientific Publications, Oxford (1997). . The analysis techniques referred to in this thesis detect both simultaneously. Therefore, throughout the section only the expression agglomeration will be used to refer to both types of particle adhesion for mutual convenience.

stripping peak potential is consistent with the particles on the surface being of the order of 80 ± 20 nm in radius. For an array of diffusionally independent particles with radii of 80 nm the peak potential is predicted to be at +0.363 V (*vs.* Ag/AgCl/Cl^- [1 M]). However, even for the lowest experimental surface coverage (Γ_{Ag} = 3.47 × 10^{-7} mol m^{-2}) such a particle size would lead to an average inter-particle distance of approximately 24 μm. Given the likely magnitude of the diffusion layer cf. 100 μm (as consistent with the experimental case 4 data), this value of 24 μm is still comparably small. Consequently, it must be concluded that under such experimental conditions (Γ_{Ag} ≤ 1.5 × 10^{-6} mol m^{-2}) the stripping of the silver is consistent with a case 3 diffusion regime. Thus, the far smaller – but non-zero – variation in the peak potential with the surface coverage of silver, at low surface coverages, relates to the decreasing diffusion layer overlap between the adjacent silver clusters. As the magnitude of the surface coverage decreases further the peak potential will tend towards the case 2 limit in which the clusters are diffusionally independent.

Although it has been concluded that the peak potential at low surface coverages is consistent with a case 3 diffusion regime i.e. one in which the diffusion layers are not strongly overlapping, the change in the response of the peak potential as a function of the surface coverage gives valuable information regarding the dispersity of the nanoparticles upon the electrode surface. For a more ideally dispersed sample the peak potential would continue to decrease linearly as a function of the log of the surface coverage beyond that seen experimentally. Consequently, the transition from the diffusional case 4 to case 3 limit as a function of the surface coverage gives a readily investigable route to estimating the size of the surface clusters. Hence, knowledge of the surface cluster sizes as compared to the size of the nanoparticles in solution gives insight into the degree of surface agglomeration.

4.1.6 Conclusions

New general analytical expressions for the stripping voltammetry of metallic nanoparticles have been presented. These equations clearly demonstrate, first, that the oxidation peak potential for the stripping of metallic nanoparticles is expected to be well below (by hundreds of millivolts) the

formal potential for the oxidation. This shift occurs even when the thermodynamics for the oxidation are unaltered from that of the bulk material. Second, it is shown that for many experimental cases the dominant size effect upon the measured voltammetry will relate to the change in the surface coverage of the metallic species. Moreover, from the inclusion of the Plieth correction to the formal potential into the models, it is highlighted that the change of the oxidation thermodynamics on the nano-scale is only predicted to be influential for particles with diameters less than 30 nm. Even for particles of 10 nm in diameter the alteration in the peak potential – due to the increased surface energy – is only predicted to be of the order of 50 mV (assuming the surface energies are comparable to that of the bulk material).

This newly presented theory was subsequently used to analyse the voltammetric response of the anodic stripping of silver nanoparticles. At high surface coverage ($\geq 3 \times 10^{-6}$ mol m^{-2}) the voltammetry is consistent with the case 4 diffusion regime. Here the diffusion fields of each nanoparticle or nanoparticle cluster overlap strongly, leading to the mass-transport of the Ag^+ away from the electrode being linear across the whole of the electrode. Conversely, at lower surface coverages ($\leq 1.5 \times 10^{-6}$ mol m^{-2}), the voltammetry is shown to deviate away from this case 4 limit. This deviation occurs due to the aggregation of the nanoparticles upon the electrode surface. Due to the larger inter-cluster distances the diffusion layers originating from the clusters only overlap weakly (case 3). The transition from the case 4 to the case 3 limit as a function of the surface coverage of the silver nanoparticles gives a new route by which the aggregation of the silver nanoparticles upon the surface may be investigated. With the knowledge of stripping voltammetry in mind, the next section looks at the other method of 'nano-impacts' and its key advantage over optical methods.

4.2 'Nano-impacts': Sizing in Optically Opaque Solutions

4.2.1 Introduction

As nanoparticles are defined by the International Union of Pure and Applied Chemistry (IUPAC) to be any material with a single dimension below 100 nm, it is difficult to measure materials of such

scale.[49] Yet, the size of the nanoparticle is a crucial attribute because it can influence its properties.[51, 60, 72, 232] For example, the catalytic properties of a nanoparticle can change with varying size. Small silver nanoparticles catalyse the reduction of oxygen to hydrogen peroxide instead of water.[72, 232] With decreasing size, silver nanoparticles are also known to absorb light at a smaller wavelength[51] and are electrochemically oxidised at a lower potential (Section 4.1).[62] Although microscopy methods such as SEM and TEM are capable of resolving nanoparticles down to 3 nm and 0.1 nm, respectively; both of these are ex situ methods.[93, 233] However, it is important that the nanoparticle size is measured in the solution phase as the removal of solvent could result in aggregation or agglomeration (Section 4.1). Therefore, many techniques such as NTA and DLS, which analyse nanoparticle size in the solution phase, have been developed.

As mentioned in Chapter 2, Section 2.2, NTA uses a laser to illuminate the particles and a microscope to detect the movement of the individual particles, whilst DLS measures the particle size through the light scattered by the nanoparticles.[103, 106] However, an opaque sample can contain large particulates, which can strongly affect both DLS and NTA measurements. In DLS, the opaque sample would scatter or absorb the majority of the light, thus, the light scattered by the nanoparticle would be overwhelmed. For NTA, as the laser shines on the sample, the particulates could be illuminated or they could absorb most of the light from the laser. Thus, the nanoparticles would remain in the shadow, making detection difficult or impossible.

Given that both NTA and DLS are strongly dependent on light to record their signals and the presence of large amount of inert macroparticulates can reflect or absorb most of the light, DLS and NTA measurement is effectively impossible in an optically opaque suspension. Therefore, there is a need for a technique that is capable of measuring nanoparticle size in an opaque medium. Anodic particle coulometry (via 'nano-impacts') is a novel technique developed within the last 20 years that works on the basis of recording single nanoparticle–electrode impact events through electrochemistry.[148] These events are recorded though the electrochemical signal generated by the redox reaction occurring on the nanoparticle. In this case, the citrate capped silver nanoparticle

diffuses under Brownian motion and hits the carbon microelectrode held at a suitable oxidising potential. Thus, the silver nanoparticle is oxidised into silver(I) ions, generating a current 'spike' which is observed in the chronoamperogram recorded. Through the use of Faraday's law, the size of the spherical nanoparticle can be estimated via the equation below.[42, 194]

$$r_{NP} = \sqrt[3]{\frac{3QA_r}{4\pi F\rho}} \qquad \text{Equation 4.30}$$

where r_{NP} is the nanoparticle radius, Q is the total charge passed under a single 'spike', A_r is the atomic molecular mass, F is the Faraday constant and ρ is the density. In this section, citrate-capped silver nanoparticles are detected in an optically opaque suspension that contains a high concentration of alumina particles. First, the potential of the citrate-capped silver nanoparticle oxidation is determined through anodic stripping voltammetry. Second, 'nano-impact' experiments are performed in a suspension of silver nanoparticles, alumina particulates, and the electrolyte of sodium nitrate. The size distribution of silver nanoparticles is matched against independent TEM measurements to evaluate the size measured by 'nano-impacts' in the opaque medium.

4.2.1 Experimental

4.2.1.1 Nanoparticles

Citrate capped silver nanoparticles was obtained from NanoComposix, San Diego, USA. Size characterisations were carried out using a JEOL 2010 analytical TEM (Herts, UK), which has a LaB_6 electron gun and can be operated between 80 and 200 kV. This instrument has a resolution of 0.19 nm, an electron probe size down to 0.5 nm and a maximum specimen tilt of ± 10 degrees along both axes. The instrument is equipped with an Oxford Instruments LZ5 windowless energy dispersive X-ray spectrometer (EDX) controlled by INCA software. It has facilities for point analysis as well as mapping and line scanning through the SemiStem controller. The TEM samples were prepared by depositing a drop of the silver nanoparticle suspension received on a carbon coated copper TEM grid and dried at room temperature for several hours before examination in the TEM. The TEM images were taken by Dr. Kerstin Jurkschat. They are sized by TEM in to be 14.8 ± 2.2

nm. ImageJ software developed at the National Institutes of Health, USA was used to size the nanoparticles recorded on the TEM images.

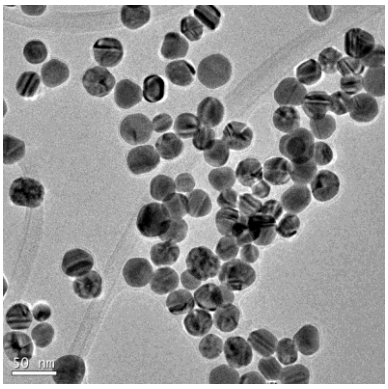

Figure 4.11 TEM image of the citrate capped silver nanoparticles.

4.2.1.2 Electrochemical Apparatus

A glassy carbon electrode was used as the working electrode for anodic stripping voltammetry. For anodic particle coulometry, a carbon microdisc electrode was used as the working electrode. Prior to all experiments, they were polished according the procedure in Chapter 3, Section 3.2. A mercury/mercurous sulphate electrode (MSE) was used as a reference electrode.

4.2.1.3 Electrode for Anodic Stripping Voltammetry

For the silver nanoparticle modified electrode, 3 µL of the silver nanoparticle suspension supplied was drop cast on the glassy carbon electrode. For alumina powder modified electrode, 3 µL of 5% w/v suspension of alumina powder (0.05 µm) was dropcast on the glassy carbon electrode. The modified electrodes were dried under flowing nitrogen. After drying, the nanoparticle modified electrode was immediately used to perform a cyclic voltammogram swept from -0.6 V to +0.5 V *vs*. MSE at a scan rate of 50 mV s^{-1}.

4.2.1.4 Anodic Particle Coulometry

Prior to every anodic particle coulometry experiment, the electrochemical cell was soaked in aqua regia (3 HCl: 1 HNO_3) for at least 30 minutes and sonicated in ultrapure water for 15 minutes to avoid any contamination by rogue nanoparticles. The experiments were performed at the potential of +0.6 V *vs*. MSE The silver nanoparticle suspension was diluted with 20 mM sodium nitrate

solution containing 0.25% (w/v) alumina powder to give an aliquot of 100 pM of silver nanoparticles used for experiments.

4.2.2 Results and Discussion

Silver nanoparticle modified glassy carbon electrodes prepared as described in the Section 4.2.1.3 were used to determine the potential of citrate-capped silver nanoparticle oxidation in the presence of alumina powder (0.05 µm). An optically opaque electrolyte solution was obtained by suspending 0.25% w/v alumina powder in 20 mm sodium nitrate solution. The suspension has the colour and appearance of milk. Then, using voltammetric methods, the nanoparticle modified electrode was scanned oxidatively from –0.6 V *vs.* MSE in the opaque electrolyte. In Figure 4.12, it is seen that the silver oxidation signal occurs around +0.05 V *vs.* MSE. The experiment was repeated three times to ensure reproducibility. It was inferred that the oxidation of metallic silver to silver(I) ions (Ag (s)→Ag^{+} (aq) +e^{-} (m)) is not influenced by the presence of alumina powder. From the black dashed line in Figure 4.12, it is also concluded that alumina powder is inert under these conditions. After determining the potential at which silver nanoparticles are oxidised in the opaque electrolyte, 'nano-impact' experiments were performed in the opaque solution. The opaque solution used for 'nano-impact' experiment is depicted in Figure 4.13 (sample on the right). The yellow silver nanoparticles present in the suspension causes it to appear as a yellow milky suspension. 'Nano-impact' experiments were performed by using chronoamperometry. Current-time transients of a fixed duration (50 s) were recorded at an overpotential of +0.6 V *vs.* MSE. The results are summarised in Figure 4.14. In the absence of silver nanoparticles, no 'spikes' were observed; in presence of silver nanoparticles, current 'spikes' were observed. This indicates that alumina powder did not give any 'spikes', no 'rogue' nanoparticles were present, and the 'spikes' observed are solely attributed to the silver nanoparticles.

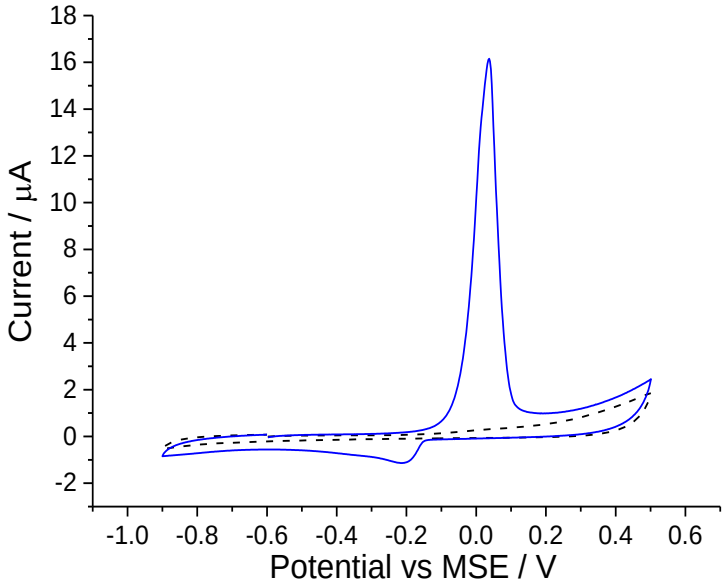

Figure 4.12 Blue solid line: The oxidation of citrate capped silver nanoparticles on a glassy carbon electrode in 20 mM sodium nitrate and 0.25% w/v alumina powder (0.05 µm) at a scan rate of 50 mV s^{-1}. Black dashed line: Cyclic voltammogram of alumina powder modified glassy carbon electrode in 20mM sodium nitrate at a scan rate of 50 mV s^{-1}.

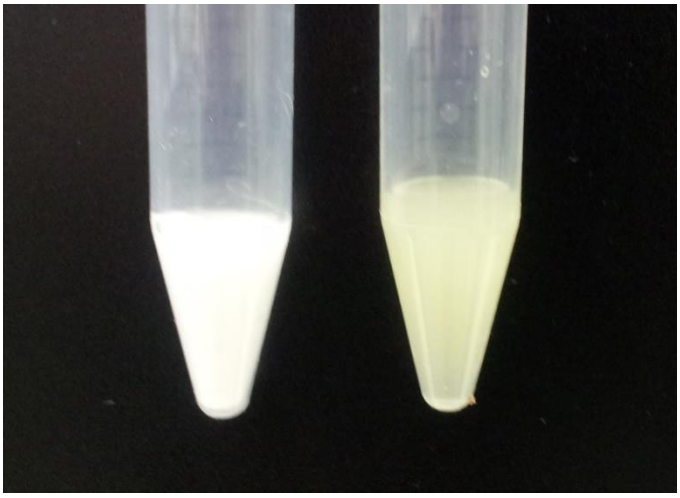

Figure 4.13 5% w/v alumina (0.05µm) powder solution (left). Solution containing 100 pM of citrate capped silver nanoparticle, sodium nitrate and alumina powder (used for anodic particle coulometry experiments) (right).

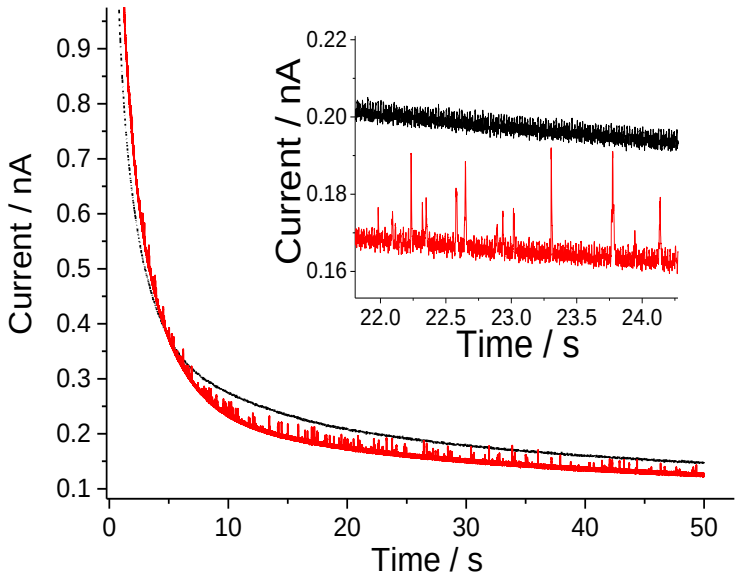

Figure 4.14 Fifty seconds chronoamperomogram for a carbon fibre microelectrode (radius = 4.9 µm) immersed in 20 mM sodium nitrate and 0.25% w/v alumina powder (0.05 µm) measured at +0.6 V (*vs.* MSE). Black: containing no nanoparticles. Red: containing 100 pM of citrate capped silver nanoparticles. Inset: A close up of individual signals observed.

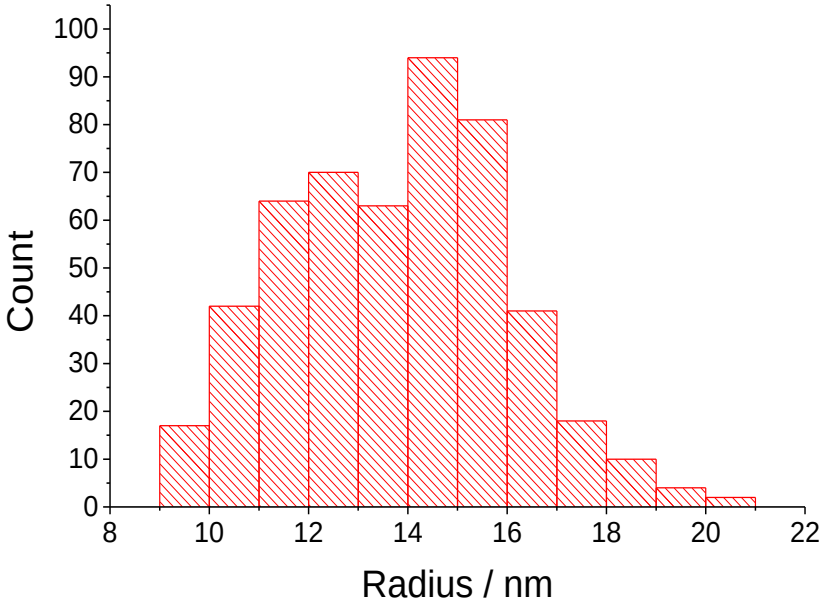

Figure 4.15 Histogram showing the size distribution of the citrate capped silver nanoparticles obtained from the chronoamperomogram.

In total, 498 spikes were recorded from 28 scans. The size distribution is depicted in Figure 4.15. The average radius of the nanoparticles was calculated to be 13.8 ± 2.2 nm. This is in excellent agreement with the TEM sizing of 14.6 ± 2.1 nm of the same batch of nanoparticles performed in Section 4.2.1.1. It can be concluded that the nanoparticles sizes are consistent and that 'nano-impact' experiments can be performed in opaque media.

4.2.3 Conclusions

In summary, 'nano-impact' experiments were performed for silver nanoparticles in an optically opaque medium (a suspension of sodium nitrate and alumina powder). Comparing the sizes of silver nanoparticles obtained from TEM and 'nano-impact' experiments, the radii obtained were consistent with one another. The 'nano-impact' technique allows measurement of nanoparticle size in opaque medium, which proves advantageous over optical techniques, notably NTA and DLS.

Since both stripping voltammetry and 'nano-impacts' have been individually addressed, in the next section, the two electrochemical methods are compared and contrasted via the oxidation of silver nanoparticles with various capping agents.

4.3 The Influence of the Nanoparticle Capping Agent: 'Nano-impacts' versus Stripping Voltammetry

4.3.1 Introduction

Scientific research has placed much emphasis on nanoparticles as their special properties are appealing towards many commercial applications.[27, 54, 234, 235] Due to the decrease in size, nanoparticles tend to have a higher surface energy compared to bulk material, which may lead to instability.[54, 60] Hence, nanoparticles often require capping agents to aid their stabilisation.[236, 237] Capping agents work through various mechanisms which can be broadly categorised into five different types: electrostatic stabilisation, steric stabilisation, stabilisation by hydration forces, depletion stabilisation and stabilisation by van de Waals forces.[236, 237] Occasionally, multiple mechanisms can occur with certain capping agents, for example, in the case of branched polyethylenimine (BPEI) where it stabilises silver nanoparticles both electrostatically and sterically.[65]

The choice of capping agents on nanoparticles is crucial as the properties (such as size, shape and the interaction with solvent surroundings) of the nanoparticle are strongly influenced by it.[238] For example, the polymeric chain length of polyethylene glycol (PEG) is important in silver nanoparticle synthesis as the number of monomers in PEG affects the nanoparticle size.[239] Apart from their main

role of stabilising nanoparticles, some capping agents (i.e. citrate) are capable of the additional role of reducing metal ions (e.g. silver ions reduced by citrate ions) into metal nanoparticles.[240, 241] Therefore, the choice of capping agent is vital in the nanoparticle synthesis process.

Apart from their strong influence in the synthesis process, capping agents also affect nanoparticle properties.[242-244] For example, gold nanoparticles with organic capping agents with changed side chains (alkyl, aromatic or cholesterol groups) display different interactions with gelatin solutions, forming composites of contrasting morphologies.[242] In another example reported by Kuhn *et al.*, it was demonstrated that the capping agents containing amine groups on platinum nanoparticles poisoned the catalytic properties of the nano-platinum, leading to a lower efficiency for ethylene hydrogenation and carbon monoxide oxidation.[243] Otherwise, having a capping agent on a nanoparticle surface can promote certain properties. In an anti-bacterial study of silver nanoparticles, the usage of any of the three capping agents (Tween-80, sodium dodecyl sulphate (SDS) or polyvinylpyrrolidone (PVP)) resulted in an enhanced anti-bacterial activity.[244]

Given the significant influence of capping agents on nanoparticle properties, the question arises as to whether capping agents affect the techniques used for nanoparticle detection and quantification. Optical methods such as UV-vis spectrometry and Fourier transform infrared (FTIR) spectroscopy are often used to characterise nanoparticles.[51, 245-247] For UV-vis spectroscopy, spherical silver nanoparticles provide a characteristic maximum absorbance around 400 nm whilst spherical gold nanoparticles have a strong absorbance around 500 nm.[51, 245, 246] Studies have shown that by varying the concentration of capping agents (polyvinyl alcohol (PVA) or L-glutamic acid) on silver nanoparticles, the UV-vis absorbance signal shifts and changes shape.[248, 249] Similarly, literature has reported that the UV-vis and FTIR signals of cadmium telluride (CdTe) semi-conductor nanocrystals change with the capping agent on their surface.[247] Thus, CdTe nanocrystals capped by mercaptoacetic acid, mercaptopropionic acid or 2-mercaptoethanol show different responses for the optical methods. Hence, the influence from the capping agents may result in possible scenarios where the data obtained may be misleading. For example, the possible scenario of oversizing the

nanoparticles when a blueshift in UV-vis signal could be due to a concentration change in capping agent instead of a change in nanoparticle size.

In this section, the electrochemical techniques of anodic stripping voltammetry and anodic particle coulometry ('nano-impacts') are studied to determine *if* there is any influence from the capping agents on the response of silver nanoparticles. Anodic stripping voltammetry determines the concentration of metals ions in solution by pre-concentrating and oxidising them on a suitable electrode.[1, 2] It gives an improved sensitivity because of its pre-concentration step.[1, 2] Recently, it has also been adapted to detect nanoparticles.[133, 138-140, 250] One of the most commonly used techniques for pre-concentrating nanoparticles is drop casting, where an analyte solution is deposited onto the working electrode, the solvent is evaporated and a layer of analyte is left behind on the electrode.[251] Section 4.1 has reported that this method causes silver nanoparticles to aggregate on the electrode surface because of solvent evaporation. As increasingly aggregated nanoparticles are found on the surface, the percentage oxidation of the cast material in anodic stripping voltammetry decreases, leading to the phenomenon of partial oxidation ("incomplete stripping").[202] Since capping agents play a crucial role in nanoparticle stabilisation and their aggregation kinetics, it is plausible to speculate that they might have a significant effect on the aggregation caused by drop casting and hence on the signal obtained in anodic stripping voltammetry.[65] Therefore, to determine if the capping agents *may* have influence on the electrochemical behaviour of silver nanoparticle aggregates, anodic stripping voltammetry are performed on five spherical, similar sized silver nanoparticles samples each with a different capping agent (BPEI, citrate, lipoic acid, PEG or PVP) as shown in Figure 4.16.

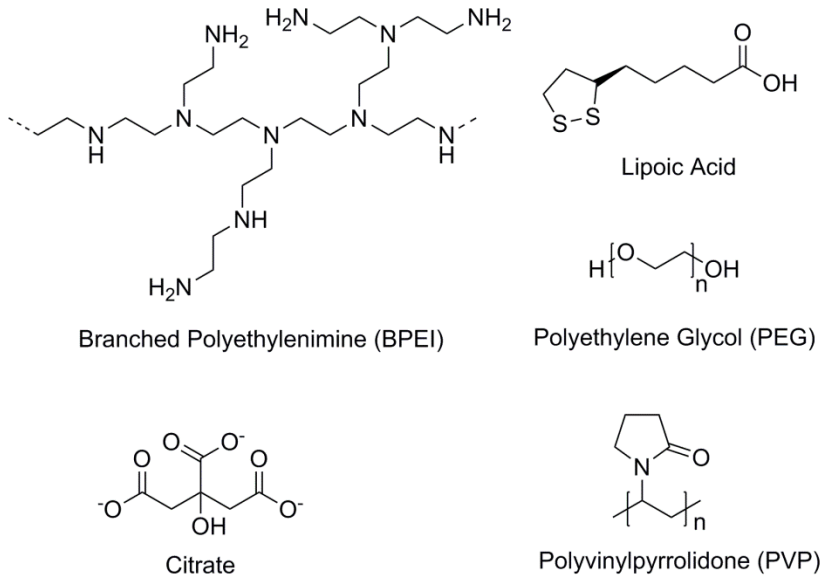

Figure 4.16 The chemical structures of the capping agents studied.

To further investigate the partial oxidation of nanoparticle aggregates, a study of single nanoparticle oxidation is essential. Therefore, 'nano-impacts' is pursued as a method well-suited for this purpose. It records the electrochemical signals of single nanoparticles impacting the electrode surface under Brownian motion in solution.[39-42] As the silver nanoparticle hits the electrode surface held at a suitable oxidising potential, it is oxidised into silver(I) ions and this generates a current 'spike' which appears in a chronoamperogram. In turn, the charge passed under the 'spike' can be related to the size of the nanoparticles via Faraday's law and hence the effects of capping agents on the extent of partial oxidation of a single nanoparticle can be studied. To the best of our knowledge, anodic particle coulometry has only been performed on silver nanoparticles capped with citrate.[39, 41, 42, 163] Therefore, this work is the first to report on the influence of capping agents (i.e. BPEI, citrate, lipoic acid, PEG and PVP) on silver nanoparticles using 'nano-impacts'.

4.3.2 Experimental

4.3.2.1 Nanoparticles

Five samples of silver nanoparticles with different capping agents were received from NanoComposix, San Diego, USA. The five samples used were BPEI capped silver nanoparticle, citrate

capped silver nanoparticle, lipoic acid capped silver nanoparticle, PEG capped silver nanoparticle and PVP capped silver nanoparticle.

4.3.2.2 Electrochemical Apparatus

A glassy carbon electrode was used for anodic stripping voltammetry. For anodic particle coulometry, a carbon microdisc electrode was employed. A MSE was used as a reference electrode. The rest of the experimental details are detailed in Chapter 3, Section 3.2.

4.3.2.3 Nanoparticle Characterisation

The TEM images were taken by Dr. Kerstin Jurkschat and the details on TEM are described in Section 4.2.1.1. The silver nanoparticles capped by BPEI, citrate, lipoic acid, PEG and PVP were sized to have an average radius of 15.0 ± 1.6 nm (30 particles), 14.6 ± 2.1 nm (109 particles) (Figure 4.11), 13.5 ± 3.9 nm (18 particles), 9.6 ± 2.0 nm (43 particles) and 13.5 ± 1.9 nm (33 particles) respectively. Figure 4.17 shows the TEM images of the spherical silver nanoparticles. The TEM image of citrate capped silver nanoparticles is found in Section 4.2, Figure 4.11.

4.3.2.1 Silver Nanoparticle Modified Electrode for Anodic Stripping Voltammetry

The silver nanoparticle suspension supplied was diluted by a factor of 2.23 with ultrapure water to ensure the total nanoparticle concentration was 100 pM. The glassy carbon electrode was drop cast with 3 µL of the diluted nanoparticle suspension and dried under a nitrogen flow. After drying, the nanoparticle modified electrode was immediately used for electrochemical experiments. A cyclic voltammogram was swept starting from -0.6 V to +0.5 V *vs.* MSE at a scan rate of 50 mV s^{-1} to perform anodic stripping voltammetry.

4.3.2.1 Anodic Particle Coulometry

Prior to every anodic particle coulometry experiment, the electrochemical cell was soaked in aqua regia (3 HCl: 1 HNO_3) for at least 30 minutes and sonicated in ultrapure water for 15 minutes to avoid any contamination by rogue nanoparticles. The silver nanoparticle suspension received was diluted with 20 mM sodium nitrate solution to give an aliquot of 100 pM of silver nanoparticles

used for experiments. Chronoamperometric scans were recorded at the potential of +0.6 V *vs.* MSE.

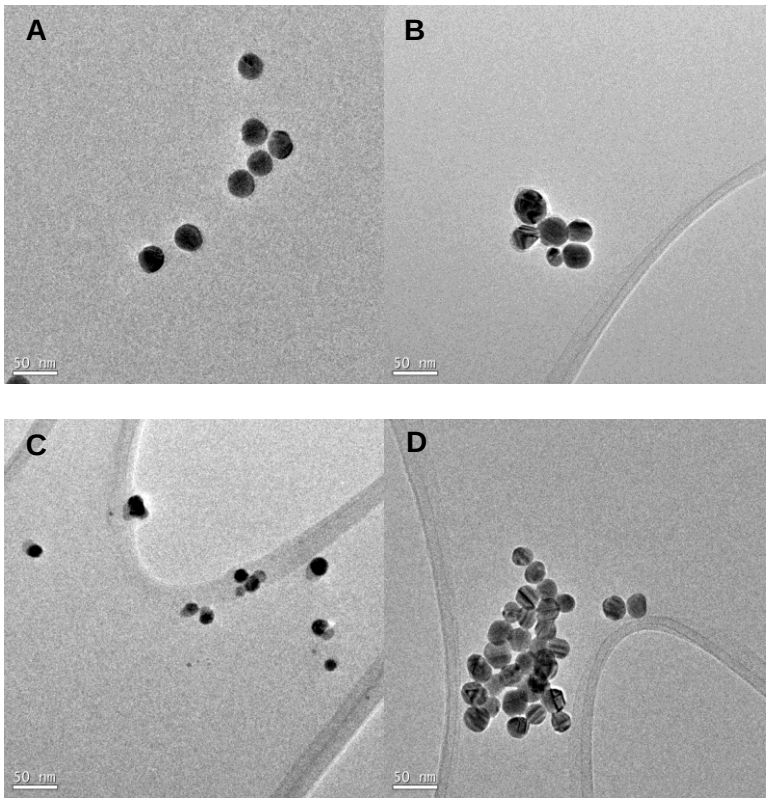

Figure 4.17 TEM images of spherical silver nanoparticles with different capping agents. The scale bar is 50 nm in each image. A: BPEI capped silver nanoparticles; B: Lipoic acid capped silver nanoparticles; C: PEG capped silver nanoparticles; D: PVP capped silver nanoparticles.

4.3.3 Results and Discussion

Five different samples of commercially available silver nanoparticles with various capping agents (i.e. BPEI, citrate, lipoic acid, PEG and PVP) were studied via anodic stripping voltammetry and anodic particle coulometry.

Silver nanoparticle suspensions of 100 pM were drop cast onto a glassy carbon electrode and the modified electrode was used for anodic stripping voltammetry. It is found that the silver oxidation signal differs in size with the variance of capping agent. Next, the five silver samples were used for anodic particle coulometry and it is observed that the 'spikes' obtained (sizes inferred from the measured current) is quantitatively constant with the TEM characterisation data. Comparing the data from the two electrochemical techniques, it is deduced that the capping agent induces the

partial oxidation of the silver nanoparticle in anodic stripping voltammetry; the latter are likely aggregated (as seen in Section 4.1).

4.3.3.1 Anodic Stripping Voltammetry

Silver nanoparticle modified glassy carbon electrodes prepared as described in the Section 4.3.2.1 were used to perform anodic stripping voltammetry. All electrodes were modified with the same amount of silver. The electrochemical experiments were performed with five samples of commercially available silver nanoparticles each containing a different capping agent (BPEI, citrate, lipoic acid, PEG or PVP). Each experiment was repeated 3 times to ensure reproducibility. The voltammetric scan started oxidatively from -0.6 V *vs.* MSE in a 20 mM sodium nitrate solution at a scan rate of 50 mV s^{-1} and the resulting voltammograms are summarised in Figure 4.18. A broad oxidation signal with a peak potential around +0.05 V *vs.* MSE was observed for all five samples. In light of Section 4.1 and Chapter 6, Section 6.2, it is assigned to the oxidation of metallic silver to silver(I) ions (Ag (NP)- e^- (m) → Ag^+ (aq)). The five scans show an oxidation signal which varies greatly in size. A slight difference in onset of the oxidation signal is likely due to the influence of the capping agent on the nanoparticle surface. The silver content of the 100 pM nanoparticle suspension used to modify the glassy carbon electrode was 0.099 mg mL^{-1}. Through Faraday's law, it is expected that the oxidative charge from anodic stripping voltammery is 26 µC. As the oxidative charge under the signal from Figure 4.18 is recorded and plotted against the expected charge, it is observed that for all five types of the nanoparticles, slightly less than 100% oxidation occurred, as depicted in Figure 4.19. It is also seen that the capping agents on the nanoparticle surface influence the size and height of the oxidation signal. In Figure 4.19, PEG capped silver nanoparticles are seen to give the oxidative signal of the largest magnitude (59% oxidation) while PVP capped silver nanoparticles gave the lowest signal among the five (10% oxidation). BPEI capped silver nanoparticles had 16% oxidation while citrate capped silver nanoparticles and lipoic acid capped silver nanoparticles gave 31% and 36% oxidation respectively.

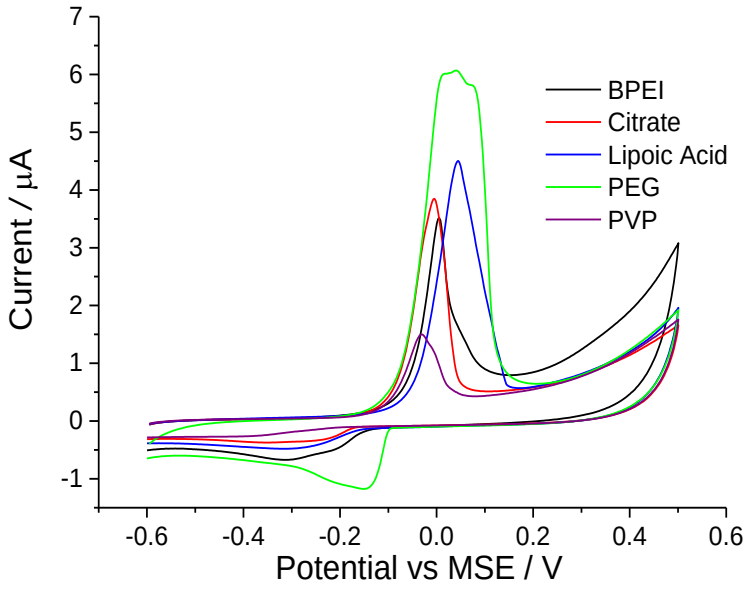

Figure 4.18 The oxidation of silver nanoparticles with different capping agents on a glassy carbon electrode in 20 mM sodium nitrate at a scan rate of 50 mV s^{-1}. Black: BPEI capped silver nanoparticle; Red: Citrate capped silver nanoparticle; Blue: Lipoic acid capped silver nanoparticle; Green: PEG capped silver nanoparticle; Purple: PVP capped silver nanoparticle.

For these anodic stripping voltammetry experiments, the working electrode was prepared through the method of drop casting. Section 4.1 reported that drop casting nanoparticles on the electrode surface causes aggregation to occur. Previous study reported that the aggregated nanoparticles are stripped incompletely through anodic stripping voltammetry.[202] Hence, it is reasonable to propose that in Figure 4.19, there is an incomplete stripping of the silver nanoparticles. To compare the oxidation of nanoparticle aggregates against single nanoparticles, further investigation of the electrochemical behaviour of single nanoparticles is carried out through anodic particle coulometry in Section 4.3.3.2.

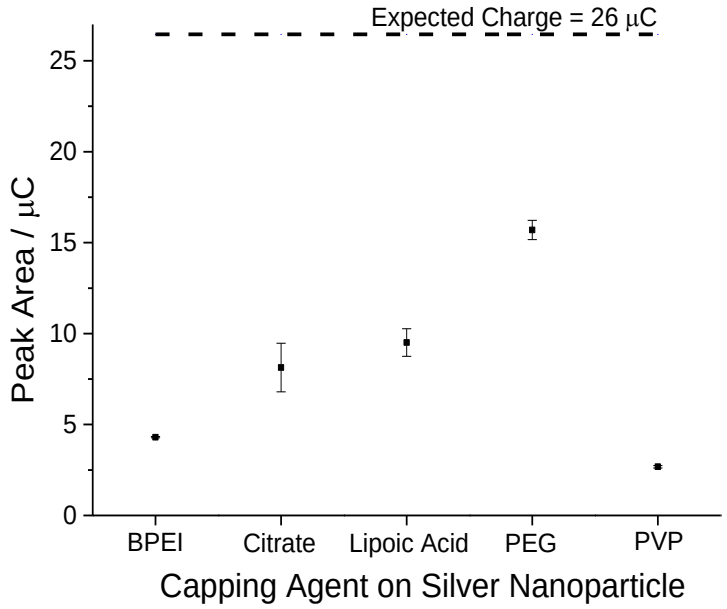

Figure 4.19 The oxidative charge under the peak area as the silver nanoparticles with different capping agents are oxidised on a glassy carbon electrode in 20 mM sodium nitrate at a scan rate of 50 mV s^{-1}. The black dashed line indicates the amount of charge expected.

4.3.3.2 Anodic Particle Coulometry

For 'nano-impact' experiments, chronoamperograms of fifty seconds duration were recorded at +0.6 V *vs.* MSE. To ensure that a blank scan (Figure 4.20 black line) was obtained before any experiment with nanoparticles was performed, a current-time transient was measured on a carbon microdisc electrode placed in a 20 mM sodium nitrate solution. This ensures that no contamination of nanoparticles arises from previous experiments. A typical blank is shown as the black line in Figure 4.20. It has been shifted vertically upwards by 33 pA for clarity. The red line in Figure 4.20 shows a typical scan that depicts single nanoparticles hitting the electrode through the observation of 'spikes' in the current-time transient. Here, the 'spike' is the increase in current caused by the quantitative oxidation of the silver nanoparticle as it diffuses and hits the working electrode held at the oxidising potential.[39, 42] In Figure 4.20 inset, multiple 'spikes' can be seen occurring over a time scale of milliseconds. When the chronoamperometric scan was held at 0 V *vs.* MSE in the presence of silver nanoparticles, no 'spikes' were observed, as shown in Figure 4.20. Thus, the spikes are only observed when the potential held at the electrode is beyond the onset potential of silver oxidation, allowing us to attribute the 'spikes' to the oxidation of the silver nanoparticles impacting the

electrode.[39, 42] The blank scans carried out before the experiment at +0.6 V *vs.* MSE also ensured that the 'spikes' observed in the chronoamperometry scan are caused by the nanoparticles added to the aliquot instead of any possible contamination.

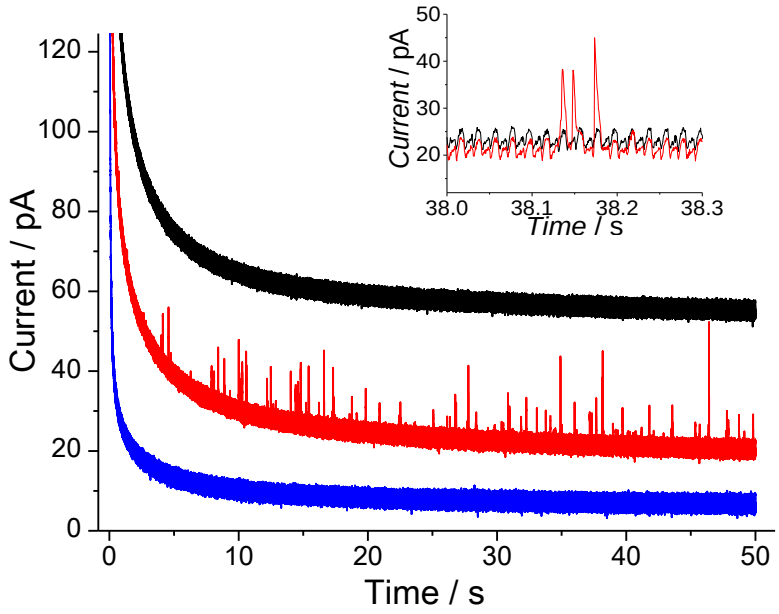

Figure 4.20 Fifty seconds chronoamperomogram for a carbon microdisc electrode (radius = 4.9 µm) immersed in 20 mM sodium nitrate. Black: containing no nanoparticles measured at +0.6 V (*vs*. MSE). The black line is shifted vertically upwards by 33 pA for clarity. Red: containing 100 pM of PEG capped silver nanoparticles measured at +0.6 V (*vs*. MSE). Blue: containing 100 pM of PEG capped silver nanoparticles measured at +0.6 V (*vs*. MSE). Inset: A close up of individual signals observed.

The charge passed under each 'spike' can be used to calculate the nanoparticle radius through the Equation 4.30 in Section 4.2. The 'spikes' recorded can be converted into a histogram which depicts the size distribution of the nanoparticle sample.[39, 42] For each of the five nanoparticle samples, multiple current-time transients were recorded until about 500 'spikes' were counted. Then, the data were processed to give a size distribution of the nanoparticle radii depicted in Figure 4.21. The average radius of the five samples measured by anodic particle coulometry and TEM are tabulated in Table 4.2.

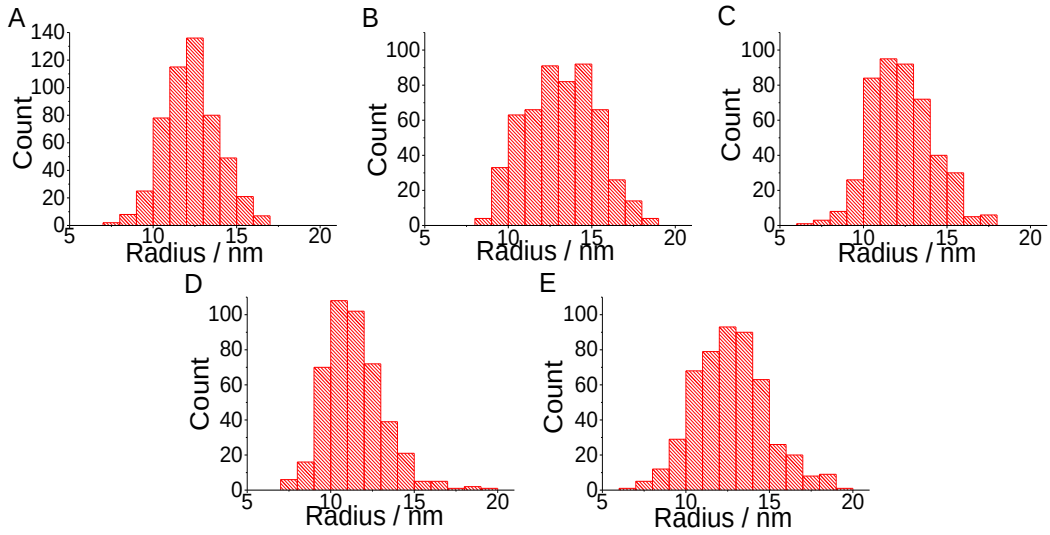

Figure 4.21 Histogram showing the size distribution of the nanoparticles obtained from the chronoamperomogram. A: BPEI capped silver nanoparticles; B: Citrate capped silver nanoparticles; C: Lipoic acid capped silver nanoparticles; D: PEG capped silver nanoparticles; E: PVP capped silver nanoparticles.

Silver Nanoparticle Capping Agent	Sizing from Anodic Particle Coulometry (nm)	Number of Spikes Processed	Number of Scans Recorded	TEM (nm)
BPEI	12.3 ± 1.6	505	30	15.0 ± 1.6
Citrate	13.2 ± 2.1	541	14	14.6 ± 2.1
Lipoic Acid	12.3 ± 1.9	469	85	13.5 ± 3.9
PEG	11.4 ± 1.7	448	27	9.6 ± 2.0
PVP	12.7 ± 2.2	500	39	13.5 ± 1.9

Table 4.2 Table showing the size of silver nanoparticles with different capping agent based on the two techniques of anodic particle coulometry and TEM.

The size of the nanoparticle obtained by TEM is not affected by capping agents as the difference in electron density allows the easy differentiation of the silver core and capping agents. Comparing the radii measured by the two methods, it is seen that the nanoparticle sizes are similar. Therefore, it can be concluded that the single nanoparticles of all five samples are fully oxidised in anodic particle coulometry. Previous anodic particle coulometry papers on the citrate capped silver nanoparticle has also shown a complete oxidation of the silver nanoparticles by matching the radius calculated from 'spikes' to the sizing by microscopy methods.[39, 40, 42]

Please note that Table 4.2 includes data relating to the impact frequency. These values are approximately consistent with an estimated frequency based on a simple Fickian diffusion model but the latter is known to overestimate the values because of electrode adsorption effects and also shielding of the micro disk electrode by adsorption on the insulating sheath.[26, 200, 252, 253] Also, the effects of hindered diffusion near surfaces can influence the data.

4.3.3.3 Influence of Capping Agents on Oxidation

In the previous section (Section 4.1) and literature,[202] it was reported that drop casting can cause nanoparticle aggregation, resulting in incomplete stripping during anodic stripping voltammetry. Therefore, it is expected that the anodic stripping voltammetry performed by electrode modified via drop casting might result in an incomplete stripping.[202] This results obtained in Figure 4.19 where the oxidative charges obtained from the five samples are lower than the expected charge of 26 μC is consistent with the idea of incomplete stripping. In Section 4.3.3.2, it was established that all five types of single nanoparticle, regardless of the capping agent, undergoes complete oxidation during 'nano-impacts'. Thus, comparing the electrochemical behaviour of single nanoparticle and drop casted nanoparticles, it is highly unlikely that the trend of partial oxidation in aggregates is caused by incomplete stripping of single nanoparticles. Therefore, the trend of partial oxidation observed in anodic particle coulometry is likely caused by the electrochemical behaviour of aggregates where some of the aggregates may entirely be inactivated or alternatively each aggregate may be partially oxidised.[202]

This section presents the first time where silver nanoparticles capped with BPEI, lipoic acid, PEG and PVP are characterised by anodic particle coulometry. In a previous literature, platinum nanoparticles were capped with thiols of different alkyl chain length and it was found for chain length beyond 12 carbons, no signal was observed in the nano-imapct experiments.[195] Hence, large capping agents such as 12-mercaptodececanic acid and 16-mercaptohexadecanoic acid have been reported to prevent the oxidation of the platinum nanoparticles.[195] However, none of the five capping agents used in this section prevent the *complete* oxidation of single nanoparticles in anodic particle

coulometry. Therefore, it proves that the capping agents involved in these five samples are not large enough to block the redox reaction of the nanoparticle occurring on the electrode surface despite the large size of BPEI, PEG and PVP.

In anodic stripping voltammetry, the large difference in the partial oxidation of aggregates in Figure 4.18 suggests a significant influence of the capping agent on the behaviour of the aggregates. Thus, the different capping agents likely affected the partial oxidation of the nanoparticle aggregates to varying extents in anodic stripping voltammetry. This is crucially relevant to the use of anodic stripping voltammetry for nanoparticle quantification because most nanoparticles have capping agents on their surfaces. Therefore, careful analysis of anodic stripping voltammetry data is required when analysing nanoparticle aggregates with capping agent to avoid problems where the amount of nanoparticles on the surface may be severely underestimated by the oxidation signal.

4.3.4 Conclusions

In this section, the electrochemical techniques of anodic stripping voltammetry and anodic particle coulometry were performed on five differently capped silver nanoparticles to determine *if* there is a capping agent influence. From anodic particle coulometry, it was seen that the five capping agents considered do not affect the complete oxidation of the single silver nanoparticle. It is the first time where BPEI, lipoic acid, PEG and PVP capped silver nanoparticles are studied through 'nano-impacts'. Hence, it is viable to use the technique for nanoparticle detection and particle sizing in particular. In contrast, with anodic stripping voltammetry, it is observed that capping agents strongly affect the size of the silver oxidation signal. It was found that PEG capped silver nanoparticles give an oxidation signal of the largest magnitude among the five (the greatest percentage stripping was only 59%) while PVP capped silver nanoparticles had the smallest stripping peak despite the same amount of silver deposited on the electrode surface. Therefore, it must be noted that the quantification of nanoparticles *may* be markedly underestimated in anodic stripping voltammetry because of capping agent effects.

Therefore, in this chapter, the two main methods for nanoparticle detection have been investigated. Analytical expressions for the anodic stripping voltammetry of metallic nanoparticles from an electrode have been provided. The equations demonstrated how the peak potential for the stripping process is expected to occur at values negative of the formal potential for the redox process in which the surface immobilised nanoparticles are oxidised to the corresponding metal cation in the solution phase. Next, 'nano-impacts' was found to have a significant advantage over optimal techniques such as NTA and DLS for its capability to detect silver nanoparticles in the presence of high levels of alumina particulates causing a milky white suspension. Lastly, the comparison between the two mentioned techniques found that stripping voltammetry is more susceptible to capping agent effects. In the next chapter, we look at the accidental discovery of the oxidation signal of CTAB whilst comparing the differences between the capping agents on the silver nanoparticles.

Chapter 5 Detection of Single Micelles through 'Nano-Impacts'

In Chapter 4, the detection of silver nanoparticles was discussed. By looking at different capping agents on the silver nanoparticles in Chapter 4, Section 4.3, it was found that cetyltrimethylammonium bromide (CTAB) capped silver nanoparticles behave differently from the rest of the five capping agents studied. Figure 5.1 shows the oxidation of silver nanoparticles at a nanoparticle modified electrode made with the procedure detailed in Section 5.2.4. A stripping signal around 0 V *vs.* mercury/mercurous sulphate electrode (MSE) was seen for citrate capped silver nanoparticles while no silver signal was observed for CTAB capped silver nanoparticles. The absence of a silver stripping signal may be due to the long alkyl chain present in CTAB hindering electron transfer to and from the electrode.[195] However, a signal is seen beyond 0.5 V *vs.* MSE and assigned to the capping agent CTAB. This finding inspired the work in this chapter where the redox active CTAB is detected through 'nano-impacts' of the self-assembled micelles. This chapter thus electrochemically detects a new class of 'soft' particles, micelles, via 'nano-impacts' for the first time. This chapter is published in Chemical Science.[254]

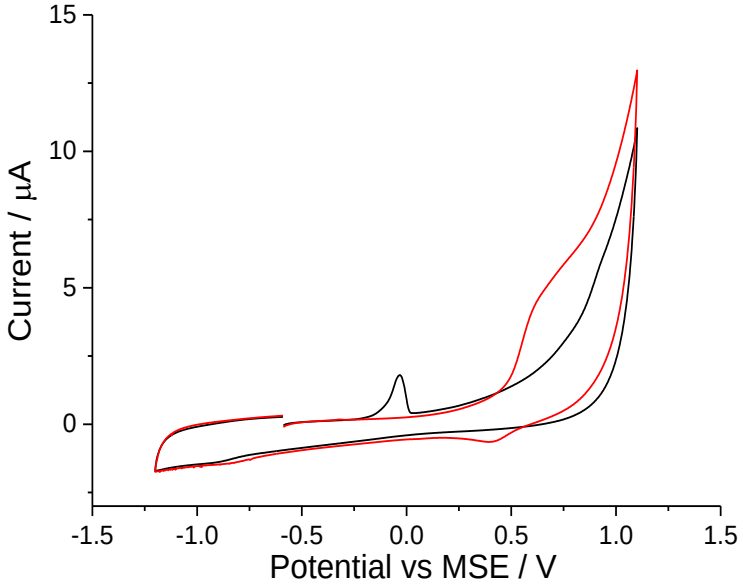

Figure 5.1 The oxidative stripping of silver nanoparticle modified electrode in 0.1 M sodium nitrate at 25 mV s^{-1}. Black: citrate capped silver nanoparticle, red: CTAB capped silver nanoparticle.

5.1 Introduction

As mentioned throughout the thesis, 'nano-impacts' is a novel method developed to analyse single particles.[148] It works by recording the electrochemical signal generated when a single particle hits the electrode held at a suitable potential.[42] For direct electrochemical detection, a redox reaction of the particle occurs upon electrical contact with the electrode, Faradaic current is generated and this results in a short increase in current ('spike') on the chronoamperogram.

Typically, this is used to detect 'hard' metallic nanoparticles like silver[26, 42], gold[171, 172], nickel[26, 171] and mercury halides[198, 255]. However, 'soft' particles are also detectable through 'nano-impacts'[156, 177, 178, 256, 257], starting with the work of Hasse *et al.* where lecithin liposomes were recorded through capacitative 'spikes'.[156] Recently, the direct oxidation of the encapsulated materials such as vitamin C[177] and catecholamine hormones[178] have been used to determine the presence of liposomes.

Hitherto, most 'soft' particles analysed by 'nano-impacts' are liposomes.[156, 177, 178, 256, 257] These lipid vesicles are aqueous compartments enclosed by a lipid bilayer.[258] Figure 5.2 Illustrates their capability to capture a small volume of aqueous solution. Therefore, detection is often based on the redox active components encapsulated within.[177, 178, 256] However, in the current study, the direct detection of micelles using 'nano-impacts' is explored. These are globular structures with polar head groups surrounded by water whilst their hydrocarbon tails are isolated inside, facing one another and away from the aqueous environment.[258] Figure 5.2 shows the close packing of the hydrophobic groups of the micelle which confers thermodynamic stability.[259] Within the digestive system, bile salts forms micelles to aid in the uptake of fat soluble vitamins (i.e. vitamin A, D, E and K).[260] They are also often used as soap as they emulsify oil, allowing water to wash away oil-containing micelles.[261]

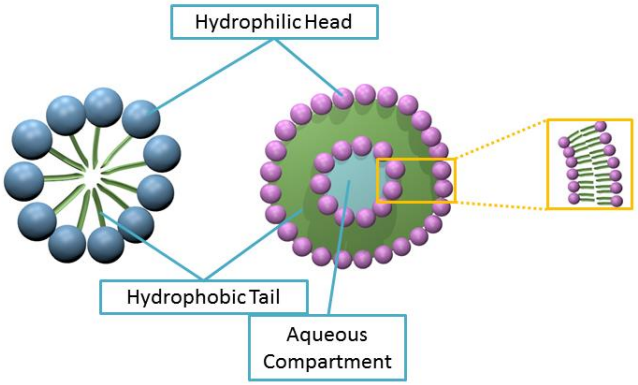

Figure 5.2 The structure of micelle (left) and liposome (right). The spheres represent the hydrophilic groups of the amphipathic molecule. The hydrophobic groups are represented by the green lines.

In the present study, CTAB is used as the analyte to form the micelles for detection. As shown in Figure 5.3, it is a cationic agent containing a quaternary ammonium cation and a bromide anion.[262] CTAB forms micelles as it only has a single hydrocarbon chain;[263] molecules with two hydrocarbon tails prefer to form liposomes due to their bulky hydrophobic groups.[264] In addition, CTAB is a regular reagent for DNA extraction in plants.[265-267] Due to its importance, the critical micelle concentration (CMC) of this micellar agent is well-studied.[268-271]

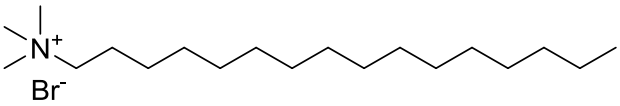

Figure 5.3 The chemical structure of CTAB.

Herein, the detection of CTAB micelles is performed through the electrochemical method of 'nano-impact'. The electrochemical oxidation of CTAB was first studied on a macro electrode system and compared to the oxidation of free bromide ions in aqueous solution. Next, 'nano-impacts' were used to determine the potential onset of the 'spikes' and the influence of CTAB concentration on the chronoamperograms. Dynamic light scattering (DLS) was also performed to analyse the size distribution of the CTAB micelles.

5.2 Experimental

5.2.1 Chemicals

Citrate capped silver nanoparticles are of approximately 50 nm in diameter and supplied by NanoComposix, San Diego, USA. CTAB capped silver nanoparticles are also approximately of 50 nm diameter and were bought from Nanopartz, Loveland, USA.

5.2.2 Electrochemical Apparatus

For cyclic voltammetry experiments, a glassy carbon electrode was used. For chronoamperometric experiments, a carbon microdisc working electrode was used. The reference electrode used was a MSE. The preparation procedure is detailed in Chapter 3, Section 3.2.

5.2.3 Chronoamperometric Experiments

Prior to every chronoamperometric experiment, the electrochemical cell was cleaned by sonication in a mixture of ethanol and water (1:1 ratio) for at least 30 minutes to avoid any contamination by leftover CTAB. All electrodes were rinsed with ethanol and ultrapure water to ensure no CTAB is carried over from previous experiments.

5.2.4 Silver Nanoparticle Modified Electrode

The CTAB capped silver nanoparticle suspension supplied was used as received. The amount of silver surface coverage was kept consistent by diluting citrate capped silver nanoparticle by a factor of four. The working electrode was drop cast with 3 µL of the diluted nanoparticle suspension and dried under a nitrogen flow. After drying, the nanoparticle modified electrode was immediately used for electrochemical experiments. A cyclic voltammogram was swept from -0.6 V to +0.5 V *vs.* MSE at a scan rate of 50 mV s^{-1} to perform anodic stripping voltammetry.

5.3 Results and Discussion

First, a solution of CTAB was oxidised on a macro glassy carbon electrode via cyclic voltammetry to determine the oxidation arising from the bromide ion content. Next, the oxidation study of CTAB

was performed on a carbon microdisc electrode to ensure that the data obtained on the two types of electrodes can be compared across both cyclic voltammetric and chronoamperometric data. Then, current-time transients were performed to observe the 'spikes' generated by the CTAB micelles impacting the microelectrode. The onset potential of the signals was determined by holding different potentials on the electrode during chronoamperometry. It is compared to the oxidation signal obtained in cyclic voltammetry to ensure the 'spikes' originated from the CTAB micelles. Next, the CTAB concentration was varied to determine its correlation to 'spike' frequency and magnitude. Last, DLS was employed to determine the size distribution of the micelles and it is inferred that only the large CTAB micelles are detected via the 'nano-impact' method.

5.3.1 Cyclic Voltammetry Studies

A freshly polished macro glassy carbon electrode was dipped into a solution containing 5.0 mM of CTAB and 0.10 M of sodium nitrate supporting electrolyte. A cyclic voltammetric scan started oxidatively from -0.6 V *vs.* MSE towards +1.1 V *vs.* MSE at a scan rate of 25 mV s^{-1}. This experiment (red line in Figure 5.4) gave two distinct peaks at +0.7 V and +0.9 V *vs.* MSE. In the absence of CTAB (black dashed line in Figure 5.4), no oxidative signals are observed. To determine if the peaks arose from the bromide ion in CTAB, the same cyclic voltammetry experiment was performed with 5.0 mM of potassium bromide instead of CTAB. Two similar distinctive signals at +0.6 V and +0.9 V *vs.* MSE are recorded for potassium bromide (green line in Figure 5.4). Overlaying the two voltammograms, the slight difference in potential can be attributed to the ion pairing present with CTAB. Thus, from literature, the two peaks correspond respectively to:[272, 273]

$$\text{1st wave: } 3Br^-(aq) \rightarrow Br_3^-(aq) + 2e^-(m) \qquad \text{Equation 5.1}$$

$$\text{2nd wave: } 2Br^-(aq) \rightarrow Br_2(aq) + 2e^-(m) \qquad \text{Equation 5.2}$$

Since these signals are both observed in the voltammogram of CTAB and potassium bromide, it is highly likely that the electrochemical oxidation of CTAB involves its bromide counter ion.

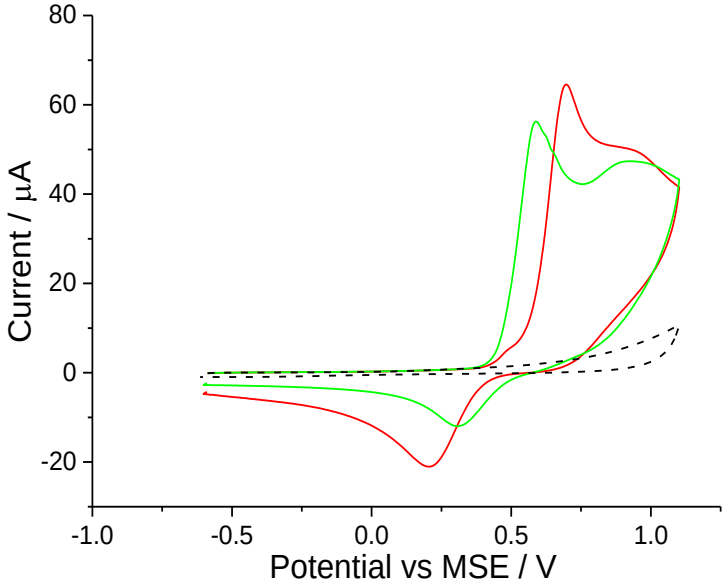

Figure 5.4 The cyclic voltammogram measured on a glassy carbon electrode in 0.10 M sodium nitrate at a scan rate of 25 mV s^{-1}. Black dashed line: blank scan; red solid line: in electrolyte containing 5.0 mM CTAB; green solid line: in electrolyte containing 5.0 mM potassium bromide.

Next, the oxidation of CTAB on a carbon microdisc electrode was investigated to ensure that the mechanism remains similar to the one observed on a macro electrode. This is to provide a basis for chronoamperometric studies where a micro electrode was used to lower background noise. Thus, a carbon microdisc electrode was immersed in a solution of 0.10 M sodium nitrate electrolyte and various concentrations of CTAB. Cyclic voltammetry was performed with the same potential window of -0.6 V to +1.1 V *vs.* MSE at a scan rate of 10 mV s^{-1} and these voltammograms are summarised in Figure 5.5. The increase in anodic current around +0.7 V *vs.* MSE is clearly noticeable at 1.0 mM, 5.0 mM and 10.0 mM of CTAB in Figure 5.5 (green, blue and cyan line respectively). This corresponds to the first oxidation signal occurring on the macro glassy carbon electrode at +0.7 V *vs.* MSE in Figure 5.4. In addition, at 10.0 mM CTAB, the voltammogram has a two-step increase in current at +0.7 V and +0.9 V *vs.* MSE which correlates to the two peaks (i.e. +0.7 V and +0.9 V *vs.* MSE) observed in Figure 5.4. The slight difference in onset potential can be attributed to the common occurrence of finding reversible electrochemistry on a macro electrode appearing as less reversible on a microelectrode as a result of the increased roles of mass transport. Thus, there is no significant difference between the oxidation of CTAB on a macro glassy carbon electrode and

a carbon microdisc electrode. At 100 μM of CTAB, no increase of anodic current is observed as the CTAB concentration has fallen below the detection limit of the cyclic voltammetric system.

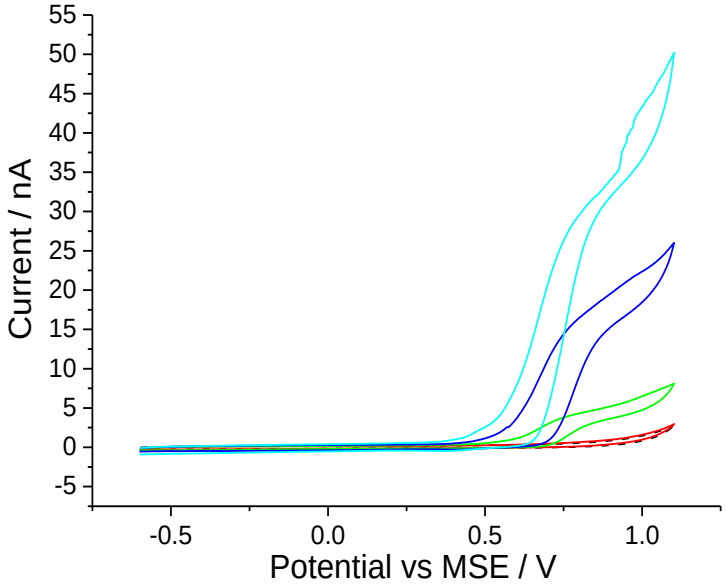

Figure 5.5 The cyclic voltammogram on a carbon microdisc electrode in 0.10 M sodium nitrate at a scan rate of 10 mV s^{-1}. Black dashed line: blank scan; red solid line: 100 μM CTAB; green solid line: 1.0 mM CTAB; blue solid line: 5.0 mM CTAB; cyan solid line: 10.0 mM CTAB.

5.3.2 Chronoamperometric Studies

The 'nano-impact' method involves performing current-time transients with a carbon microdisc electrode held at a fixed potential.[42] As a single micelle comes into contact with the oxidising electrode surface, the redox species (i.e. CTAB) is oxidised, generating a 'spike'.

Two different experiments were performed in this study to ensure that the signals are caused by CTAB micelles. First, multiple blank chronoamperometric scans were performed before the start of every 'nano-impact' experiment. The electrode was placed in 0.10 M sodium nitrate and held at a potential of +1 V *vs.* MSE for fifty seconds. No 'spikes' were observed for blank scans in the absence of CTAB. 'Spikes' were only observed after an aliquot of CTAB was added into the solution.

Second, it was determined that the onset potential for the 'spikes' matches the potential of CTAB oxidation observed in the cyclic voltmmograms. Current-time transients were performed in a

solution of 10.0 mM of CTAB and 0.10 M sodium nitrate at different potentials ranging from +0.6 V to +1 V *vs.* MSE. In Figure 5.6, the number of 'spikes' observed per scan is overlaid with the cyclic voltammogram of a solution containing 10.0 mM CTAB and 0.10 M sodium nitrate.

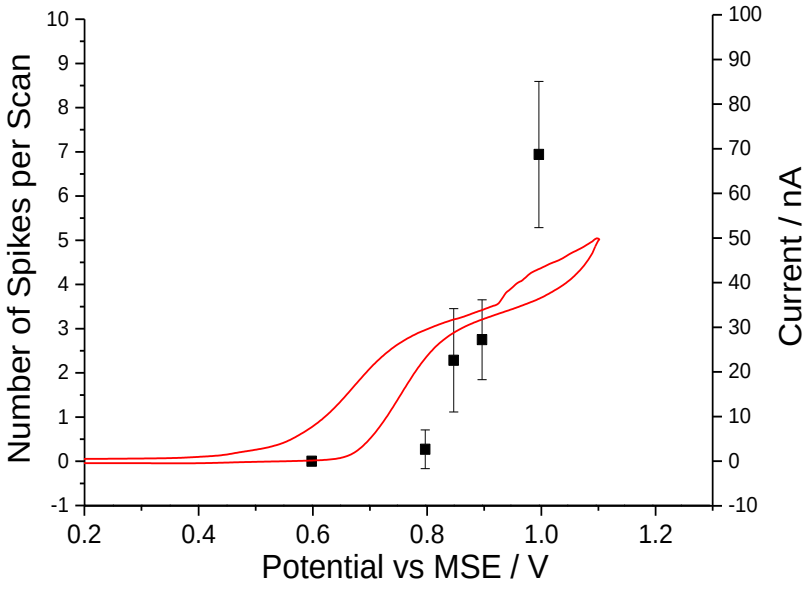

Figure 5.6 The cyclic voltammogram on a microcarbon electrode in 0.10 M sodium nitrate and 10.0 mM CTAB at a scan rate of 10 mV s^{-1} overlaid with a plot of the number of spikes observed per scan against the potential the chronoamperograms are performed.

At +0.6 V *vs.* MSE, no 'spike' is seen in the chronoamperograms and no oxidation is occurring in cyclic voltammogram. At +0.8 V *vs.* MSE, a clear increase in anodic current is seen in the cyclic voltammogram and 3 'spikes' are seen in a total of 11 current-time transients. At +1 V *vs.* MSE, a total of 229 'spikes' are counted from 33 chronoamperograms whilst CTAB is oxidised at this potential in the cyclic voltammograms. Thus, the onset potential of the 'spikes' has a slight overpotential compared to its cyclic voltammogram counterpart. The small overpotential is required to oxidise the bromide content in the stabilised micelles compared to the non-micellar bromide ions in solution. Hence, the comparison of the onset potential of the 'spikes' and the oxidation signal in cyclic voltammogram indicated that the 'spikes' are caused by CTAB micelles. The mechanism of oxidation of the micelles might occur either via electron hopping as described by Amatore *et al.* for

the case of a dendrimer molecule or via coupled oxidation of bromide ions and loss of cationic surfactant molecules.[274]

Next, chronoamperometric scans were performed across different concentrations of CTAB (i.e. 0.01 mM to 20 mM) in 0.10 M sodium nitrate to determine the concentration effects on 'spikes'. All fifty-second current-time transients were recorded at +1 V *vs.* MSE with a carbon microdisc electrode. The individual chronoamperograms at each concentration can be found in Figure 5.7. Examples of the 'spikes' observed in the chronoamperograms are displayed in Figure 5.8. The background current increases with CTAB concentration due to the increase in free CTAB molecules present in the solution.

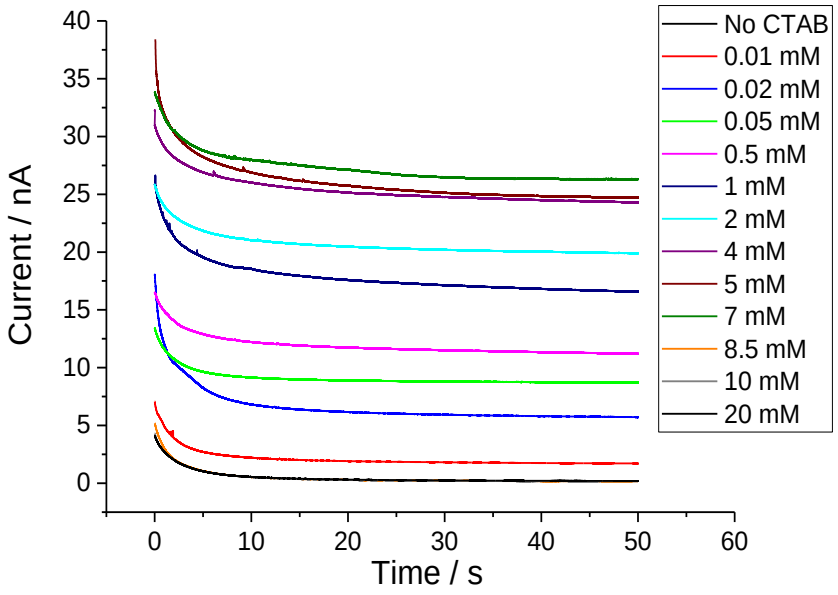

Figure 5.7 The chronoamperograms performed on solutions with 0.1 M sodium nitrate and different CTAB concentrations.

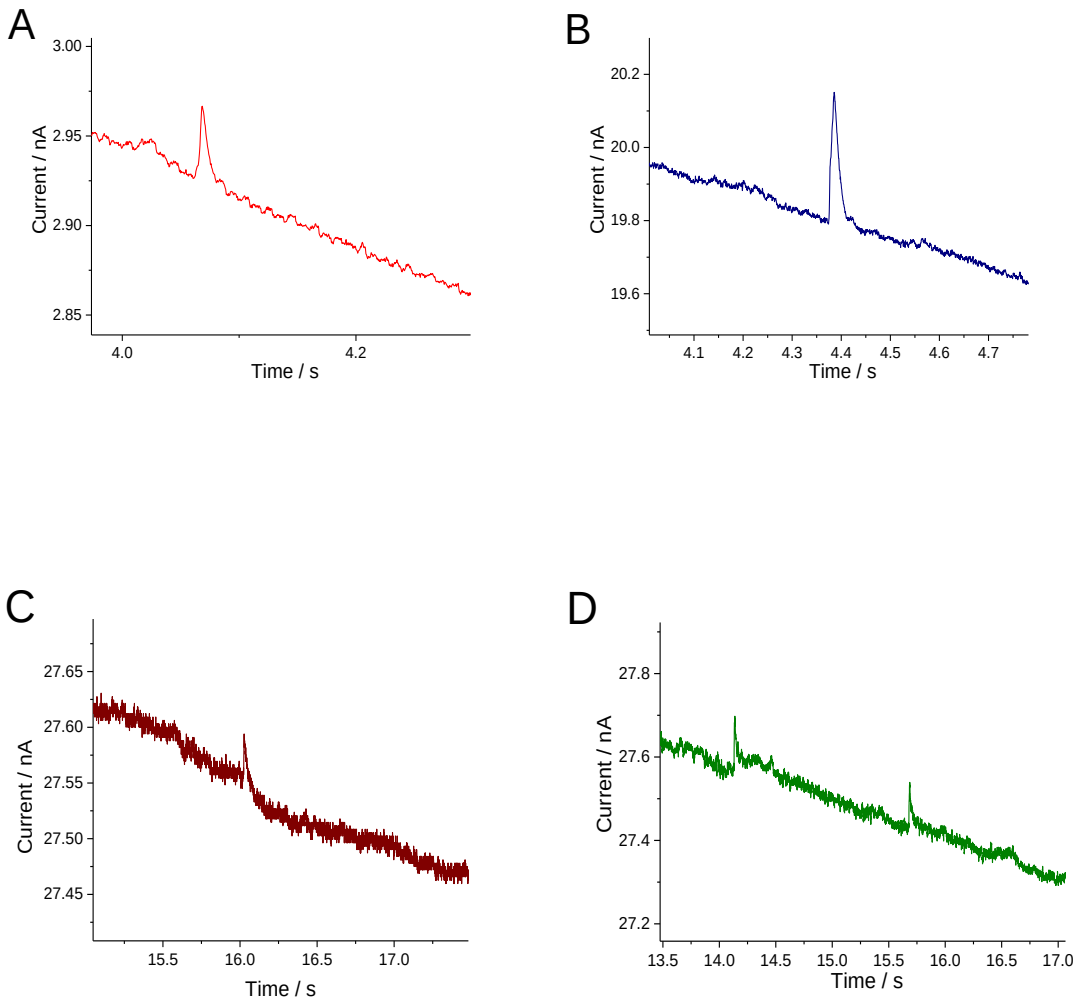

Figure 5.8 Examples of 'spikes' observed in the chronoamperogram at CTAB concentrations of A) 0.5 mM B) 5 mM C) 10 mM D) 20 mM.

In Figure 5.9, the number of 'spikes' observed per scan are plotted against the CTAB concentration. Figure 5.10 is a close up on the lower concentration range of Figure 5.9. It is seen that with increasing amount of CTAB, the number of 'spikes' observed increases. The onset of signals (at least one 'spike' per scan) coincides with the CTAB CMC of 0.05 mM.[268] This indicates that the significant number of 'spikes' recorded are attributed to the CTAB micelles formed above CMC. This could possibly provide a novel method for CMC determination instead of the traditional technique of surface tension measurement.

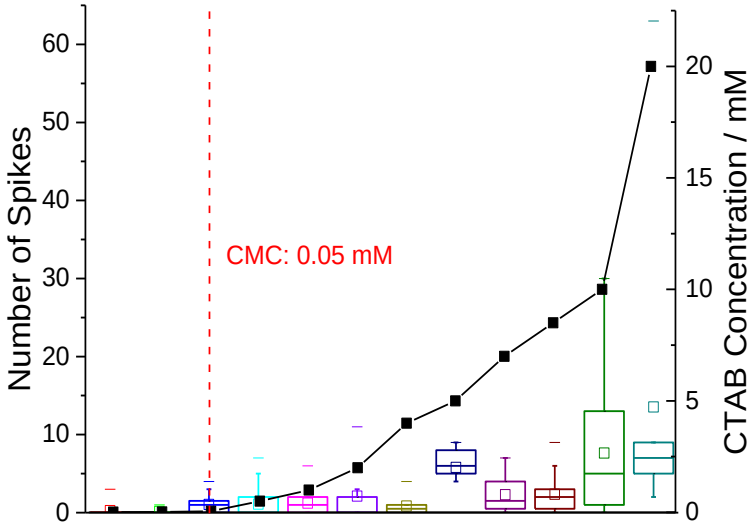

Figure 5.9 The number of spikes observed per scan (box plot) and the concentration of CTAB at which the spikes are recorded (scatter plot). Inlay: The number of spikes recorded per scan against the full range of CTAB concentration tested. Red dotted line: The CMC of 0.05 mM from literature.[268] The box reflects the 25th and 75th percentile. The short dash represents the maximum number of spikes observed per scan while the square represents the mean. The error bars represent the standard deviation of the data.

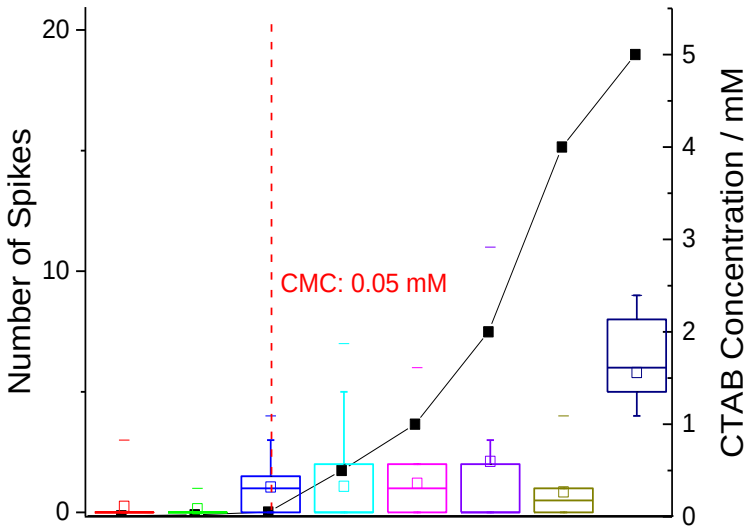

Figure 5.10 A close up of part of Figure 5.9.

In Figure 5.11, the charge passed under a 'spike' is plotted against the amount of CTAB in solution with the standard deviations plotted as error bars. As observed in Figure 5.11, there is no correlation between the amount of current passed and the CTAB concentration. The average charge measured per 'spike' across all concentrations of CTAB is 2.1 pC. If all the current measured is Faradaic, this corresponds to the oxidation of 1.3 x 10^7 CTAB molecules given that CTAB oxidation is a one electron reaction. Thus, very large micelles must be responsible for the Faradaic charge measured. Additionally, there might be capacitive coupling whereby the Faradaic signal is amplified by the change in interfacial capacitance on impact. The possibility of 'spikes' originating only from a capacitative nature is ruled out because a control experiment was performed at negative potentials (i.e. -0.8 V to -1 V *vs.* MSE) and no 'spikes' were recorded.

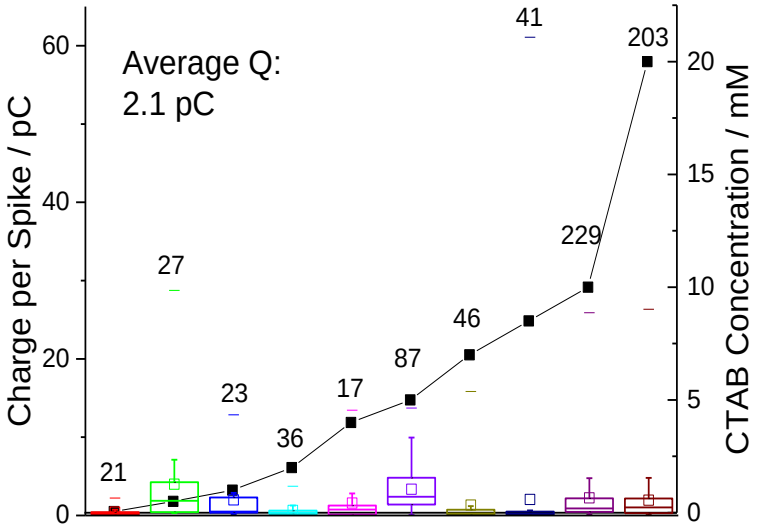

Figure 5.11 The charge under a spike (box plot) is plotted with the CTAB concentration (scatter plot) where the spikes are recorded. The number of spikes recorded at each concentration is listed near the datum point. The box reflects the 25th and 75th percentile. The short dash represents the maximum number of spikes observed per scan while the square represents the mean. The error bars represent the standard deviation of the data.

The distribution of the charge passed under each 'spike' across all CTAB concentrations are displayed in Figure 5.12. Most of the recorded 'spikes' are small and 37% of them have a charge lower than 0.5 pC. In fact, 80% of all 'spikes' recorded contained less than 3 pC. From Figure 5.12,

the charge distribution resembles the tail of a log normal distribution. Thus, it is hypothesized that only the large CTAB micelles are recorded on the chronoamperograms under the assumption that the micelles follow a log normal or similar size distribution. This hypothesis is supported by the data in Figure 5.9 and Figure 5.11. In Figure 5.9, as the concentration of CTAB increases, the number of large micelles grows, thus leading to an increase in frequency of 'spikes'. However, the average charge per 'spike' is independent of CTAB concentration (Figure 5.11). This is because size differences among the larger micelles do not change the current measured significantly compared to micelles of a smaller size. Assuming a surface reaction, a 2% increase in current is observed when a particle changes from 100 nm to 101 nm while a 21% increase is seen as a particle changes from 10 nm to 11 nm. Therefore, to show that the CTAB micelles indeed follow an approximate log normal size distribution, DLS was next performed to support the hypothesis.

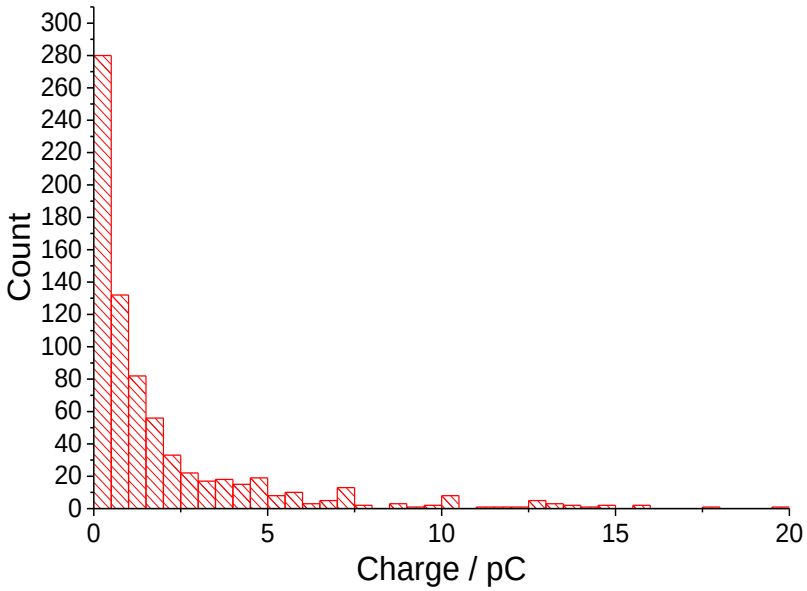

Figure 5.12 The charge distribution of the current recorded under a spike.

5.3.3 Dynamic Light Scattering Studies

DLS was performed on a sample of 10.0 mM CTAB in 0.10 M sodium nitrate to measure the size distribution of the CTAB micelles. The raw data were weighted according to the particle scattering intensity and the intensity weighted size distribution is summarised in Figure 5.13. The black line

shows the CTAB micelle sample approximately following a log normal distribution with an average hydrodynamic diameter of 41.2 nm and a mode of 56.7 nm. The sample has a polydispersity index of 0.245. This observation of a log normal size distribution strongly supports the hypothesis of the 'nano-impact' method measuring only the larger micelles and the tail of the size distribution is detected through the chronoamperograms in Figure 5.12.

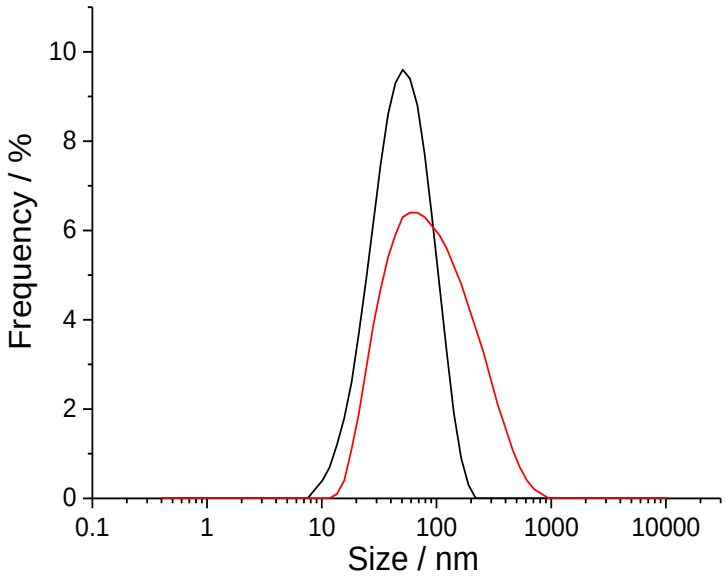

Figure 5.13 The intensity weighted hydrodynamic diameter of the CTAB micelles in sodium nitrate solution containing 10.0 mM CTAB at 25 ^{o}C. Black: 0.10 M sodium nitrate; red: 0.50 M sodium nitrate

To carry this hypothesis further, the electrolyte concentration was varied for the DLS and 'nano-impact' experiments. From literature, it is known that smaller micelles are formed in the presence of a lower electrolyte concentration.[268] From Table 5.1, it is observed that at 0.05 M sodium nitrate, the CTAB micelles have an average diameter of 11.7 nm compared to 41.2 nm (0.10 M sodium nitrate, black line in Figure 7) and 61.7 nm (0.50 M sodium nitrate, red line in Figure 7) at higher concentrations of electrolyte. The counterpart electrochemical control experiment was performed with 10.0 mM CTAB in a lower electrolyte concentration of 0.05 M sodium nitrate via 'nano-impacts'. No 'spike' was observed in the chronoamperograms. This is likely due to the absence of very large micelles in the lower electrolyte concentration environment. Thus, this further strengthens the hypothesis where 'nano-impacts' are detecting the large micelles present in the

CTAB solution. It is to be taken note that DLS was attempted with 0.05 M sodium nitrate in the current study. However, the polydispersity nature of the sample resulted in an unsuccessful measurement.

$[NaNO_3]$/M	Average Hydrodynamic Diameter/nm	Mode/nm	Polydispersity Index	Temperature /°C	Reference
0.05	11.7	-	0.23	30	[268]
0.10	41.2	56.7	0.24	25	Current study
	38.4	-	0.24	30	[268]
0.50	61.7	119.5	0.43	25	Current study
	71.0	-	0.51	30	[268]

Table 5.1 DLS results of the solutions containing 10.0 mM CTAB and various concentrations of sodium nitrate.

Despite the micelles having an average hydrodynamic diameter of 41.2 nm at 0.10 M sodium nitrate, most of the particles are not detected via 'nano-impacts'. In the literature, silver nanoparticles of 6 nm diameter have been successfully analysed and sized.[179] Comparing with a previous study in Chapter 4, Section 4.3 where the exact same set-up and microcarbon electrode were utilised, silver nanoparticles of an average diameter of 24 nm were detected. The silver nanoparticles gave an average charge of 0.66 pC with a background noise level of 6 pA. In the current study, the average charge measured was 2.1 pC. As mentioned previously, the background current increases with the CTAB concentration due to the increased amount of free CTAB molecules in solution (Figure 5.7). It is also observed that the variation of CTAB concentration resulted in different background noise: 6 pA (0.5 mM CTAB), 20 pA (4.0 mM CTAB) and 40 pA (20.0 mM CTAB). Thus, the magnitude of the background noise correlates with the amount of CTAB present in the solution. With a higher noise, there is a greater difficulty to differentiate the signals from the background noise. Hence, the rest of the smaller micelles remain undetected as the 'spikes' they generate cannot be resolved from the background noise. Therefore, 'nano-impacts' has detected the larger single CTAB micelles towards the tail of the size distribution.

5.4 Conclusions

This chapter reports for the first time, 'nano-impacts' to be a novel method for the detection of large CTAB micelles. From the cyclic voltammetric experiments, it is found that CTAB oxidation is attributed to the oxidation of its bromide ion. This one electron oxidation is responsible for the Faradaic current generating the 'spikes' in 'nano-impacts'. In the chronoamperometric scans, the onset potential of the 'spikes' matches the potential of CTAB oxidation in the cyclic voltammogram. Hence, the signals are attributed to the CTAB micelles present in the solution. By varying the concentration of CTAB, it is found that the number of 'spikes' per scan increases with concentration as more CTAB micelles are formed. Comparing the charge distribution of the 'spikes' and DLS data, it is concluded that large CTAB micelles are detectable by 'nano-impacts'. This represents an entirely new class of 'soft' particles that can be studied via this means. While Chapter 4 and Chapter 5 focus their attention on nanomaterial detection, in the next chapter, the nanoparticles themselves are used for quantifying other analytes.

Chapter 6 The Application of Silver Nanoparticles in Electroanalysis

The previous chapters illustrated the application of electrochemical techniques towards the detection of silver nanoparticles. As mentioned in Chapter 2, nanoparticles are employed in numerous consumer products. In this chapter, we look at the possible application of silver nanoparticles as the basis of sensors for the analysis of silver ions (Section 6.1), chloride ions (Section 6.2) and iodide ions (Section 6.3). These three works have been published in Sensors and Actuators B: Chemical[275] and the Analyst[276, 277]. They were performed in collaboration with Dr. Christopher Batchelor-McAuley, Dr. Kristina Tschulik and Ms. Christine Damm. The experimental interpretation in Section 6.1 was done together with Dr. Christopher Batchelor-McAuley. Ms. Christine Damm performed the transmission electron microscope (TEM) imaging for the silver nanoparticles used in Section 6.1 with Dr. Kristina Tschulik's coordination. Dr. Christopher Batchelor-McAuley and Dr. Kristina Tschulik helped with nanosight track analysis (NTA) in Section 6.2 and the scientific interpretation of the experimental results in Section 6.2 and 6.3. Dr. Kristina Tschulik was responsible for silver nanoparticles synthesis and the scanning electron microscope (SEM) image of the silver nanoparticles used in Section 6.2. Dr. Sven Ernst helped with the home made reference electrode used in Section 6.2. The silver nanoparticles in Section 6.3 were synthesised with Ms. Jessica C. Lees.

6.1 Using Pre-created Nucleation Centres to Improve the Limit of Detection in Anodic Stripping Voltammetry

6.1.1 Introduction

Anodic stripping voltammetry is a very well established technique for the detection of trace metals and sometimes other materials.[2, 278] It is characterised by a high level of sensitivity coming from the pre-concentration of the target onto an electrode by reduction to the metallic form. The pre-concentrated metal is analysed by means of a positive going ('anodic') potential sweep. A similar

approach is used in cathodic stripping voltammetry except that the target metal ions are typically concentrated as metal oxides rather than metals and the analysis is via a cathodic potential sweep.[135, 136, 279, 280]

The anodic stripping voltammetry technique can be optimised in various ways to allow for greater sensitivity or lower limits of detection. One obvious approach is to prolong the pre-concentration step so as to enhance the amount of metal deposited. Note that because of the interplay of nucleation and growth, this is not necessarily a simple linear effect; in particular for progressive nucleation, non-linear effects in time may be anticipated.[281] A different approach is to modify the potential sweep so as to enhance the measurement sensitivity, for example, by replacing a linear sweep with a pulse voltammetric approach (for the benefits mentioned in Chapter 2, Section 2.3).[282-287] Equally, the prevailing mass transport conditions can be enhanced to promote a greater flux of material to the electrode surface. In particular, the use of microelectrodes rather than macroelectrodes can increase sensitivity,[288] as well as reproducibility of transport conditions,[286] and the use of microelectrodes array[289] are further developments. Alternatively, forced convection approaches can be utilised, of which sonovoltammetric methods are perhaps the best in terms of sensitivity enhancement.[290-292] In addition, surface modification of electrode surface with organic molecules or other metals has been attempted to make the surface more favourable for metal deposition.[287, 293-298]

In this section, we present a proof-of-concept method of an alternative strategy for improving the sensitivity and limit of detection of anodic stripping voltammetry. Metal nanoparticles of the target metal ion are employed for an electrode pre-treatment procedure to provide nucleation centres in advance for the analyte of interest. A schematic diagram is provided in Figure 6.1 to illustrate the concept. By pre-treating the electrode via depositing and stripping of metal nanoparticles, small metal nuclei that are not detectable electrochemically are left behind on the electrode surface.[299, 300] During the pre-concentration step of the anodic stripping voltammetry, these small metal nuclei then act as nucleation centres for metal ions of the same identity so as to enhance the deposition.

Thus, more metal is deposited onto the electrode surface with the same pre-concentration duration as nucleation sites are already pre-created. This speeds up the deposition process because nucleation site formation can be a slow process that requires a high overpotential compared to metal growth.[301] Hence, a larger peak charge can be measured within the same time frame with a pre-treated electrode as compared to an untreated electrode. The greatest advantage of this strategy lies in its simplicity. The pre-treatment only involves a simple drop casting of a metal nanoparticle suspension and then oxidising the nanoparticles. No other foreign materials or impurities are introduced apart from the metal of interest. In this section, silver is taken as an example to illustrate this proof-of-concept.

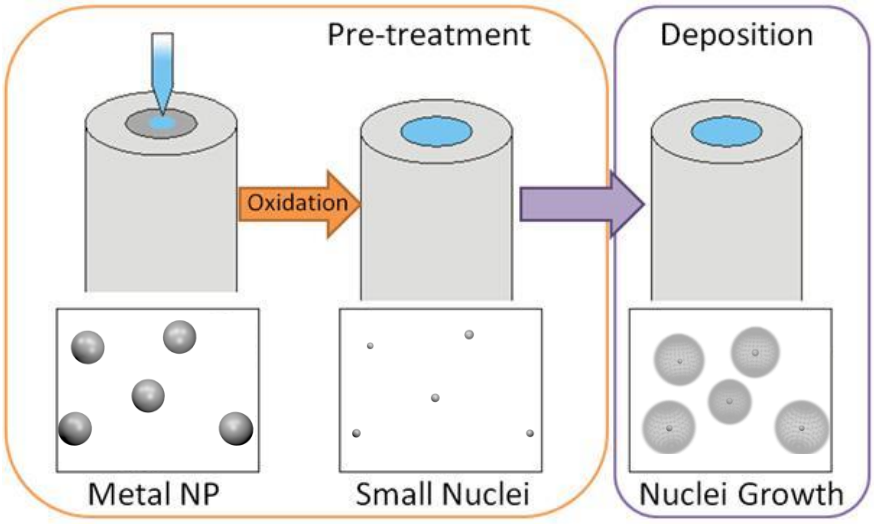

Figure 6.1 Schematic diagram showing the concept of improving the limit of detection of anodic stripping voltammetry. Pre-treatment starts with drop casting of metal nanoparticles suspension onto the electrode surface which are then oxidised. Small metal nuclei are left behind from this pre-treatment and the pre-treated electrode is immediately used for deposition experiments. The metal ions in deposition experiment are deposited onto the small nuclei, resulting in nuclei growth and improved analytical sensitivity.

6.1.2 Experimental

6.1.2.1 Voltammetry

The working electrode was a glassy carbon electrode. A mercury/mercurous sulphate electrode (MSE) was used as a reference electrode. The rest of the conditions are detailed in Chapter 3, Section 3.2.

6.1.2.2 Silver Nanoparticle Synthesis and Characterisation

Silver nanoparticles capped with citrate were synthesised based on a method by Wan *et al.*[302] In summary, 20 mL of 1% (w/v) trisodium citrate solution and 75 mL of ultrapure water was heated to 70 °C for 15 minutes. 1.7 mL of 1% (w/v) silver nitrate solution and 2 mL of freshly prepared 0.1% (w/v) sodium borohydride were added in quick succession to the heated solution. The mixture was stirred vigorously for another hour at 70 °C. After cooling to room temperature, ultrapure water was added to make the final volume of the nanoparticle suspension 100 mL. A clear yellow suspension of silver nanoparticles with a total silver concentration of 1 mM was obtained. All glassware were cleaned thoroughly with aqua regia (a mixture of concentrated hydrochloric acid and concentrated nitric acid in 3:1 ratio) prior to silver nanoparticle synthesis.

The characterisation of the silver nanoparticle suspension was performed by ultra-violet visible (UV-vis) spectroscopy and TEM (FEI TECNAI T20, 200 kV accelerating voltage, lanthanium hexaboride (LaB_6) filament). For UV-vis analysis, the nanoparticle suspension was diluted by a factor of 24 with ultrapure water. A wavelength scan from 600 nm to 250 nm at a scan rate of 400 nm min^{-1} was performed. The surface plasmon peak is known to be affected by the size and shape of silver nanoparticles and the maximum absorption wavelength decreases with the nanoparticle size.[51, 303] A surface plasmon peak at 392 nm was recorded and this indicated the presence of spherical silver nanoparticles smaller than a diameter of 29 nm.[51] Ms. Christine Damm recorded the TEM images of the nanoparticles. The nanoparticles represented in the TEM images were analysed with the software Image J (National Institutes of Health, USA). The areas of the clearly defined nanoparticles were measured and nanoparticle radii were calculated from the areas to take into account slightly non-spherical nanoparticles. A total count of 1223 nanoparticles gave a measurement of an average radius of 4.7 ± 1.8 nm. Figure 2.2 and Figure 6.2 display a TEM brightfield image of the silver nanoparticles. Figure 6.3 shows the size distribution of silver nanoparticles and the UV-vis spectra measured.

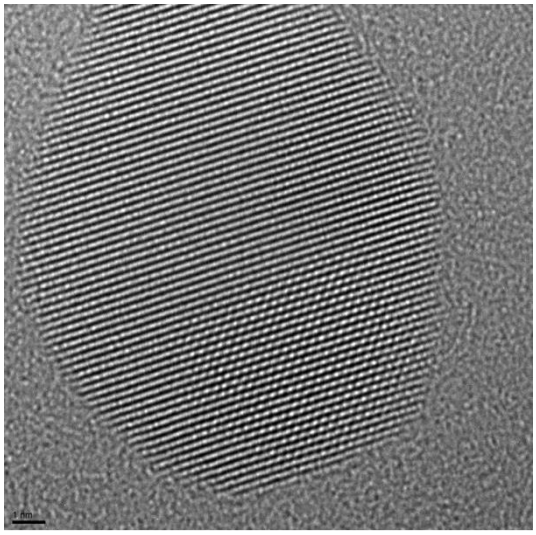

Figure 6.2 A high resolution TEM image of the silver nanoparticles used in this section. The scale bar represents 1 nm.

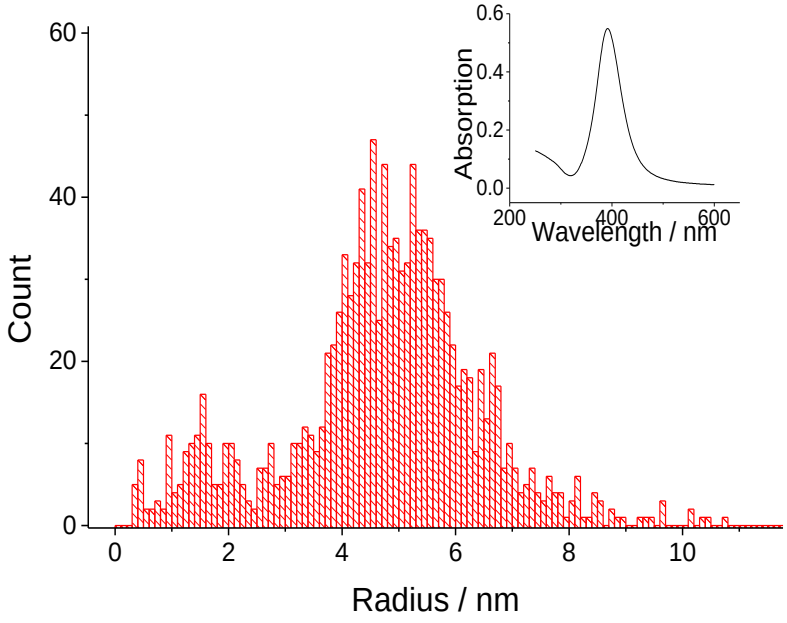

Figure 6.3 Size distribution of silver nanoparticles. Average radius of 4.7 ± 1.8 nm. Inlay: UV-vis spectrum of silver nanoparticles showing a distinct surface plasmon peak at 392 nm.

6.1.2.3 Electrode Pre-treatment Procedure

The glassy carbon electrode was pre-treated to deposit silver nuclei to enhance subsequent electrodeposition using the following approach. First, nanoparticle modification of the glassy carbon electrode was carried out by drop casting 3 µL of the diluted silver nanoparticle suspension onto the electrode surface and drying the electrode under a flowing nitrogen atmosphere. The silver

nanoparticle suspension had a total silver concentration of 1 mM and was diluted with ultrapure water by a factor of 500 before drop casting. Next, linear sweep voltammetry was performed with the modified electrode by scanning from -0.3 V to 0.2 V *vs.* MSE. A signal was observed at around 0 V *vs.* MSE which corresponds to the oxidation of silver to silver ions. The linear sweep voltammetry removed most but not all of the silver cast. A second scan from -0.1 V to 0.5 V *vs.* MSE was conducted and no silver oxidation signal was observable. The second linear sweep voltammetry began at a higher potential of -0.1 V *vs.* MSE instead of -0.3 V *vs.* MSE to ensure fresh silver ion generated from oxidation in the first scan did not deposit back onto the electrode, causing a false positive. The absence of signal in the second scan showed that any small metal nuclei left behind are not electrochemically detectable and the oxidation signal from the deposition experiments comes solely from the deposited silver. As the pre-treatment is performed ex-situ (i.e. not in sample solution) and the majority of the silver utilised is removed, the possibility of contamination of the sample by pre-treatment is minimal. In addition, even if one was to assume that *all* of the nanomaterial used during the pre-treatment was to act as a contaminant, an absolute maximum contamination of ~6 x 10^{-12} moles is possible. Taking the sample volume to be 10 mL, the contamination will result in an error of 0.6 nM of silver. This is significantly lower than the lowest concentration (i.e. 30 nM Ag^{+}) detected in this section. In addition, it is not expected that the citrate capping agent will influence the experiment as during the linear sweep voltammetry performed during the pre-treatment, the citrate capping agent will have been concomitantly removed along with the majority of the drop cast silver. After the first linear sweep voltammetry from -0.3 V to 0.2 V *vs.* MSE, the electrode is considered as "pre-treated". The electrode was rinsed in a vial of water and used for silver deposition experiment immediately.

6.1.3 Results and Discussion

In this section, pre-treated electrodes are shown to be more favourable for subsequent silver deposition as compared to a bare untreated glassy carbon electrode. In Section 6.1.3.1, the proof-of-concept is presented with a deposition experiment with 300 nM of silver nitrate. In Section

6.1.3.2, a range of silver nitrate concentrations are used in deposition experiments to display the effects of silver ion concentration on the amount of silver deposited.

6.1.3.1 Proof of Concept

Silver deposition experiments were performed on two types of electrodes – first a bare untreated glassy carbon electrode which was polished to a mirror finish and second on an electrode pre-treated with the procedure described in Section 6.1.2.3. On both electrodes, the deposition of silver was performed at a potential of -0.4 V *vs*. MSE for 15 minutes in a solution containing 300 nM of silver nitrate and 0.1 M sodium nitrate as the electrolyte. A stirring rate of 200 rotations per minute was maintained with a magnetic stir bar (25 mm in length) for deposition and stirring was switched off 2 minutes before the scan (after the first 13 minutes of deposition). Stirring was crucial to the experiment as it reproducibly delivered metal ions to the electrode surface and kept the diffusion layer thickness of the electrode to a minimum. The diffusion of the metal ions alone within the time of 15 minutes was insufficient to deposit a substantial amount of metal onto the electrode surface for electrochemical analysis. Consequently, stirring during deposition ensures that the analysis can be performed within shorter timescales. Throughout the 15 minute deposition, silver ions were pre-concentrated and deposited as silver onto the working electrode. After that, an anodic stripping voltammetry starting from -0.3 V to 0.2 V *vs*. MSE and sweeping back to -0.6 V *vs*. MSE was performed at 0.05 V s^{-1}. A broad oxidative stripping peak was obtained at around 0 V *vs*. MSE and the charge underneath the signal was measured to determine the amount of silver deposited upon the surface. The voltammogram obtained from deposition experiments with electrolyte containing 300 nM of silver nitrate for both the bare untreated glassy carbon electrode and the pre-treated electrode are plotted in Figure 6.4. As observed, the silver stripping signal of the pre-treated electrode is larger than the untreated electrode. Upon closer inspection, the amount of silver deposited on a pre-treated electrode is ~ 40 times greater than a bare untreated glassy carbon electrode.

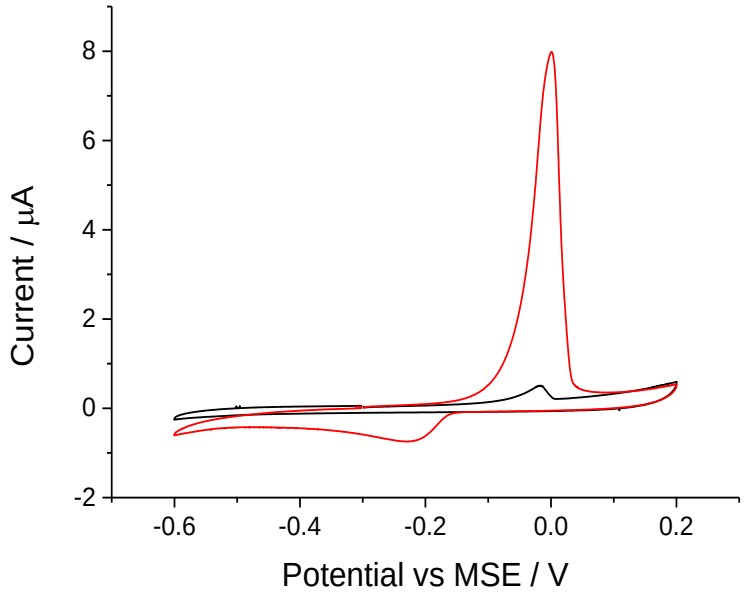

Figure 6.4 The oxidative stripping of silver from a glassy carbon electrode after deposition at -0.4 V *vs*. MSE for 15 minutes in 0.1 M sodium nitrate spiked with 300 nM of silver nitrate at a scan rate of 0.05 V s^{-1}. Stirring at 200 rotations per minute was maintained for the first 13 minutes of the deposition. Black line: Bare untreated glassy carbon electrode. Red line: Pre-treated glassy carbon electrode.

Although the electrodes used in the pre-treated and untreated experiments were both glassy carbon electrodes, it is concluded that the pre-treatment provided small amounts of silver clusters on the electrode surface. These clusters improved the signal of the pre-treated electrode by providing pre-existing nucleation centres for immediate deposition of silver, where for the untreated electrodes, nucleation must occur before deposition can take place. Within the literature, silver has been known to deposit at a lower potential when nucleation centres are present.[301] Previous studies showed TEM images where the electrochemical oxidation via a linear sweep voltammetry is insufficient to remove all the silver drop cast or deposited and the small nuclei were relatively stable and only completely removed when an overpotential of 500 mV *vs*. Ag/Ag^{+} is maintained for a duration of more than an hour.[299, 300] Thus, the pre-treatment is inferred to have left sufficient nucleation centres for more silver to be deposited onto the electrode surface during the 15 minutes deposition period, leading to a greater peak charge. Here, peak charge is defined as the Faradaic charge measured under the peak. Consequently, this provides a possible route for

lowering the detection limit of anodic stripping voltammetry. Moreover, in the next section, the experiment was repeated with various silver nitrate concentrations to further develop this idea.

6.1.3.2 Response to Different Silver Nitrate Concentrations

Deposition experiments with pre-treated electrodes and bare untreated glassy carbon electrodes were performed at 7 different concentrations of silver nitrate. The silver nitrate concentrations tested were 30 nM, 50 nM, 100 nM, 200 nM, 300 nM, 600 nM and 1 μM. Otherwise, identical parameters were used as the ones in the experiments above in Section 6.1.3.1. Figure 6.5 depicts the peak charge measured at various concentrations of silver nitrate with a pre-treated electrode or a bare untreated glassy carbon electrode. Figure 6.6 is a close up of Figure 6.5 at the lower concentration range. At silver nitrate concentrations equal or less than 100 nM, there was no signal recorded for silver oxidation for a glassy carbon electrode without pre-treatment. However, at all concentrations from 30 nM to 1 μM of silver nitrate, a silver oxidation signal, which is *at least* three times larger than the untreated electrode, was observed for the pre-treated electrode. This variable enhancement reflects the fact that upon the bare, untreated electrode, nucleation centre formation is easiest with high concentrations of silver ions. Conversely, it is this requirement of nucleation centre formation which hinders the conventional electrochemical stripping analysis for lower metal ion concentration (i.e. the deposition is limited by the formation of nucleation centres). Therefore, via by-passing the nucleation step with pre-treatment of the electrode, this resulted in the largest signal enhancement in the lower nanomolar range.

As seen in both Figure 6.5 and Figure 6.6, the relationship between measured peak charge and silver nitrate concentration is not linear despite the trend of increasing peak charge with increasing silver nitrate concentration. During the deposition period, there are two main processes of nucleation and growth. Nucleation refers to formation of a 'seed' on the electrode surface while growth refers to the additional deposition of silver onto the 'seed'. Nucleation requires a higher overpotential than growth.[301] The presence of existing nucleation centres speeds up the process of growth since nucleation is no longer essential. Hence, the difference in rate for both processes

accounts for the non-linear trend observed cross the various silver nitrate concentrations. Accordingly, given that signal amplification is observed with the pre-treated electrode, detection of silver ions at a much lower concentration is possible. Hence, the threshold value of this analysis had been lowered and it is demonstrated how the use of nanoparticles can enhance the voltammetric signal allowing lower concentrations of metal ions to be readily estimated. This is achieved by circumventing the issue of nucleation by providing pre-existing nucleation centres allowing deposition to occur even at very low metal ion concentrations.

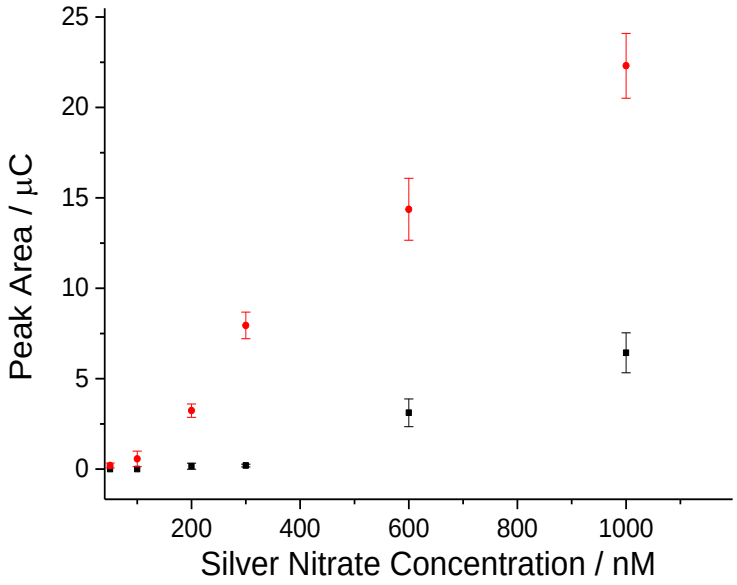

Figure 6.5 The oxidative stripping of silver from a glassy carbon electrode after deposition at -0.4 V *vs*. MSE for 15 minutes at a scan rate of 0.05 V s^{-1}. Deposition was performed in 0.1 M sodium nitrate spiked with different concentrations of silver nitrate. Stirring at 200 rotations per minute was maintained for the first 13 minutes of the deposition. The peak charge of the voltammetric signal is plotted against the concentration of silver nitrate. Each datum point consists of a minimum of 3 repeats. Black squares: bare untreated glassy carbon electrode. Red diamonds: pre-treated glassy carbon electrode.

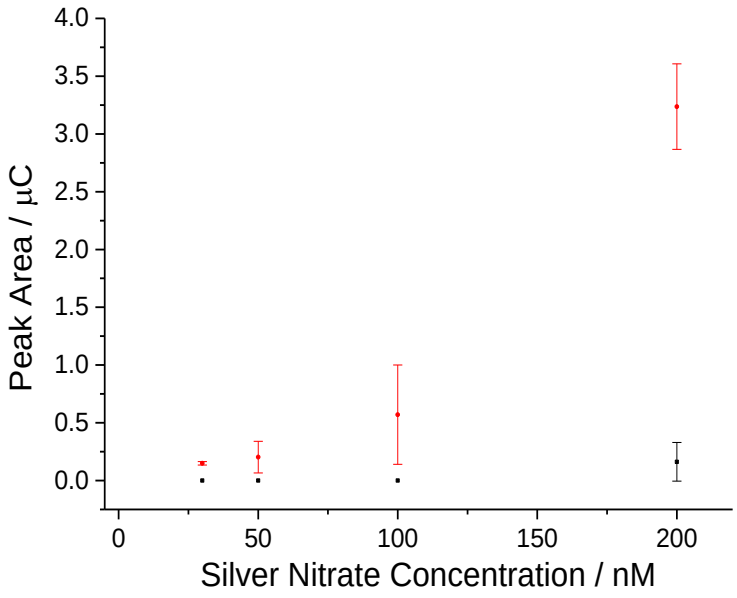

Figure 6.6 A close up of part of Figure 6.5.

To further lower the detection limit, the deposition time can be altered. When the deposition time is extended, more time is given for the growth process and at a lower concentration of silver nitrate, a larger signal is recorded and the detection limit is lowered. Thus, experiments with different deposition time were performed (see Figure 6.7). With a silver nitrate concentration of 30 nM, the pre-treated electrode underwent various deposition time of 7.5, 15, 22.5 and 30 minutes. Similar to the experiments reported in Section 6.1.3.1, a stirring rate of 200 rpm was maintained and switched off 2 minutes before the voltammetric scan. This meant that the stirring was sustained for 5.5, 13, 20.5 and 28 minutes respectively. The oxidation of deposited silver on the electrode surface gave a signal and the peak charge was measured and plotted against deposition time to give Figure 6.7. It shows that with increasing deposition time, more silver deposits onto the electrode surface and the peak charge measured increases. Hence, smaller concentrations of silver ions can be detected when deposition time is prolonged.

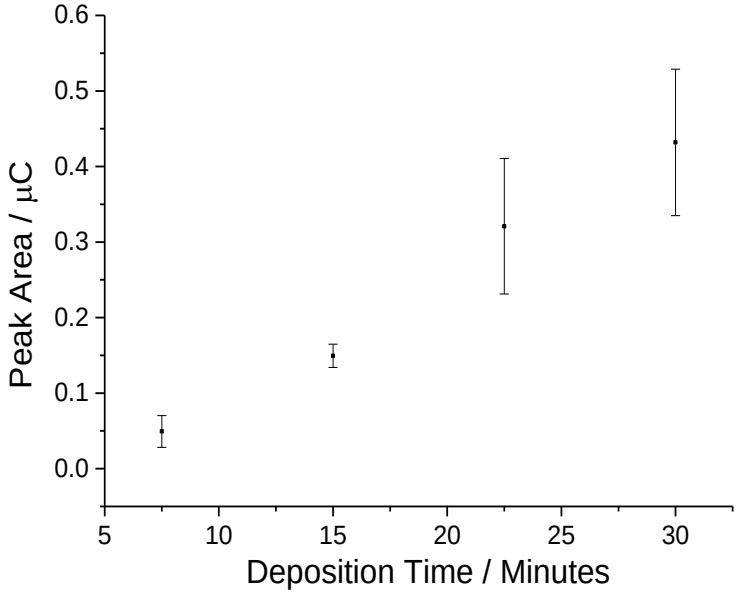

Figure 6.7 The oxidative stripping of silver from a pre-treated glassy carbon electrode after deposition at -0.4 V *vs*. MSE for various time frames in 0.1 M sodium nitrate spiked with 30 nM of silver nitrate at a scan rate of 0.05 V s^{-1}. Stirring at 200 rotations per minute was maintained during deposition and switched off 2 minutes prior to the scan. The peak charge of the voltammetric signal is plotted against the deposition time. Each datum point consists of a minimum of 3 repeats.

6.1.4 Conclusions

Anodic stripping voltammetry is a very common method of quantifying the amount of metal ions in solution and within the literature, many studies have been attempted to lower the detection limit by adding organic molecules or other metals.[287, 293-298] This section aims to provide a simple proof-of-concept, where the detection limit can be lowered without complicated pre-treatment or modification, illustrated for the case of silver deposition. By pre-treating the electrode, small silver clusters, not detectable by electrochemical means but their presence are confirmed by TEM, can be formed and act as nucleation centres for the subsequent deposition of silver and amplify the signal obtained from anodic stripping voltammetry of silver. The pre-treated electrode gave a signal which is *at least* three times larger than the bare untreated glassy carbon electrode across the concentration range of 30 nM to 1 µM of silver nitrate. At 300 nM of silver nitrate, there is a 40 fold increase of the peak charge with pre-treated electrode compared to the bare glassy carbon electrode. For silver nitrate concentration equal or below 100nm, no signal is recorded on the untreated electrode. In contrast, an analysable signal is still obtained on the pre-treated electrode.

The strength of this simple strategy lies in the fact that greatest signal enhancement occurs for the lower concentration range. To further lower the detection limit, the deposition time of silver can be extended.

In the next section, the strong silver-halide interaction is utilised as a basis to develop a chloride ion sensor based on silver nanoparticle modified electrode. This sensor can potentially be applied for the preliminary screening of the genetic disease of cystic fibrosis (CF).

6.2 Detection of Chloride Levels in Sweat: A Basis for the Preliminary Screening for Cystic Fibrosis

6.2.1 Introduction

CF is a common genetic disease caused by an autosomal recessive gene known as the cystic fibrosis transmembrane conductance regulator (CFTR) gene.[304] It affects multiple organs including the lungs and the intestines. The defective gene leads to an expression of a non-functional channel protein, leading to irregular transport of sodium and chloride ions across the epithelial cells.[305, 306] In the bronchial tissues, chloride ions are unable to move across the epithelial cells, leading to a high chloride concentration in the mucus in the lungs. CF patients suffer from chronic bacterial lung infection as the salt-sensitive antibodies are inactivated.[307, 308] It is a life-long incurable disease with only symptom alleviation available.[309] A person is diagnosed as a CF patient when one has high sweat chloride content and two genetic mutations of CFTR gene.[309, 310] Since one of the main symptoms for CF is a high level of chloride in sweat, a borderline sweat test is used in hospitals as the primary screening and diagnosis method for CF, along with genetic analysis of CFTR gene as a diagnosis test.[305, 306, 309] For the borderline sweat test, the sweat chloride level is measured and matched against a guideline. The references for sweat chloride levels for adults are categorised into: less than 39 mM (negative), 40 - 59 mM (borderline) and greater than 60 mM (positive). For infants, sweat chloride levels are categorised as: less than 29mM (negative), 30 - 59 mM (borderline) and greater than 60 mM (positive).[310-319] The Cystic Fibrosis Foundation from the USA

recommends a sweat chloride sensor range to be 10 - 160 mM.[315] The Association of Clinical Biochemistry from the UK states that the maximum level of sweat chloride in human is 160 mM.[319, 320]

Current methods for determination of chloride levels include colorimetry, coulometry, indirect/direct ion selective electrodes and manual titration using Schales procedure.[315,319] The Association of Clinical Biochemistry based in UK recommends coulometry out of the various methods available.[319] This method uses argentometry where a standard silver ion solution (e.g. silver nitrate) is used to titrate the chloride ions through the spontaneous formation of silver chloride. The conductivity of excess silver ions is used to determine the end point and hence the chloride level in sweat. Nonetheless, the coulometry equipment faces laboratory constraints. Trained personnel are required to operate the equipment and special buffers are required for selectivity and sensitivity.[321]

Electrochemistry opens up the alternative possibility of having a point-of-care system to detect sweat chloride levels. Ideally, this would involve the use of a low cost and disposable screen printed electrode which has a three electrode system consisting of the working, reference and counter electrode. It has been reported previously that oxidation of silver is sensitive to chloride ion concentration.[322] Here, we use silver nanoparticle modified screen printed electrodes to detect chloride levels in sweat, giving proof-of-concept for a CF screening system. The basis of such a procedure is depicted in Figure 6.8; layers of silver nanoparticles are deposited onto the working electrode of a screen printed electrode and anodically stripped off to generate silver cations. In the absence of chloride ions, the anodic stripping voltammetry of silver nanoparticles yields a single silver oxidation peak. Conversely, in the presence of chloride ions, the favourable conditions of formation of silver chloride causes two stripping peaks to be voltammetrically recorded, one for formation of silver chloride (AgCl (s)) and another for the oxidation of silver to silver ions (Ag^{+}(aq)). Herein, it is demonstrated that the silver chloride peak may be used for the quantitative determination of chloride concentration.[322] Silver nanoparticles are chosen for the experiments as

they provide a facile method for producing a *finite* surface coverage on carbon electrodes which is needed to give the peaked responses. The usage of silver nanoparticles further ensures that the signal for the formation of silver chloride from silver is not dominated by the signal for silver oxidation to silver cations.[63, 322] In the following sections, chloride ion quantification is performed using a silver nanoparticle modified screen printed electrode.

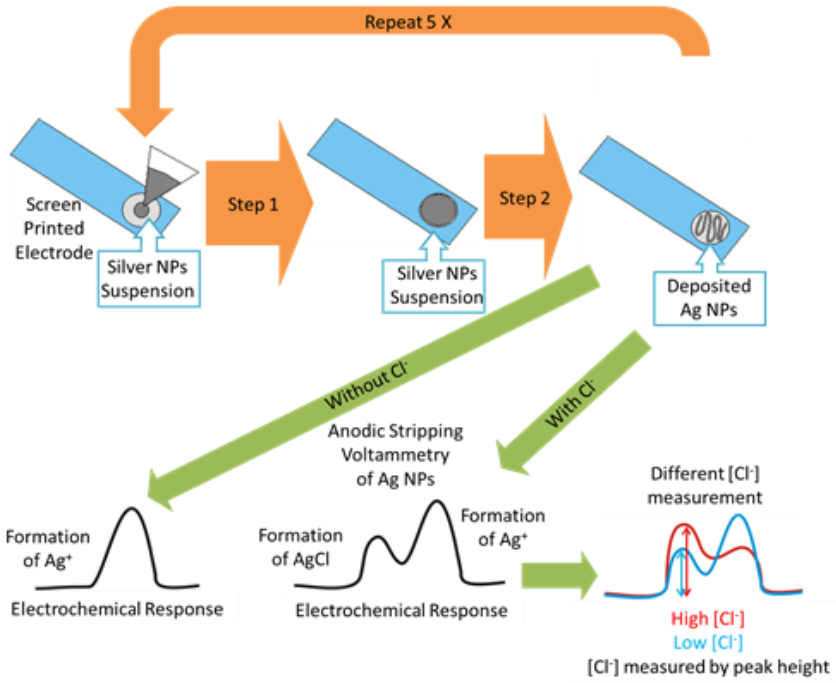

Figure 6.8 Schematic diagram for the preparation and use of the silver nanoparticle modified screen printed electrode and the anodic stripping voltammogram of silver nanoparticles. Step 1: Drop casting of silver nanoparticle suspension onto a screen printed electrode with micropipette. Step 2: Dry electrode in a 50 ^{o}C oven for 12 minutes. The modified electrodes are used for anodic stripping voltammetry in two conditions: in the absence of chloride ions and in the presence of chloride ions. In the presence of different concentration of chloride ions, the peak height of the voltammetric signal at the lower potential increases with increasing chloride concentration.

6.2.2 Experimental

6.2.2.1 Chemicals

Synthetic sweat sample 1 was obtained from Synthetic Urine e.k., Eberdingen, Germany. The solid given was dissolved in water. The solution was tuned to the required pH of 6.5 ± 0.1 with the given ammonia hydroxide solution and 0.1 M nitric acid. The final volume was ensured to be 100 mL.

Synthetic sweat sample 1 had a sodium chloride concentration of 5 g/L, which equates to 85.5 mM of chloride ions in the sample. Synthetic sweat sample 2 was prepared following British Standard (BS 1811-1999). However, a reduced sodium chloride concentration (10% of original value) was used.[323] It was then tuned to pH 6.5 with the same ammonia hydroxide solution and 0.1 M nitric acid used for synthetic sweat sample 1. It contained a sodium chloride concentration of 1.08 g/L, which equates to 18.5 mM of chloride ions present in the sample. The sweat samples were then diluted by a factor of four with sodium nitrate solution (0.133 M). The diluted samples contained a quarter of the original chloride concentration and 0.1 M of sodium nitrate.

6.2.2.2 Silver Nanoparticle Synthesis and Characterisation

Silver nanoparticles capped with citrate were synthesised based on a method devised by Lee and Miesel.[226] Dr. Kristina Tschulik synthesised the nanoparticles and recorded the SEM images. In summary, 25 mL of silver nitrate (0.1 M) solution was added to a flask containing 25 mL of ultrapure water. The solution mixture was heated in a 110 °C oil bath with violent magnetic stirring. 1 g of trisodium citrate was dissolved in 100 mL ultrapure water. 5 mL of the trisodium citrate solution was added into the boiling silver nitrate solution. The solution was left to boil for an hour before it was cooled in a cold water bath. The resulting solution of silver nanoparticle obtained was washed with ultrapure water twice and the supernatant was removed each time. The suspension was centrifuged at 4200 rpm for 27 minutes for each step. The pellet which remained after the second wash from 13.5 mL of unwashed silver nanoparticle suspension was made into a 3 mL washed silver nanoparticle suspension. All glassware was cleaned thoroughly with "piranha" solution (30% hydrogen peroxide solution and concentrated sulphuric acid in 1:3 ratio) prior to the synthesis of silver nanoparticles.

The washed silver nanoparticle suspension was characterised by UV-vis spectroscopy. For the analysis, the washed nanoparticle suspension was diluted by a factor of 30 with ultrapure water. A wavelength scan from 600 nm to 250 nm with a scan rate of 400 nm min^{-1} was run. A broad surface plasmon peak at 419 nm was observed and indicated the presence of silver nanoparticles.

NTA was performed to size the silver nanoparticles in solution-phase. NTA was performed by Dr. Christopher Batchelor-McAuley and Dr. Kristina Tschulik. Figure 6.9 shows the nanoparticle tracking analysis for the sample. The mean diameter of the nanoparticles was 35 ± 12 nm. SEM (LEO Gemini 1530, Zeiss, Oberkochen, Germany) was used to confirm that the synthesized nanoparticles were about 40 nm in diameter (Figure 6.10).

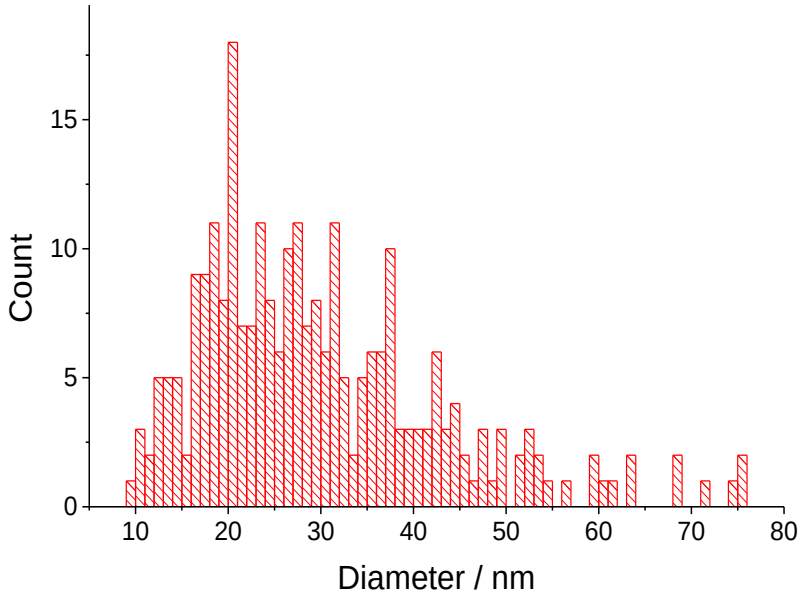

Figure 6.9 Nanoparticle tracking analysis for silver nanoparticles. Mean = 35 ± 12 nm.

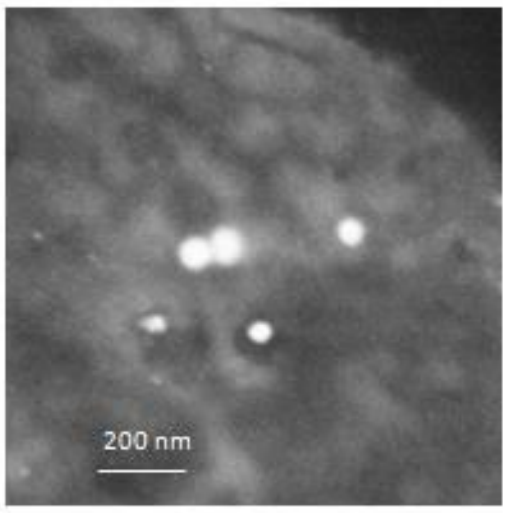

Figure 6.10 SEM image of the synthesised silver nanoparticles.

6.2.2.3 Voltammetry

A glassy carbon electrode was used as the working electrode. A homemade reference electrode of $Ag/AgNO_3$ (10 mM) & $NaNO_3$ (90 mM) was used. Dr. Sven Ernst helped with the fabrication of the homemade reference electrode. It was calibrated against a hexammineruthenium(III) chloride solution (1 mM hexaammineruthenium(III) chloride and 0.1 M sodium nitrate). The redox peaks were found to differ by +0.45 V compared to an experiment with a saturated calomel electrode (SCE) (+0.24 V *vs*. SHE).[17] Thus, the $Ag/AgNO_3$(10 mM) & $NaNO_3$ (90 mM) reference electrode has a potential of +0.69 V *vs*. SHE. The reference electrode consists of a silver wire submerged in a solution of 10 mM silver nitrate and 90 mM sodium nitrate. The silver nitrate/sodium nitrate solution was changed regularly to maintain electrode stability. All experiments were performed under a nitrogen atmosphere and all solutions were degassed thoroughly with nitrogen.

Screen printed electrodes consisted of a 4.0 mm diameter carbon working electrode, a silver pseudo reference electrode and a carbon counter electrode. 50 µL of solution was used to fully cover the electrode. The rest of the experimental details are mentioned in Chapter 3, Section 3.2.

The glassy carbon electrode was polished as detailed in Chapter 3, Section 3.2. Nanoparticle modification of the glassy carbon electrode involved drop casting of 3 µL of washed silver nanoparticle sample onto the clean electrode surface and drying the electrode in an oven at 50 °C for 10 minutes. Five coatings of silver nanoparticles were applied to the glassy carbon electrode. Screen printed electrodes were modified in a similar manner with 5.3 µL of washed silver nanoparticle sample to compensate for the difference in working electrode area. Each coat was dried for 12 minutes in a 50 °C oven. Three repeats were done for each experiment.

6.2.3 Results and Discussion

First, control experiments were performed on glassy carbon electrodes (section 6.2.3.1). Silver nanoparticles were coated onto the glassy carbon electrode and anodic stripping voltammetry was undertaken in sodium nitrate solutions spiked with different concentration of potassium chloride. A linear correlation of the voltammetric peak height and chloride ion concentration is found. In Section

6.2.3.2, analogous experiments were performed on screen printed electrodes and similar correlation between peak height and chloride ion concentration was observed. In Section 6.2.3.3, we repeat measurements and calculations of the sweat chloride levels for two synthetic sweat samples using the calibration plot obtained from the linear correlation of peak height and chloride ion concentration obtained from Section 6.2.3.2.

6.2.3.1 Glassy Carbon Electrode Experiments

Sweat chloride levels are crucial to the diagnosis of CF. Hence, a set of experiments in an electrochemical cell with a silver nanoparticle modified glassy carbon electrode was performed to determine if chloride detection is possible in an electrochemical system. The oxidation of silver nanoparticles to form silver chloride in the presence of chloride ions is the main concept behind this work. Thus, the anodic stripping of silver nanoparticles was performed in a 0.1 M sodium nitrate solution with varied chloride ions concentration to observe silver nanoparticles' behaviour in the presence and absence of chloride ions. Silver nanoparticles were drop cast onto a glassy carbon electrode through five coatings of 3.0 µL of washed silver nanoparticle aliquot. Each of the coatings was dried in an oven at 50 °C for 10 minutes. The modified electrodes were used in cyclic voltammetric experiments, which started at -0.7 V *vs.* $Ag/AgNO_3$ (10 mM) & $NaNO_3$ (90 mM), swept towards +0.4 V before returning back to -0.7 V in a cell filled with 0.1 M sodium nitrate and varying concentration of potassium chloride (2 mM – 40 mM). For every new scan, the electrodes were polished to a mirror finish before silver nanoparticles were drop cast on. Each experiment was repeated for three times. Sodium nitrate was chosen as the electrolyte, as the nitrate ion is a weakly co-ordinating anion. Hence, it does not affect the peak positions as it does not form a strong ionic pair or precipitate with the silver ions. The nitrate ion is also not expected to alter the diffusion coefficient of silver ion or the rate constant for silver oxidation.

To determine the behaviour of silver nanoparticles in the absence of chloride ions, a control experiment was performed. As seen in the green line of Figure 6.11, without the presence of potassium chloride, only a broad peak at around +0.2 V *vs.* $Ag/AgNO_3$(10 mM) & $NaNO_3$ (90 mM)

(peak B) was observed. In the presence of potassium chloride (all the lines in Figure 6.11 except the green line), two broad peaks at around -0.25 V *vs.* $Ag/AgNO_3$(10 mM) & $NaNO_3$ (90 mM) and +0.2 V (peaks A and B) were observed. In the absence of chloride ions, only peak B was observed. Peak B corresponds to the one electron oxidation of metallic silver:[62]

$$Ag\ (s) \rightarrow Ag^+\ (aq) + e^-\ (m) \qquad \text{Equation 6.1}$$

The formal potential of the redox pair of Ag/Ag^+ (Equation 6.1) is +0.80 V *vs.* SHE.[17] Given that the reference electrode had a potential of +0.69 V *vs.* SHE, the oxidation of metallic silver is expected to occur at +0.11 V under the experiment condition. The slight apparent overpotential of +0.1 V observed in experiments can be accounted by the high surface coverage of the silver nanoparticles. At high surface coverages, linear diffusion of silver ions away from the whole geometric surface of electrode surface takes place. Under this diffusion regime, it has been previously shown in Chapter 4, Section 4.1 that the stripping peak potential varies with the silver surface coverage. Since the oxidation of silver to silver cation occurs at +0.11 V under experimental conditions, peak A, which occurs around -0.25 V in presence of potassium chloride, does not account for oxidation of silver to silver cations. We deduce that at peak A, the following reaction occurs:

$$Ag\ (s) + Cl^-(aq) \rightarrow AgCl\ (aq) + e^-\ (m) \qquad \text{Equation 6.2}$$

First, this conclusion is evidenced by the observations in Figure 6.11 inlay. The peak height of peak A correlates linearly with the concentration of chloride ions. Second, the formal potential of the redox couple of Ag/AgCl (Equation 6.2) corrected for the concentration of chloride ions at 20 mM is +0.32 V *vs.* SHE. Given that the formal potential of the Ag/Ag^+ redox couple (Equation 6.1) is +0.80 V *vs.* SHE, peak A and B should have a theoretical potential difference of ~0.48 V; which is close to the experimentally measured difference of 0.45 V.[17] Third, when peak A increases in height, the height of peak B decreases. This indicates that the process at peak A has consumed some of the silver nanoparticles attached to the working electrode, causing less charge to be passed under peak B. Due to the finite surface coverage of silver nanoparticles on the glassy carbon

electrode, at higher chloride concentrations, the peak height no longer correlates linearly with chloride ion concentrations. As observed from the inlay of Figure 6.11, the linear range of the glassy carbon electrode system is between 2 mM and 40 mM of potassium chloride with a sensitivity of 1.64 x 10^{-5} A M^{-1}. The sensitivity of the system should not be affected by the size, the size distribution and the surface density of the silver nanoparticles as long as there is sufficient silver present for the formation of silver chloride and silver ion. In this case, 67.5 nanomoles of silver was deposited on the electrode surface to maintain sensitivity.

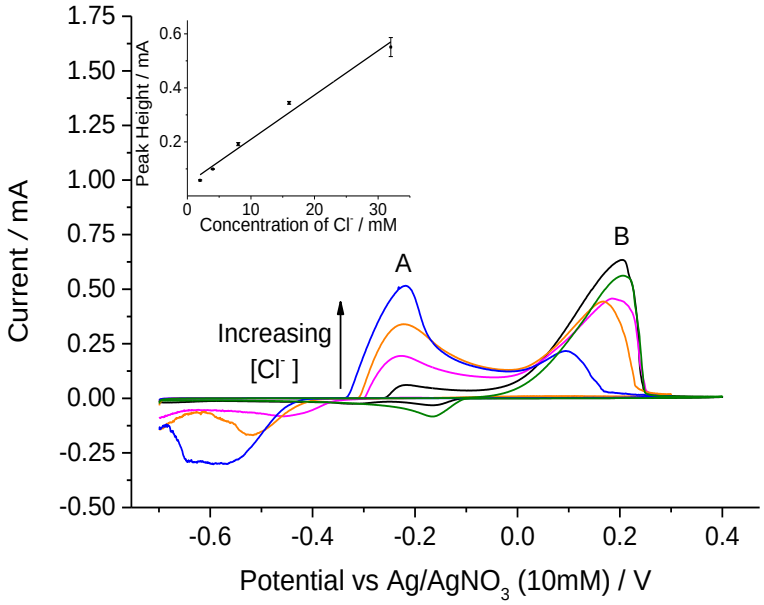

Figure 6.11 The oxidative stripping of silver nanoparticles from a glassy carbon electrode in 0.1 M sodium nitrate spiked with different amount of potassium chloride (KCl) at a scan rate of 0.05 V s^{-1}. Green: No KCl; Black: 2mM KCl; Pink: 8mM KCl; Orange: 16mM KCl; Blue: 32mM KCl. Reference electrode: $Ag/AgNO_3$ (10 mM) & $NaNO_3$ (90 mM) Counter electrode: Platinum mesh; Inlay: Calibration plot of peak height of peak A against the concentration of chloride ions. Each datum point consists of a minimum of 3 repeats.

6.2.3.2 Screen Printed Electrode Experiments

Having developed an electrochemical system capable of determining chloride levels accurately below 40 mM, to achieve the objective of developing a point-of-care sensor, the concept was reinvestigated using disposable screen printed electrodes. The disposable screen printed electrode has a 4.0 mm diameter carbon working electrode, a silver pseudo reference electrode and a carbon counter electrode. In order to achieve comparable surface coverages of silver nanoparticles, each

coat was changed from 3.0 µL to 5.3 µL of washed silver nanoparticle suspension. The five coatings of silver nanoparticles were dried in a 50 °C oven for 12 minutes each. For the voltammetric measurements, 50 µL of analyte solution was used to cover the entire screen printed electrode. The analyte consisted of 0.1 M sodium nitrate and varying concentrations of potassium chloride from 2 mM to 40 mM. Each experiment was repeated for three times. The same trend for peak A and peak B was observed for the measurements done on the screen printed electrodes. The voltammetric signal height of peak A forms a direct linear correlation with concentration of chloride for up to 40 mM with a sensitivity of 1.14×10^{-5} A M^{-1} and the calibration graph has been plotted in Figure 6.12.

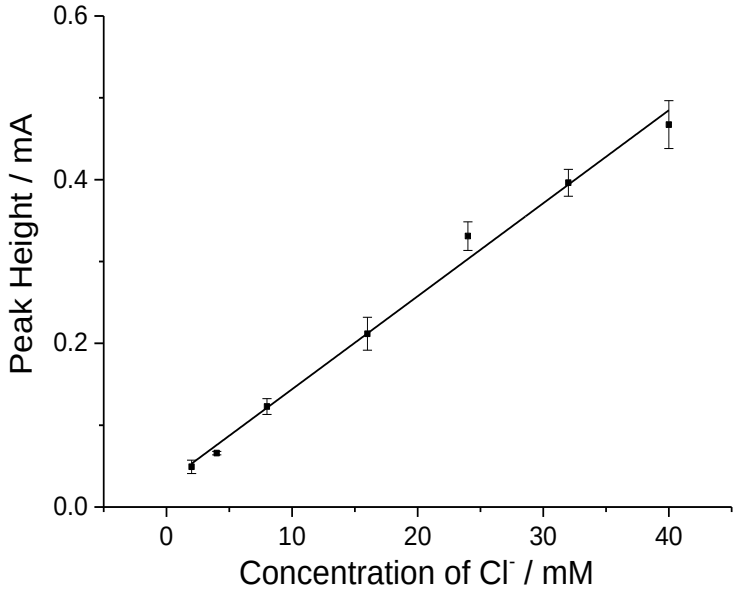

Figure 6.12 The oxidative stripping of silver nanoparticles from a screen printed electrode in 0.1 M sodium nitrate spiked with different amount of potassium chloride at a scan rate of 0.05 V s^{-1}. The peak height of peak A (see Figure 6.11) is plotted against concentration of chloride. Each datum point consists of a minimum of 3 repeats.

6.2.3.3 Synthetic Sweat Sample Analysis

To evaluate the feasibility for a practical CF borderline sweat test, two synthetic sweat samples fulfilling industrial standards were tested against the system. Synthetic sweat is made up of the major components of sodium chloride, lactic acid, urea and ammonium hydroxide while real human sweat contains more minor components such as amino acids, sugar and metals.[324] However, the

minor components should not interfere with the measurements as the concentration of chloride ion is of more than one order of magnitude greater than the minor components.[324] Synthetic sweat sample 1 was prepared in accordance to the German industrial standard (DIN-53160-2). Synthetic sweat sample 2 was prepared from a recipe from the British Standard (BS 1811-1999) but the amount of sodium chloride used was 10% of its original value. This is because the original chloride amount was beyond the 160 mM recommended by authorities and beyond the sensing range of 2 mM to 40 mM.[315, 319, 320] Each sweat sample was diluted with sodium nitrate solution by a factor of four with final concentration of chloride ion being a quarter of the original and the concentration of sodium nitrate being 0.1 M. The dilution of sweat sample by a factor of four ensures that the sensing range of 2 mM to 40 mM of chloride ions complies with the recommended range of 10 mM to 160 mM of chloride ions. Dilution with sodium nitrate solution also brings about advantages of lowering the amount of sweat sample required to 12.5 µL and providing the electrochemical system the essential supporting electrolyte. 50 µL of the diluted synthetic sweat sample is dropped onto the disposable silver nanoparticles modified screen printed electrode.

Cyclic voltammograms were recorded from -0.2 V to +0.8 V *vs.* Ag before sweeping back to -0.2 V. Each experiment was repeated three times. Figure 6.13 shows the voltammograms recorded from the synthetic sweat samples. Similar to the glassy carbon electrode system, 119 nanomoles of silver was deposited onto the disposable screen printed electrode to maintain the sensitivity of the system. By measuring the peak height of peak A in Figure 6.13, the measured concentration of chloride ion in the diluted sweat samples was calculated. The experimentally measured value was 18.9 ± 1.3 mM and 3.9 ± 0.6 mM for diluted synthetic sweat samples 1 and 2 respectively. The expected chloride ion concentrations for diluted synthetic sweat samples 1 and 2 are 21.4 mM and 4.6 mM respectively. Table 6.1 summarises the values of the expected and measured chloride ion concentration. The inlay in Figure 6.13 displays the synthetic sweat samples at the expected chloride concentration. As seen in Figure 6.13 inlay and Table 6.1, the synthetic sweat samples had a slightly lower measured concentration compared to the expected chloride ion concentration. Since the system targets giving patients a pre-screening test, the resolution will not affect the

answers of 'positive', 'borderline' or 'negative'. The system could be employed as a pre-screening test before the hospital tests for the high sweat chloride ion level and two genetic mutations for confirmation of CF.[309, 310]

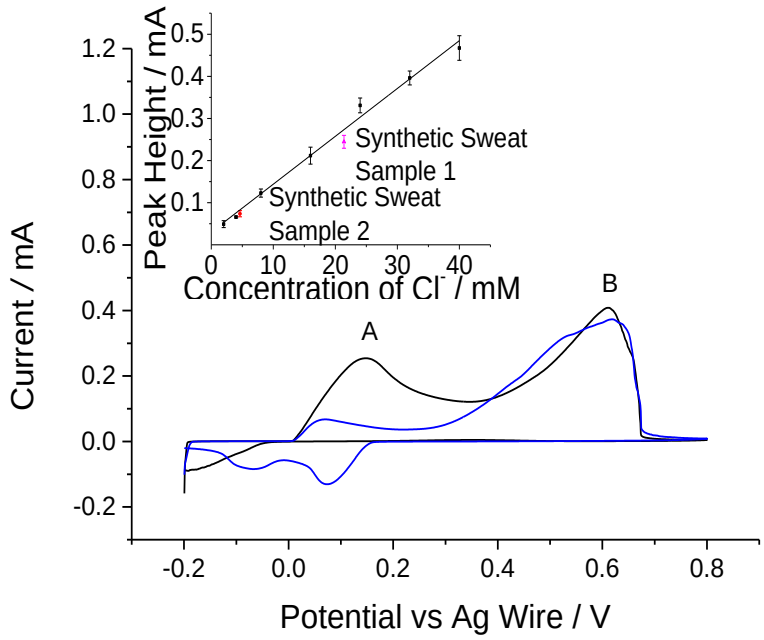

Figure 6.13 The oxidative stripping of silver nanoparticles from a screen printed electrode in 0.1 M sodium nitrate with different synthetic sweat samples (diluted by a factor of 4) at a scan rate of 0.05 V s^{-1}. Black: Synthetic sweat sample 1; Blue: Synthetic sweat sample 2. Inlay: Black line: Calibration plot of peak height of peak A against concentration of chloride from screen printed electrode data; Pink: Diluted synthetic sweat sample 1; Red: Diluted synthetic sweat sample 2. Each datum point consists of three repeats.

	Expected Chloride Concentration/mM		Measured Chloride Concentration/mM
Synthetic Sweat Sample	Undiluted Sample	Diluted Sample	Diluted Sample
1	85.5	21.4	18.9 ± 1.3
2	18.5	4.6	3.9 ± 0.6

Table 6.1 Summary of the expected chloride concentration and the measured chloride concentration of various synthetic sweat samples.

6.2.4 Conclusions

CF is an important and common disease which can be diagnosed in a preliminary manner with sweat chloride levels. Given the sensitivity of oxidised silver nanoparticles towards chloride ions in anodic stripping experiments, the chloride content can be qualified from the analysis of voltammetry peaks. The experiments involving synthetic sweat samples concluded that sweat chloride content determination is possible on screen printed electrodes. The system was found to allow reliable chloride ion quantification in a measurement range from 2 mM to 40 mM of chloride ions. Thus, the dilution of sweat sample by a factor of four allows the recommendation range of 10 mM to 160 mM to be sampled. In conclusion, this section presents a proof-of-concept for a point-of-care system which can be as a screening system for CF.

In the next section, the silver-halide concept used in this section is applied to fabricate an iodide ion sensor. When applied to detect urinary iodide levels, it is capable of indicating iodine deficiency or excess iodine in the body.

6.3 Quantification of Iodide Ions in Synthetic Urine

6.3.1 Introduction

Iodine deficiency can cause goitre, hyperthyroidism, hypothyroidism and intellectual disability.[325-330] The most conventional test is an absorbance based urinary iodine analysis because 90% of iodine is excreted through urine.[86] A spot urine test (collection of a single sample) or a 24 hour urine sample collection can be used for sample collection.[325] The Sandell-Kolthoff reaction, involving iodide ions catalysing the reduction of yellow cerium (IV) ions to the colourless form of cerium (III), is used to determine the iodide ion concentration in urine.[331] After the urine sample is collected, ammonium persulfate is added to oxidise any possible interference species.[332] Then, arsenic acid and cerium ammonium sulphate is added to the sample. The absorbance signal at 420 nm corresponding to the cerium(IV) ion concentration is measured after 30 minutes and then the number is converted into the urinary iodine concentration.[333] The current test requires a toxic, carcinogenic reagent (arsenic

acid, H_3AsO_3) and laboratory handling for synthesis, storage and disposal of the reagents. A simpler and non-toxic approach to iodide ion determination is developed in this section.

In this section, we provide a proof-of-concept for an alternative, simple and robust electrochemical method capable of detecting iodide ion levels in synthetic urine. The targeted iodide concentration range is geared to match the World Health Organisation guidelines in Table 6.2.[333] Thus, the biological relevant iodide concentration in this section is defined as 0.3 µM to 6.0 µM.

Median Urinary Iodine (µg/L)	Corresponding Iodide Concentraton (µM)	Iodine Status
< 20	< 0.32	Severe deficiency
20 – 49	0.32 - 0.77	Moderate deficiency
50 – 99	0.79 - 1.56	Mild deficiency
100 – 199	1.58 - 3.14	Optimal
200 – 299	3.15 - 4.71	More than adequate
≥ 300	≥ 4.73	Excess

Table 6.2 Urinary iodine guidelines for assessing individuals ≥ 6 years old.[333]

The main advantages of the proposed method are that the chemicals required in this method are non-toxic and the sample can be processed within a few minutes. The concept behind this present method is the ready formation of silver iodide by oxidation of silver in presence of iodide ions. The iodide sensor is illustrated as a schematic diagram in Figure 6.14. The test proposed works as follows, a clean glassy carbon electrode was drop cast with silver nanoparticles and dried under nitrogen atmosphere. The modified electrode was exposed to electrolyte spiked with iodide ions and cyclic voltammetry was performed. In the absence of iodide ions, no signal was observed. In the presence of iodide ions, two signals were recorded. Peak I corresponded to the oxidation of silver to silver iodide. The reduction signal of silver iodide is represented by peak II and its peak height was used to derive a calibration curve for the iodide concentration. From there, the unknown iodide concentrations in urine can be determined. In the present method, it is crucial that silver nanoparticles are used instead of a bulk silver electrode. The large surface area present allows the

pre-concentration of silver iodide on the surface. Using the linear relationship between the reduction peak height and iodide concentration, this system holds great potential for further development into a point-of-care system for urinary iodine detection.

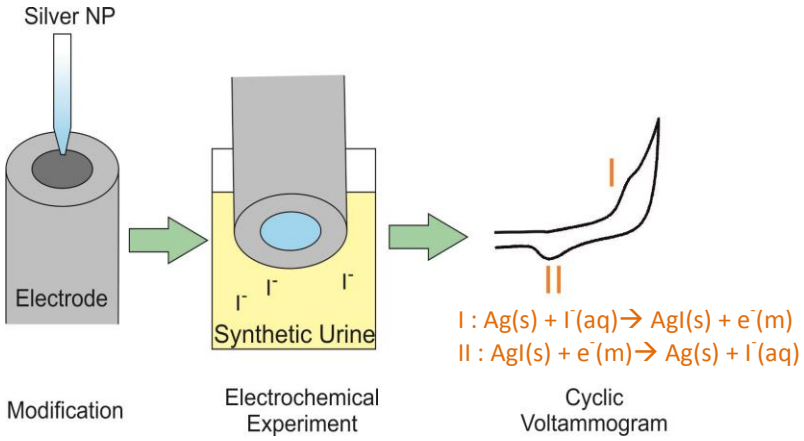

Figure 6.14 Schematic diagram of silver nanoparticle based iodide sensor.

6.3.2 Experimental

6.3.2.1 Chemicals

Synthetic urine was obtained from Synthetic Urine e.k., Eberdingen, Germany and used as received. The synthetic urine received adheres to the standards of DIN EN 1616. It contains 0.2 M of chloride ions and no iodide ions.

6.3.2.2 Voltammetry

A glassy carbon electrode was used as the working electrode. For chloride-free experiments, a MSE was used as a reference electrode. For the synthetic urine experiments, a SCE was used as a reference electrode. All solutions were thoroughly degassed with nitrogen prior to the experiments. The other experimental details can be found in Chapter 3, Section 3.2.

6.3.2.3 Nanoparticle Synthesis and Characterisation

The silver nanoparticles used are capped with citrate and synthesized using the method developed by Wan *et al.*[302] They have been fully characterised in a previous paper as Batch II by Lees *et al.*[164] The silver nanoparticle suspension has a total silver concentration of 3.1 mM and they were sized

by SEM to be 13.6 ± 3.7 nm in radii. The nanoparticles are synthesised together with Ms. Jessica C. Lees.

6.3.2.4 Detection Procedures

A freshly prepared silver nanoparticle modified electrode was used for electrochemical experiments. The modification was performed by diluting the synthesized silver nanoparticle suspension with ultrapure water by a factor of 100 to ensure the diluted suspension contained 31 μM of silver. The glassy carbon electrode was polished with the procedure in Chapter 3, Section 3.2. 3 μL of the diluted nanoparticle suspension was drop cast onto a glassy carbon electrode and dried under a nitrogen flow. The dried electrode was used immediately. The concentrations of potassium iodide (KI) tested were 0.3 μM, 0.8 μM, 1.6 μM, 3.2 μM, 4.7 μM and 6.0 μM. The solutions were all degassed with nitrogen before the start of the experiments.

6.3.2.4.1 Detection Procedures in Sodium Nitrate

0.3 μM to 6.0 μM of KI were made up by dissolving different amounts of KI in 0.1 M sodium nitrate. The scan rate was 10 mV s^{-1} and a MSE was used as a reference electrode to maintain the chloride-free environment to circumvent the possible interferences from other halides. The voltammetric scan started by scanning oxidatively from -0.6 V to -0.2 V and back to -0.7 V *vs*. MSE.

6.3.2.4.2 Detection Procedures in Synthetic Urine

Different amounts of KI were dissolved in synthetic urine to make up the range from 0.3 μM to 6.0 μM. They were used as the electrolyte for the electrochemical experiments. A SCE reference electrode was used. The cyclic voltammetric scan started from -0.2 V to +0.045 V and then back to -0.3 V *vs*. SCE at 5 mV s^{-1}.

6.3.2.4.3 Detection Procedures for Standard Addition

A synthetic urine sample containing 0.2 μM of KI was separated into portions and an additional 0.5 μM, 1.0 μM and 1.5 μM of KI were spiked in the separate sample portions. Then, a freshly prepared silver nanoparticle modified electrode was used to perform the cyclic voltammetry which started from -0.2 V to +0.045 V and back to -0.3 V *vs*. SCE at 5 mV s^{-1}.

6.3.3 Results and Discussion

Herein, the detection of iodide ions using a silver nanoparticle modified electrode is reported. The diluted silver nanoparticle suspension was drop cast onto a polished glassy carbon electrode, dried under a nitrogen atmosphere and used to record a cyclic voltammogram in a degassed electrolyte containing iodide ions. An oxidative peak was observed for the oxidation of silver to silver iodide and a reductive peak was observed for the reverse reaction. The peak height of the latter was used to establish a calibration curve to measure the iodide concentration.

One important factor to be considered in this system is the presence of chloride ions. The formation of silver iodide is thermodynamically favoured compared to the formation of silver(I) ions. Therefore, the oxidation to silver iodide occurs at a lower potential compared to the oxidation to silver(I) ions. In Section 6.2, this concept has also been applied to chloride detection. The thermodynamically favoured formation of silver chloride also decreases the oxidation peak potential. Therefore, the iodide sensor was first tested in a chloride-free environment to prevent the possible interference from chloride ions (Section 6.3.3.1). Nonetheless, the ultimate aim was to detect iodide ions in synthetic urine and synthetic urine contains 0.2 M of chloride ions. The redox potentials for the formation of silver chloride and silver iodide both depend greatly upon of the halide ion concentrations. In the presence of 0.2 M of chloride ions, the oxidation signal for the formation of silver iodide, at the medically relevant iodide concentrations, occurs at a lower potential than the silver-silver chloride redox couple. Thus, the potential window was optimised to stop before the bulk formation of silver chloride (Section 6.3.3.2). Hence, it is possible to detect the iodide ions in the presence of chloride ions. In Section 6.3.3.3, the measurement of a low iodide concentration was attempted through the standard addition method.

6.3.3.1 Iodide Calibration in Sodium Nitrate

Figure 6.15 shows the close up of the voltammograms for silver nanoparticle oxidation in the presence of different concentrations of KI. In the absence of KI (dashed grey line in Figure 6.15), no

voltammetric peak was observed. In the presence of KI, an anodic peak occurred between -0.3 V to -0.4 V and it corresponds to the oxidation of silver to silver iodide.

$$Ag\ (s) + I^-\ (aq) \rightarrow AgI\ (s) + e^-\ (m) \qquad \text{Equation 6.3}$$

A reduction signal occurred between -0.4 V to -0.55 V in the presence of KI and it is accounted by the reduction of the previously formed silver iodide to silver.

$$AgI\ (s) + e^-\ (m) \rightarrow Ag\ (s) + I^-\ (aq) \qquad \text{Equation 6.4}$$

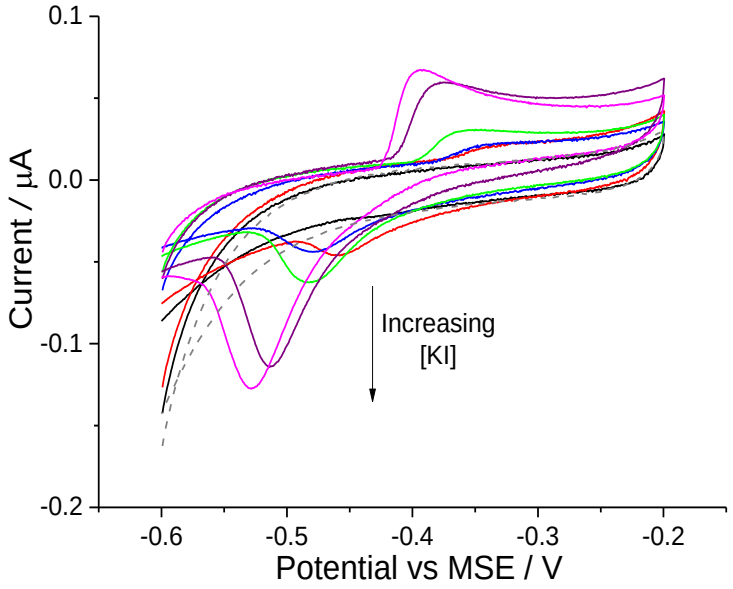

Figure 6.15 The oxidation of silver nanoparticles on a glassy carbon electrode in 0.1 M sodium nitrate spiked with different concentrations of KI at a scan rate of 10 mV s^{-1}. Grey dashed: No KI; Black: 0.3 µM KI; Red: 0.8 µM KI; Blue: 1.6 µM KI; Green: 3.2 µM KI; Purple: 4.7 µM KI; Pink: 6.0 µM KI.

Both the oxidation and reduction signal correlate linearly with the concentration of KI present. The reduction signal has a larger peak height as it is a surface bound wave and reflects the quantity of silver iodide present. Thus, the peak height of the reduction signal was plotted against the concentration of KI in Figure 6.16 to achieve a greater sensitivity. The experiment at each individual KI concentration was repeated for at least three times with a freshly prepared silver nanoparticle modified electrode (Section 6.3.2.4) to determine a standard deviation. A linear relationship was found, giving a slope of 1.46 x 10^{-2} A M^{-1} and a R^2 (coefficient of determination) value of 0.999.

The R^2 is a value between 0 and 1 and a high number indicates a good correlation between the data points and the trend. The linear relationship is determined to be:

$$[I^-]=(m_1)(I_p)+C_1 \qquad \text{Equation 6.5}$$

where $[I^-]$ is concentration of iodide ions (mol dm^{-3}), m_1 is the gradient of 1.46 x 10^{-2} A mol^{-1} dm^3, I_p is the peak height (A) and C_1 is the intercept of -2.7 x 10^{-9} mol dm^{-3}.

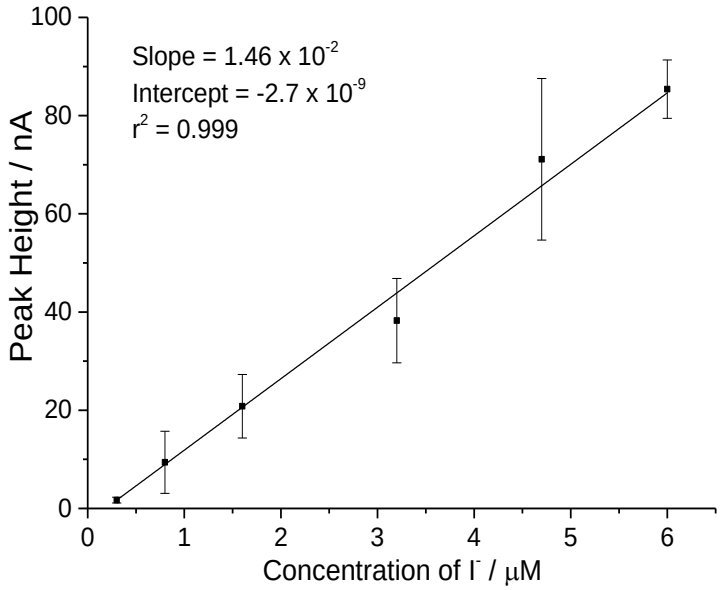

Figure 6.16 Calibration plot of reduction peak height against the concentration of KI in 0.1 M sodium nitrate. Each datum point consists of a minimum of 3 repeats.

6.3.3.2 Iodide Calibration in Synthetic Urine

The analytical system introduced in Section 6.3.3.1 was further optimised to determine the iodide ions concentration in synthetic urine. The synthetic urine supplied contains 0.2 M of chloride ions. The synthetic urine sample did not contain iodide ions and iodine. Hence, the same range of KI as in Section 6.3.3.1 (0.3 μM to 6.0 μM) was spiked into the synthetic urine. No additional supporting electrolyte was added. Due to the presence of chloride ions, the reference electrode was changed from a MSE to a SCE. It is known that silver nanoparticles oxidise to silver chloride in the presence of chloride ions.[334] The large signal which arises from the formation of silver chloride might dominate the signal of interest. The solubility product of silver iodide and silver chloride at 25 °C are

1.5 x 10^{-16} mol^2 dm^{-6} and 1.6 x 10^{-10} mol^2 dm^{-6} respectively.[17] The stronger affinity of iodide to silver causes the oxidation of silver to silver iodide to occur at a lower potential compared to the oxidation of silver chloride. Hence, cyclic voltammetry was performed by sweeping oxidatively from -0.2 V to +0.045 V and then back to -0.3 V *vs.* SCE to limit the potential window so as to exclude potential at which silver chloride is formed.[d] No signal of interest was detected for 0.3 µM KI when the system was applied in synthetic urine. Neither the oxidation of silver to silver iodide nor the reduction of silver iodide was seen. Only the initial onset of the oxidation of silver to silver chloride was observed. Therefore, the scan rate was reduced from 10 mV s^{-1} to 5 mV s^{-1} to ensure that the signal of interest was observed across the entire concentration range of interest. The optimised detection procedure is summarised in Section 6.3.2.4 and Section 6.3.2.4.2. Performing the experiments with the optimised system, the close-up of the voltammograms recorded with different concentrations of iodide ions are depicted in Figure 6.17. It can be seen that the oxidation of silver to silver iodide at -0.02 V to +0.045 V *vs.* SCE occurred on the steep slope which was the start of a large oxidation signal of silver to silver chloride. The peak of interest now occurred as a reductive signal between 0 V to -0.15 V *vs.* SCE. The peak height of the signal was plotted against the concentration of KI in Figure 6.18 and a linear calibration curve was obtained. A slope of 3.58 x 10^{-3} A M^{-1} was measured and a R^2 value of 0.942 was obtained. The linear relationship is determined to be:

$$[I^-]=(m_2)(i_p)+C_2 \qquad \text{Equation 6.6}$$

where $[I^-]$ is the concentration of iodide ions (mol dm^{-3}), m_2 is the gradient of 3.58 x 10^{-3} A mol^{-1} dm^3, I_p is the peak height (A) and C_2 is the intercept of 1.1 x 10^{-8} mol dm^{-3}. This showed that silver nanoparticles can be employed to detect iodide ions in synthetic urine.

[d] The corresponding potential window *vs.* MSE is -0.58 V to -0.335 V to -0.68 V.

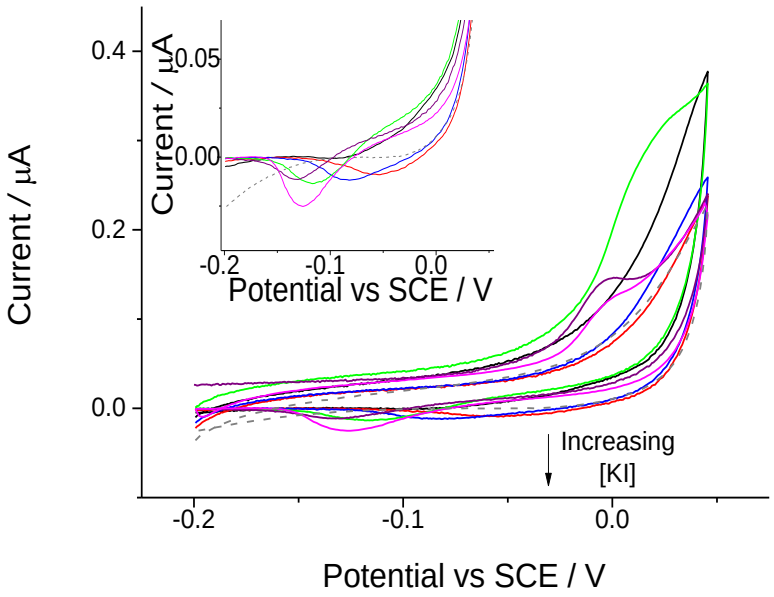

Figure 6.17 The oxidation of silver nanoparticles on a glassy carbon electrode in synthetic urine spiked with different concentrations of KI at a scan rate of 5 mV s^{-1}. Grey dashed: No KI; Black: 0.3 µM KI; Red: 0.8 µM KI; Blue: 1.6 µM KI; Green: 3.2 µM KI; Purple: 4.7 µM KI; Pink: 6 µM KI. Inlay: a further close up of the reduction signal of interest at different concentrations of KI.

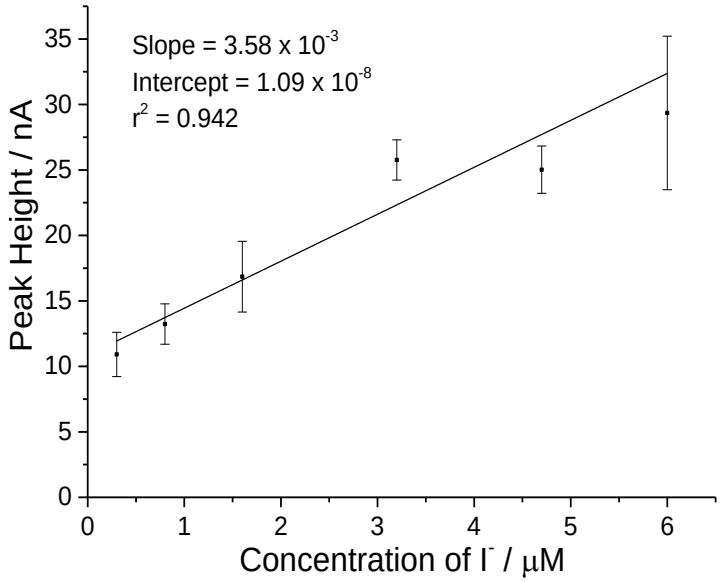

Figure 6.18 Calibration plot of peak height against the concentration of KI in synthetic urine. Each datum point consists of a minimum of 3 repeats.

6.3.3.3 Application of the Standard Addition Method

To further validate this method, the standard addition method was used on a sample of synthetic urine containing (spiked with) 0.2 µM of KI. This particularly low concentration was chosen as it is challenging to measure very low iodide concentrations. The chosen method of standard addition refers to the addition of known concentrations of analyte to deduce the unknown amount of analyte present in the sample.[335] Here, a synthetic urine sample containing 0.2 µM of KI was separated into portions and an additional 0.5 µM, 1.0 µM and 1.5 µM of KI were spiked in the separate sample portions. The optimised system in Section 6.3.3.2 was used to measure the concentration of iodide ions in the spiked samples. The iodide concentration measured was derived from the calibration Equation 6.6 obtained in Section 6.3.3.2 Instead of the traditional standard addition plot where the measured signal is plotted against the KI concentration added, in Figure 6.19, the concentration measured was plotted against added concentration. This is because the calibration plot in Figure 6.18 has a non-zero intercept and this is attributed to the underlying electrochemical reduction of silver chloride formed. It is seen that the results of this standard addition test deemed the urine sample to contain 0.29 ± 0.11 µM. This is a good estimate as the actual KI concentration in the urine sample is 0.2 µM.

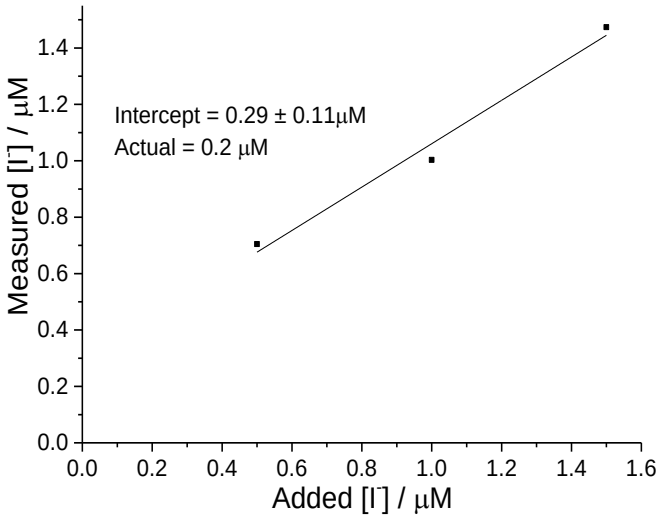

Figure 6.19 Standard addition plot to determine the concentration of iodide in synthetic urine. Calculations are based on the calibration graph in synthetic urine in Equation 6.6.

6.3.4 Conclusions

The measurement of urinary iodine concentration is a key indicator of the health of the thyroid. Both excess and insufficient iodine in the body can lead to swelling of the thyroid. Hyperactivity or hypoactivity of the gland is also possible. Although the urine samples are easily obtainable, the standard assessment based on Sandell-Kolthoff reaction requires a carcinogenic reagent and a thirty minutes incubation before an UV-vis absorbance measurement. In this section, the silver nanoparticle modified electrode used is capable of detecting the biologically relevant iodide range of 0.3 μM to 6.0 μM in the synthetic urine. Moreover, the sample processing time is reduced to a few minutes. In samples with very low iodide concentration, standard addition can be performed to determine the urinary iodide concentration. Therefore, this system is capable of detecting the iodide concentration in urine. To utilise this sensor for urinary iodine test, a reducing agent can be added to convert the iodine in urine. This in turn allows to the distinguishing of the various iodine statuses (deficiency, optimal or excess) in individuals in a reliable and non-toxic manner.

Therefore, in this chapter, the approach which silver nanoparticles can be used as electrochemical sensors is discussed. The anodic stripping voltammetry signal can be enhanced by leaving behind small silver nuclei via pre-treatment to bypass the nucleation stage. The favourable formation of silver halide complexes allowed the use of silver nanoparticle modified electrode to detect chloride and iodide ions as a point-of-care system. This resulted in a pre-screening system for the genetic disease, CF, and the determination of the one's iodine status in the body. With the silver-halide interaction in mind, in the next chapter, we look at another class of molecules, thiols, which also have a strong interaction with silver.

Chapter 7 Interactions between Silver Nanoparticles and Thiols: A Comparison of Mercaptohexanol against Cysteine

Chapter 6, Sections 6.2 and 6.3 showed that the interaction of halides with silver has a huge impact on the electrochemical oxidation of the silver nanoparticles. Herein, we look at the influence of thiol on silver nanoparticles oxidation. UV-visible (UV-vis) spectra were also recorded to deduce the nature of silver-thiol interactions. This work was performed in collaboration with Dr. Christopher Batchelor-McAuley and Dr. Kristina Tschulik who also helped with the scientific interpretation of the experimental results. The silver nanoparticles were synthesised together with Ms. Jessica C. Lees. This work has been published in Science China: Chemistry.[336]

7.1 Introduction

Silver exists as silver metal and silver ions of different oxidation states of +1, +2, +3 and +4.[337] The most common states of silver are silver(0) metal and silver(I) ion and both of them interact with thiols in their own complex manner. A well-known reaction of silver metal is the tarnishing of silverware to form silver(I) sulphide. It was discovered in 1930 that apart from the presence of hydrogen sulphide gas, oxygen is also required in this reaction:[338, 339]

$$4Ag\ (s) + 2H_2S\ (g) + O_2(g) \rightarrow 2Ag_2S\ (s) + 2H_2O\ (g) \qquad \text{Equation 7.1}$$

The role of oxygen varies from the intermediate formation of silver(I) oxide to being the hydrogen acceptor to form water or hydroxide ions.[338, 339] The overall reaction of silver tarnishing forms the product silver sulphide (Ag_2S) but there are case specific mechanisms depending on conditions such as pH, oxygen level, ultraviolet light presence and moisture levels.[338-340]

Silver(I) ion complexes with both inorganic and organic thiols with no redox reaction involved. With inorganic thiols like HS^- and S^{2-}, it is possible to form many species such as AgSH, $[Ag(SH)_2]^-$ and $[Ag_2(SH)_2S]^{2-}$ depending on the concentration of the anions present.[341] With organic thiols, silver(I) ion forms the thermodynamically favourable complex of silver(I) thiolate (AgSR) with log K_f ~ 13

$mol^2\ dm^{-6}$.[341] Silver(I) thiolate compounds, depending on the substituent group, are able to form polymer chains with various structures and formulas. A linear chain polymer is favoured with linear substituent groups while a double helix-like structure is favoured with bulky side groups.[341, 342] For cysteine and glutathione, they form polymers with various silver to thiol ratios.[343]

It is known that silver nanoparticle properties differ from those of the bulk metal and thus the interaction between silver nanoparticles and thiols may vary from bulk silver and silver(I) ions.[72, 78, 340, 344] Silver nanoparticles have been widely utilised to exploit their novel properties (e.g. anti-bacterial properties,[80, 345, 346] catalysis[57, 58, 347] and biosensing[348-350]) and their possible risks (e.g. toxicity[351] and possible cancer risk[352, 353]) have been researched extensively. With thiols, silver nanoparticles have been proposed to form various types of compounds with different structures.[354-356] One of the plausible reaction routes suggested for organothiols is: [354, 355]

$$4RSH\ (l) + 4Ag\ (s) + O_2(g) \rightarrow 4AgSR\ (s) + 2H_2O\ (g) \qquad \text{Equation 7.2}$$

It has been shown that with organothiols, AgSR remained on the surface, forming a shell, as evidenced by SEM.[354] Battocchio *et al.* suggested a shell of more than one species of silver thiolates – a mix of AgSR and Ag_2S-like complexes, were formed when organothiols were added during silver nanoparticle synthesis.[356] In the typical environmental setting with plenty of oxygen, moisture and naturally existing thiols, given sufficient time, the final product of redox reaction of silver nanoparticles and thiols in the environment is speculated to be Ag_2S with many possible intermediates such as AgSR.[339, 341, 354, 355] Utilising the silver sulphide concept, water treatment plants have been proposed to make use of the naturally occurring thiols to transform silver nanoparticles into a harmless version of silver sulphide (Ag_2S) to combat the possible toxicity concerns brought by silver nanoparticles.[357, 358] An important question that has to be answered is: Do the naturally existing thiols have the capability to convert silver nanoparticles into a final product of silver sulphide?

Beyond studying the basic interaction between silver nanoparticles and thiols, many analytical sensors have exploited the strong silver-thiol affinity. UV-vis spectroscopy, fluorescence studies

and electrochemical studies have all been employed as methods to monitor levels of cysteine, glutathione and silver nanoparticles.[142, 344, 348-350, 359] Apart from for detection purposes, cysteine and glutathione have also been employed as a capping agent for silver nanoparticles to prevent aggregation.[360, 361] At alkaline pH, the negatively charged carboxylic group keeps the cysteine capped silver nanoparticles apart and hence stabilises them. However, in mildly acidic pH, when both the carboxylic acid and amino group are charged, they interact electrostatically, causing the silver nanoparticles to aggregate.[360]

As highlighted above, the reaction between silver nanoparticles and thiols is complicated. In the formation of polymeric silver(I) thiolates from silver(I) ions and thiols, the effect of the substituent groups is evident.[341-343] It may be anticipated that silver nanoparticles show different behaviour or interaction with different thiols. With the possibility of many products like Ag_2S and AgSR and the complex kinetics and solubility constants that are involved, the question arises as to whether there is a general mechanism for silver-thiol interactions which can be applied or if each thiol needs to be considered individually? Given that the interaction between silver nanoparticle and thiols is a redox reaction, electrochemical methods are naturally employed in the present work to determine if a general mechanism of silver-thiol interaction exists. UV-vis spectroscopy was also used in this study of silver nanoparticles to further support the electrochemical observations. Two different thiols are chosen to determine if they react in a similar way with silver nanoparticles. Mercaptohexanol is chosen as a model compound; its basic structure consists simply of a thiol group (-SH) and a hydroxyl group (-OH). The simple structure of this compound allows the study of the effect of thiol groups on silver and circumvents possible effect of other functional groups. In addition, cysteine is chosen as an analyte with strong biological importance. It acts as an antioxidant and a precursor to peptides like glutathione.[362, 363] The considerable difference between mercaptohexanol and cysteine in terms of silver-thiol interactions is explained in this chapter through electrochemical experiments and UV-vis studies. The voltammograms ascertain the changes in the ease and extent of oxidation of silver nanoparticles to silver(I) ions whilst the UV-vis

spectra examine the changes in the nanoparticles' surface properties. Through this, a comparative view of silver-thiol interaction for mercaptohexanol and cysteine is presented.

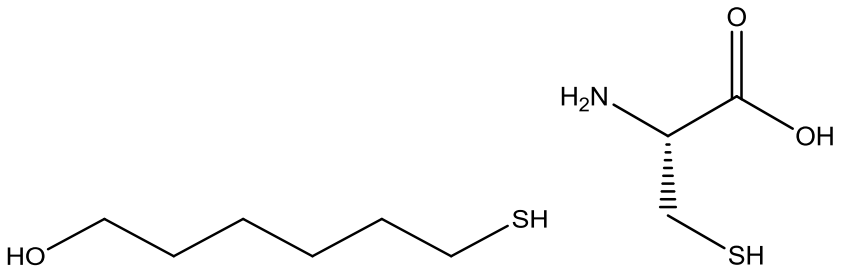

Figure 7.1 The chemical structures of mercaptohexanol and L-cysteine.

7.2 Experimental

7.2.1 Chemicals

All solutions were degassed with nitrogen for 15 minutes thoroughly for both electrochemical and UV-vis spectroscopy experiments.

7.2.2 Nanoparticle Synthesis and Characterisation

Silver nanoparticles capped with citrate were synthesised using the method developed by Wan *et al.*[302] Two different batches of silver nanoparticles were synthesized and the smaller nanoparticles had a total silver concentration of 1.0 mM in the suspension and were sized as having radii of 4.7 ± 1.8 nm by transmission electron microscope (TEM) as reported in Chapter 6, Section 6.1. The bigger nanoparticles were synthesized through seeded growth synthesis. They had a total silver concentration of 3.1 mM in the suspension and were sized by scanning electron microscope (SEM) as 13.6 ± 3.7 nm in radii.[164] The bigger nanoparticles were synthesised together with Ms. Jessica C. Lees. All glassware were cleaned thoroughly with aqua regia (a mixture of concentrated hydrochloric acid and concentrated nitric acid in 3:1 ratio) prior to silver nanoparticle synthesis.

In summary, to synthesis the smaller batch of silver nanoparticles, 20 mL of 1% (w/v) trisodium citrate solution and 75 mL of ultrapure water was heated to 70 °C for 15 minutes. 1.7 mL of 1% (w/v) silver nitrate solution and 2 mL of freshly prepared 0.1% (w/v) sodium borohydride were

added in quick succession to the heated solution. The mixture was stirred vigorously for another hour at 70 °C. After cooling to room temperature, ultrapure water was added to make the final volume of the nanoparticle suspension 100 mL. A clear yellow suspension of silver nanoparticles with a total silver concentration of 1 mM was obtained.

The silver nanoparticles with radii 13.6 ± 3.7 nm was synthesised in a two step reaction. First, 80 mL of ultrapure water and 2 mL of 1% citrate solution were boiled for 10 minutes. Then, 10 mL of nanoparticle suspension of radii 4.7 ± 1.8 nm, following by 1.7 mL of 1% (w/v) silver nitrate solution was added. The mixture was stirred and refluxed for one hour before cooling to room temperature. Ultrapure water was added to make the final volume of nanoparticle suspension 100 mL. Next, 2 mL of 1% (w/v) trisodium citrate solution and 75 mL of ultrapure water was boiled for 15 minutes. Then, 10 mL of the nanoparticle suspension obtained in the previous step and 1.7 mL of 1% (w/v) silver nitrate solution was added to the mixture. Vigorous stirring and reflux was maintained for 1 hour before another 1.7 mL of 1% (w/v) silver nitrate solution and 2 mL of 1% (w/v) trisodium citrate solution was added. Both stirring and reflux was maintained for another hour. A further 1.7 mL of 1% (w/v) silver nitrate solution and 2 mL of 1% (w/v) trisodium citrate solution was added and after another hour of reflux and stirring, the mixture was cooled to room temperature. Ultrapure water was added to bring the volume up to 100 mL to give the nanoparticle suspension.

7.2.3 Voltammetry

A glassy carbon electrode and a mercury/mercurous sulphate electrode (MSE) were used as a part of the three electrode system. The rest of the details with regards to voltammetry can be found in Chapter 3, Section 3.2.

7.2.4 Silver Nanoparticle modified Electrode

The silver nanoparticle suspensions of particles of radii 4.7 ± 1.8 nm and 13.6 ± 3.7 nm were diluted with ultrapure water by a factor of 10 and 31 respectively to ensure the diluted samples contain a total concentration of 0.1 mM of silver. 3 µL of the diluted nanoparticle suspension was

drop cast onto the glassy carbon electrode and dried under a nitrogen flow. The electrode after drying was used immediately for electrochemical experiments. A cyclic voltammetry was swept starting from -0.3 V *vs.* MSE to +0.5 V and then reductively to -1.8 V *vs.* MSE to perform the electrochemical experiments.

7.2.5 UV-vis Spectroscopy

UV-vis spectroscopy was performed using a spectrometer with a wavelength scan from 700 nm to 250 nm at a scan rate of 400 nm min^{-1}. For UV-vis analysis, the nanoparticle suspensions of radii 4.7 ± 1.8 nm and 13.6 ± 3.7 nm were diluted by a factor of 24 and 48 with ultrapure water respectively to obtain absorbance in the analytically meaningful range of below 1.

7.3 Results and Discussion

Herein, the electrochemical and UV-vis spectroscopic results of the interaction between silver nanoparticles and thiols are summarised. First, all the experimental data for mercaptohexanol is summarised, the observations were grouped and explained using a hypothesised silver-mercaptohexanol interaction. Next, the experiments performed with cysteine are tabulated and the observation were also categorised and interpretated with a possible silver-cysteine interaction mechanism. Lastly, the changes in silver nanoparticle oxidation and the silver nanoparticle surface plasmon peaks in presence of mercaptohexanol and cysteine are compared and contrasted.

7.3.1 Mercaptohexanol

7.3.1.1 Electrochemical Oxidation of Silver Nanoparticles in the Presence of Mercaptohexanol

A silver nanoparticle modified glassy carbon electrode was electrochemically oxidised In the presence of the model compound mercaptohexanol. Cyclic voltammetry was performed by sweeping oxidatively from -0.3 V *vs.* MSE with a degassed electrolyte containing mercaptohexanol and 0.1 M sodium nitrate at a scan rate of 0.05 V s^{-1}. Two batches of silver nanoparticles, measuring 4.7 ± 1.8 nm and 13.6 ± 3.7 nm respectively, were studied. In order to study the silver-

thiol interaction, two different sets of experiments were performed. In the first set of experiments, the modified electrode was electrochemically oxidised *immediately* after the exposure to the electrolyte containing different concentrations of mercaptohexanol ranging from 1 – 100 µM. In the second set of experiments, the modified electrode was electrochemically oxidised *after* soaking in the mercaptohexanol containing electrolyte for a period ranging from 5 minutes to 16 hours.

In Figure 7.2, cyclic voltammograms of silver oxidation for the nanoparticles of radii of 13.6 ± 3.7 nm with increasing mercaptohexanol concentrations are presented. In the absence of mercaptohexanol, as depicted by the black dashed line in Figure 7.2, the silver nanoparticles bound to the working electrode were oxidised to silver(I) ion to give a signal at +0.05 V *vs*. MSE. In the presence of mercaptohexanol, the potential shifted positively from 0 V *vs*. MSE to +0.2 V *vs*. MSE depending of mercaptohexanol concentration. An analogous set of experiments was performed with the smaller nanoparticles (radii = 4.7 ± 1.8 nm) and the voltammogram are shown in Figure 7.3; the increase in potential of the signal was also observed for these smaller nanoparticles. The oxidative charge measured under the voltammetric signals can be related to the amount of metallic silver present on the electrode as described by Faraday's law. The total oxidative charge under the voltammetric peaks for both batches of nanoparticles was measured and tabulated against the mercaptohexanol concentrations in Figure 7.4. As seen, the oxidative charges decreased when mercaptohexanol was added to the electrolyte. Thus, the amount of metallic silver available for electrochemical oxidation decreased in the presence of mercaptohexanol. Moreover, the nanoparticle batches both showed an inverse relationship between mercaptohexanol concentration and peak area. With increasing mercaptohexanol concentrations, the single oxidation signal split into two. As seen in Figure 7.2 and Figure 7.3, the second oxidation signal at +0.2 V *vs*. MSE grew in dominance as the concentration of mercaptohexanol increased.

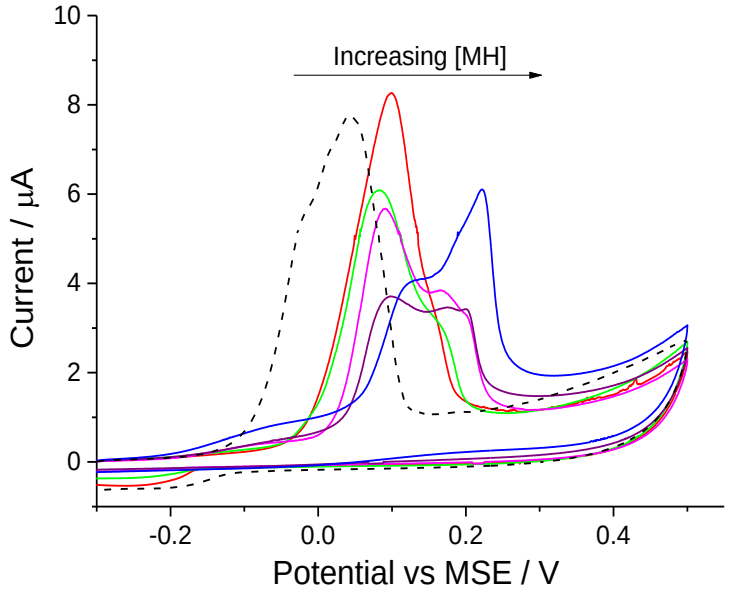

Figure 7.2 The oxidative stripping of silver nanoparticles with radii of 13.6 ± 3.7 nm from a glassy carbon electrode in 0.1 M sodium nitrate spiked with varying concentrations of mercaptohexanol measured at a scan rate of 0.05 V s^{-1}. Black dashed line: No mercaptohexanol; Red: 10 µM; Green: 25 µM; Pink: 50 µM; Purple: 75 µM; Blue: 100 µM.

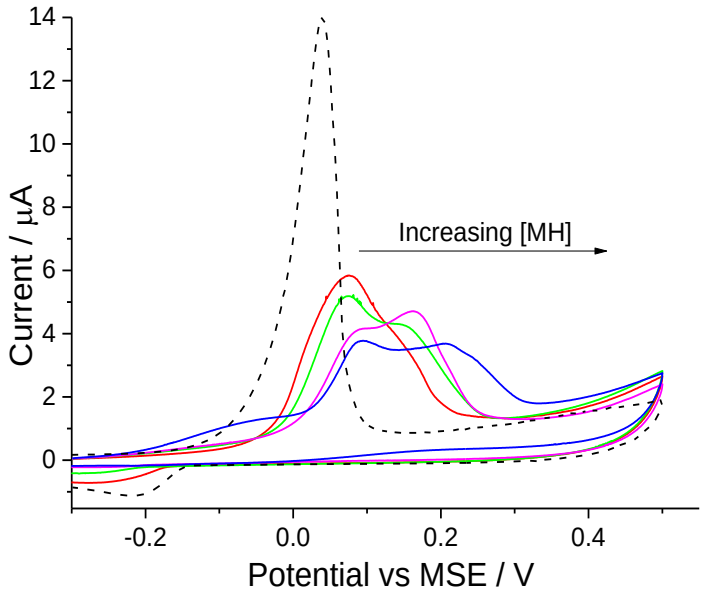

Figure 7.3 The oxidative stripping of silver nanoparticles (radii = 4.7 ± 1.8 nm) from a glassy carbon electrode in 0.1 M sodium nitrate spiked with varying concentrations of mercaptohexanol measured at a scan rate of 0.05 V s^{-1}. Black dashed line: No mercaptohexanol; Red: 10 µM; Green: 25 µM; Pink: 50 µM; Blue: 100 µM.

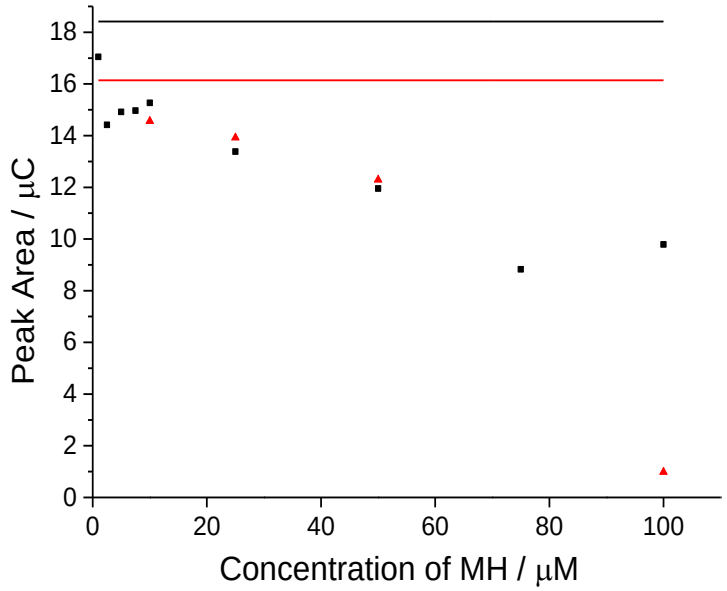

Figure 7.4 The oxidative stripping charge of silver nanoparticles from a glassy carbon electrode in 0.1 M sodium nitrate spiked with different concentrations of mercaptohexanol recorded at a scan rate of 0.05 V s^{-1}. Nanoparticles of two different size distributions were used. Red triangles: silver nanoparticles of radii 4.7 ± 1.8 nm; Black squares: silver nanoparticles of radii 13.6 ± 3.7 nm. Solid lines: average peak charge under the oxidation signal when no mercaptohexanol is present.

In the time variation experiments, the silver nanoparticle (radii = 13.6 ± 3.7 nm) modified electrode was soaked in 0.1 M sodium nitrate containing 10 μM of mercaptohexanol for various times before electrochemical oxidation via cyclic voltammetry was performed. The voltammograms and oxidative peak charge underneath the signals are summarised respectively in Figure 7.5 and Figure 7.6. As seen in Figure 7.5, increasing the mercaptohexanol exposure time gave rise to a split oxidation signal where the dominance of the second peak grew with time. Figure 7.6 shows the oxidative charges (obtained by integration under the peaks) remained relatively constant as the soaking time increased. Comparing the two sets of experiments involving varying concentrations and exposure times, there is a key difference between the two: the oxidative peak charge had a negative correlation with mercaptohexanol concentration (Figure 7.4) whilst the recorded peak charge remained effectively constant with exposure time (Figure 7.6).

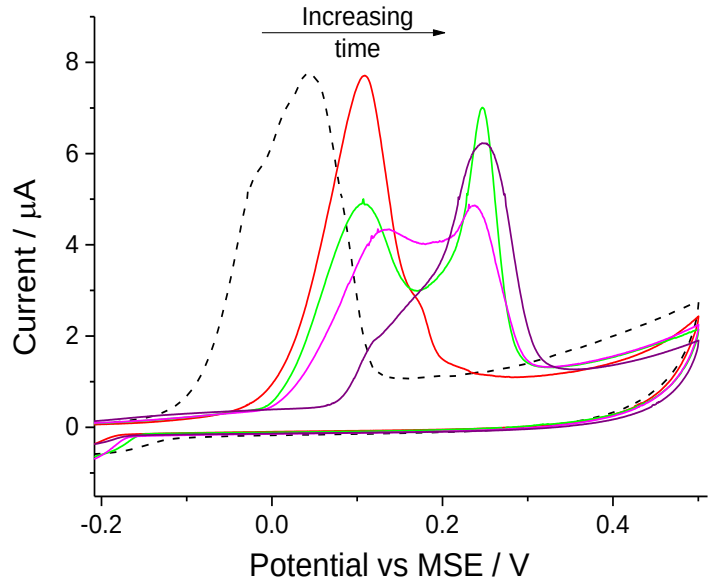

Figure 7.5 The oxidative stripping of silver nanoparticles (radius = 13.6 ± 3.7 nm) from a glassy carbon electrode in 0.1 M sodium nitrate spiked with 10 µM mercaptohexanol with different exposure times recorded at a scan rate of 0.05 V s^{-1}. Black dashed: voltammogram recorded immediately with NO mercaptohexanol; Red: voltammogram recorded immediately with 10 µM mercaptohexanol; Green: voltammogram recorded after electrode was exposed to 10 µM mercaptohexanol for 15 minutes; Pink: 30 minutes; Purple: 16 hours.

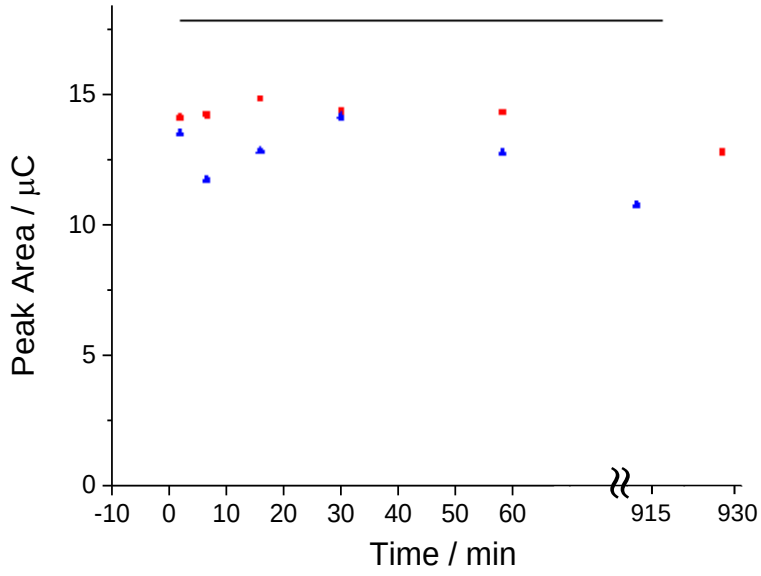

Figure 7.6 The oxidative stripping of silver nanoparticles (radii = 13.6 ± 3.7 nm) from a glassy carbon electrode in 0.1 M sodium nitrate spiked with different amounts of mercaptohexanol measured at a scan rate of 0.05 V s^{-1}. The peak charge under the oxidation signal is plotted against the exposure time to mercaptohexanol. Red squares: 10 µM mercaptohexanol in electrolyte; blue triangles: 25 µM mercaptohexanol in electrolyte. Solid line: peak charge under oxidation signal when no mercaptohexanol was added and the voltammogram was recorded immediately.

To explain the trends observed above, the existing literature research summarised within the introduction has to be considered. Knowing that AgSR and Ag_2S are probable products in this redox reaction between silver nanoparticles and mercaptohexanol, therefore, two sets of control experiments involving AgSR and Ag_2S were performed.

First, equal amounts of silver nitrate (50 mM) and mercaptohexanol (50 mM) was mixed and a sparingly soluble white product of $AgSR_m$ (where R_m = $-(CH_2)_6OH$)) was precipitated. The latter was drop cast onto the electrode and a cyclic voltammetry was performed. From Figure 7.7, no oxidation signal was recorded and a reduction signal at -1.7 V was seen in the first scan. Hence, the absence of oxidation signals reveals that $AgSR_m$ is not responsible for the oxidative charge and it is a possible candidate that caused the decrease of peak charge. The reduction signal at -1.7 V corresponded to the reduction of $AgSR_m$ into silver which is supported by the observation of a silver oxidation peak at +0.05 V in the second scan.

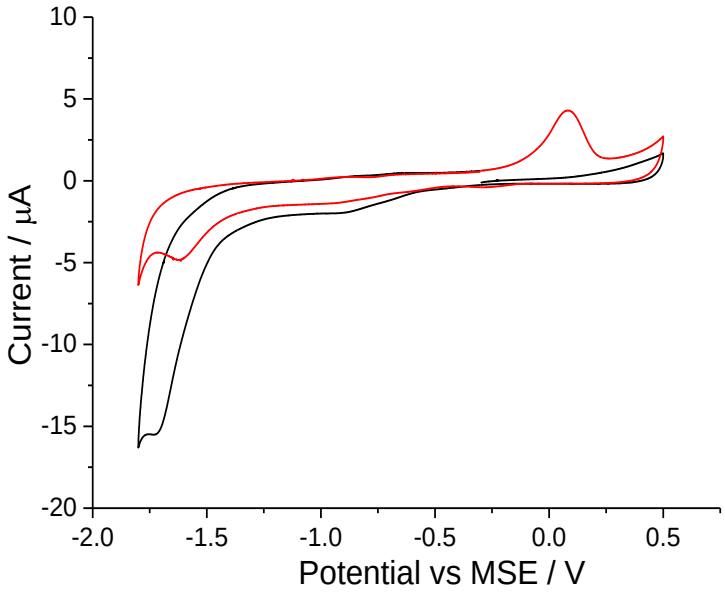

Figure 7.7 The oxidative stripping of sparingly soluble solid formed by mixing 50 mM of silver nitrate and 50 mM of mercaptohexanol from a glassy carbon electrode in 0.1 M sodium nitrate at a scan rate of 0.05 V s^{-1}. Black: first scan; Red: second scan.

Second, to form Ag_2S, silver nanoparticles (radii = 13.6 ± 3.7 nm) were oxidised in the presence of Na_2S. From Figure 7.8, the oxidative charge recorded under the signal decreased with increasing concentration of sodium sulphide. No split oxidation peaks was observed as silver sulphide, Ag_2S, was formed and the oxidation signal remained at the same potential.[364] Thus, silver sulphide did not contribute to the oxidative charge or caused the split oxidation signals. However, the formation of silver sulphide can cause a decrease in oxidation peak charge as it oxidises silver for its formation.

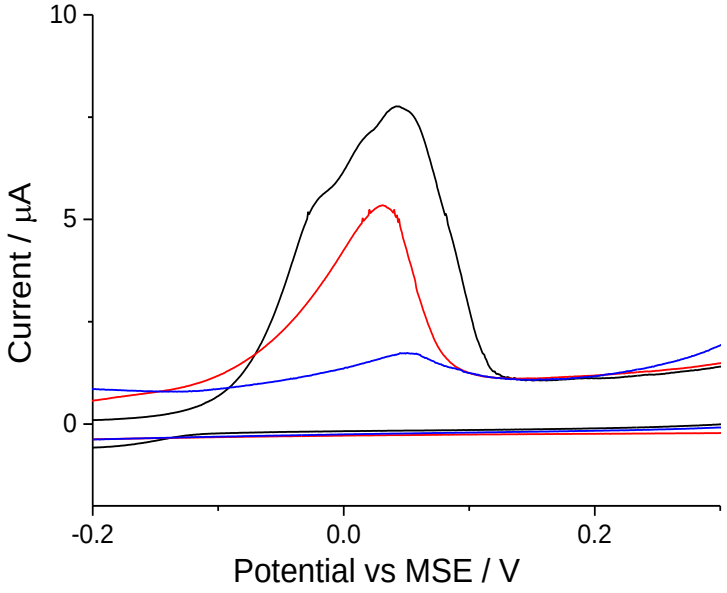

Figure 7.8 The oxidative stripping of silver nanoparticles (radii = 13.6 ± 3.7 nm) modified glassy carbon electrode in 0.1 M sodium nitrate spiked with different amount of sodium sulphide (Na_2S) at a scan rate of 0.05 V s^{-1}. Black: No sodium sulfide; Red: 100 µM; Blue: 500 µM.

7.3.1.2 UV-vis Spectroscopy of Silver Nanoparticles in the Presence of Mercaptohexanol

To further support the electrochemical findings, UV-vis spectroscopy of silver nanoparticles in the presence and absence of mercaptohexanol was performed. The citrate capped silver nanoparticles exhibit a surface plasmon peak around 400 nm in a UV-vis spectrum.[51] The surface plasmon peak is known to be sensitive to several factors such as size, capping agent, solvent and shape.[44, 51, 115, 303, 364, 365] Through the process of aggregation or increasing the size of silver nanoparticles, the surface plasmon peak red shifts.[51]

Similar to the electrochemical experiments, the two factors of concentration and time were varied. For the concentration experiments, both batches of silver nanoparticles were diluted and exposed to different concentrations of mercaptohexanol. In the time variation experiments, the nanoparticles of radii 4.7 ± 1.8 nm and 13.6 ± 3.7 nm were diluted by a factor of 24 and 48, spiked with 5 μM and 10 μM of mercaptohexanol and monitored over a period of 45 minutes and 15 minutes respectively. All the solutions were thoroughly degassed with nitrogen in both sets of experiments.

In the time study, as depicted in Figure 7.9 and Figure 7.10, without mercaptohexanol, a sharp surface plasmon peak at about 395 nm indicated the presence of silver nanoparticles.[51] As seen in Figure 7.9, for the smaller silver nanoparticle (radii = 4.7 ± 1.8 nm), increasing mercaptohexanol exposure time caused the peak to broaden within a short period. Conversely, in Figure 7.10, the bigger silver nanoparticle (radii = 13.6 ± 3.7 nm) had a drop in the absorbance peak at around 400 nm and a new peak around 500 - 600 nm appeared with increasing mercaptohexanol exposure time.

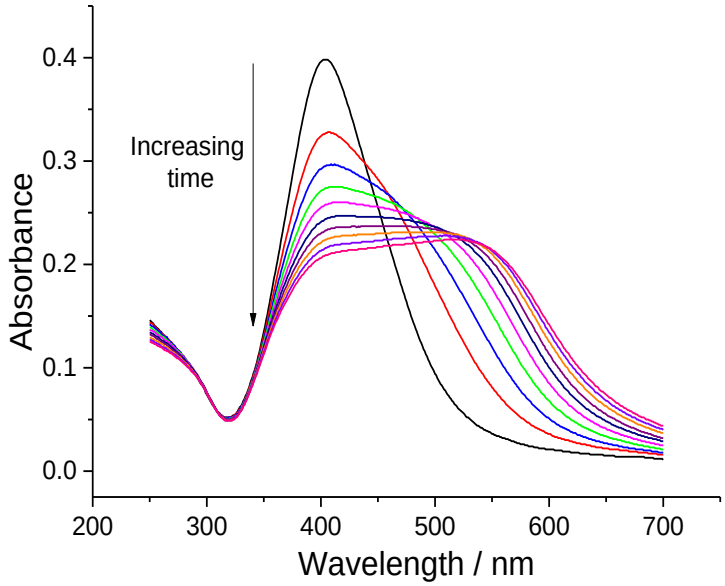

Figure 7.9. UV-vis spectrum of silver nanoparticles (radii = 4.7 ± 1.8 nm) after exposure to 5 μM of mercaptohexanol for different amounts of time. Black: No mercaptohexanol; Red: immediate. Blue: 5 mins. Cyan: 45 mins. Measurements were taken at intervals of 5 minutes for 45 minutes.

For the concentration variation experiments, with increasing mercaptohexanol concentration, the effect of mercaptohexanol on the spectrum was the same as increasing mercaptohexanol exposure time. The spectra of increasing mercaptohexanol concentration are recorded in Figure 7.11 and Figure 7.12.

In addition, a control UV-vis spectrum was recorded for silver nanoparticles (radii = 13.6 ± 3.7 nm) mixed with different concentrations of sodium sulphide (Na_2S). With increasing sodium sulphide concentration, the surface plasmon peak at 395 nm showed a decrease in absorbance but no peak around 500 - 600 nm appeared. Hence, the additional signal detected was not due to the presence of Ag_2S formation on the nanoparticle.[364] (Figure 7.13)

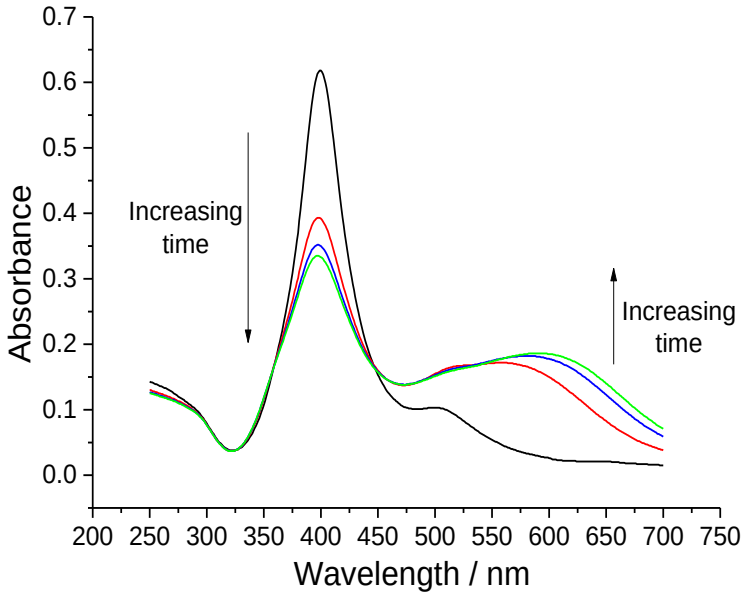

Figure 7.10 UV-vis spectrum of silver nanoparticles (radii = 13.6 ± 3.7 nm) after exposure to 10 µM of mercaptohexanol for different amounts of time. Black: No mercaptohexanol; Red: immediate; Blue: 5 mins; Green: 10 mins; Pink: 15 mins.

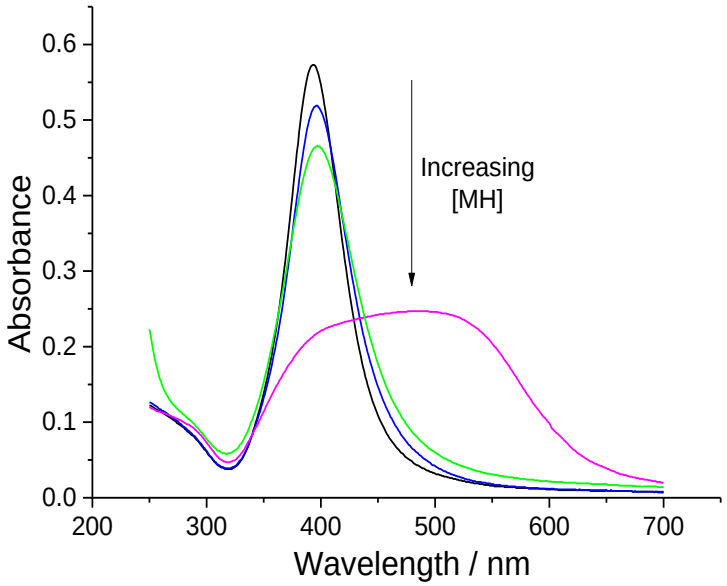

Figure 7.11 UV-vis spectrum of silver nanoparticles (radii = 4.7 ± 1.8 nm) exposed to different concentrations of mercaptohexanol. Black line: no mercaptohexanol; Blue: 1 µM; Green: 5 µM; Pink: 10 µM.

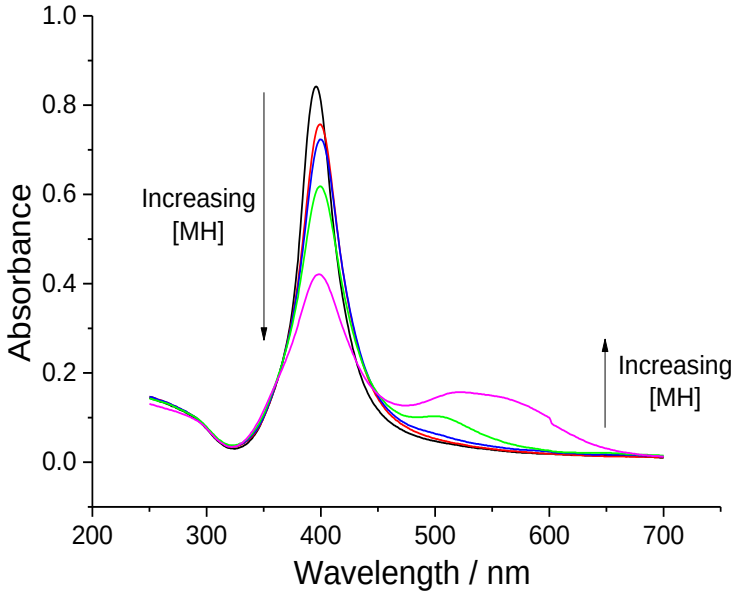

Figure 7.12 UV-vis spectrum of silver nanoparticles (radii = of 13.6 ± 3.7 nm) exposed to different concentrations of mercaptohexanol. Black line: silver nanoparticles with no mercaptohexanol; Blue: 1 µM; Green: 5 µM; Pink: 10 µM; Red: 100 µM.

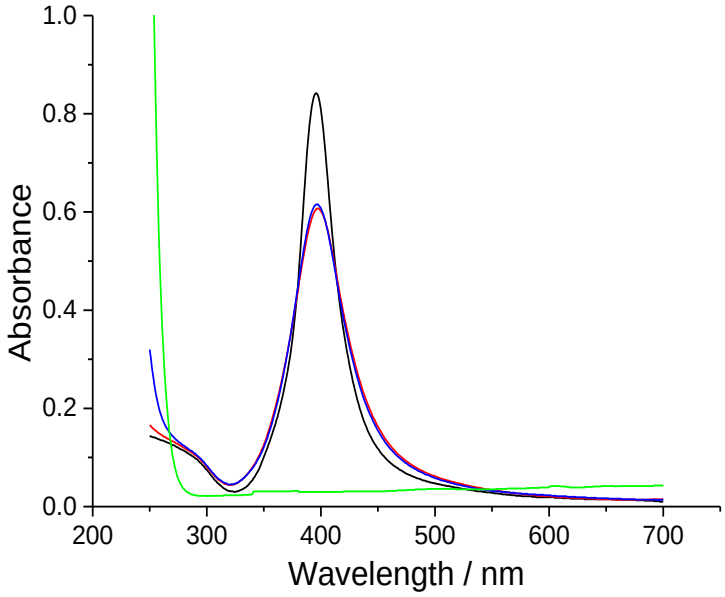

Figure 7.13 UV-vis spectrum displaying interaction between silver nanoparticles (radii = 13.6 ± 3.7 nm) and sodium sulphide (Na_2S). Black dashed line: silver nanoparticle with no Na_2S; Red: silver nanoparticle with 100 µM Na_2S; Blue: silver nanoparticle with 1 mM Na_2S; Green: 100 mM of Na_2S in absence of silver nanoparticles.

Hence, there are six major observations for the interaction between silver and mercaptohexanol to be accounted for, as follows.

- The decreasing oxidative peak charge with increasing mercaptohexanol concentration (Figure 7.4)
- The increase in peak potential in the presence of mercaptohexanol (Figure 7.2 and Figure 7.3)
- The occurrence of the split electrochemical oxidation signal with increasing mercaptohexanol concentration or increasing exposure time (Figure 7.2, Figure 7.3 and Figure 7.5)
- The constant electrochemical oxidative charge with increasing mercaptohexanol exposure time (Figure 7.6)
- The *apparent* absence of a size effect in electrochemical experiments (Figure 7.4)

- The decreasing absorbance and change in UV-vis peak shape with increasing mercaptohexanol concentration or increasing exposure time (Figure 7.9, Figure 7.10, Figure 7.11 and Figure 7.12)

Taking all the observations into consideration, an overview of the silver-mercaptohexanol interaction is provided below, giving a full and consistent explanation.

7.3.1.3 The Decreasing Oxidative Peak Charge with Increasing Mercaptohexanol Concentration

Thiols consume metallic silver by oxidising it to silver (I) to form silver-thiol complexes. This reaction concomitantly results in reduction products such as protons, hydrogen gas or water depending on pH and the availability of oxygen.[339, 354] Hence, the cause of the decreasing peak charge is likely related to the redox reaction resulting in the formation of $AgSR_m$ or Ag_2S-like complexes (Figure 7.4).[356, 366, 367] Given that $AgSR_m$ is an intermediate in the formation of Ag_2S - like complexes, it is likely that $AgSR_m$ formation is responsible for the initial drop in oxidative charges.[e] With different concentrations of mercaptohexanol, varying amounts of $AgSR_m$ are formed, leading to the variation of the measured peak charge.

7.3.1.4 The Increase in Peak Potential in the Presence of Mercaptohexanol

In the control experiments of AgSR and Ag_2S, no oxidation signal from +0.1 V to +0.3 V *vs.* MSE was found (Section 7.3.1.1). Thus, the observed increase in redox potential is not due to silver being oxidised to form $AgSR_m$ or Ag_2S (Figure 7.2, Figure 7.4, Figure 7.5, Figure 7.7 and Figure 7.8). Since neither $AgSR_m$ nor Ag_2S is involved, the oxidation signal is related to the oxidation of silver to silver(I) ions. It is speculated that mercaptohexanol reacts with silver nanoparticles to give a shell of $AgSR_m$ as reported in the literature.[354] Given that $AgSR_m$ was observed to be a sparingly soluble solid in the control experiments (Section 7.3.1.1), $AgSR_m$ might form an insoluble shell which

[e] In this case, the $AgSR_m$ shell formed on the nanoparticle surface[352] is suggested to be a solution phase chemical reaction and not detected electrochemically.

encapsulates the silver metal core. The trend of oxidation signal shifting to a higher potential (+0.1 V *vs*. MSE) in the presence of mercaptohexanol can be explained by the slowed kinetics of silver nanoparticle oxidation due to the insoluble $AgSR_m$ shell.

7.3.1.5 The Occurrence of the Split Oxidation Signal with Increasing Mercaptohexanol Concentration or Increasing Exposure Time

As described above, the oxidation of silver to silver(I) ions is the sole contributor to the observed oxidative peak charge since oxidation of silver to either $AgSR_m$ or Ag_2S are not likely responsible for the oxidative charges (Section 7.3.1.4). Hence, the silver-mercaptohexanol interaction must have further obstructed the kinetics of silver oxidation to silver(I) ions to cause the observed split oxidation signals. In the previous Section 7.3.1.3, it was surmised that an insoluble $AgSR_m$ shell is formed on the nanoparticle surface. Battocchio *et al.* reported a mixture of AgSR and Ag_2S-like complexes was found in the shell that encapsulated the silver nanoparticles.[356] Therefore, it is possible that given time or sufficient mercaptohexanol concentration, the $AgSR_m$ shell may undergo a phase transition to form a compact shell with a mixture of $AgSR_m$ and Ag_2S-like complexes. Thus, the kinetics of silver oxidation would be further obstructed after this phase transition occurred. This would give rise to a split oxidation signal where the silver oxidation kinetics are hindered by two different extents – one by the insoluble shell of $AgSR_m$ (+0.1 V *vs*. MSE) and another by the compact shell of AgSR and Ag_2S-like complexes (+0.2 V *vs*. MSE). In addition, a phase transition can have a delayed onset compared to the quick formation of $AgSR_m$, hence the peak at +0.2 V gains dominance with increasing time and is more favoured when mercaptohexanol concentration increases.

7.3.1.6 The Constant Oxidative Charge with Increasing Mercaptohexanol Exposure Time

With increasing exposure time to mercaptohexanol, the peak charge under the oxidation signals remained effectively constant as depicted in Figure 7.6. Therefore, following Faraday's law, no more metallic silver was oxidised by mercaptohexanol with increasing time. As suggested in Section 7.3.1.3, $AgSR_m$ is formed on the nanoparticle surface in the presence of mercaptohexanol. This

sparingly soluble shell of $AgSR_m$ can stop the approach of additional mercaptohexanol which diffuses to the surface with increasing exposure time. Thus, with increasing time, no additional $AgSR_m$ is formed, no more silver metal was consumed and the measured oxidative charge remained effectively constant with increasing mercaptohexanol exposure time.

7.3.1.7 The *Apparent* Absence of a Size Effect

As shown in Figure 7.4, two different batches of nanoparticles of radii 4.7 ± 1.8 nm and 13.6 ± 3.7 nm were used in the experiments. Given that the nanoparticles have different surface areas and $AgSR_m$ is speculated to form a shell on the nanoparticle surface, one might anticipate a possible difference in the decrease of the oxidative charges. However, no significant difference was found between the two batches of nanoparticles. It was observed in Figure 7.6 that the formation of $AgSR_m$ (drop in oxidative charge) occurred effectively instantaneously (time scale of at most a few seconds). It is surmised that the rate of $AgSR_m$ formation is controlled by the rate of mercaptohexanol diffusion to the surface. Considering the diffusional regime which occurs at this high silver surface coverage (4.2×10^{-5} mol m^{-2}), there is a complete overlap of the individual diffusional domains to give a linear diffusion profile across the entire working electrode (Chapter 4, Section 4.1).[222] In this linear diffusion regime, based on calculations, it takes less than one second to cover the surface with thiol through diffusion if the concentration of mercaptohexanol is at 10 μM.[252] Taking into account the convection caused by electrode insertion into the electrolyte, the actual time taken for mercaptohexanol to cover surface is even shorter. The short time which is required for thiol to diffuse to the surface and form $AgSR_m$ might explain the instantaneous drop in peak charge. Moreover, at this diffusion regime where there is a linear diffusion to the electrode, the amount of mercaptohexanol diffusing to the electrode surface is solely dependent on electrode area instead of nanoparticles' surface area. Since the working electrode used for both batches of nanoparticles is the same, similar amounts of mercaptohexanol reached the electrode surface. This would result in similar amount of $AgSR_m$ formed, explaining the apparent indifference in the decrease of peak charge between both batches of nanoparticles in Figure 7.4. Hence, it is very

probable that the interaction between silver nanoparticles and mercaptohexanol is a diffusion limited process.

7.3.1.8 The Decreasing Absorbance and Change in UV-vis Peak Shape with Increasing Mercaptohexanol Concentration or Increasing Exposure Time

With increasing exposure time or mercaptohexanol concentrations, a broadening of the absorbance signal at 395 nm was seen for nanoparticles of radii 4.7 ± 1.8 nm in Figure 7.9. For the bigger nanoparticles (radii = 13.6 ± 3.7 nm), the absorbance signal at 395 nm decreases and a signal at 500 – 600 nm grows (Figure 7.10). The red shift of an absorbance signal is often linked to an increase in size or aggregation.[51, 344] The observations in the experiments may thus be related to aggregation. It is known that the larger the silver nanoparticles, the greater the red shift.[51] It was observed in Figure 7.9 and Figure 7.10 that the red shift of the peak occurred to a different extent. If this was solely due to aggregation, one would expect the two different nanoparticle batches to have the same response as they both aggregate into large particles. Moreover, when the electrochemical data is considered, aggregation cannot explain the electrochemical trend of split oxidation signals seen in Figure 7.2 and Figure 7.5.

It is known from previous literature and Chapter 4, Section 4.1 that at this surface coverage where the linear diffusional regime across the electrode is dominant, the peak potential is solely dependent on the silver surface coverage instead of the size of nanoparticles.[62] If only aggregation was occurring, there should be a continuous size distribution with unchanged silver surface coverage and the surface coverage will remain constant. Thus, no change in electrochemical peak potential should be observed. Hence, another process must have taken place to explain the observations.

The hypothesis of a phase transition supports the observations of split oxidation signals (Section 7.3.1.5) and the change in shape of the UV-vis signals. The work of A. Henglein established that a change in surface plasmon peak can be caused by different coatings on the silver nanoparticles surface.[364, 365] The absorbance signal of silver nanoparticles with different thickness of silver oxide have been known to red shift to different extents.[44] This phenomenon supports the theory of a

phase transition taking place, proposed in Section 7.3.1.5 where a phase transition causes the surface plasmon peak to occur at different wavelengths. Hypothesising that phase transition is a process where the $AgSR_m$ shell transforms into a shell containing $AgSR_m$ and Ag_2S-like complexes, there are two populations in the silver nanoparticles suspension during the UV-vis experiment. Hence, the signal at 400 nm could be attributed to the nanoparticles with $AgSR_m$ on the surface before phase transition. On the other hand, the absorbance peak at 500 – 600 nm may be linked to the nanoparticles that underwent phase transition. The phase transition could cause a change in shell composition, giving rise to two distinct populations to cause two separate signals where one of them is red shifted to 500 – 600 nm. The smaller silver nanoparticles (radii = 4.7 ± 1.8 nm) have a broadening signal instead of two distinct signals. It is known that the shell thickness may affect the degree of the red shift of surface plasmon signal.[44] As the two batches of silver nanoparticle differ in size, the $AgSR_m$ shell on the nanoparticle surface can be of different thickness, resulting in a milder extent of red shift of the surface plasmon peak. Therefore, from both UV-vis spectra and electrochemical observations, it is proposed that it is more likely that the phase transition of silver nanoparticles caused the change in shape of absorbance peak instead of aggregation. In addition, given that the second signal did not appear in the control experiment of Na_2S, it signifies that the substituent group on mercaptohexanol is crucial to phase transition even though it may not be directly involved in the silver-mercaptohexanol interaction.

7.3.1.9 Summary of the Interaction between Silver Nanoparticles and Mercaptohexanol

In summary, all six major observations are explained above with strong supporting evidence. First, the drop in oxidative charge with increasing mercaptohexanol concentration can be explained by the immediate formation of $AgSR_m$ that consumes metallic silver. Second, the increase of peak potential in the presence of mercaptohexanol could be due to the formation of $AgSR_m$ on the nanoparticle surface which obstructs the oxidation process of silver to silver(I) ions. Third, the split oxidative peak with increasing mercaptohexanol concentration or exposure time can be explained by the instant formation of $AgSR_m$ on the nanoparticle surface which obstructs the silver oxidation kinetics, giving the first oxidation signal at +0.1 V *vs.* MSE. A phase transition can occur with $AgSR_m$

on nanoparticle surface to form a compact layer of $AgSR_m$ and Ag_2S-like complexes which further hinder the kinetics of silver oxidation, giving rise to the second oxidation signal at +0.2 V *vs.* MSE. Fourth, the constant oxidative charge with increasing mercaptohexanol exposure time may be explained by the instant formation of the sparingly soluble $AgSR_m$ shell which slows the approach of incoming mercaptohexanol and decreases the formation of $AgSR_m$ and the consumption of silver metal to a minimum. With increasing exposure time, it is suggested that only phase transition of $AgSR_m$ is occurring, resulting in a growing dominance of the second signal at +0.2 V *vs.* MSE without decreasing the oxidative charge. Fifth, the linear diffusional regime of mercaptohexanol towards the electrode may cause similar amounts of mercaptohexanol to reach both batches of nanoparticles; hence, no apparent size effect is observed. Sixth, the spectroscopic data also supports the hypothesis of phase transition through the appearance of the second absorbance signal at 500 – 600 nm.

7.3.2 Cysteine

7.3.2.1 Electrochemical Oxidation of Silver Nanoparticles in the Presence of Cysteine

In this section, experiments analogous to those performed in Section 7.3.1 were carried out between silver nanoparticles and cysteine for the ease of comparison and contrast with silver-mercaptohexanol interaction. Thus, concentration and time studies were carried out with cysteine. For the concentration studies, an electrode modified with silver nanoparticles of either radii 4.7 ± 1.8 nm or 13.6 ± 3.7 nm was electrochemically oxidised in the presence of different concentrations from 10 nM to 1 mM of cysteine.

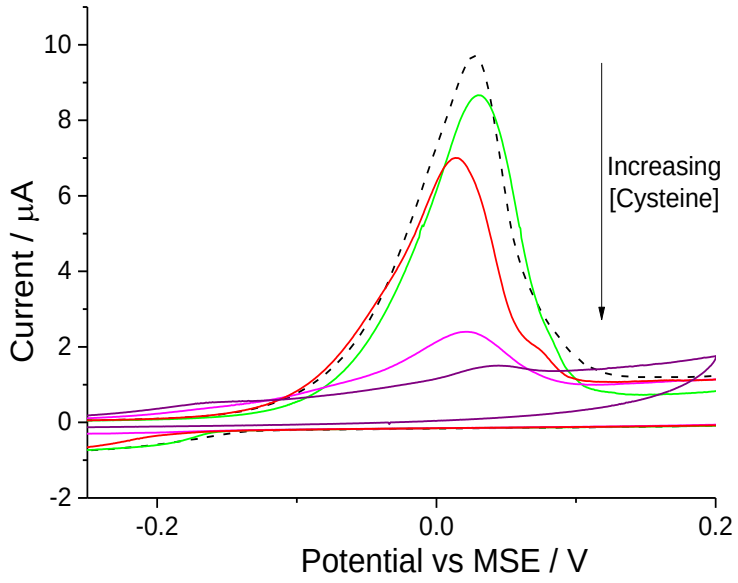

Figure 7.14 The oxidative stripping of silver nanoparticles (radii = 4.7 ± 1.8 nm) from a glassy carbon electrode in 0.1 M sodium nitrate spiked with different amounts of cysteine measured at a scan rate of 0.05 V s^{-1}. Black dashed line: No cysteine; Red: 500 nM; Green: 1 µM; Pink: 25 µM; Purple: 100 µM.

Cyclic voltammetry was performed by sweeping oxidatively from -0.3 V *vs.* MSE at a scan rate of 0.05 V s^{-1} *once* the modified working electrode was exposed to the degassed 0.1 M sodium nitrate containing cysteine. The voltammograms of silver nanoparticles (radii = 4.7 ± 1.8 nm) exposed to increasing concentrations of cysteine are shown in Figure 7.14. The voltammograms for the bigger silver particles (radii = 13.6 ± 3.7 nm) are found in Figure 7.15. It is seen that the peak potential of silver to silver(I) ions remained essentially constant and split oxidation signals were not observed.

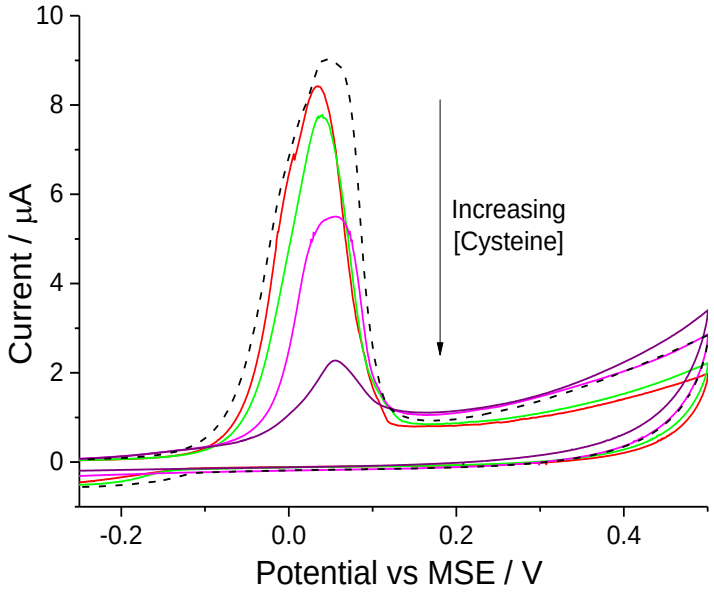

Figure 7.15 The oxidative stripping of silver nanoparticles (radii = 13.6 ± 3.7 nm) from a glassy carbon electrode in 0.1 M sodium nitrate spiked with different amounts of cysteine measured at a scan rate of 0.05 V s^{-1}. Black dashed line: No cysteine; Red: 500 nM; Green: 1 µM; Pink: 25 µM; Purple: 100 µM.

In Figure 7.16, the oxidative peak charge measured (integration underneath the voltammetric signals) was plotted against the concentration of cysteine. Similar to mercaptohexanol, with increasing cysteine concentration, the peak charge decreased. Considering the inherent variability of the experiments, it is not possible to show a significant difference between the two batches of nanoparticles. Hence, with increasing cysteine concentration, a decrease in oxidative peak charge, a constant oxidative potential and an absence of a split oxidation signal are reported. In contrast, the mercaptohexanol studies showed an increase in peak potential and the appearance of split oxidation signals with increasing mercaptohexanol concentration. Therefore, the two thiol compounds have silver-thiol interactions which differ from one another.

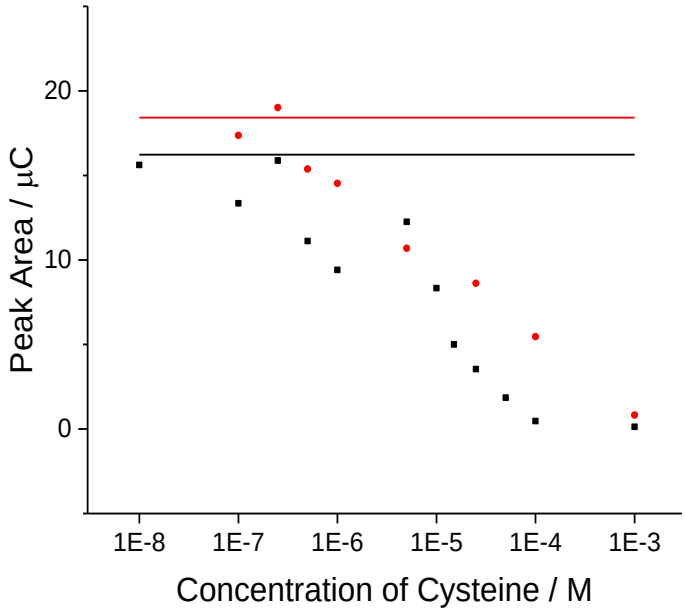

Figure 7.16 The oxidative stripping charge of silver nanoparticles from a glassy carbon electrode in 0.1 M sodium nitrate spiked with different amounts of cysteine measured at a scan rate of 0.05 V s^{-1}. Black squares: silver nanoparticles of radii 4.7 ± 1.8 nm; Red diamonds: silver nanoparticles of radii 13.6 ± 3.7 nm. Black line: average peak charge under the oxidation signal when no mercaptohexanol is present for nanoparticles of radii 4.7 ± 1.8 nm. Red line: average peak charge under the oxidation signal when no mercaptohexanol is present for nanoparticles of radii 13.6 ± 3.7 nm.

Next, time studies were performed by soaking a silver nanoparticle (radii = 4.7 ± 1.8 nm) modified electrode in degassed sodium nitrate containing 5 µM cysteine for a duration varying from 60 minutes to 945 minutes before cyclic voltammetry was performed. The voltammograms are shown in Figure 7.17 and it was observed that there was an inverse correlation between cysteine exposure time and the oxidative peak charge under the signal. Moreover, a constant peak potential but no split oxidation signals were observed for silver oxidation even after 16 hours of exposure to cysteine.

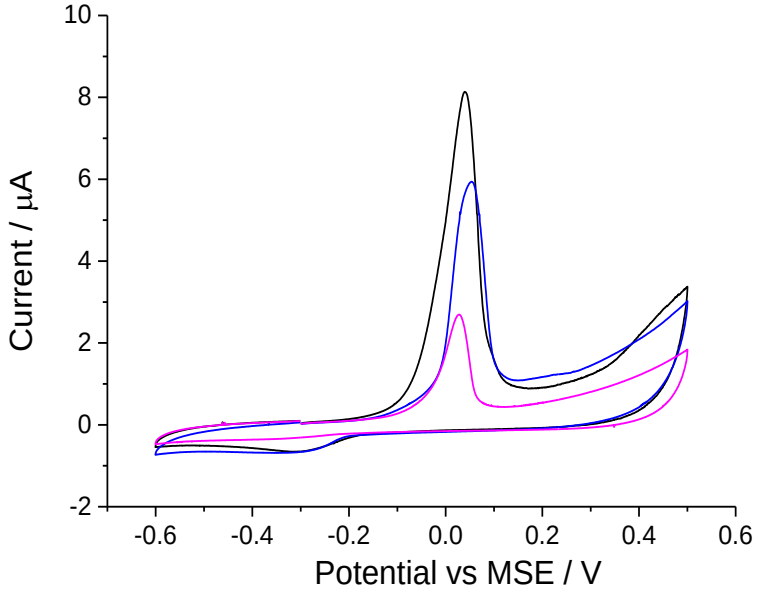

Figure 7.17 The oxidative stripping of silver nanoparticles (radii = 4.7 ± 1.8 nm) from a glassy carbon electrode in 0.1 M sodium nitrate spiked with 5 µM cysteine with different exposure times recorded at a scan rate of 0.05 V s^{-1}. Black: voltammogram recorded immediately; Blue: voltammogram recorded after electrode was soaked for 60 minutes; Pink: voltammogram recorded after electrode was soaked for 15 hours 15 minutes.

7.3.2.2 UV-vis Spectroscopy of Silver Nanoparticles in Presence of Cysteine

Both batches of the nanoparticles were diluted for UV-vis spectroscopy and cysteine was added. Both cysteine concentration and exposure time were varied. The cysteine concentration study for the nanoparticles are summarised in Figure 7.18 and Figure 7.19. The time variation study was performed with nanoparticles of radii 4.7 ± 1.8 nm with 1 mM cysteine and the spectrum is recorded in Figure 7.20. For both batches of silver nanoparticles, with increasing cysteine concentration, the absorbance signal remains effectively constant with the exception of the small initial drop. With increasing exposure time, there is a small constant decrease in absorbance at 400nm. For all the UV-vis experiments, no new surface plasmon peak was observed.

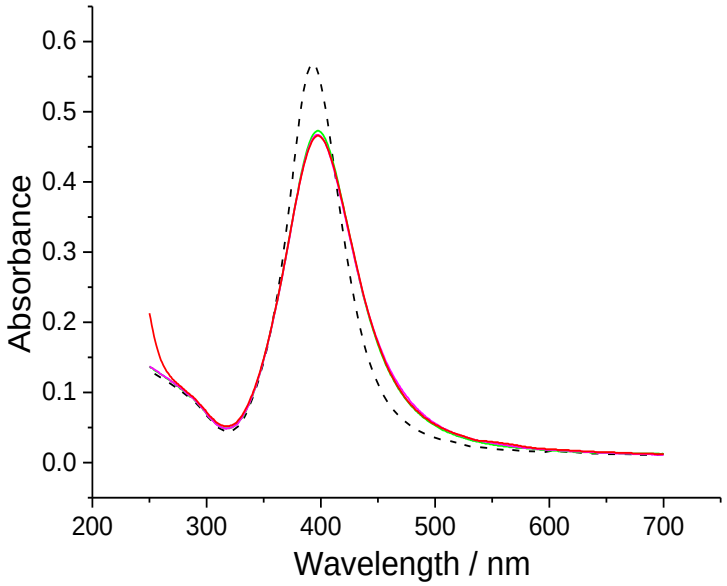

Figure 7.18 UV-vis spectrum of silver nanoparticles (radii = 4.7 ± 1.8 nm) exposed to different concentrations of cysteine. Black dashed line: silver nanoparticles with no cysteine; Green: 5 µM; Pink: 10 µM; Red: 1 mM.

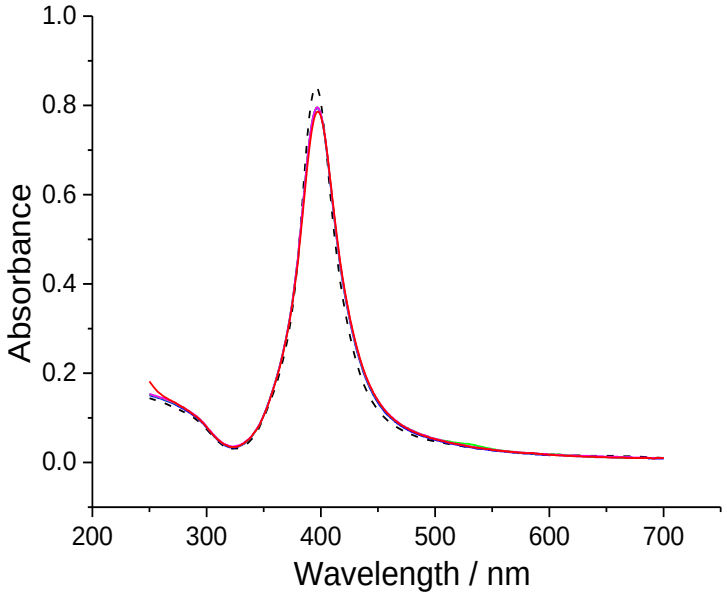

Figure 7.19 UV-vis spectrum of silver nanoparticles (radii = 13.6 ± 3.7 nm) exposed to different concentrations of cysteine. Black dashed line: silver nanoparticle with no cysteine; Blue: 1 µM; Green: 5 µM; Pink: 10 µM; Red: 1 mM.

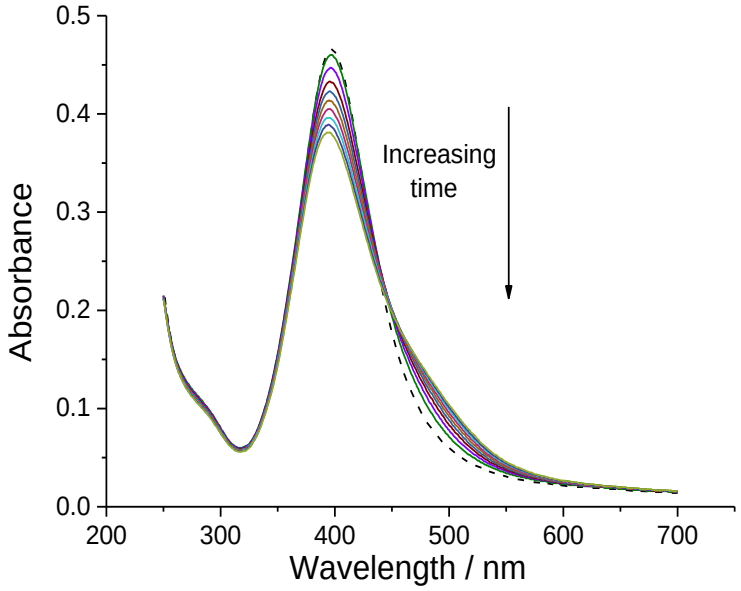

Figure 7.20 UV-vis spectrum of silver nanoparticles (radii = 4.7 ± 1.8 nm) after exposure to 1 mM of cysteine for different amount time. Black: immediate. Green: 10 mins. Light green: 90 mins. Measurements were taken at intervals of 10 minutes for 90 minutes.

Consequently, there are three main group of observations for the behaviour of silver nanoparticles in the presence of cysteine which need to be accounted for:

- The decreasing electrochemical oxidative charge and constant UV-vis absorbance signal with increasing cysteine concentration (Figure 7.16, Figure 7.18 and Figure 7.19)
- The constant electrochemical peak potential, the absence of split oxidation signals and the absence of a UV-vis absorbance signal at 500 – 600 nm with increasing cysteine concentration or increasing exposure time (Figure 7.14, Figure 7.17, Figure 7.18 and Figure 7.19)
- The apparent absence of a size effect (Figure 7.16)

Developing the model hypothesized in the mercaptohexanol studies, the difference in behaviour between mercaptohexanol and cysteine is explained in the following sections.

7.3.2.3 The Decreasing Electrochemical Oxidative Charge and Constant UV-vis Absorbance Signal with Increasing Cysteine Concentration

With increasing cysteine concentration or increasing exposure time, the oxidative charge decreased. The amount of oxidative charge is linked to the amount of silver available for oxidation, hence, the amount of metallic silver available for oxidation on the electrode decreased. It was suggested in the mercaptohexanol studies (Section 7.3.1) that the decreasing oxidation charge with concentration and time was related to the formation of $AgSR_m$ from silver nanoparticles and mercaptohexanol. Following the mechanism of mercaptohexanol studies, if the silver(I) thiolate complex $AgSR_c$ (where $R_c = -C_3H_6NO_2$) was formed continuously, the silver nanoparticles would get smaller. At this range of nanoparticle size, the extinction coefficient decreases with size, thus, the UV-vis spectrum should display a decrease in UV-vis absorbance with increasing cysteine concentration.[51, 245] However, it is seen that the UV-vis absorbance signal at 400 nm remained effectively constant in Figure 7.18 and Figure 7.19. Therefore, the mechanism which applies to cysteine is different from one which operates for mercaptohexanol. It is proposed that cysteine replaces the citrate capping agent around the silver nanoparticles to give cysteine-capped silver nanoparticles.[360]

To prove the presence of cysteine capped nanoparticles, a control experiment was performed by mixing citrate capped silver nanoparticles (radii = 4.7 ± 1.8 nm) with cysteine and UV-vis spectra were recorded at different pH. Silver nanoparticles (radii = 4.7 ± 1.8 nm) diluted by a factor of 24 with water was exposed to 1 mM of cysteine. The mixture at pH 6.9 had a UV-vis spectrum recorded in Figure 7.21. 8 µL of 0.1 M citric acid was added change the solution pH to pH 5.7 and another UV-vis spectrum was recorded as shown in the red line of Figure 7.21. The solution had about 0.4 mM citric acid in order to lower the pH. The sudden shift in the UV-vis spectrum matches the previous literature on cysteine capped silver nanoparticles where the UV-vis responses changes with different pH.[360] The synthesized cysteine capped silver nanoparticles aggregated at pH 5.7 while maintaining their form at pH 6.9. This indicates that cysteine capped nanoparticles are formed

when cysteine and silver nanoparticles are mixed.[360] No such behaviour occurred with citrate capped silver nanoparticles at different pH, as seen in Figure 7.22.

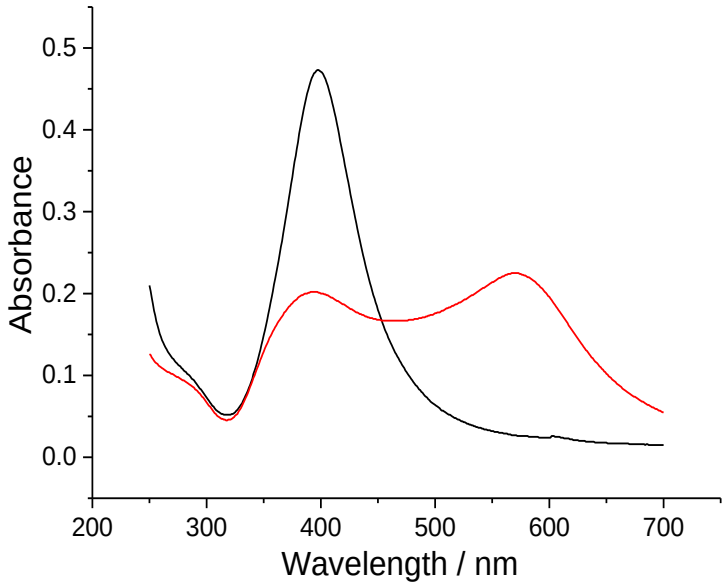

Figure 7.21 UV-vis spectrum of "cysteine capped silver nanoparticles" (silver nanoparticles (radii = 4.7 ± 1.8 nm) with 1 mM of cysteine) at different pH. Black: pH 6.9; Red: pH 5.7.

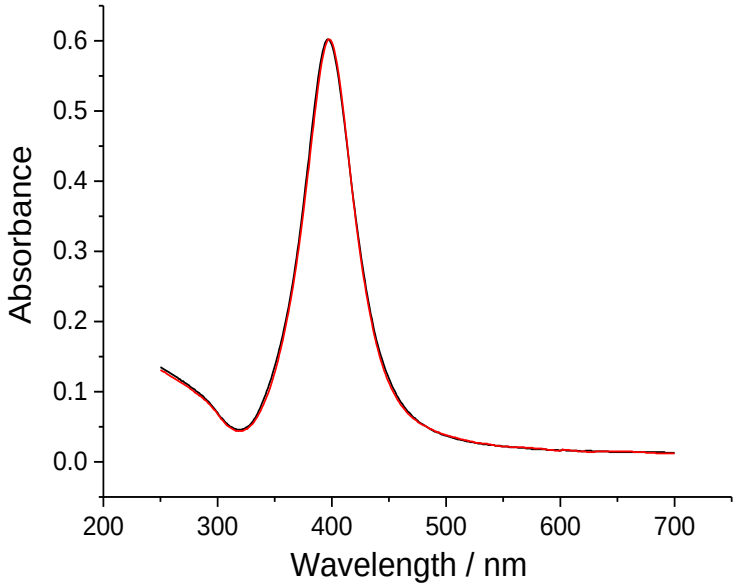

Figure 7.22 UV-vis spectrum of citrate-capped silver nanoparticles (radii = 4.7 ± 1.8 nm) in at different pH. Black: pH 7.7; Red: pH 5.5.

In the UV-vis experiments, similar to the citrate capped silver nanoparticles, cysteine capped silver nanoparticles give an absorbance signal at 400 nm.[360] A slight drop in UV-vis absorbance corresponded to the oxidation of silver metal by cysteine to covalently attach itself to the silver nanoparticle. Assuming a thin layer formation of $AgSR_c$ on the silver nanoparticle surface to form the cysteine capping layer, a constant amount of silver is required to form the cysteine capped nanoparticles. Thus, the silver nanoparticle size drops slightly to a similar extent with a thin cysteine capping layer formed. Consequently, the absorbance signal recorded on the spectrum remains effectively constant as the cysteine concentration changes.

Speculating that a fixed amount of silver is consumed to form the cysteine capped nanoparticles, in the electrochemical experiments, the oxidative charge measured in the presence of cysteine should have remained effectively constant. However, it was observed in Figure 7.16 that the measured oxidative charge has an inverse relationship with cysteine concentration.

Therefore, another control experiment was performed. Silver nanoparticles of radii 4.7 ± 1.8 nm diluted by a factor of 10 with water were exposed to 10 mM of cysteine to synthesize the cysteine capped silver nanoparticles. 3 µL of the synthesized nanoparticles were drop cast on onto the glassy carbon electrode and dried under a nitrogen flow. The electrode after drying was used immediately for electrochemical experiments. From Figure 7.23, no oxidation signals were observed at the window of 0 V to +0.3 V *vs.* MSE for the cysteine capped silver nanoparticles although the same amount of silver was drop cast onto the electrode compared to the citrate capped nanoparticles. Therefore, the cysteine capping agent might have either inactivated the silver surface, stopping silver oxidation or caused detachment of the nanoparticles from the electrode. Both will cause the drop in electrochemical oxidative charge with increasing cysteine concentration. Hence, having cysteine capped silver nanoparticles as a product of silver nanoparticle-cysteine interaction can explain the constant absorbance signal and the decrease in the electrochemical oxidative charge measured.

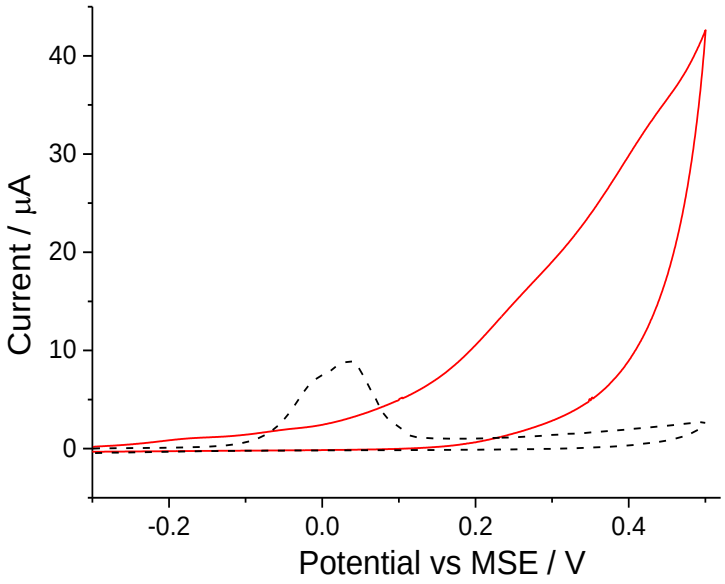

Figure 7.23 Black dashed line: the oxidative stripping of citrate capped silver nanoparticles (radii = 4.7 ± 1.8 nm) from a glassy carbon electrode in 0.1 M sodium nitrate; Red line: the oxidative stripping of synthesized cysteine capped silver nanoparticles from a glassy carbon electrode in 0.1 M sodium nitrate. Scan rate: 0.05 V s^{-1}.

7.3.2.4 The Constant Electrochemical Peak Potential, the Absence of Split Oxidation Signals and the Absence of UV-vis Absorbance Signal at 500 – 600 nm with Increasing Cysteine Concentration or Increasing Exposure Time

It is surmised that cysteine forms a capping shell with inactivation of the nanoparticle surface or nanoparticle detachment from the electrode. Therefore, only the silver nanoparticles with incomplete replacement of citrate by cysteine contribute to the oxidative charges. Thus, despite the presence of cysteine, the kinetics of silver oxidation remained unaltered and the oxidation peak potential remained constant and no split oxidation signals was recorded. Therefore, in the UV-vis experiments, given that the solution consisted of citrate capped silver nanoparticles and cysteine capped silver nanoparticles, the species which caused an absorbance signal at 500 – 600 nm with mercaptohexanol is not present in the cysteine experiment. In short, the trends observed in the mercaptohexanol studies were not observed in the cysteine studies due to significant differences in the silver-thiol interactions.

7.3.2.5 The Apparent Absence of a Size Effect

As seen in Figure 7.18 and Figure 7.19, two different sizes of nanoparticles of 4.7 ± 1.8 nm and 13.6 ± 3.7 nm were used in experiments. Due to the experimental inherent variability, it is not possible to show a significant size effect. From Section 7.3.1.7, the silver-thiol interaction is a diffusion limited process where the high silver surface coverage (4.2×10^{-5} mol m^{-2}) causes a linear diffusion profile across the entire working electrode. Based on similar calculations to those presented in Section 7.3.1.7, it takes less than 10 milliseconds for sufficient cysteine to diffuse and cover the surface at 10 μM of cysteine. In the actual experiment, it takes even lesser time due to the convection caused by electrode insertion into the electrolyte. Therefore, within the short time scale that the linear diffusion profile is applicable, the amount of cysteine reaching the electrode surface is similar for both batches of nanoparticles. However, the kinetics of cysteine replacing citrate as capping agent is unknown. Moreover, the extent of how much cysteine replacement is needed to exhibit cysteine capped nanoparticles' characteristics is also unspecified. Thus, further detailed kinetics studies on how cysteine displaces citrate have to be attempted before the effects of the nanoparticle size can be explained and quantified in detail.

7.3.2.6 Summary on the Interaction between Silver Nanoparticles and Cysteine

In summary, cysteine interacts with silver nanoparticles in a way different from mercaptohexanol. Cysteine likely replaces the citrate capping agent and bonds covalently with silver nanoparticles to give a UV-vis absorbance signal at 400 nm regardless of cysteine concentration. In the electrochemical experiments, the oxidative charge measured decreased with increasing cysteine concentrations. This was speculated to be an inactivation of silver surface through cysteine capping or the detachment of cysteine capped nanoparticles from the electrode surface.

7.4 Conclusions

The two thiols compounds studied, mercaptohexanol and cysteine, interacted with silver nanoparticles differently despite both having a thiol group as the primary structure motif. Figure 7.24 summarises the hypothesised silver-thiol interactions of the two investigated thiols.

Mercaptohexanol was suggested to form a sparingly soluble shell of $AgSR_m$ with silver, which remains on the nanoparticle surface, allowing further phase transition to occur. Both mercaptohexanol's electrochemical and UV-spectroscopy data have shown an additional signal which is speculated to be due to formation of a compact layer of $AgSR_m$ and Ag_2S-like complexes via phase transition of initially formed $AgSR_m$ shell on the nanoparticle surface. In contrast, cysteine is surmised to displace the citrate capping agent to give cysteine capped nanoparticles. The change in capping agent can cause an inactivation of the nanoparticles or the detachment of the nanoparticles from the electrode surface. Thus, the oxidation signal decreases with cysteine concentration. The UV-vis spectrum remained similar with the presence of cysteine as the silver nanoparticles (regardless of citrate capped or cysteine capped) gave the same surface plasmon peak near 400 nm. In conclusion, it is evident that no general mechanism for the interactions of thiol with silver nanoparticles exist and that each thiol should be treated individually.

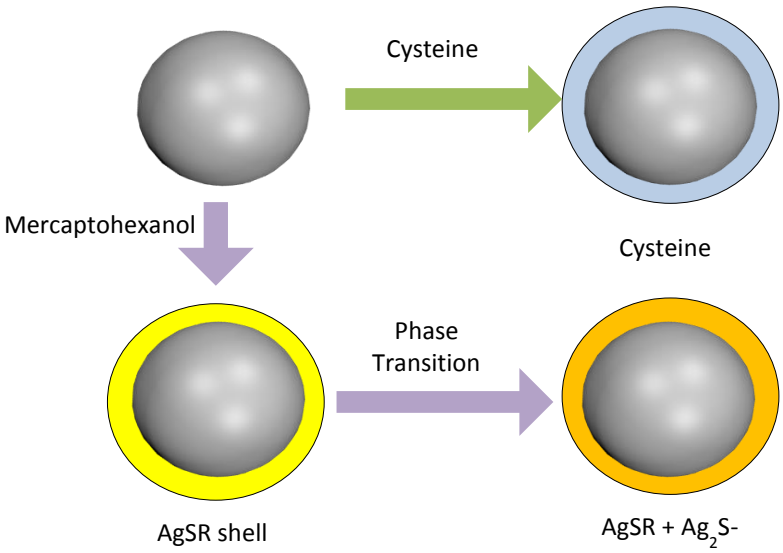

Figure 7.24 A schematic diagram showing the hypothesised mechanism of the silver-thiol interaction for mercaptohexanol and cysteine. The grey spheres represent silver nanoparticles.

Chapter 8 Conclusions

There is a growing importance and application of silver nanoparticles in consumer and industrial products partly due its anti-bacterial properties. Despite its wide-spread usage, nanoparticles are still not completely understood. Thus, the first step to regulating nanoparticle usage to circumvent any possible negative implications is through reliable detection.

Herein, the detection of the nanoparticles was approached and realised with two different techniques, stripping voltammetry and 'nano-impacts'. For stripping voltammetry, theoretical expressions based on the different possible diffusion regimes at the nanoparticle surface were developed to analyse the potential of metallic nanoparticle oxidation. The surface coverage of the nanoparticles on the electrode was found to have a stronger influence on the potential shift compared to the change in nanoparticle surface energy. Silver nanoparticles were also found to aggregate when they were drop cast onto the electrode. To overcome the problem of aggregation in ex-situ methods, the novel method of 'nano-impacts' was used to analyse nanoparticles in the solution phase. To expand the possible matrices and suspensions used for 'nano-impacts', individual silver nanoparticles were successfully detected and sized in an optically opaque suspension. This confers 'nano-impacts' a significant advantage over in-situ optical techniques such as dynamic light scattering (DLS) and nanosight tracking analysis (NTA).

Next, a comparison between the two electrochemical methods was undertaken via the investigation of capping agent effects. It was found that the capping agents on the nanoparticles have different influences depending on the methods utilised. In stripping voltammetry, the silver nanoparticles (various capping agents, similar size and surface coverage) gave significantly different current under the oxidation signal. The variation of peak charge was attributed to the change in aggregation with capping agent. In comparison, the change in capping agent on silver nanoparticles did not affect the capability of 'nano-impacts' to size the single particles. All five samples were detected, electrochemically sized and matched to the ex-situ method of transmission electron microscopy (TEM). Thus, using stripping voltammetry to determine the quantity of nanoparticles

should be used with caution to avert underestimation while 'nano-impacts' is definitely a promising technique to be considered for single nanoparticle detection and characterisation.

Admist the comparison of capping agents on silver nanoparticles, cetyltrimethylammonium bromide (CTAB) (a common capping agent) was found to be electroactive via its bromide oxidation. At high concentration, CTAB forms self-assembled micelles in aqueous solution. This inspired a study where CTAB micelles were detected via 'nano-impacts'. The oxidation of the micellar bromide content resulted in a direct detection of the presence of large micelles in solution and allows the measurement of the critical micelle concentration without recourse to surface tension measurements. This widens the range of nanomaterials which 'nano-impacts' can characterise.

Apart from exploring the techniques for nanoparticle detection, this thesis also applied silver nanoparticles in potential practical electroanalytical sensors. Comparing with bulk material, nanoparticles has a much large surface area to volume ratio, thus the latter greatly reduces the amount of metal required for the same purpose. Here, the separate analyses of silver ions, chloride ions or iodide ions were developed using silver nanoparticle modified electrodes. First, the anodic stripping voltammetry signal from silver ions was significantly enhanced. Since the former pre-concentrates metallic ions onto the electrode by reducing them to their metal form, nucleation is often the greatest barrier that the process has to overcome. By pre-treating the electrode with silver nanoparticles, stripping and leaving behind meta-stable silver clusters which are undetected electrochemically, the stage of nucleation can be averted in subsequent anodic stripping voltammetry of silver ions. Comparing to an untreated electrode, an improved signal (by at least factor of three) on the pre-treated electrode was observed for silver deposition. Second, making use of silver-halide interactions, a proof-of-concept sensor for cystic fibrosis (CF) pre-screening was developed. In presence of halide ions, the silver oxidation signal changes shape due to the formation of the stable silver halide. Since high sweat chloride content is a characteristic symptom of CF patients, the detection of chloride ions is used as a pre-screening and diagnostics method. By measuring the peak height of the silver chloride formation signal on a silver nanoparticle modified

screen print electrode, the chloride content in synthetic sweat was determined, suggesting the possibility of pre-screening if one has the genetic disease of CF in a quick, robust and cost-efficient route. Third, using a related concept, a silver nanoparticle modified electrode was used to analyse the concentration of iodine ions in synthetic urine. The iodide level in urine is used as an indicator of health where excess or deficiency of iodide can lead to thyroid diseases. The possible interference of chloride ions in urine was avoided as the silver iodide formation signal occurs at a lower potential compared to silver chloride formation. The reduction of silver iodide concentrated on the electrode was used to measure the iodide content as the surface bound wave has a better defined shape. From the amount of iodide ions in urine, information on health status can be obtained as one is capable of judging if there is deficiency or excess iodine in the body. Hence, using silver-halide interaction, the biological relevant concentrations of chloride and iodide ions were analysed and proof-of-concept systems for a CF pre-screening device and a urinary iodide sensor were developed.

Finally, given the successful examples of using silver-halide interaction to develop sensors, the silver-thiol interaction was also studied. Thiols are of a more complex nature due to the variety of side chains linked to the thiol group. Cyclic voltammograms and UV-vis spectra recorded with silver nanoparticles and two different thiols were used to gauge if all thiols interact in a similar manner. It was found that mercaptohexanol, a simple thiol with a hydroxyl group, was suggested to form a sparingly soluble shell of $AgSR_m$ on the nanoparticle surface which undergoes a further phase transition. In contrast, cysteine is hypothesised to form cysteine capped silver nanoparticles via the displacement of the citrate capping agent. Hence, each thiol must be treated as a separate entity for silver-thiol interaction.

Bibliography

1. R. G. Compton and C. E. Banks, *Understanding Voltammetry*, 2nd edn., Imperial College Press, London, 2011.
2. J. Wang, *Analytical Electrochemistry*, 3rd edn., John Wiley & Sons, Inc., New Jersey, 2006.
3. R. G. Compton and G. H. W. Sanders, *Electrode Potentials*, Oxford University Press, Oxford, 1996.
4. A. J. Bard and L. R. Faulkner, *Electrochemical Methods : Fundamentals and Applications*, 2nd edn., John Wiley & Sons, Lnc., New York, 2001.
5. L. R. Faulkner, *J. Chem. Educ.*, 1983, **60**, 262-264.
6. J. R. Runo and D. G. Peters, *J. Chem. Educ.*, 1993, **70**, 708-713.
7. J. A. V. Butler, *Trans. Faraday Soc.*, 1924, **19**, 659-665.
8. J. A. V. Butler, *Trans. Faraday Soc.*, 1924, **19**, 729-733.
9. J. A. V. Butler, *Trans. Faraday Soc.*, 1924, **19**, 734-739.
10. J. Nikolic, E. Expósito, J. Iniesta, J. González-Garcia and V. Montiel, *J. Chem. Educ.*, 2000, **77**, 1191-1194.
11. W. D. Ellis, *J. Chem. Educ.*, 1973, **50**, A131-A147.
12. J. J. Van Benschoten, J. Y. Lewis, W. R. Heineman, D. A. Roston and P. T. Kissinger, *J. Chem. Educ.*, 1983, **60**, 772-776.
13. D. Marín, F. Medicuti and C. Teijeiro, *J. Chem. Educ.*, 1994, **71**, A277-A278.
14. H. H. Thorp, *J. Chem. Educ.*, 1992, **69**, 250-252.
15. R. D. Caton, Jr., *J. Chem. Educ.*, 1973, **50**, A571-A578.
16. K. Kusuda, *J. Chem. Educ.*, 1989, **66**, 531.
17. *CRC Handbook of Chemistry and Physics 2012-2013*, ed. W. M. Haynes, 93rd edn., CRC Press, Florida, 2012.
18. P. T. Kissinger and W. R. Heineman, *J. Chem. Educ.*, 1983, **60**, 702-706.
19. G. A. Mabbott, *J. Chem. Educ.*, 1983, **60**, 697-702.
20. A. S. Barnes, I. Streeter and R. G. Compton, *J. Electroanal. Chem.*, 2008, **623**, 129-133.
21. H. Matsuda and Y. Ayabe, *Z. Elektrochem.*, 1955, **59**, 494-503.
22. J. B. Conant and M. F. Pratt, *J. Am. Chem. Soc.*, 1926, **48**, 3178-3192.
23. R. G. Compton, R. G. Wellington, P. J. Dobson and P. A. Leigh, *J. Electroanal. Chem.*, 1994, **370**, 129-133.
24. K. Aoki and J. Osteryoung, *J. Electroanal. Chem. Interfacial Electrochem.*, 1981, **122**, 19-35.
25. D. Shoup and A. Szabo, *J. Electroanal. Chem. Interfacial Electrochem.*, 1982, **140**, 237-245.
26. E. J. E. Stuart, Y.-G. Zhou, N. V. Rees and R. G. Compton, *RSC Adv.*, 2012, **2**, 6879-6884.
27. Project on Emerging Nanotechnologies Analysis, http://www.nanotechproject.org/cpi/about/analysis/ (Accessed 4 Feb 2014).
28. V. Y. Prinz, *Microelectron. Eng.*, 2003, **69**, 466-475.
29. B. Tian, X. Zheng, T. J. Kempa, Y. Fang, N. Yu, G. Yu, J. Huang and C. M. Lieber, *Nature (London, U. K.)*, 2007, **449**, 885-889.
30. K. Takeda, K.-I. Suzuki, A. Ishihara, M. Kubo-Irie, R. Fujimoto, M. Tabata, S. Oshio, Y. Nihei, T. Ihara and M. Sugamata, *J. Health Sci.*, 2009, **55**, 95-102.
31. Y. Lee, J. Choi, P. Kim, K. Choi, S. Kim, W. Shon and K. Park, *Toxicol. Res. (Cambridge, U. K.)*, 2012, **28**, 139-141.
32. A. Weir, P. Westerhoff, L. Fabricius, K. Hristovski and N. von Goetz, *Environ. Sci. Technol.*, 2012, **46**, 2242-2250.
33. K. Donaldson, D. Brown, A. Clouter, R. Duffin, W. MacNee, L. Renwick, L. Tran and V. Stone, *J. Aerosol Med.*, 2002, **15**, 213-220.
34. W. Z. Teo, A. Ambrosi and M. Pumera, *Electrochem. Commun.*, 2013, **28**, 51-53.

35. M. Giovanni and M. Pumera, *Electrochem. Commun.*, 2011, **13**, 203-204.
36. M. Giovanni, A. Ambrosi and M. Pumera, *Chem.-Asian. J.*, 2012, **7**, 702-706.
37. A. Gillespie, D. Jao, A. Andriola, T. Duda, C. F. Yang and L. Yu, *Anal. Lett.*, 2012, **45**, 1310-1320.
38. E. J. E. Stuart, K. Tschulik, J. Ellison and R. G. Compton, *Electroanalysis*, 2014, **26**, 285-291.
39. E. J. Stuart, K. Tschulik, D. Omanovic, J. T. Cullen, K. Jurkschat, A. Crossley and R. G. Compton, *Nanotechnology*, 2013, **24**, 444002.
40. E. J. E. Stuart, N. V. Rees, J. T. Cullen and R. G. Compton, *Nanoscale*, 2013, **5**, 174-177.
41. E. J. E. Stuart, K. Tschulik, C. Batchelor-McAuley and R. G. Compton, *ACS Nano*, 2014, **8**, 7648-7654.
42. Y.-G. Zhou, N. V. Rees and R. G. Compton, *Angew. Chem. Int. Ed.*, 2011, **50**, 4219-4221.
43. S. J. Kwon, F.-R. F. Fan and A. J. Bard, *J. Am. Chem. Soc.*, 2010, **132**, 13165-13167.
44. A. Kuzma, M. Weis, S. Flickyngerova, J. Jakabovic, A. Satka, E. Dobrocka, J. Chlpik, J. Cirak, M. Donoval, P. Telek, F. Uherek and D. Donoval, *J. Appl. Phys.*, 2012, **112**, 103531.
45. J. Manson, D. Kumar, B. J. Meenan and D. Dixon, *Gold Bull.*, 2011, **44**, 99-105.
46. Y. Tan, Y. Li and D. Zhu, *Langmuir*, 2002, **18**, 3392-3395.
47. E. Tomaszewska, K. Soliwoda, K. Kadziola, B. Tkacz-Szczesna, G. Celichowski, M. Cichomski, W. Szmaja and J. Grobelny, *J. Nanomater.*, 2013, **2013**, Article ID 313081.
48. R. F. Domingos, M. A. Baalousha, Y. Ju-Nam, M. M. Reid, N. Tufenkji, J. R. Lead, G. G. Leppard and K. J. Wilkinson, *Environ. Sci. Technol.*, 2009, **43**, 7277-7284.
49. M. Vert, Y. Doi, K.-H. Hellwich, M. Hess, P. Hodge, P. Kubisa, M. Rinaudo and F. Schué, *Pure Appl. Chem.*, 2012, **84**, 377-410.
50. M. I. Stockman, *Opt. Express*, 2011, **19**, 22029-22106.
51. D. D. Evanoff, Jr. and G. Chumanov, *J. Phys. Chem. B*, 2004, **108**, 13957-13962.
52. I. Diez and R. H. A. Ras, *Nanoscale*, 2011, **3**, 1963-1970.
53. A. Otto, *Z. Phys. A: Hadrons Nucl.*, 1968, **216**, 398-410.
54. C. N. R. Rao, G. U. Kulkarni, P. J. Thomas and P. P. Edwards, *Chem. Soc. Rev.*, 2000, **29**, 27-35.
55. J. Li and J.-J. Zhu, *Analyst*, 2013, **138**, 2506-2515.
56. C. Nützenadel, A. Züttel, D. Chartouni, G. Schmid and L. Schlapbach, *Eur. Phys. J. D*, 2000, **8**, 245-250.
57. K. Esumi, R. Isono and T. Yoshimura, *Langmuir*, 2004, **20**, 237-243.
58. N. Pradhan, A. Pal and T. Pal, *Colloids Surf., A*, 2002, **196**, 247-257.
59. L. Yin and J. Liebscher, *Chem. Rev.*, 2007, **107**, 133-173.
60. W. J. Plieth, *J. Phys. Chem.*, 1982, **86**, 3166-3170.
61. F. G. Shi, *J. Mater. Res.*, 2011, **9**, 1307-1314.
62. S. E. Ward Jones, F. W. Campbell, R. Baron, L. Xiao and R. G. Compton, *J. Phys. Chem. C*, 2008, **112**, 17820-17827.
63. M. Giovanni and M. Pumera, *Electroanalysis*, 2012, **24**, 615-617.
64. X. Li, J. J. Lenhart and H. W. Walker, *Langmuir*, 2010, **26**, 16690-16698.
65. A. M. El Badawy, K. G. Scheckel, M. Suidan and T. Tolaymat, *Sci. Total Environ.*, 2012, **429**, 325-331.
66. K. A. Huynh and K. L. Chen, *Environ. Sci. Technol.*, 2011, **45**, 5564-5571.
67. J. Zeng, Y. Zheng, M. Rycenga, J. Tao, Z.-Y. Li, Q. Zhang, Y. Zhu and Y. Xia, *J. Am. Chem. Soc.*, 2010, **132**, 8552-8553.
68. T. R. Jensen, M. D. Malinsky, C. L. Haynes and R. P. Van Duyne, *J. Phys. Chem. B*, 2000, **104**, 10549-10556.
69. A. K. Singh, V. Viswanath and V. C. Janu, *J. Lumin.*, 2009, **129**, 874-878.
70. X. Liu, M. Atwater, J. Wang and Q. Huo, *Colloids Surf., B*, 2007, **58**, 3-7.
71. *Progress in Medicinal Chemistry*, ed. G. P. Ellis and D. K. Luscombe, Elsevier, Amsterdam, 1992.
72. C. Batchelor-McAuley, K. Tschulik, C. C. M. Neumann, E. Laborda and R. G. Compton, *Int. J. Electrochem. Sci.*, 2014, **9**, 1132-1138.

73. C. Carlson, S. M. Hussain, A. M. Schrand, L. K. Braydich-Stolle, K. L. Hess, R. L. Jones and J. J. Schlager, *J. Phys. Chem. B*, 2008, **112**, 13608-13619.
74. H.-L. Su, C.-C. Chou, D.-J. Hung, S.-H. Lin, I.-C. Pao, J.-H. Lin, F.-L. Huang, R.-X. Dong and J.-J. Lin, *Biomaterials*, 2009, **30**, 5979-5987.
75. A. Lapresta-Fernández, A. Fernández and J. Blasco, *TrAC, Trends Anal. Chem.*, 2012, **32**, 40-59.
76. Silvercare, http://www.silvercare.co.za/ (Accessed 4th Feb 2014).
77. Magical Socks Nanosilver with Silver Nanoparticles, http://www.nanosilver.eu/Tema/Why-Nanosilver/Magical-Socks-Nanosilver-with-Silver-Nanoparticles (Accessed 4th Feb 2014).
78. C. Musante and J. C. White, *Environ. Toxicol.*, 2012, **27**, 510-517.
79. R. K. Kunkalekar, M. M. Naik, S. K. Dubey and A. V. Salker, *J. Chem. Technol. Biotechnol.*, 2013, **88**, 873-877.
80. Y. Park, H. J. Noh, L. Han, H.-S. Kim, Y.-J. Kim, J. S. Choi, C.-K. Kim, Y. S. Kim and S. Cho, *J. Nanosci. Nanotechnol.*, 2012, **12**, 7087-7095.
81. B. Vaseeharan, P. Ramasamy and J. C. Chen, *Lett. Appl. Microbiol.*, 2010, **50**, 352-356.
82. ZinClear™ IM Zinc Oxide Dispersions, http://www.dow.com/personalcare/technologies/uvtechnologies/zinclear.htm (Accessed 5th Feb 2014).
83. F. J. Moloney, S. Collins and G. M. Murphy, *Am. J. Clin. Dermatol.*, 2002, **3**, 185-191.
84. A. Walther and A. H. E. Müller, *Soft Matter*, 2008, **4**, 663-668.
85. A. Synytska, R. Khanum, L. Ionov, C. Cherif and C. Bellmann, *ACS Appl. Mater. Interfaces*, 2011, **3**, 1216-1220.
86. Nanotechnology: A Realistic Market Assessment, http://www.bccresearch.com/market-research/nanotechnology/nanotechnology-market-applications-products-nan031e.html (Accessed 4th Feb 2014).
87. E. Mantovani, A. Porcari. M. D. Morrison and R. E. Geertsma, *Developments in Nanotechnologies Regulation and Standards 2011 - Report of The Observatory Nano.,* http://www.steptoe.com/assets/htmldocuments/DevelopmentsInNanotechnologiesRegulationandStandards_20111.pdf (Accessed 4th Feb 2014).
88. MHRA - How we regulate nanotechnology, http://www.mhra.gov.uk/Howweregulate/Nanotechnology/ (Accessed 4th Feb 2014)
89. European Commission - Nanotechnology, http://ec.europa.eu/nanotechnology/policies_en.html#strategy (Accessed 4th Feb 2014)
90. Legifrance - Décret n° 2012-232 du 17 février 2012 relatif à la déclaration annuelle des substances à l'état nanoparticulaire pris en application de l'article L. 523-4 du code de l'environnement, http://www.legifrance.gouv.fr/affichTexte.do?cidTexte=JORFTEXT000025377246&dateTexte=&categorieLien=id (Accessed 4th Feb 2014).
91. D. S. L. Jarvis and N. Richmond, Regulation and Governance of Nanotechnology in China: Regulatory Challenges and Effectiveness. *European Journal of Law and Technology*, **2011,** Vol. 2, No.3.
92. G. Oberdörster, A. Maynard, K. Donaldson, V. Castranova, J. Fitzpatrick, K. Ausman, J. Carter, B. Karn, W. Kreyling, D. Lai, S. Olin, N. Monteiro-Riviere, D. Warheit and H. Yang, *Part. Fibre Toxicol.*, 2005, **2**, 8.
93. S. L. Flegler, J. W. Heckman Jr. and K. L. Klomparens, *Scanning and Transmission Electron Microscopy: An Introduction*, Oxford University Press, New York, 1993.
94. A. M. Collins, *Nanotechnology Cookbook*, Elsevier, Oxford, UK, 2012.
95. *Handbook of Charged Particle Optics,* ed. J. Orloff, 2nd edn.,CRC Press, Florida, 2008.
96. R. F. Egerton, P. Li and M. Malac, *Micron*, 2004, **35**, 399-409.
97. D. B. Williams and C. B. Carter, *Transmission Electron Microscope*, 2nd edn., Springer, New York, 1996.
98. P. E. Batson, N. Dellby and O. L. Krivanek, *Nature (London, U. K.)*, 2002, **418**, 617-620.
99. D. Philip, *Phys. E (Amsterdam, Neth.)*, 2010, **42**, 1417-1424.

100. L. Reimer and H. Kohl, *Transmission Electron Microscopy*, 5th edn., Springer, New York, 2008.
101. R. F. Egerton, *Ultramicroscopy*, 1980, **5**, 521-523.
102. K. J. J. Mayrhofer, S. J. Ashton, J. C. Meier, G. K. H. Wiberg, M. Hanzlik and M. Arenz, *J. Power Sources*, 2008, **185**, 734-739.
103. Nanosight - Nanoparticle Tracking Analysis, http://www.nanosight.com/technology/nanoparticle-tracking-analysis-nta (Accessed 23 Mar 2014).
104. J. T. Edward, *J. Chem. Educ.*, 1970, **47**, 261-270.
105. Nanosight - FAQs, http://www.nanosight.com/resources/faqs (Accessed 23 Mar 2014).
106. *Dynamic Light Scattering: Applications of Photon Correlation Spectroscopy,* ed. R. Pecora, Springer, New York, 1985.
107. P. van der Meeren, H. Bogaert, J. Vanderdeelen and L. Baert, *Part. Part. Syst. Char.*, 1992, **9**, 138-143.
108. Malvern Instruments Ltd - Zetasizer Nano Range, http://malvern.bsky.net/labeng/products/zetasizer/zetasizer_nano.htm (Accessed 28 Mar 2014)
109. *Principles, Methods and Application of Particle Size Analysis,* ed. J. P. M. Syvutski, Cambridge University Press, Cambridge, 1997.
110. Perkin Elmer - The 30-Minute Guide to ICP-MS, http://www.perkinelmer.co.uk/CMSResources/Images/44-74849tch_icpmsthirtyminuteguide.pdf (Accessed 26 Mar 2014).
111. C. G. Herbert and R. A. W. Johnstone, *Mass Spectrometry Basics*, CRC Press LLC, Florida, 2003.
112. Y. Waseda, E. Matsubara and K. Shinoda, *X-ray Diffraction Crystallography: Introduction, Examples and Solved Problem*, Springer-Verlag, Berlin, 2011.
113. B. E. Warren, *X-ray diffraction*, Courier Dover Publication, New York, 2012.
114. *Practical Surface Analysis: Auger and X-ray Photoelectron Spectroscopy,* ed. D. Briggs and M. P. Seah, 2nd edn., John Wiley and Sons Ltd, Chichester, 1990.
115. K. L. Kelly, E. Coronado, L. L. Zhao and G. C. Schatz, *J. Phys. Chem. B*, 2003, **107**, 668-677.
116. A. Morrin, A. J. Killard and M. R. Smyth, *Anal. Lett.*, 2003, **36**, 2021-2039.
117. J. Wang, M. Pedrero, H. Sakslund, O. Hammerich and J. Pingarron, *Analyst*, 1996, **121**, 345-350.
118. V. K. Rao, M. K. Sharma, P. Pandey and K. Sekhar, *World J. Microbiol. Biotechnol.*, 2006, **22**, 1135-1143.
119. N. Thiyagarajan, J.-L. Chang, K. Senthilkumar and J.-M. Zen, *Electrochem. Commun.*, 2014, **38**, 86-90.
120. A. A. Rowe, A. J. Bonham, R. J. White, M. P. Zimmer, R. J. Yadgar, T. M. Hobza, J. W. Honea, I. Ben-Yaacov and K. W. Plaxco, *PLoS One*, 2011, **6**, e23783.
121. K. E. Toghill and R. G. Compton, *Int. J. Electrochem. Sci.*, 2010, **5**, 1246-1301.
122. J. Wang, *Chem. Rev.*, 2008, **108**, 814-825.
123. X.-J. Huang, L. Aldous, A. M. O'Mahony, F. J. del Campo and R. G. Compton, *Anal. Chem.*, 2010, **82**, 5238-5245.
124. M. C. Buzzeo, C. Hardacre and R. G. Compton, *Anal. Chem.*, 2004, **76**, 4583-4588.
125. S. Neethirajan, D. S. Jayas and S. Sadistap, *Food Bioprocess Technol.*, 2008, **2**, 115-121.
126. J. Wang, *Electroanalysis*, 2005, **17**, 1341-1346.
127. D. Q. Hung, O. Nekrassova and R. G. Compton, *Talanta*, 2004, **64**, 269-277.
128. R. T. Kachoosangi, G. G. Wildgoose and R. G. Compton, *Analyst*, 2008, **133**, 888-895.
129. S. A. Blaser, M. Scheringer, M. Macleod and K. Hungerbühler, *Sci. Total Environ.*, 2008, **390**, 396-409.
130. E. Laborda, J. González and Á. Molina, *Electrochem. Commun.*, 2014, **43**, 25-30.
131. J. Wang, *Analytical Electrochemistry*, 2nd edn., Wiley-VCH, New York, 2001.
132. X.-F. Zhou, W. Cheng, C. Batchelor-McAuley, K. Tschulik and R. G. Compton, *Electroanalysis*, 2014, **26**, 248-253.

133. M. Pumera, M. Aldavert, C. Mills, A. Merkoçi and S. Alegret, *Electrochim. Acta*, 2005, **50**, 3702-3707.
134. C. E. Banks, J. Kruusma, R. R. Moore, P. Tomčík, J. Peters, J. Davis, S. Komorsky-Lovrić and R. G. Compton, *Talanta*, 2005, **65**, 423-429.
135. A. J. Saterlay, C. Agra-Gutiérrez, M. P. Taylor, F. Marken and R. G. Compton, *Electroanalysis*, 1999, **11**, 1083-1088.
136. A. J. Saterlay, J. S. Foord and R. G. Compton, *Analyst*, 1999, **124**, 1791-1796.
137. A. J. Saterlay, D. F. Tibbetts and R. G. Compton, *Analytical Sciences*, 2000, **16**, 1055-1060.
138. K. Tschulik, C. Batchelor-McAuley, H. S. Toh, E. J. Stuart and R. G. Compton, *Phys. Chem. Chem. Phys.*, 2014, **16**, 616-623.
139. C. C. M. Neumann, C. Batchelor-McAuley, K. Tschulik, H. S. Toh, P. Shumbula, J. Pillay, R. Tshikhudo and R. G. Compton, *ChemElectroChem*, 2014, **1**, 87-89.
140. Y. Wang, E. Laborda, B. J. Plowman, K. Tschulik, K. R. Ward, R. G. Palgrave, C. Damm and R. G. Compton, *Phys. Chem. Chem. Phys.*, 2014, **16**, 3200-3208.
141. R. G. Compton, F. J. Davis and S. C. Grant, *J. Appl. Electrochem.*, 1986, **16**, 239-249.
142. K. Tschulik, R. G. Palgrave, C. Batchelor-McAuley and R. G. Compton, *Nanotechnology*, 2013, **24**, 295502.
143. W. Cheng, E. J. E. Stuart, K. Tschulik, J. T. Cullen and R. G. Compton, *Nanotechnology*, 2013, **24**, 505501.
144. E. J. E. Stuart, K. Tschulik, D. Lowinsohn, J. T. Cullen and R. G. Compton, *Sens. Actuators, B*, 2014, **195**, 223-229.
145. C. Batchelor-McAuley, A. Martinez-Marrades, K. Tschulik, A. N. Patel, C. Combellas, F. Kanoufi, G. Tessier and R. G. Compton, *Chem. Phys. Lett.*, 2014, **597**, 20-25.
146. S. Munteanu, J. P. Roger, Y. Fedala, F. Amiot, C. Combellas, G. Tessier and F. Kanoufi, *Faraday Discuss.*, 2013, **164**, 241-258.
147. C. K. Chua and M. Pumera, *Electrophoresis*, 2013, **34**, 2007-2010.
148. N. V. Rees, *Electrochem. Commun.*, 2014, **43**, 83-86.
149. W. Wang and N. Tao, *Anal. Chem.*, 2014, **86**, 2-14.
150. N. V. Rees, Y.-G. Zhou and R. G. Compton, *RSC Adv.*, 2012, **2**, 379-384.
151. W. Cheng and R. G. Compton, *TrAC, Trends Anal. Chem.*, 2014, **58**, 79-89.
152. A. B. Holland and J. R. Sawers, *Photogr. Sci. Eng.*, 1973, **17**, 295-298.
153. V. Žutić, V. Svetlicic and J. Tomaic, *Pure Appl. Chem.*, 1990, **62**, 2269-2276.
154. V. Svetličić, V. Žutić, J. Chevalet and J. Clavilier, *Mol. Cryst. Liq. Cryst.*, 1984, **113**, 93-104.
155. F. Scholz, D. Hellberg, F. Harnisch, A. Hummel and U. Hasse, *Electrochem. Commun.*, 2004, **6**, 929-933.
156. D. Hellberg, F. Scholz, F. Schauer and W. Weitschies, *Electrochem. Commun.*, 2002, **4**, 305-309.
157. C. E. Banks, N. V. Rees and R. G. Compton, *J. Electroanal. Chem.*, 2002, **535**, 41-47.
158. C. E. Banks, N. V. Rees and R. G. Compton, *J. Phys. Chem. B*, 2002, **106**, 5810-5813.
159. N. V. Rees, C. E. Banks and R. G. Compton, *J. Phys. Chem. B*, 2004, **108**, 18391-18394.
160. A. D. Clegg, N. V. Rees, C. E. Banks and R. G. Compton, *ChemPhysChem*, 2006, **7**, 807-911.
161. Y.-G. Zhou, B. Haddou, N. V. Rees and R. G. Compton, *Phys. Chem. Chem. Phys.*, 2012, **14**, 14354-14357.
162. N. V. Rees, Y.-G. Zhou and R. G. Compton, *ChemPhysChem*, 2011, **12**, 1645-1647.
163. J. Ellison, K. Tschulik, E. J. Stuart, K. Jurkschat, D. Omanović, M. Uhlemann, A. Crossley and R. G. Compton, *ChemistryOpen*, 2013, **2**, 69-75.
164. J. C. Lees, J. Ellison, C. Batchelor-McAuley, K. Tschulik, C. Damm, D. Omanović and R. G. Compton, *ChemPhysChem*, 2013, **14**, 3895-3897.
165. E. J. E. Stuart, K. Tschulik, D. Omanović, J. T. Cullen, K. Jurkschat, A. Crossley and R. G. Compton, *Nanotechnology*, 2013, **24**, 444002.
166. Y.-G. Zhou, N. V. Rees and R. G. Compton, *Chem. Commun.*, 2012, **48**, 2510-2512.
167. N. V. Rees, Y.-G. Zhou and R. G. Compton, *Chem. Phys. Lett.*, 2012, **525-526**, 69-71.
168. Y.-G. Zhou, N. V. Rees and R. G. Compton, *ChemPhysChem*, 2011, **12**, 2085-2087.

169. K. Tschulik, B. Haddou, D. Omanović, N. V. Rees and R. G. Compton, *Nano Res.*, 2013, **6**, 836-841.
170. Y.-G. Zhou, N. V. Rees and R. G. Compton, *Phys. Chem. Chem. Phys.*, 2013, **15**, 761-763.
171. Y.-G. Zhou, E. J. E. Stuart, J. Pillay, S. Vilakazi, R. Tshikhudo, N. V. Rees and R. G. Compton, *Chem. Phys. Lett.*, 2012, **551**, 68-71.
172. Y.-G. Zhou, N. V. Rees, J. Pillay, R. Tshikhudo, S. Vilakazi and R. G. Compton, *Chem. Commun.*, 2012, **48**, 224-226.
173. D. Qiu, S. Wang, Y. Zheng and Z. Deng, *Nanotechnology*, 2013, **24**, 505707.
174. W. Cheng, X.-F. Zhou and R. G. Compton, *Angew. Chem. Int. Ed.*, 2013, **52**, 12980-12982.
175. Y.-G. Zhou, N. V. Rees and R. G. Compton, *Chem. Phys. Lett.*, 2011, **511**, 183-186.
176. X.-F. Zhou, W. Cheng and R. G. Compton, *Nanoscale*, 2014, **6**, 6873-6878.
177. W. Cheng and R. G. Compton, *Angew. Chem. Int. Ed.*, 2014, **53**, 13928-13930.
178. J. Dunevall, H. Fathali, N. Najafinobar, J. Lovric, J. Wigstrom, A. S. Cans and A. G. Ewing, *J. Am. Chem. Soc.*, 2015, **137**, 4344-4346.
179. C. Batchelor-McAuley, J. Ellison, K. Tschulik, P. L. Hurst, R. Boldt and R. G. Compton, *Analyst*, 2015, **140,** 5048-5054.
180. G. P. Santos, A. F. A. A. Melo and F. N. Crespilho, *Phys. Chem. Chem. Phys.*, 2014, **16**, 8012-8018.
181. E. J. E. Stuart, N. V. Rees and R. G. Compton, *Chem. Phys. Lett.*, 2012, **531**, 94-97.
182. X. Xiao and A. J. Bard, *J. Am. Chem. Soc.*, 2007, **129**, 9610-9612.
183. J. M. Kahk, N. V. Rees, J. Pillay, R. Tshikhudo, S. Vilakazi and R. G. Compton, *Nano Today*, 2012, **7**, 174-179.
184. N. P. Sardesai, D. Andreescu and S. Andreescu, *J. Am. Chem. Soc.*, 2013, **135**, 16770-16773.
185. X. Xiao, F.-R. F. Fan, J. Zhou and A. J. Bard, *J. Am. Chem. Soc.*, 2008, **130**, 16669-16677.
186. H. Zhou, J. H. Park, F.-R. F. Fan and A. J. Bard, *J. Am. Chem. Soc.*, 2012, **134**, 13212-13215.
187. J. H. Park, A. Boika, H. S. Park, H. C. Lee and A. J. Bard, *J. Phys. Chem. C*, 2013, **117**, 6651-6657.
188. I. J. Streeter and R. G. Compton, *J. Phys. Chem. C*, 2007, **111**, 18049-18054.
189. K. R. Ward, N. S. Lawrence, R. Seth Hartshorne and R. G. Compton, *J. Electroanal. Chem.*, 2012, **683**, 37-42.
190. P. A. Bobbert, M. M. Wind and J. Vlieger, *Physica A (Amsterdam)*, 1987, **141**, 58-72.
191. R. Dasari, D. A. Robinson and K. J. Stevenson, *J. Am. Chem. Soc.*, 2013, **135**, 570-573.
192. S. E. F. Kleijn, B. Serrano-Bou, A. I. Yanson and M. T. M. Koper, *Langmuir*, 2013, **29**, 2054-2064.
193. A. Fernando, S. Parajuli and M. A. Alpuche-Aviles, *J. Am. Chem. Soc.*, 2013, **135**, 10894-10897.
194. E. J. F. Dickinson, N. V. Rees and R. G. Compton, *Chem. Phys. Lett.*, 2012, **528**, 44-48.
195. X. Xiao, S. Pan, J. S. Jang, F.-R. F. Fan and A. J. Bard, *J. Phys. Chem. C*, 2009, **113**, 14978-14982.
196. H. Zhou, F.-R. F. Fan and A. J. Bard, *J. Phys. Chem. Lett.*, 2010, **1**, 2671-2674.
197. Y.-G. Zhou, N. V. Rees and R. G. Compton, *Chem. Phys. Lett.*, 2011, **514**, 291-293.
198. T. R. Bartlett, S. V. Sokolov and R. G. Compton, *ChemistryOpen*, 2015, DOI: 10.1002/open.201500061.
199. S. E. F. Kleijn, S. C. S. Lai, T. S. Miller, A. I. Yanson, M. T. M. Koper and P. R. Unwin, *J. Am. Chem. Soc.*, 2012, **134**, 18558-18561.
200. S. Eloul and R. G. Compton, *ChemElectroChem*, 2014, **1**, 917-924.
201. J. Ellison, C. Batchelor-McAuley, K. Tschulik and R. G. Compton, *Sens. Actuators, B*, 2014, **200**, 47-52.
202. S. J. Cloake, H. S. Toh, P. T. Lee, C. Salter, C. Johnston and R. G. Compton, *ChemistryOpen*, 2015, **4**, 22-26.
203. H. S. Toh, C. Batchelor-McAuley, K. Tschulik, M. Uhlemann, A. Crossley and R. G. Compton, *Nanoscale*, 2013, **5**, 4884-4893.

204. H. S. Toh and R. G. Compton, *ChemistryOpen*, 2015, **4**, 261-263.
205. H. S. Toh, K. Jurkschat and R. G. Compton, *Chem.-Eur. J.*, 2015, **21**, 2998-3004.
206. M. Pumera, S. Sánchez, I. Ichinose and J. Tang, *Sens. Actuators, B*, 2007, **123**, 1195-1205.
207. C. M. Welch and R. G. Compton, *Anal. Bioanal. Chem.*, 2006, **384**, 601-619.
208. F. W. Campbell and R. G. Compton, *Anal. Bioanal. Chem.*, 2010, **396**, 241-259.
209. M. T. Castañeda, A. Merkoçi, M. Pumera and S. Alegret, *Biosens. Bioelectron.*, 2007, **22**, 1961-1967.
210. I. Willner, B. Willner and R. Tel-Vered, *Electroanalysis*, 2011, **23**, 13-28.
211. C. Batchelor-McAuley, G. G. Wildgoose and R. G. Compton, *Biosens. Bioelectron.*, 2009, **24**, 3183-3190.
212. A. Merkoçi, *Electroanalysis*, 2013, **25**, 15-27.
213. K. E. Toghill and R. G. Compton, *Electroanalysis*, 2010, **22**, 1947-1956.
214. K. Z. Brainina, L. G. Galperin and E. V. Vikulova, *J. Solid State Electrochem.*, 2012, **16**, 2357-2363.
215. B. Medasani, Y. H. Park and I. Vasiliev, *Phys. Rev. B: Condens. Matter Mater. Phys.,* 2007, **75**, 235436.
216. K. K. Nanda, A. Maisels, F. E. Kruis, H. Fissan and S. Stappert, *Phys. Rev. Lett.*, 2003, **91**, 106102.
217. K. Z. Brainina, L. G. Galperin, E. V. Vikulova, N. Y. Stozhko, A. M. Murzakaev, O. R. Timoshenkova and Y. A. Kotov, *J. Solid State Electrochem.*, 2010, **15**, 1049-1056.
218. K. Z. Brainina, L. G. Galperin and A. L. Galperin, *J. Solid State Electrochem.*, 2009, **14**, 981-988.
219. K. Z. Brainina, L. G. Galperin, T. Y. Kiryuhina, A. L. Galperin, N. Y. Stozhko, A. M. Murzakaev and O. R. Timoshenkova, *J. Solid State Electrochem.*, 2011, **16**, 2365-2372.
220. L. Tang, X. Li, R. C. Cammarata, C. Friesen and K. Sieradzki, *J. Am. Chem. Soc.*, 2010, **132**, 11722-11726.
221. T. J. Davies, C. E. Banks and R. G. Compton, *J. Solid State Electrochem.*, 2005, **9**, 797-808.
222. T. J. Davies and R. G. Compton, *J. Electroanal. Chem.*, 2005, **585**, 63-82.
223. C. Amatore, S. Szunerits, L. Thouin and J.-S. Warkocz, *J. Electroanal. Chem.*, 2001, **500**, 62-70.
224. A. Molina, J. González, E. Laborda and R. G. Compton, *Phys. Chem. Chem. Phys.*, 2013, **15**, 2381-2388.
225. A. Molina, J. González, M. C. Henstridge and R. G. Compton, *Electrochim. Acta*, 2011, **56**, 4589-4594.
226. P. C. Lee and D. Meisel, *J. Phys. Chem.*, 1982, **86**, 3391-3395.
227. A. Pyatenko, M. Yamaguchi and M. Suzuki, *J. Phys. Chem. C*, 2007, **111**, 7910-7917.
228. J. J. Mock, M. Barbic, D. R. Smith, D. A. Schultz and S. Schultz, *J. Chem. Phys.*, 2002, **116**, 6755-6759.
229. A. P. Stevenson, D. Blanco Bea, S. Civit, S. Antoranz Contera, A. Iglesias Cerveto and S. Trigueros, *Nanoscale Res. Lett.*, 2012, **7**, 151.
230. *IUPAC. Compendium of Chemical Terminology, (the "Gold Book").* Compiled by A. D. McNaught and A. Wilkinson. 2nd ed., Blackwell Scientific Publications, Oxford, 1997.
231. K. Z. Brainina, L. G. Galperin, E. V. Vikulova and A. L. Galperin, *J. Solid State Electrochem.*, 2012, **17**, 43-53.
232. C. C. M. Neumann, E. Laborda, K. Tschulik, K. R. Ward and R. G. Compton, *Nano Res.*, 2013, **6**, 511-524.
233. D. B. Williams and C. B. Carter, *Transmission Electron Microscopy*, Springer, New York, USA, 1996.
234. H. Bönnemann and Ryan M. Richards, *Eur. J. Inorg. Chem.*, 2001, **2001**, 2455-2480.
235. W. Z. Teo and M. Pumera, *RSC Adv.*, 2014, **4**, 5006-5011.
236. K. D. Kim, D. N. Han and H. T. Kim, *Chem. Eng. J.*, 2004, **104**, 55-61.
237. B. Dobias, X. Qiu and W. V. Rybinski, *Solid-Liquid Dispersions*, Mercel Dekker Inc., New York, 1999, vol. 81, pp. 127,255.
238. P. Raveendran, J. Fu and S. L. Wallen, *J. Am. Chem. Soc.*, 2003, **125**, 13940-13941.

239. C. Luo, Y. Zhang, X. Zeng, Y. Zeng and Y. Wang, *J. Colloid Interface Sci.*, 2005, **288**, 444-448.
240. Z. S. Pillai and P. V. Kamat, *J. Phys. Chem. B*, 2004, **108**, 945-951.
241. A. Pyatenko, M. Yamaguchi and M. Suzuki, *J. Phys. Chem. B*, 2005, **109**, 21608-21611.
242. S. Bhattacharya, A. Srivastava and A. Pal, *Angew. Chem. Int. Ed.*, 2006, **118**, 3000-3003.
243. J. N. Kuhn, C.-K. Tsung, W. Huang and G. A. Somorjai, *J. Catal.*, 2009, **265**, 209-215.
244. L. Kvítek, A. Panáček, J. Soukupová, M. Kolář, R. Večeřová, R. Prucek, M. Holecová and R. Zbořil, *J. Phys. Chem. C*, 2008, **112**, 5825-5834.
245. D. D. Evanoff, Jr. and G. Chumanov, *ChemPhysChem*, 2005, **6**, 1221-1231.
246. W. Haiss, N. T. K. Thanh, J. Aveyard and D. G. Fernig, *Anal. Chem.*, 2007, **79**, 4215-4221.
247. M. S. Abd El-sadek, A. Y. Nooralden, S. Moorthy Babu and P. K. Palanisamy, *Opt. Commun.*, 2011, **284**, 2900-2904.
248. M. K. Temgire and S. S. Joshi, *Radiat. Phys. Chem.*, 2004, **71**, 1039-1044.
249. M. Stevanović, B. Kovačević, J. Petković, M. Filipič and D. Uskoković, *Int. J. Nanomed.*, 2011, **6**, 2837-2847.
250. X.-F. Zhou, W. Cheng, C. Batchelor-Mcauley, K. Tschulik and R. G. Compton, *Electroanalysis*, 2014, **26**, 248-253.
251. M. Mannini, *Molecular Magnetic Materials on Solid Surfaces*, Firenze University Press, Firenze, 2008.
252. E. Kätelhön, W. Cheng, C. Batchelor-McAuley, K. Tschulik and R. G. Compton, *ChemElectroChem*, 2014, **1**, 1057-1062.
253. E. Kätelhön and R. G. Compton, *Analyst*, 2014, **139**, 2411-2415.
254. H. S. Toh and R. G. Compton, *Chem. Sci.*, 2015, **6**, 5053-5058.
255. T. R. Bartlett, C. Batchelor-McAuley, K. Tschulik, K. Jurkschat and R. G. Compton, *ChemElectroChem*, 2015, **2**, 522-528.
256. B. K. Kim, J. Kim and A. J. Bard, *J. Am. Chem. Soc.*, 2015, **137**, 2343-2349.
257. A. Oleinick, F. Lemaître, M. G. Collignon, I. Svir and C. Amatore, *Faraday Discuss.*, 2013, **164**, 33-55.
258. L. Stryer, *Biochemistry*, W. H. Freeman and Company, New York, US, 1995.
259. G. Taddei, *Colloid. Polym. Sci.*, 1994, **272**, 1300-1305.
260. G. R. Thompson, *J. Clin. Pathol., Suppl. (R. Coll. Pathol.)*, 1971, **5**, 85-89.
261. H. Hart, C. M. Hadad, L. Craine and D. J. Hart, *Organic Chemistry: A Short Course*, 13th edn., Brooks/Cole, Belmont, 2012.
262. *Electrokinetic Chromatography: Theory, Instrumentation and Applications*, John Wiley & Sons, Ltd, Chichester, 2006.
263. S. Svenson, *Reactions And Synthesis In Surfactant Systems*, Marcel Dekker, Inc., New York, 2001.
264. P. Atkins and J. de Paula, *Physical Chemistry for the Life Sciences*, 2nd edn., Oxford University Press, Oxford, 2011.
265. S. Porebski, L. G. Bailey and B. R. Baum, *Plant Mol. Biol. Rep.*, 1997, **15**, 8-15.
266. S. O. Rogers and A. J. Bendich, *Plant Mol. Biol.*, 1985, **5**, 69-76.
267. M. A. Lodhi, G.-N. Ye, N. F. Weeden and B. I. Reisch, *Plant Mol. Biol. Rep.*, 1994, **12**, 6-13.
268. K. Kuperkar, L. Abezgauz, K. Prasad and P. Bahadur, *J. Surfactants Deterg.*, 2010, **13**, 293-303.
269. M. Khamis, B. Bulos, F. Jumean, A. Manassra and M. Dakiky, *Dyes Pigm.*, 2005, **66**, 179-183.
270. A. Chatterjee, S. Maiti, S. K. Sanyal and S. P. Moulik, *Langmuir*, 2002, **18**, 2998-3004.
271. M. J. Blandamer, P. M. Cullis, L. G. Soldi, K. Chowdoji Rao and M. C. S. Subha, *J. Therm. Anal.*, 1996, **46**, 1583-1588.
272. G. D. Allen, M. C. Buzzeo, C. Villagrán, C. Hardacre and R. G. Compton, *J. Electroanal. Chem.*, 2005, **575**, 311-320.
273. V. Livshits, A. Ulus and E. Peled, *Electrochem. Commun.*, 2006, **8**, 1358-1362.
274. C. Amatore, Y. Bouret, E. Maisonhaute, J. I. Goldsmith and H. D. Abruña, *Chem.-Eur. J.*, 2001, **7**, 2206-2226.

275. H. S. Toh, C. Batchelor-McAuley, K. Tschulik, C. Damm and R. G. Compton, *Sens. Actuators, B*, 2014, **193**, 315-319.
276. H. S. Toh, K. Tschulik, C. Batchelor-McAuley and R. G. Compton, *Analyst*, 2014, **139**, 3986-3990.
277. H. S. Toh, C. Batchelor-McAuley, K. Tschulik and R. G. Compton, *Analyst*, 2013, **138**, 4292-4297.
278. K. H. Brainina and E. Neyman, *Electroanalytical Stripping Methods*, Wiley, New York, 1994.
279. S. E. Ward Jones, F. G. Chevallier, C. A. Paddon and R. G. Compton, *Anal. Chem.*, 2007, **79**, 4110-4119.
280. O. M. S. Filipe and C. M. A. Brett, *Talanta*, 2003, **61**, 643-650.
281. W. Davison and J. A. Harrison, *J. Electroanal. Chem. Interfacial Electrochem.*, 1973, **44**, 213-219.
282. J. C. Ball and R. G. Compton, *Electroanalysis*, 1997, **9**, 1305-1310.
283. G. Forsberg, J. W. O'Laughlin, R. G. Megargle and S. R. Koirtyihann, *Anal. Chem.*, 1975, **47**, 1586-1592.
284. J. C. Duinker and C. J. M. Kramer, *Mar. Chem.*, 1977, **5**, 207-228.
285. G. Gillain, G. Duyckaerts and A. Disteche, *Anal. Chim. Acta,* 1979, **106**, 23-37.
286. J. C. Ball and R. G. Compton, *J. Phys. Chem. B*, 1998, **102**, 3967-3973.
287. D. E. Schildkraut, P. T. Dao, J. P. Twist, A. T. Davis and K. A. Robillard, *Environ. Toxicol. Chem.*, 1998, **17**, 642-649.
288. S. Daniele, C. Bragato, M. A. Baldo and I. Ciani, *Talanta*, 2008, **77**, 235-240.
289. X.-C. Fu, X. Chen, Z. Guo, L.-T. Kong, J. Wang, J.-H. Liu and X.-J. Huang, *Electrochim. Acta*, 2010, **56**, 463-469.
290. R. P. Akkermans, J. C. Ball, F. Marken and R. G. Compton, *Electroanalysis*, 1998, **10**, 26-32.
291. C. Agra-Gutiérrez, J. L. Hardcastle, J. C. Ball and R. G. Compton, *Analyst*, 1999, **124**, 1053-1057.
292. F. Marken, T. O. Rebbitt, J. Booth and R. G. Compton, *Electroanalysis*, 1997, **9**, 19-22.
293. M. Kopanica and F. Vydra, *J. Electroanal. Chem. Interfacial Electrochem.*, 1971, **31**, 175-181.
294. S. P. Perone, *Anal. Chem.*, 1963, **35**, 2091-2094.
295. J. Wang, R. Li and H. Huiliang, *Electroanalysis*, 1989, **1**, 417-421.
296. F. Wang, C. Xin, Y. Wu, Y. Gao and B. Ye, *J. Anal. Chem.*, 2011, **66**, 60-65.
297. L. Liu, C. Wang and G. Wang, *Anal. Methods*, 2013, **5**, 5812-5822.
298. A. Ceresa, A. Radu, S. Peper, E. Bakker and E. Pretsch, *Anal. Chem.*, 2002, **74**, 4027-4036.
299. K. H. Ng, H. Liu and R. M. Penner, *Langmuir*, 2000, **16**, 4016-4023.
300. M. E. Hyde, C. E. Banks and R. G. Compton, *Electroanalysis*, 2004, **16**, 345-354.
301. R. G. Barradas, S. Fletcher and S. Szabo, *Can. J. Chem.*, 1977, **55**, 4037-4044.
302. Y. Wan, Z. Guo, X. Jiang, K. Fang, X. Lu, Y. Zhang and N. Gu, *J. Colloid Interface Sci.*, 2013, **394**, 263-268.
303. J. J. Mock, M. Barbic, D. R. Smith, D. A. Schultz and S. Schultz, *J. Chem. Phys.*, 2002, **116**, 6755-6759.
304. B. Kerem, J. Rommens, J. Buchanan, D. Markiewicz, T. Cox, A. Chakravarti, M. Buchwald and L. Tsui, *Science*, 1989, **245**, 1073-1080.
305. M. R. Knowles and P. R. Durie, *N. Engl. J. Med.*, 2002, **347**, 439-442.
306. S. M. Rowe, S. Miller and E. J. Sorscher, *N. Engl. J. Med.*, 2005, **352**, 1992-2001.
307. M. J. Goldman, G. M. Anderson, E. D. Stolzenberg, U. P. Kari, M. Zasloff and J. M. Wilson, *Cell*, 1997, **88**, 553-560.
308. T. Z. Khan, J. S. Wagener, T. Bost, J. Martinez, F. J. Accurso and D. W. Riches, *Am. J. Respir. Crit. Care. Med.*, 1995, **151**, 1075-1082.
309. B. P. O'Sullivan and S. D. Freedman, *Lancet*, 2009, **373**, 1891-1904.
310. P. M. Farrell, B. J. Rosenstein, T. B. White, F. J. Accurso and C. Castellani, *J. Pediatr.*, 2008, **153**, 4.

311. M. Seia, L. Costantino, V. Paracchini, L. Porcaro, P. Capasso, D. Coviello, C. Corbetta, E. Torresani, D. Magazzu, V. Consalvo, A. Monti, D. Costantini and C. Colombo, *Clin. Biochem.*, 2009, **42**, 611-616.
312. A. Green and J. Kirk, *Ann. Clin. Biochem.*, 2007, **44**, 25-34.
313. J. Coakley, S. Scott and J. Doery, *Clin. Biochem. Rev.*, 2006, **27**, 1-7.
314. J. H. Baumer, *Arch. Dis. Child.*, 2003, **88**, 1126-1127.
315. V. A. LeGrys, J. R. Yankaskas, L. M. Quittell, B. C. Marshall, P. J. Mogayzel, Jr. and F. Cystic Fibrosis, *J. Pediatr.*, 2007, **151**, 85-89.
316. I. Sermet-Gaudelus, A. Munck, M. Rota, M. Roussey, D. Feldmann and T. Nguyen-Khoa, *Arch. Pediatr.*, 2010, **17**, 1349-1358.
317. J. R. Yankaskas, B. C. Marshall, B. Sufian, R. H. Simon and D. Rodman, *Chest*, 2004, **125**, 1S-39S.
318. M. Wilschanski and P. R. Durie, *Gut*, 2007, **56**, 1153-1163.
319. The Association for Clinical Biochemistry, Guidelines developed with ACB involvement, Guidelines for the Performance of the Sweat Test for the Investigation of Cystic Fibrosis in the UK, http://www.acb.org.uk/docs/default-source/committees/scientific/guidelines/acb/sweat-guideline-v2-1.pdf (accessed 15 July 2015).
320. I. J. Schulz, *J. Clin. Invest.*, 1969, **48**, 1470-1477.
321. Sherwood Scientific Ltd, Model 926 Chloride Analyzer, http://www.sherwood-scientific.com/chloride/chloridemeters.html. (Accessed 29 Mar 2013).
322. A. G. Brolo and S. D. Sharma, *Electrochim. Acta*, 2003, **48**, 1375-1384.
323. K. Kulthong, S. Srisung, K. Boonpavanitchakul, W. Kangwansupamonkon and R. Maniratanachote, *Part. Fibre Toxicol.*, 2010, **7**, 8.
324. C. J. Harvey, R. F. LeBouf and A. B. Stefaniak, *Toxicol. In Vitro*, 2010, **24**, 1790-1796.
325. M. B. Zimmermann, *Endocr. Rev.*, 2009, **30**, 376-408.
326. G. M. Abrams and P. R. Larsen, *J. Clin. Invest.*, 1973, **52**, 2522-2531.
327. F. Delange, M. Camus and A. M. Ermans, *J. Clin. Endocrinol. Metab.*, 1972, **34**, 891-895.
328. P. Laurberg, C. Cerqueira, L. Ovesen, L. B. Rasmussen, H. Perrild, S. Andersen, I. B. Pedersen and A. Carle, *Best Pract. Res. Clin. Endocrinol. Metab.*, 2010, **24**, 13-27.
329. E. Nyström, G. E. B. Berg, S. K. G. Jansson, O. Tørring and S. V. Valdemarsson, *Thyroid Disease in Adults*, Springer, Berlin, Germany, 2011.
330. F. Delange, *Postgrad. Med. J.*, 2001, **77**, 217-220.
331. E. B. Sandell and I. M. Kolthoff, *Mikrochim. Acta*, 1937, **1**, 9-25.
332. S. Pino, S.-L. Fang and L. E. Braverman, *Clin. Chem. (Washington, DC, U. S.),* 1996, **42**, 239-243.
333. Assessment of Iodine Deficiency Disorders and Monitoring their Elimination, WHO, http://www.who.int/nutrition/publications/micronutrients/iodine_deficiency/WHO_NHD_01.1/en/ (Accessed 15 July 2015).
334. C. Villagran, C. E. Banks, C. Hardacre and R. G. Compton, *Anal. Chem.*, 2004, **76**, 1998-2003.
335. D. A. Skoog, D. M. West, F. J. Holler and S. R. Crouch, *Fundamentals of Analytical Chemistry*, Thompson Brooks/Cole, Belmont, 2004.
336. H. S. Toh, C. Batchelor-McAuley, K. Tschulik and R. G. Compton, *Sci. China: Chem.*, 2014, **57**, 1199-1210.
337. S. Riedel and M. Kaupp, *Coord. Chem. Rev.*, 2009, **253**, 606-624.
338. S. Lilienfeld and C. E. White, *J. Am. Chem. Soc.*, 1930, **52**, 885-892.
339. T. E. Graedel, J. P. Franey, G. J. Gualtieri, G. W. Kammlott and D. L. Malm, *Corros. Sci.*, 1985, **25**, 1163-1180.
340. J. D. Sinclair, *J. Electrochem. Soc.*, 1982, **129**, 33-40.
341. R. A. Bell and J. R. Kramer, *Environ. Toxicol. Chem.*, 1999, **18**, 9-22.
342. I. G. Dance, K. J. Fisher, R. M. H. Banda and M. L. Scudder, *Inorg. Chem.*, 1991, **30**, 183-187.
343. L.-O. Andersson, *J. Polym. Sci., Part A-1: Polym. Chem.,* 1972, **10**, 1963-1973.

344. W. Leesutthiphonchai, W. Dungchai, W. Siangproh, N. Ngamrojnavanich and O. Chailapakul, *Talanta*, 2011, **85**, 870-876.
345. M. Sureshkumar, D. Y. Siswanto and C. K. Lee, *J. Mater. Chem.*, 2010, **20**, 6948-6955.
346. C. Marambio-Jones and E. M. V. Hoek, *J. Nanopart. Res.*, 2010, **12**, 1531-1551.
347. T. Mitsudome, S. Arita, H. Mori, T. Mizugaki, K. Jitsukawa and K. Kaneda, *Angew. Chem. Int. Ed.*, 2008, **120**, 8056-8058.
348. L. Shang and S. Dong, *Biosens. Bioelectron.*, 2009, **24**, 1569-1573.
349. S. Chen, H. Gao, W. Shen, C. Lu and Q. Yuan, *Sens. Actuators, B*, 2014, **190**, 673-678.
350. J. Zhu, X. Song, L. Gao, Z. Li, Z. Liu, S. Ding, S. Zou and Y. He, *Biosens. Bioelectron.*, 2014, **53**, 71-75.
351. M. E. Samberg, S. J. Oldenburg and N. A. Monteiro-Riviere, *Environ. Health Perspect.*, 2010, **118**, 407-413.
352. P. V. AshaRani, G. K. M. Low, M. P. Hande and S. Valiyaveettil, *ACS Nano*, 2009, **3**, 279-290.
353. Y. S. Kim, J. S. Kim, H. S. Cho, D. S. Rha, J. M. Kim, J. D. Park, B. S. Choi, R. Lim, H. K. Chang, Y. H. Chung, I. H. Kwon, J. Jeong, B. S. Han and I. J. Yu, *Inhalation Toxicol.*, 2008, **20**, 575-583.
354. S. M. Ansar, G. S. Perera, P. Gomez, G. Salomon, E. S. Vasquez, I. W. Chu, S. Zou, C. U. Pittman, K. B. Walters and D. Zhang, *J. Phys. Chem. C*, 2013, **117**, 27146-27154.
355. A. Andrieux-Ledier, B. Tremblay and A. Courty, *Langmuir*, 2013, **29**, 13140-13145.
356. C. Battocchio, C. Meneghini, I. Fratoddi, I. Venditti, M. V. Russo, G. Aquilanti, C. Maurizio, F. Bondino, R. Matassa, M. Rossi, S. Mobilio and G. Polzonetti, *J. Phys. Chem. C*, 2012, **116**, 19571-19578.
357. C. Levard, E. M. Hotze, B. P. Colman, A. L. Dale, L. Truong, X. Y. Yang, A. J. Bone, G. E. Brown, Jr., R. L. Tanguay, R. T. Di Giulio, E. S. Bernhardt, J. N. Meyer, M. R. Wiesner and G. V. Lowry, *Environ. Sci. Technol.*, 2013, **47**, 13440-13448.
358. B. Kim, C. S. Park, M. Murayama and M. F. Hochella, *Environ. Sci. Technol.*, 2010, **44**, 7509-7514.
359. N. Zhang, F. Qu, H. Q. Luo and N. B. Li, *Biosens. Bioelectron.*, 2013, **42**, 214-218.
360. E. Csapó, R. Patakfalvi, V. Hornok, L. T. Tóth, A. Sipos, A. Szalai, M. Csete and I. Dékány, *Colloids Surf., B*, 2012, **98**, 43-49.
361. H. Li, Z. Cui and C. Han, *Sens. Actuators, B*, 2009, **143**, 87-92.
362. J. Lyons, A. Rauh-Pfeiffer, Y. M. Yu, X. M. Lu, D. Zurakowski, R. G. Tompkins, A. M. Ajami, V. R. Young and L. Castillo, *Proc. Natl. Acad. Sci. U. S. A.*, 2000, **97**, 5071-5076.
363. R. A. Patterson, D. J. Lamb and D. S. Leake, *Atherosclerosis*, 2003, **169**, 87-94.
364. A. Henglein, P. Mulvaney and T. Linnert, *Faraday Discuss.*, 1991, **92**, 31.
365. P. Mulvaney, M. Giersig and A. Henglein, *J. Phys. Chem.*, 1993, **97**, 7061-7064.
366. S. Krzewska and H. Podsiadły, *Polyhedron*, 1986, **5**, 937-944.
367. C. Levard, B. C. Reinsch, F. M. Michel, C. Oumahi, G. V. Lowry and G. E. Brown, *Environ. Sci. Technol.*, 2011, **45**, 5260-5266.

Appendix A

A. Theory for Section 4.1

For easy illustration of the equations, a one electron oxidation of a metallic NP, M, is considered.

$$M(s) \rightarrow M^{+}(aq) + e^{-}(m) \qquad \text{Equation A.1}$$

The Nernst expression for this oxidation is:

$$E = E_f^{\theta} + \frac{RT}{F} ln \frac{[M^{+}]}{[\,]^0} \qquad \text{Equation A.2}$$

where E is the applied potential, E_f^{θ} is the formal potential, R is the gas constant, T is the temperature, F is the Faraday's constant, $[M^{+}]$ is the surface concentration of metal ions at the electrode and $[\,]^0$ is the standard concentration of 1 mol dm^{-3}.

The applied potential E is defined as:

$$E = E_i + \upsilon t \qquad \text{Equation A.3}$$

where E_i is the initial potential applied, υ is the scan rate and t is the time.

Combining Equation A.2 and A.3, we obtain an expression of $[M^{+}]$, surface concentration of metal ions at the electrode surface, in terms of potential and time.

$$E_i + \upsilon t = E_f^{\theta} + \frac{RT}{F} ln \frac{[M^{+}]}{[\,]^0} \qquad \text{Equation A.4}$$

$$\frac{F}{RT}\left(\upsilon t + E_i - E_f^{\theta}\right) = ln \frac{[M^{+}]}{[\,]^0} \qquad \text{Equation A.5}$$

$$[M^{+}] = [\,]^0 \exp(\theta) \qquad \text{Equation A.6}$$

where $\theta = \frac{F\upsilon t}{RT} + \theta_i$ and $\theta_i = \frac{F}{RT}\left(E_i - E_f^{\theta}\right)$

Since the surface area of a spherical nanoparticle, A_{NP}, can be written as:

$$A_{NP} = 4\pi(r_{NP})^2 \quad \text{Equation A.7}$$

where r_{NP} is the radius of the nanoparticle. The number of atoms in a nanoparticle, N_{NP}, is given as:

$$N_{NP} = \frac{4\pi}{3}(r_{NP})^3 \cdot \frac{\rho}{A_r} \quad \text{Equation A.8}$$

where ρ is the density and A_r is the atomic molecular mass.

Therefore, the rate of change in the number of moles of metallic ions at a nanoparticle with regards to the radius of the nanoparticle, dN_{NP}/dr_{NP} can be defined as:

$$\frac{dN_{NP}}{dr_{NP}} = 4\pi(r_{NP})^2 \cdot \frac{\rho}{A_r} \quad \text{Equation A.9}$$

From Equation A.8, the charge passed under a voltammetric peak, Q, can defined as:

$$Q = n_{NP} \cdot \frac{4\rho}{3A_r} \cdot \pi nF\left((r_{NP})^3 - (r_{NP,t})^3\right) \quad \text{Equation A.10}$$

where at time t, where the radius of nanoparticle is expressed as $r_{NP,t}$ and at time equals to zero and the radius of the nanoparticles is defined as r_{NP}.

The predicted current can be obtained by differentiating the charge, Q, with regards to potential, E.

$$I = \upsilon \frac{dQ}{dE} \quad \text{Equation A.11}$$

A.1 Reversible Electron Transfer, Case 4

The surface coverage of the nanoparticles, Γ_{NP}, is defined as:

$$\Gamma_{NP} = \frac{n_{NP}}{A_{elec}} \quad \text{Equation A.12}$$

where n_{NP} is the number of nanoparticles on the electrode surface and A_{elec} is the area of the electrode.

At Case 4 diffusional regime, there is linear diffusion of metallic ions away from the electrode surface. Hence, the flux across the electrode, j, will be the combination of the rate of metal ions generated at all of the nanoparticles.

$$j = \frac{1}{A_{elec}} \cdot \frac{dN_{NP}}{dt} \cdot n_{NP} \qquad \text{Equation A.13}$$

where dN_{NP}/dt is the rate of change of the concentration of metallic atoms at each nanoparticle with regards to time.

Putting Equation A.12 into Equation A.13, we obtain an expression of flux in terms of nanoparticle surface coverage.

$$j = \Gamma_{NP} \cdot \frac{dN_{NP}}{dt} \qquad \text{Equation A.14}$$

Combining Equation A.9 with Equation A.14,

$$j = \Gamma_{NP} \cdot 4\pi(r_{NP})^2 \cdot \frac{\rho}{A_r} \cdot \frac{dr_{NP}}{dt} \qquad \text{Equation A.15}$$

The flux can also be defined as:

$$j = -\frac{D}{\delta}[M^+] \qquad \text{Equation A.16}$$

where the surface concentration of $[M^+]$ generated at the electrode surface is related to D, the diffusion coefficient and δ is the diffusional layer thickness. The negative sign accounts for the phenomenon of moving down a concentration gradient.

Combining Equation A.15 with Equation A.16, we can express the radius of the nanoparticle at time t.

$$\Gamma_{NP} \cdot 4\pi(r_{NP})^2 \cdot \frac{\rho}{A_r} \cdot \frac{dr_{NP}}{dt} = -\frac{D}{\delta}[M^+] \qquad \text{Equation A.17}$$

$$(r_{NP})^2\, dr = -\frac{D}{4\pi\delta\Gamma_{NP}} \cdot \frac{A_r}{\rho} \cdot [M^+]\, dt \qquad \text{Equation A.18}$$

Equation A.18 is integrated with the limits of at time t, where the radius of nanoparticle is expressed as $r_{NP,t}$ and at time equals to zero and the radius of the nanoparticles is defined as r_{NP}.

$$\int_{r_{NP}}^{r_{NP,t}} (r_{NP})^2\, dr = \int_0^t -\frac{D}{4\pi\delta\Gamma_{NP}} \cdot \frac{A_r}{\rho} \cdot [M^+]\, dt \qquad \text{Equation A.19}$$

Substituting Equation A.6 into Equation A.19,

$$\int_{r_{NP}}^{r_{NP,t}} (r_{NP})^2\, dr = \int_0^t -\frac{D}{4\pi\delta\Gamma_{NP}} \cdot \frac{A_r}{\rho} \cdot [\,]^0 \cdot \exp\theta\, dt \qquad \text{Equation A.20}$$

Considering $\theta = \frac{F\upsilon t}{RT} + \theta_i$ and $\theta_i = \frac{F}{RT}\left(E_i - E_f^{\theta}\right)$,

$$\int_{r_{NP}}^{r_{NP,t}} (r_{NP})^2\, dr = -\frac{D}{4\pi\delta\Gamma_{NP}} \cdot \frac{A_r}{\rho} \cdot [\,]^0 \cdot \exp\theta_i \cdot \int_0^t \exp\frac{F\upsilon t}{RT}\, dt \qquad \text{Equation A.21}$$

If we choose the starting potential, E_i, to be the much more negative than the formal potential,E_f^{θ}, Equation A.21 can be expressed as:

$$\int_{r_{NP}}^{r_{NP,t}} (r_{NP})^2\, dr = -\frac{D}{4\pi\delta\Gamma_{NP}} \cdot \frac{A_r}{\rho} \cdot [\,]^0 \cdot exp\theta_i \int_0^t \exp\frac{F\upsilon t}{RT}\, dt \qquad \text{Equation A.22}$$

$$\left[\frac{1}{3} \cdot (r_{NP})^3\right]_{r_{NP}}^{r_{NP,t}} = -\frac{D}{4\pi\delta\Gamma_{NP}} \cdot \frac{A_r}{\rho} \cdot [\,]^0 \cdot \exp\theta_i \cdot \frac{RT}{\upsilon F}\left[exp\frac{F\upsilon t}{RT}\right]_0^t \qquad \text{Equation A.23}$$

$$\frac{1}{3}\left((r_{NP,t})^3 - (r_{NP})^3\right) = -\frac{D}{4\pi\delta\Gamma_{NP}} \cdot \frac{A_r}{\rho} \cdot [\,]^0 \cdot \frac{RT}{\upsilon F} \cdot exp\theta \qquad \text{Equation A.24}$$

$$r_{NP,t} = \left((r_{NP})^3 - \frac{3D}{4\pi\delta\Gamma_{NP}} \cdot \frac{A_r}{\rho} \cdot [\,]^0 \cdot \frac{RT}{\upsilon F} \cdot exp\theta\right)^{1/3} \qquad \text{Equation A.25}$$

Hence, plotting Equation A.25 with various time will allow one to determine the change in nanoparticle radius under Case 4 diffusion regime.

A.2 Reversible Electron Transfer, Case 2

Considering Equation A.1, the diffusion only mass transport limiting current, I_{lim}, for a spherical nanoparticle on a flat electrode is given as:

$$I_{lim} = 4\pi nFCDr_{NP}ln2 \qquad \text{Equation A.26}$$

where C is the concentration of the reactant. Given that the current generated at a single nanoparticle is,

$$I = -FA_{NP}j_{NP} \qquad \text{Equation A.27}$$

where the surface area of the nanoparticle, A_{NP}, is the area at which Equation A.1 takes place. j_{NP} is the flux at a single nanoparticle. Hence,

$$j_{NP} = -\frac{I}{nFA_{NP}} \quad \text{Equation A.28}$$

Considering the current generated at the nanoparticle is related to the concentration of M^+; thus, at limiting current, substituting Equation A.26 into Equation A.28 gives:

$$j_{NP} = -\frac{4\pi[M^+]Dr_{NP}ln2}{A_{NP}} \quad \text{Equation A.29}$$

With a further substitution of Equation A.7 into Equation A.29,

$$j_{NP} = -\frac{Dln2[M^+]}{r_{NP}} \quad \text{Equation A.30}$$

At a single nanoparticle, the flux of ions is equal to the amount of ions generated by metal oxidation at the electrode surface. Hence, the flux of metal ion at a single nanoparticle, j_{NP}, can be defined as:

$$j_{NP} = \frac{1}{A_{NP}} \cdot \frac{dN_{NP}}{dt} \quad \text{Equation A.31}$$

where A_{NP} is the surface area of a nanoparticle and dN_{NP}/dt is the change in the number of moles of metal atoms with regards to time.

Substituting Equation A.7 and A.9 into Equation A.31, we get an expression for flux at a single nanoparticle, j_{NP}, as a function of the rate of change of nanoparticle radius with time, dr_{NP}/dt.

$$j_{NP} = \frac{1}{4\pi(r_{NP})^2} \cdot \frac{\rho}{A_r} \cdot 4\pi(r_{NP})^2 \cdot \frac{dr_{NP}}{dt} \quad \text{Equation A.32}$$

$$j_{NP} = \frac{\rho}{A_r} \cdot \frac{dr_{NP}}{dt} \quad \text{Equation A.33}$$

Combining Equation A.30 and A.33, we obtain:

$$j_{NP} = \frac{Dln2[M^+]}{r_{NP}} = -\frac{\rho}{A_r} \cdot \frac{dr_{NP}}{dt} \quad \text{Equation A.34}$$

Hence, Equation A.34 can be solved to obtain an expression of $r_{NP,t}$, nanoparticle radius at time t, in terms of time:

$$r_{NP}\,dr = -\frac{Dln2[M^+]A_r}{\rho}\,dt \qquad \text{Equation A.35}$$

Equation A.35 is solved with the limits of time t and zero, where the radius of nanoparticle is expressed as $r_{NP,t}$ and r_{NP} respectively. The starting potential, E_i, is set to be much more negative than the formal potential, E_f^{θ}. Substituting in Equation A.6,

$$\int_{r_{NP}}^{r_{NP,t}} r_{NP}\,dr = \int_0^t -\frac{Dln2A_r}{\rho}[\,]^0 exp\theta\,dt \qquad \text{Equation A.36}$$

$$\frac{1}{2}[r_{NP}]_{r_{NP}}^{r_{NP,t}} = -\frac{Dln2A_r[\,]^0}{\rho} exp\theta_i \int_0^t exp\frac{F\upsilon t}{RT}\,dt \qquad \text{Equation A.37}$$

$$\frac{1}{2}\left((r_{NP,t})^2 - (r_{NP})^2\right) = -\frac{Dln2A_r[\,]^0}{\rho}\cdot\frac{RT}{F\upsilon}\cdot exp\theta \qquad \text{Equation A.38}$$

Hence, the radius of the nanoparticle at time t can be expressed as:

$$r_{NP,t} = \left((r_{NP})^2 - \frac{2ln2\mathrm{D}A_r[\,]^0}{\rho}\cdot\frac{RT}{F\upsilon}\cdot exp\theta\right)^{1/2} \qquad \text{Equation A.39}$$

Hence, plotting Equation A.39 with various time will allow one to determine the change in nanoparticle radius under Case 2 diffusion regime.

A.3 Irreversible Electron Transfer

Considering the irreversible reaction of Equation A.1 and A.27, the Butler-Volmer expression at a single nanoparticle is expressed as:

$$I = -FA_{NP}k^0\left(exp\left[-\frac{\alpha F\eta}{RT}\right]\cdot[M^+] - exp\left[\frac{\beta F\eta}{RT}\right]\cdot[\mathrm{M}]\right) \qquad \text{Equation A.40}$$

where k^0 is the rate constant, $[M^+]$ is the surface concentration of the metallic ion, α and β are transfer coefficient which sums up to be 1. $[M]$ is the surface concentration of the metal, which is taken to be unity since it is a solid. Hence, Equation A.40 can be rewritten as:

$$I = -FA_{NP}k^0\left(exp\left[-\frac{\alpha F\eta}{RT}\right]\cdot[M^+]\right) \quad \text{Equation A.41}$$

From Equation A.27 and A.41, we know that the flux at a single nanoparticle can be expressed as:

$$j_{NP} = -k^0\left(exp\left[-\frac{\alpha F\eta}{RT}\right]\cdot[M^+]\right) \quad \text{Equation A.42}$$

Since it is an irreversible reaction, the electrochemical response is not limited by mass transport and all the equations in Section A.3 can be applicable to all four cases of diffusional regime.

Substituting Equation A.6 into Equation A.42,

$$j_{NP} = -k^0\left(exp\left[-\frac{\alpha F\eta}{RT}\right]\cdot[\,]^0\exp\theta\right) \quad \text{Equation A.43}$$

$$j_{NP} = -k^0\left(exp\left[-\frac{\alpha F\eta}{RT}\right]\cdot[\,]^0\exp\frac{F(E-E_f^\theta)}{RT}\right) \quad \text{Equation A.44}$$

and $E\text{-}E_f^\theta$ equals to the overpotential η. Thus,

$$j_{NP} = -k^0\left(exp\left[-\frac{\alpha F\eta}{RT}\right]\cdot[\,]^0\exp\frac{F\eta}{RT}\right) \quad \text{Equation A.45}$$

$$j_{NP} = -k^0\left([\,]^0 exp\left[\frac{(1-\alpha)F\eta}{RT}\right]\right) \quad \text{Equation A.46}$$

Since Equation A.1 is an one electron reaction, α plus β equals to one. Hence, Equation A.46 can be written as:

$$j_{NP} = -k^0([\,]^0 exp[\beta\theta]) \quad \text{Equation A.47}$$

Since it is an irreversible reaction, the equation for flux (Equation A.33) also holds true for this case. Thus, combining Equation A.33 and A.47,

$$j_{NP} = -k^0([\,]^0 exp[\beta\theta]) = \frac{\rho}{A_r}\cdot\frac{dr_{NP}}{dt} \quad \text{Equation A.48}$$

$$dr_{NP} = -k^0\cdot\frac{A_r}{\rho}\cdot([\,]^0 exp[\beta\theta])\,dt \quad \text{Equation A.49}$$

Equation A.49 is solved with the limits of time t and zero, where the radius of nanoparticle is expressed as $r_{NP,t}$ and r_{NP} respectively. The starting potential, E_i, is set to be much more negative than the formal potential, E_f^{θ}.

$$\int_{r_{NP}}^{r_{NP,t}} dr_{NP} = \int_0^t -k^0 \cdot \frac{A_r}{\rho} \cdot ([\,]^0 exp[\beta\theta])\, dt \qquad \text{Equation A.50}$$

$$r_{NP,t} - r_{NP} = -k^0 \cdot \frac{A_r}{\rho} \cdot [\,]^0 \cdot exp\theta_i \int_0^t \cdot \left(exp\left[\frac{\beta \upsilon t F}{RT}\right]\right) dt \qquad \text{Equation A.51}$$

$$r_{NP,t} = r_{NP} - k^0 \cdot \frac{A_r}{\rho} \cdot [\,]^0 \cdot \frac{RT}{\beta \upsilon F} exp[\beta\theta] \qquad \text{Equation A.52}$$

Hence, plotting Equation A.52 with various time will allow one to determine the change in nanoparticle radius under irreversible oxidation.